Dissertation
submitted to the
Combined Faculty of Mathematics, Engineering and Natural Sciences
of Heidelberg University, Germany
for the degree of
Doctor of Natural Sciences

Put forward by

Jonas Kuhn
born in Sigmaringen, Germany

Oral examination: 12 May 2022

Novel approaches to the analysis of volcanic degassing

Referees: Prof. Dr. Ulrich Platt

Prof. Dr. Thomas Leisner

Novel approaches to the analysis of volcanic degassing

Volcanic gases are part of the fundamental geochemical cycles on Earth. They provide information on the planet's interior and influence the climate and the oxidation state of the atmosphere. However, there remain severe inconsistencies between field observations and models within the field of volcanic gas analysis. This cumulative thesis aims to improve the understanding of volcanic degassing processes by combining three different but related approaches: (1) A model for the chemical kinetics within the early turbulent mixing process of hot magmatic gases with atmospheric air is developed. It questions conventional approaches that assume thermodynamic equilibrium during the gas emission phase and, hence, has severe implications for current interpretations of volcanic gas measurements. (2) A high-resolution spectrograph is conceptualised and developed. The resolving power of ca. 10^5 exceeds that of conventional field-deployable instruments by more than two orders of magnitude. Its high light throughput and mobility enables a range of new volcanic measurements, such as the quantification of the hydroxyl radical, which is an important intermediate species in hot volcanic gases. (3) A novel imaging technique for volcanic trace gases is developed. It significantly enhances the accuracy of volcanic volatile flux quantification and shows great potential for spatially resolving the still poorly constrained halogen conversion processes within volcanic plumes. Prototypes of both instrument developments demonstrate their anticipated performance in field measurements. The techniques introduced in this thesis also exhibit extensive potential for further atmospheric remote sensing applications including improved measurements of greenhouse gases, air pollutants, atmospheric oxidants, or plant fluorescence.

Neue Ansätze zur Untersuchung vulkanischer Gase

Vulkangase sind ein Bestandteil der grundlegenden geochemischen Stoffkreisläufe der Erde. Sie bieten Einblick in das Innere des Planeten und beeinflussen das Klima und den Oxidationszustand der Atmosphäre. Auf dem Gebiet der Vulkangasanalyse verbleiben jedoch bedeutende Abweichungen zwischen Feldbeobachtungen und Modellrechnungen. Diese kumulative Arbeit hat das Ziel ein verbessertes Verständnis von Vulkangasemissionen zu erreichen. Sie umfasst die Ergebnisse von drei unterschiedlichen aber verwandten Ansätzen: (1) Ein kinetisches Chemiemodell wurde entwickelt, welches die turbulente Mischung von magmatischen Gasen mit Luft aus der Atmosphäre in frühen Emissionsstadien simuliert. Da es bisherige Ansätze, die von thermodynamischem Gleichgewicht während der Gasemission ausgehen, maßgeblich in Frage stellt, hat es weitreichende Folgen für derzeitig gebräuchliche Interpretationen vulkanischer Gasmessungen. (2) Ein hochauflösender Spektrograph wurde konzipiert und entwickelt. Das Auflösungsvermögen von etwa 10^5 übertrifft das von gewöhnlichen feldtauglichen Spektrographen um mehr als zwei Größenordnungen. Sein hoher Lichtdurchsatz und seine Mobilität ermöglichen eine Reihe neuer Messungen an Vulkanen, wie etwa den Nachweis von Hydroxyl Radikalen, welche eine wichtige Zwischenspezies in der Chemie heißer Vulkangase darstellen. (3) Es wurde eine neuartige bildgebende Messtechnik für Vulkangase entwickelt. Diese verbessert die Genauigkeit vulkanischer Emissionsflussmessungen und kann räumlich aufgelöste Beobachtungen zur nach wie vor viel diskutierten Halogenchemie in Vulkanfahnen ermöglichen. Prototypen beider Instrumentenentwicklungen wurden erfolgreich in Feldmessungen getestet. Die beiden in dieser Arbeit entwickelten Messtechniken zeigen darüber hinaus großes Potenzial für andere Anwendungen in Fernerkundungsmessungen in der Atmosphäre, etwa verbesserte Messungen von Treibhausgasen, Luftschadstoffen, atmosphärischer Oxidationsmittel oder der Fluoreszenz von Pflanzen.

Contents

1 Introduction

While the Universe unfolds at the firmament like an open book, Earth's interior keeps its secrets more efficiently. Whoever wants to learn about Earth's interior and its interaction with the atmosphere sooner or later finds her- or himself at a volcano.

Unknown

This is a thesis on the analysis of volcanic degassing processes and on how it may improve through the development of novel field observation tools and modeling approaches. This first chapter outlines volcanic degassing and central scientific questions in that field (Sect. 1.1). It introduces state-of-the-art analysis tools (Sect. 1.2) and the concepts that underlie the here proposed improvements (Sect. 1.3). Then, the four articles that make up the core part of this cumulative thesis are shortly introduced (Sect. 1.4).

1.1 Volcanic degassing in the Earth system

Volcanism is a fundamental part of the global geochemical cycles on Earth, which include many processes covering a vast range of time scales. Tectonic movements happen within many millennia and for instance induce subduction processes that drag parts of the upper crust down into greater depths, where they may contribute to the formation of new magma. Formation processes and rising within the planets interior causes the release of dissolved volatile magmatic components. Degassing processes, i.e. the release of gases from the magma into the atmosphere, happen on timescales of minutes to seconds and can proceed in different ways. For instance, gas bubbles form, coalesce, and either rise within the melt or carry it upward, before eventually reaching the surface. Atmospheric deposition processes then return the elements to the crust.
Divergent tectonic movements, in contrast, enable the release of melts from the upper mantle, a fundamentally different source. Here, deep formation and rising of magma, as well as further processing at shallower depths determine the magmatic gas composition.
Typically water (H_2O) is the most abundant volatile within magmatic melts, followed by carbon dioxide (CO_2), sulphur and halogen species, hydrogen, and further trace components. The degassing history, e.g. the pressure at the time of degassing as well as the interaction of gas bubbles with their hosting magma, further influences the proportions of these magmatic gas constituents before the gas leaves the magma body.
Subsequently, the magmatic gas interacts with some kind of magma-atmosphere interface that may include vents, fissures, hydrothermal systems, or even the oceans. If directly emitted into the atmosphere (e.g. at an open lava lake) the hot magmatic gas is subject to a highly dynamic atmospheric mixing and cooling process.
For comprehensive summaries on volcanic degassing see e.g. Symonds et al. (1994); Giggenbach (1996); Oppenheimer et al. (2014).

1.1.1 Messages from the planet's interior

Volcanic gases can provide an otherwise hard-to-reach insight into the planet's interior. Quantitative measurements of the composition of gases emitted by a volcano allow the determination of their magmatic source. Moreover, information on deep magma processing and mixing can be imprinted to the measured gas composition. From that, and in combination with other geological observations, basic conclusions on the tectonic setting of the volcano can be drawn (e.g. Oppenheimer et al., 2014).
Dynamic magmatic processes can influence the gas composition through differences in the solubility of volatiles in magma. In turn, these dynamics are often closely linked or even driven by volatile degassing. For instance, degassing can alter the viscosity or density of magma and thus induce buoyancy driven magma movement (e.g. Giggenbach, 1996). Magma dynamics is furthermore tied to the inner physical structure of the volcano. The analysis of (particularly temporally resolved) gas measurements can thus reveal information on volcano specific patterns of magma dynamics and shallow inner volcanic structures (e.g. Burton et al., 2007). Once signatures within the volcanic gas composition are linked to magma dynamics, gas measurements can be used for volcano monitoring and eruption forecasting (e.g. Giggenbach, 1996; Aiuppa et al., 2007b).

1.1.2 Volcanic degassing and Earth's atmosphere

It is very likely that magmatic gas emissions have crucially determined the evolution of Earth's atmosphere and still do so. Besides influencing the climate on long timescales through the release of greenhouse gases (see e.g. Kasting, 1993), volcanic gas emissions might have significantly contributed to oxidising the early atmosphere (e.g. Holland, 2002; Halevy et al., 2010; Gaillard et al., 2011), ultimately facilitating life as we know it. Apart from such long-term influences, explosive volcanic emissions can lead to severe short-term impacts on Earth's climate and other atmospheric processes, like for instance stratospheric ozone destruction and changes in global atmospheric circulation (e.g. Robock, 2000).
In addition to such global phenomena, volcanic degassing affects its local to regional surroundings. The emitted gases substantially alter the atmospheric state as they dilute in air and move leeward in so-called volcanic plumes. For instance, sulfur amounts are drastically enhanced and reactive halogen chemistry can lead to local depletion of ozone and reactive nitrogen (e.g. Gerlach, 2004; Surl et al., 2021) and to the oxidation of elemental mercury, causing its deposition in the environment (e.g. von Glasow, 2010). Generally, volcanic gases represent a health hazard for animals and vegetation (e.g. Delmelle et al., 2002).
Explosive degassing and the related large volcanic eruptions have an obvious local impact. The occurrence and intensity of volcanic eruptions remain difficult to foresee. Thus, the particularly devastating effects for instance of co-emitted stone fragments (pyroclasts) and ash, lava flows, or pyroclastic flows can have serious effects on human populations in volcanic vicinity and are not uncommonly deeply imprinted in their cultural heritage (Oppenheimer et al., 2018a).

1.1.3 Interfaces between magma and the atmosphere

The interfaces between magma and the atmosphere that the gases have to pass through (or the gas emission pathways) are manifold and primarily depend on the structure and type of the volcanic system (Fig. 1.1). These pathways of emission can strongly influence the gas composition and thereby often encrypt information on deeper processes. Besides submarine emissions or bubbling through crater lakes (Fig. 1.1f), magmatic gases often travel

Figure 1.1: This collection of photographs illustrates a selection of the manifold types of volcanic degassing. Panel (a) shows an example of explosive degassing in contrast to the so-called quiescent degassing scenarios depicted in panels (b)-(f).

considerable distances underground e.g. in vent systems, fissures or porous ground. There interaction with the host rock or hydrothermal systems alters the gas composition before reaching the atmosphere e.g. through vents, fumaroles (Fig. 1.1e) or diffusive degassing through the soil. These interactions are characterised by a broad range of heterogeneous processes and mixing with other geochemical (e.g. biogenic) volatile sources. The study of gas-rock and gas-fluid interactions allows the combined study of degassing pathways and deep processes from the measurements of e.g. fumarole emissions (e.g. Giggenbach, 1996).
Open vent volcanic systems account for a major part of global volcanic gas emissions (see Carn et al., 2017). There, for instance at open lava lakes, magmatic gases are emitted directly into the atmosphere (Fig. 1.1c). The influence of this kind of magma-atmosphere interface is less obvious and remains hardly studied and often neglected in the discussion of volcanic gas studies (e.g. Aiuppa et al., 2011; Oppenheimer et al., 2018b; Moussallam et al., 2019). The dynamic mixing process of hot magmatic gases with atmospheric air and the associated fast cooling is, however, likely to also significantly alter the volcanic gases from their initial magmatic composition. This is e.g. supported by the documented observation of flames related to direct emission of gas from lava (as discussed in e.g. Jaggar, 1917, see also Fig. 1.1d).
These dynamic high temperature interfaces can also play a central role for conversion processes during the later plume evolution (e.g. by the supply of radical species Gerlach, 2004; von Glasow, 2010; Roberts et al., 2019; Surl et al., 2021; Kuhn et al., 2022a) and thus, ultimately influence the impact of volcanic gas emissions on the atmosphere.

1.1.4 Secondary species formation in volcanic plumes

This section focuses on processes related to open vent volcanic systems. Secondary volcanic gas species are here defined as products of chemical conversion of magmatic gases after their emission from the magma body. They occur within the atmosphere on time scales between split seconds and weeks. The formation of secondary gas species in volcanic emissions is known to be an integral part of the atmospheric removal of volcanic gas species, such as the oxidation of the emitted SO_2, which – in atmospheric conditions – happens within hours to days (e.g. Beirle et al., 2014). In the following, two considerably faster processes involving secondary species formation in volcanic gases are introduced in more detail. Both processes are central parts of this thesis' research: (1) Reactive halogen chemistry can convert initially emitted bromine halide (HBr) to reactive bromine species within seconds to minutes. (2) Even earlier, in the hot and still scarcely diluted plume fast and non-linear chemical processes initiated by the intrusion of atmospheric O_2 causes fast oxidation of reduced plume constituents. Both processes are outlined in Fig. 1.2.

Reactive halogen chemistry in volcanic plumes

Fluorine and chlorine are the major halogen species emitted by volcanoes and have been in use to monitor volcanic activity (e.g. Menyailov, 1975). In the minutes-old plume these species (mostly in the form of HF of HCl) are rather inert. In contrast, the by a factor of 100-1000 lower, but highly reactive bromine emissions have a major influence on the local to regional atmospheric oxidation capacity. Furthermore, the remote quantification of reactive bromine species in the volcanic plumes (e.g. from satellites or autonomous ground-based platforms) bears a high potential for volcanic gas studies through global and long-term monitoring (e.g. Hörmann et al., 2013; Lübcke et al., 2014; Warnach et al., 2019).
The detection of bromine monoxide (BrO) in volcanic plumes (e.g. Bobrowski et al., 2003;

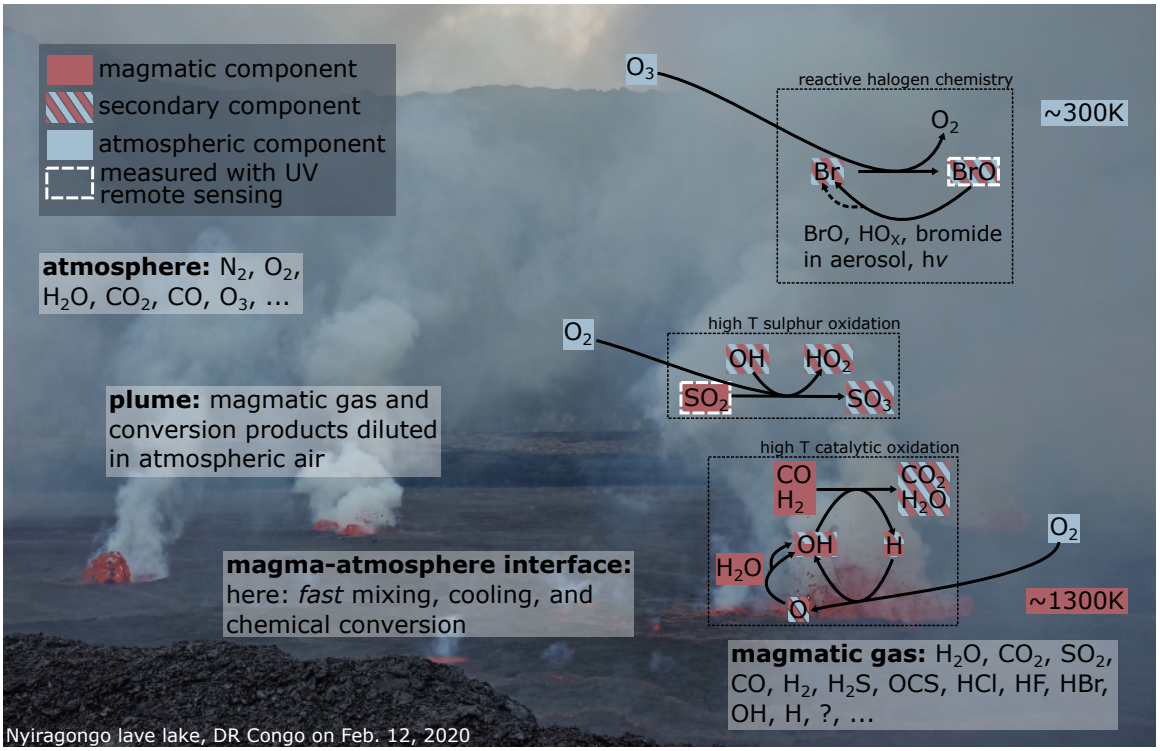

Figure 1.2: Schematic outline of some chemical conversion processes within the volcanic plume. In the early and hot emission plume, atmospheric O_2 initiates fast oxidation of reduced plume components, such as H_2O, H_2, and CO. During cooling, e.g. SO_2 oxidation converts OH to the more stable HO_2, which influences catalytic halogen oxidation in the cooled plume. Nowadays, only SO_2 and BrO are routinely measured with flexible and mobile UV remote sensing techniques.

Bobrowski and Platt, 2007) shed light on the chemical intricacy of volcanic gases interacting with Earth's atmosphere. The observed amounts of BrO (up to some hundred ppt in the plume) in combination with its high reactivity exclude the possibility of a direct magmatic emission (e.g. Gerlach, 2004). Instead, BrO continues to exist in catalytic chemical cycles involving atmospheric oxidants and photo chemistry. The present understanding of the process (see e.g. Gerlach, 2004; Bobrowski et al., 2007; von Glasow, 2010; Roberts et al., 2014, 2019; Surl et al., 2021) roughly follows that of reactive halogen observations in other parts of the troposphere (e.g. in the boundary layer of polar regions and at salt lakes, see Platt and Hönninger, 2003).

Primarily, bromine is emitted as HBr, which partly dissolves in acidified volcanic aerosol. Smaller amounts of co-emitted bromine atoms (Br, formed at high temperature, e.g. Gerlach, 2004) react with atmospheric ozone (O_3) to form BrO. Hydroperoxile radicals (HO_2) either of secondary volcanic origin (see below) or from the atmospheric background lead to the formation of HOBr, which can release gaseous bromine in form of Br_2 from the volcanic aerosol. Its rapid photolysis during daytime, forming two Br atoms, completes the chain branching step of this auto-catalytic process, often called 'bromine explosion' (e.g.

Wennberg, 1999):

$$\mathrm{Br} + \mathrm{O_3} \rightarrow \mathrm{BrO} + \mathrm{O_2} \tag{R1}$$
$$\mathrm{BrO} + \mathrm{HO_2} \rightarrow \mathrm{HOBr} + \mathrm{O_2} \tag{R2}$$
$$\mathrm{HOBr} + \mathrm{Br^-_{aq}} + \mathrm{H^+_{aq}} \rightarrow \mathrm{Br_2} + \mathrm{H_2O} \tag{R3}$$
$$\mathrm{Br_2} \xrightarrow{h\nu} 2\,\mathrm{Br} \tag{R4}$$
$$\mathrm{Br} + \mathrm{O_3} + \mathrm{HO_2} + \mathrm{Br^-_{aq}} + \mathrm{H^+_{aq}} \xrightarrow{h\nu} 2\,\mathrm{Br} + 2\,\mathrm{O_2} + \mathrm{H_2O} \tag{R5}$$

Variations of this cycle include the interplay with chlorine chemistry and reactive nitrogen species that replace HO_2 in R2 to accomplish a similar process (see Platt and Hönninger, 2003, for details). Chain termination can be invoked through the limited availability of atmospheric O_3, HO_2, or NO_2, as well as through BrO self reaction or depletion of Br^- in the aerosol phase.
Reactive halogen chemistry in volcanic plumes is still subject to scientific debate. Despite of the development of novel measurement techniques (Gutmann et al., 2018), substantial uncertainties remain in the processes' boundary conditions. Models of reactive halogen chemistry within the volcanic plume are still subject to major uncertainties. They rely on scarce field observations and show high sensitivities to the plume's composition at the time of emission, which remains poorly studied (see e.g. Bobrowski et al., 2007; Roberts et al., 2014, 2019; Surl et al., 2021, and below).
The further analysis of the long-term volcanic BrO records and their value for volcanic studies depends on the detailed understanding of the underlying chemical mechanisms.

Formation and impact of OH and HO_2 in the early and hot volcanic plume

In Earth's atmosphere, sub-ppt levels of OH radicals substantially determine the oxidation chemistry (see e.g. Stone et al., 2012, and references therein). The abundance of OH generally indicates environments characterised by fast chemical conversion, for instance combustion flames (e.g. Cattolica et al., 1982) or the oxyhydrogen explosion (Willbourn and Hinshelwood, 1946).
Due to the considerable dwelling times and the high temperatures, gases within the magma body are assumed to be in thermodynamic equilibrium (TE) (e.g. Gerlach and Nordlie, 1975; Symonds et al., 1994; Oppenheimer et al., 2018b). Thus, considerable amounts of OH and H (e.g. 1 ppm at 1370 K, Gerlach, 2004) are formed from the effective decay of water (Bonhoeffer and Reichardt, 1928) prior to their emission into the atmosphere. The following chemical mechanism can be exemplary for what happens, when atmospheric O_2 starts to mix with the hot magmatic gas (see Kuhn et al., 2022a, and Fig. 1.2):

$$\mathrm{O_2} + \mathrm{H} \rightarrow \mathrm{OH} + \mathrm{O} \tag{R6}$$
$$\mathrm{O_2} + \mathrm{H} \xrightarrow{M} \mathrm{HO_2} \tag{R7}$$
$$\mathrm{H_2O} + \mathrm{O} \rightarrow 2\,\mathrm{OH} \tag{R8}$$
$$\mathrm{R} + \mathrm{OH} \rightarrow \mathrm{RO} + \mathrm{H} \tag{R9}$$

OH rapidly oxidises the reduced plume species denoted by R (e.g. H_2, CO). The produced H atom subsequently initiates the formation of 3 further OH molecules via the chain branching steps (R6) and (R8). Thereby, OH levels are further enhanced. Particularly, (R6) is strongly temperature dependent and initiates chain termination after cooling, which is

itself mainly driven by mixing with the ambient atmosphere. At lower temperatures (R7) dominates (R6) and leads to the effective partial conversion of OH to the more stable HO_2 radical. Lower temperatures also enable the oxidation of SO_2. While not significantly altering the high SO_2 levels, this process leads to further fast OH to HO_2 conversion and to a certain amount of SO_3 that ultimately leads to sulphate in the early plume:

$$SO_2 + OH \xrightarrow{M} HOSO_2 \tag{R10}$$

$$HOSO_2 \xrightarrow{O_2} SO_3 + HO_2 \tag{R11}$$

This and e.g. the back-reaction of e.g. (R6) or (R8) lead to the quick depletion of OH in the cooled plume.

The first moments of a volcanic plume that is directly emitted into atmospheric air are thus outlined as follows: (1) Intrusion of atmospheric O_2 initiates the quick catalytic oxidation of reduced magmatic species by OH. (2) Within this process OH levels rise drastically before after sufficient cooling (3) they are depleted, while partial OH conversion leads to remaining HO_2 in the cooled plume.

These (and other) processes occurring within the first (split) seconds of the evolution of a plume at an open vent, define an interface between magma and the atmosphere. It can substantially alter the gas composition and thus, requires similar attention as that of other degassing pathways (e.g. fumarole degassing, see above) in the context of field observations. Furthermore, this high temperature interface determines the amount of oxidants (e.g. HO_2) in the cooled plume, which is yet poorly constrained and found to be an essential boundary condition to reactive halogen chemistry (e.g. Surl et al., 2021).

Nowadays, apart from some exceptions, the scientific debate on volcanic gas geochemistry is based on TE terminology (e.g. Gerlach and Nordlie, 1975; Giggenbach, 1996; Gerlach, 2004; Holland, 2002; Martin et al., 2006; Gaillard et al., 2011; Oppenheimer et al., 2018b; Moussallam et al., 2019). However, the above and many more fast kinetic processes can lead to gas compositions that strongly depend on their mixing history and that are far from TE. Few studies discuss the restoration of TE states of 'disequilibium' gas samples by the iterative modification of certain gas ratios (see Gerlach, 1993; Symonds et al., 1994). These approaches, however, largely exclude the details of the chemical processes and thus, e.g. the influence of intermediate reaction products.

It is essential for the field of volcanic gas analysis to improve the understanding of the high temperature interface between magma and the atmosphere.

1.2 Analysis of volcanic gases

More than a century ago, T. A. Jaggar studied degassing lava in Hawaii and

> [...] *found no difficulty whatever in breathing the intensely hot products of small bubblings all over these glowing surfaces and percieved almost no sulphur odors; whereas at greater distance to leeward of a positively flaming grotto or cone, the blueish fume which condenses is full of intolerable compounds of sulphur with oxygen.*
> [...] *The Selby commision determined that one ten-thousandth part of SO_2 in air is intolerable to human beings. It hardly seems probable, therefore, that as much as 50 per cent of the magmatic gas rising directly from fresh lava can be SO_2.*
>
> Jaggar (1917)

Despite the questionable conclusion of this unconventional volcanic gas sample, the author already highlights the vital topic of the formation of secondary plume components through chemical conversion of hot magmatic gases when reaching the atmosphere (see Sect. 1.1.4, above). Nowadays, this topic remains scarcely discussed and often neglected (e.g. Oppenheimer et al., 2018b; Moussallam et al., 2019). So, although a growing range of volcanic gas sampling techniques have been developed, the sensual experience of the exposure to the volcanic environment should remain as a (cautiously treated) supplement to volcanic gas studies.
Eruptive volcanic activity is characterized by extreme dynamics and multi-phase interactions of the eruption products (see e.g. Fig. 1.1a). Typically volatile emission fluxes are strongly enhanced, and in the most extreme cases, larger amounts of volatiles reach higher atmospheric altitudes, which can drastically increase their atmospheric residence time. Despite the special interest, the direct study of the emitted volcanic gases in such situations is particularly challenging and often restricted to the volcanic plume further downwind. These larger eruptions, however, e.g. through melt and volatile inclusions in minerals in their pyroclastic products, deliver vital information on degassing processes and volatile composition at greater depth (see e.g. Oppenheimer et al., 2014).
Most volcanic gas measurements are performed at milder volcanic conditions, e.g. in periods of so-called quiescent degassing (see e.g. Fig. 1.1b). Then, the daredevil volcanologist can approach the emission source and perform her or his sampling. Still, the classical volcanic gas measurement techniques in most cases expose oneself to the naturally hazardous volcanic environment. Besides the toxic and corroding gases, there is the largely unforeseeable risk related to volcanic activity. On top of that, many volcanoes are in remote areas and emit their gases in several thousand metres of altitude in harsh meteorological conditions. A measurement strategy with the appropriate sampling techniques adapted to the processes to be studied and the environment of the respective volcano is thereby essential.
This section outlines the range of tools that have been used to study volcanic gas emissions with - regarding the scope of this work - a focus on spectroscopic remote sensing methods in the ultraviolet (UV) spectral range.

1.2.1 Brief overview on volcanic gas sampling methods and strategies

For more than a century, samples of volcanic gases are taken at the volcanic source and analysed in the laboratory. During the last decades technological advances enabled temporally resolved in-situ and remote sensing measurements of volcanic plume constituents. In general, the methods can be roughly classified by the three categories direct sampling, plume sampling, and remote sensing (see Fig. 1.3).

Figure 1.3: Collection of photographs showing applied volcanic gas analysis for a selection of techniques.

Direct sampling

Direct sampling describes the collection of volcanic gases in a container for later analysis in the laboratory. Thus, sampling procedures focus on avoiding or minimising mixing with atmospheric air. For instance, titanium or quartz tubes are inserted directly into the hot outlets of fumaroles or spatter cones (see Le Guern et al., 1979, and Fig. 1.3a and 1.3b) or they are used to sample gas from bubbles or gas streams directly above the lava surface (see e.g. Gerlach, 1980).
Nowadays, sampling flasks containing a small amount of an alkaline solution and an evacuated head space are used (see e.g. Giggenbach, 1975; Symonds et al., 1994, for details). The more reactive species are captured in solution, while the more inert species reside in the head space. These flasks are for instance often sampled in line with condensors to account for the water emissions. High quality gas samples demand high levels of experience and manual dexterity of the volcanologist and, not lastly, a calm hand facing the harsh environmental conditions.
The laboratory analysis of such samples (see e.g. Giggenbach et al., 2001; Oppenheimer et al., 2014, and references therein) can take days to weeks, but allows the quantification of a high number of gas constituents and isotope ratios. Such detailed information is for instance needed to determine the geological source of the volatiles and to identify and quantify influences of degassing pathways. Due to the relatively high effort, direct sampling mostly contributes to volcano monitoring on longer time scales.

Plume sampling

In the first seconds and minutes after emission, the volcanic gases are substantially diluted in air (typically by factors in the range of 10 to 1000), and generally called a volcanic plume. Many magmatic gas constituents, even when diluted in volcanic plumes, largely exceed their atmospheric background levels and thus, can be quantified from higher distances to the emitting, hazardous source (see Fig. 1.3b). For measurements e.g. performed at the crater rim of an open vent, this comes at the cost of an increased dependence on meteorology, particularly on wind conditions. Volcanic plume gas is for instance pumped through sets of impregnated filters (e.g. Aiuppa et al., 2004) and washing bottles with alkaline solution (e.g. Wittmer et al., 2014) for later laboratory analysis.
Furthermore, real-time quantification for some plume species can be provided by combinations of electro-chemical and optical gas sensors in compact devices (e.g. Shinohara, 2005; Aiuppa et al., 2011; Tirpitz et al., 2019). Such plume sampling methods can be implemented in stationary autonomous measurement stations that deliver continuous data, enabling monitoring of the plume's gas composition with high temporal resolution (e.g. Aiuppa et al., 2007b).

Remote sensing

Characteristic interaction of the volcanic gas molecules with electromagnetic radiation can be exploited for their detection. Particularly the use of natural light sources, like scattered or direct sunlight, or the glowing lava, together with a narrow field-of-view (FOV) telescope, enables a comfortable distance between volcanologist and hazardous source.
The most widely used remote sensing technique for volcanic gas measurements is absorption spectroscopy in spectral ranges between UV and infrared (IR). In the UV, correlation spectroscopy (e.g. Moffat and Millan, 1971; Malinconico, 1979) has been largely replaced by differential optical absorption spectroscopy (DOAS, see e.g. Edner et al., 1994; Bobrowski

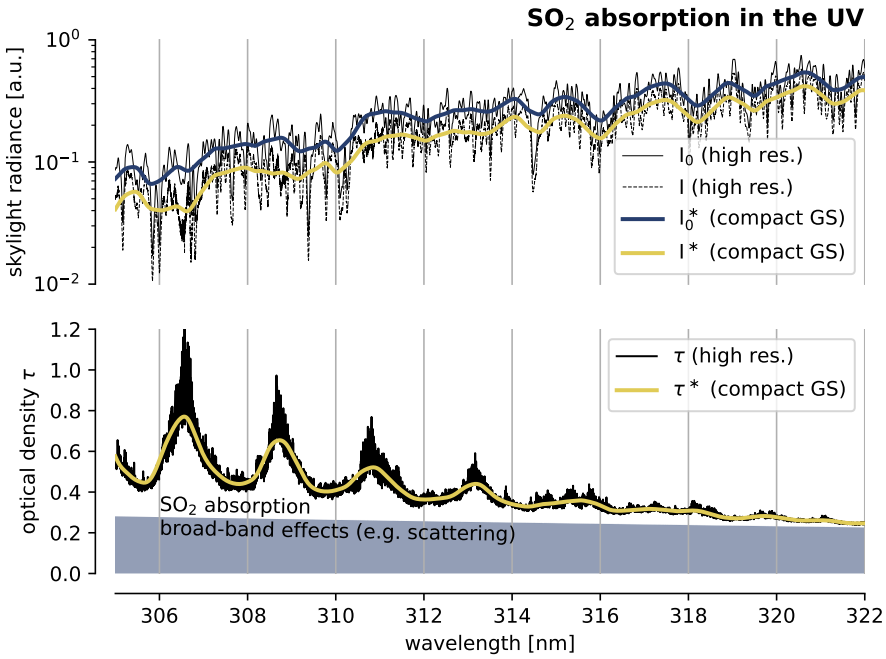

Figure 1.4: Schematic outline of a DOAS measurement. The upper panel shows the spectrum of the incident skylight radiance (Chance and Kurucz, 2010) of a light beam that traversed the volcanic plume (and experienced SO_2 absorption, I) together with a clear-sky measurement I_0. The high resolution Fraunhofer structures and details of the SO_2 absorption (Rufus et al., 2003) are not resolved by a typical DOAS GS. Vibronic bands of SO_2 are, however, resolved and enable their separation from broad-band extinction and thus, SO_2 quantification.

et al., 2003; Platt and Stutz, 2008; Galle et al., 2010; Kern and Lyons, 2018). The use of scattered or reflected sunlight as light source offers superior flexibility for plume measurements of e.g. SO_2, BrO and OClO from many different platforms (ranging from satellites to autonomous ground-based measurement stations). This and the fact that the in-plume concentrations of these gases are much higher than in the background atmosphere, enables their accurate measurement. The next section will further introduce and discuss this technique.

The quantification of additional gas species (e.g. HCl, HF, CO_2, CO, OCS) is provided by fourier transform spectroscopy (FTS) in the IR. However, the respective instrumentation is more bulky and delicate and, nowadays, still mostly relies on either, the direct sun (e.g. Butz et al., 2017) or the lava surface (e.g. Sawyer et al., 2008) as a light source. The major complication for remote sensing measurements of the main plume constituents, water and CO_2, are their abundances in the atmospheric background (e.g. Kern et al., 2017).

1.2.2 Spectroscopic remote sensing of volcanic gases in the UV and visible spectral range

Spectroscopy of scattered sunlight (skylight) in the UV and visible spectral range enables the remote detection of gas species inside the volcanic plume. Although not many volcanic species can be detected with this technique (nowadays mainly SO_2 and BrO are measured routinely), it raised volcanic gas studies on a new level during the last decades. Among the key advantages of the technique are:

1. Gas amounts can be quantified from large distances (depending on light path ge-

ometry and atmospheric scattering processes, typically several km for ground-based measurements)

2. The measurement schemes typically average over larger spatial scales. Instead of a point measurement, the average across e.g. an entire plume cross section is quantified.

3. The techniques allow an implementation in compact and robust (mobile) instrumentation

4. Most applications are calibrated intrinsically.

In summary, these listed points enable the technique to be operated in different configurations from many different platforms ranging from satellite-based (e.g. Bluth et al., 1993; Hörmann et al., 2013; Carn et al., 2017) or airborne (General et al., 2014, e.g.) to ground-based mobile measurements (e.g. Edner et al., 1994; Kern et al., 2020) and the implementation in autonomous and remote measurement stations (e.g. Galle et al., 2010; Lübcke et al., 2014). This paved the way for numerous new perspectives to volcanic gas studies through

1. the much more accurate quantification of volcanic SO_2 emission fluxes through spatially resolving plume cross sections (e.g. with a scanning telescope, see Fig. 1.3c)

2. near-global and near-real-time measurements of volcanic SO_2 emissions and BrO to SO_2 ratios from satellites

3. long time-series of gas measurements that are generally not interrupted by more eruptive activity

4. the direct, non-invasive quantification of short-lived gas species and their spatial distribution within the volcanic plume

The following paragraphs introduce the two nowadays most frequently used UV and visible volcanic gas remote sensing techniques.

Differential optical absorption spectroscopy (DOAS)

In the UV to near IR spectral range the radiative transfer of sunlight in the atmosphere is determined by scattering and absorption on molecules and aerosol particles and reflection at Earth's surface. Molecular absorption often exhibits a characteristic narrow-band spectral signature through quantised electronic, vibrational, and rotational transitions. These can be identified and easily separated from the other light-matter-interaction processes, which typically alter the more broad-band shape of the spectrum only.
The DOAS technique (e.g. Platt and Stutz, 2008) in its presently common form simplifies this procedure by exploiting the following circumstances that apply for the UV and visible spectral range: (1) Trace gas optical densities are mostly weak and (2) show spectral structures (vibro-electronic bands) that can be resolved with compact grating spectrographs (GS, around 1 nm spectral resolution) and (3) show negligible dependence on tropospheric temperature and pressure variation.
The optical density τ is described by the Beer-Lambert law and depends on the absorption cross sections σ_i and the concentration c_i of the molecule species i along a line of sight L. In DOAS applications, this line of sight is the light path difference between two radiance measurements, commonly referred to as a measurement radiance I and a reference radiance

I_0. Typically I and I_0 are recorded at different viewing geometries, where the target gas (e.g. the volcanic plume) is either present (I) or absent (I_0) in the associated light paths:

$$\tau(\lambda) = -\log \frac{I(\lambda)}{I_0(\lambda)} = \int_0^{\mathrm{L}} \sum_i \sigma_i(\lambda)\, c_i(l)\, \mathrm{d}l + b \tag{1.1}$$

In this notation, b combines all the effects on the radiance that are broad-band with respect to the spectral resolution of the observation. When examining UV to visible sunlight in Earth's atmosphere the intrinsic spectral resolution of this absorption process (width of individual rovibronic absorption lines or solar Fraunhofer lines) is on the order of some picometres. DOAS GSs measure radiance spectra with a spectral resolution of about 1 nm and thus, undersample the process by at least two orders of magnitude (see Fig. 1.4). However, the fact that the trace gas optical densities are weak allows the approximation of their contribution to the extinction τ^* measured at low resolution with effective (low resolution) absorption cross sections σ^* (see Fig. 1.4):

$$\tau^*(\lambda) = -\log \frac{I^*(\lambda)}{I_0^*(\lambda)} = \int_0^{\mathrm{L}} \sum_i \sigma_i^*(\lambda) c_i(l)\, \mathrm{d}l = \sum_i \sigma_i^*(\lambda)\, S_i + b \tag{1.2}$$

This simplification allows one to numerically fit multiple trace gas absorption cross sections (σ^* e.g. high resolution absorption data from the literature, smoothed to instrument resolution) to measured optical density spectra τ^*. Thereby, the column densities $S = \int c(l)\, \mathrm{d}l$ (fit parameter) of the individual trace gases within the differential light path L are retrieved. In this process, a polynomial accounts for all broadband effects b. Further effects e.g. infilling of Fraunhofer lines by inelastic scattering processes (so-called Ring effect, Grainger and Ring, 1962) are corrected by e.g. the introduction of appropriate pseudo-absorbers. Whenever possible, a measurement spectrum I^* is evaluated with a close-in-time reference spectrum I_0^* recorded with the same instrument. Thereby, disturbing instrumental effects (e.g. thermally induced misalignment of optical components in the set-up) as well as effects through changes in the atmospheric setting, such as a changing contribution of stratospheric trace gas optical densities as the solar elevation changes, are minimised. For further details see e.g. Platt and Stutz (2008).

If done correctly, differential spectral absorption optical densities on the order of 10^{-4} can routinely be measured. These, for instance, translate to a detection limit of about 5 ppt of BrO and 0.4 ppb of SO_2 for a 500 m light path in the volcanic plume (e.g. Fleischmann et al., 2004; Rufus et al., 2003).

At volcanoes, measurement spectra are commonly recorded with a telescope spatially scanning the volcanic plume and using a plume-free viewing direction as reference. Scanning is typically performed by a motorised tiltable telescope (see Fig. 1.3c) or by the operation from mobile platforms (backpack, car, unmanned areal vehicles, aircraft, satellite). This provides information on the spatial distribution of reactive species within the plume for chemistry studies (e.g. Bobrowski et al., 2007; General et al., 2015; Kern and Lyons, 2018) and allows recording continuous time series of BrO/SO_2 ratios (Lübcke et al., 2014). Furthermore, SO_2 emission fluxes can be accurately quantified by encompassing and averaging over the entire plume (e.g. Edner et al., 1994; Kern et al., 2020). Besides serving as a monitoring paramter (Malinconico, 1979; Galle et al., 2010) the SO_2 flux is used to determine the emission fluxes of other volcanic gases by scaling in-situ plume sampling measurements (e.g. Carn et al., 2017).

The SO_2 camera

The strongly increasing absorption of SO_2 towards lower wavelength in the UV (see Fig. 1.4 and Fig. 1.5 below) enables its quantification without using dispersive spectroscopy (i.e. without resolving the whole spectrum with e.g. a GS). A band-pass filter is sufficient to quantify UV light attenuation at around 310 nm, which at stronger emitting volcanoes is largely dominated by SO_2 absorption. The major advantage of this approach is that the band-pass filter can be placed in front of a UV camera and thereby quantify the SO_2 column density distribution within the whole camera's FOV at once (e.g. Mori and Burton, 2006; Bluth et al., 2007; Kern et al., 2010, see also Fig. 1.3c right panel). Thereby, the camera FOV should contain a plume-free sky region to serve as an instantaneous reference measurement. Furthermore, the images are corrected for aerosol extinction with the plume absorbance recorded with another band-pass filter transmitting at slightly higher wavelength, where SO_2 absorption is much lower (e.g. 325 nm).
This so-called SO_2 camera can deliver SO_2 column density distributions with mega pixel spatial resolution and a temporal resolution of around 1 Hz or better. The turbulent transport process of the plume in the atmosphere is almost fully resolved and volcanic SO_2 emission fluxes can be quantified on the time scale of a second and compared to other high resolution data (e.g. McGonigle et al., 2009; Moussallam et al., 2016). However, besides the required calibration procedures (see e.g. Lübcke et al., 2013), the technique has further major drawbacks due to the coarse spectral detection scheme (using only the absorption in two broader spectral ranges). SO_2 cameras measurements can only be performed at strong SO_2 emitters and at clear-sky conditions, due to the disturbing impact of clouds. Cross-interference to plume ash, aerosol and other trace gases add another crucial source of uncertainty (e.g. Kern et al., 2010; Lübcke et al., 2013; Kuhn et al., 2014, see also Sect. 1.3.1 below).

1.3 Novel approaches to volcanic gas remote sensing using Fabry-Pérot interferometers (FPIs)

> *Formulas have been established which express the flux given by a spectrometer as a function of the effective resolving power and of the dimension of the dispersive system (area of the base of the prism, or area of the grating, or area of the plates of the etalon). It is thus possible to compare the luminosities of the three types of instruments with, in each case, equal resolving power and equal dimension. This comparison reveals a great superiority of the grating over the prism for all regions of wavelengths, and a great superiority of the etalon over the grating.*
>
> Jacquinot (1954)

Despite of this general conclusion by Jacquinot, during the last decades, volcanic (and atmospheric) trace gas remote sensing in the UV and visible spectral range have been almost exclusively performed with grating-based instruments. A core part of this thesis is the investigation of the application of Fabry-Pérot interferometers (FPIs, or etalons) in spectroscopic remote sensing instrumentation and the potential benefits for volcanic gas studies. The FPI describes two plane-parallel reflective surfaces. Multiple reflection of an incident light beam within the FPI causes its splitting into many partial beams with different path length in between the two surfaces. When leaving the FPI, the partial beams interfere to cause a comb-shaped transmission spectrum with equidistant spectral transmission peaks (marking constructive interference). Hence, incident light is only transmitted when its wavelength is resonant to the physical FPI dimensions (optical distance between the surfaces, incidence angle). The spectral sharpness of a transmission peak - also called finesse - is determined by the number of effectively interfering partial beams and thus dependent on the reflectivity and the quality of the surfaces and their alignment. For further details, see Kuhn et al. (2019); Fuchs et al. (2021); Kuhn et al. (2021), which are part of this thesis, and Perot and Fabry (1899); Vaughan (1989); Kuhn et al. (2014); Kuhn (2015).
This section provides a basic motivation for the use of FPIs for volcanic (and generally atmospheric) gas studies and briefly outlines the two approaches of this thesis.

1.3.1 Limitations of volcanic remote sensing observations: light throughput, spectral resolution, and mobility

Spectroscopic instrumentation for atmospheric remote sensing requires optimisation with respect to the intended observation. For volcanic studies, this includes a high mobility of the instrument (i.e. a compact and robust design, low power consumption, see Kuhn et al., 2021) for field deployment, sufficiently low detection limits, and adequate spatio-temporal resolution.
The absorption of a certain amount of a trace gas along a given light path (i.e. a column density S of this trace gas, see above) can only be detected, when the corresponding optical density τ exceeds the noise of the measurement. The detection of an absorber in the atmosphere typically requires the comparison of at least two spectral regions with different absorption (e.g. on and besides an absorption band). The amplitude of this difference determines the sensitivity of the measurement and is given by the absorption cross section $\hat{\sigma}(\delta\lambda)$ as it is seen by the instrument with spectral resolution $\delta\lambda$. The measured optical density is then:

$$\tau = \hat{\sigma}(\delta\lambda)\, S \tag{1.3}$$

In applications with broad-band light sources in the UV and visible, the measurement noise is in most cases determined by photon statistics. This means that the measurement noise

can be approximated by the square root of the number N_{ph} of photons counted by the instrument's detector. The noise $\Delta\tau$ of a spectral optical density measurement for small absorption ($\tau \propto \frac{I}{I_0}$, $I \approx I_0$) is roughly given by the relative noise of a photon counting measurement:

$$\Delta\tau \approx \frac{\Delta N_{\mathrm{ph}}}{N_{\mathrm{ph}}} = \frac{1}{\sqrt{N_{\mathrm{ph}}}} \tag{1.4}$$

The number of detected photons is given by the product of the photon flux J_{ph} (photons s^{-1}) at the detector, the quantum efficiency (set to unity here) and the detector exposure time δt. The photon flux is proportional to the incident spectral radiance I (photons $\mathrm{s}^{-1}\,\mathrm{nm}^{-1}\,\mathrm{mm}^{-2}\,\mathrm{sr}^{-1}$). The proportionality factor is the product of the spectral interval $\delta\lambda$ that is resolved by the instrument and the instrument's light throughput $k(\delta\lambda)$, which itself depends on the spectral resolution:

$$N_{\mathrm{ph}} = J_{\mathrm{ph}}\,\delta t = I\,\delta\lambda\,k(\delta\lambda)\,\delta t \tag{1.5}$$

Following this consideration, the detection limit for a trace gas column density ΔS of weak atmospheric absorbers when using broadband light sources can be approximated:

$$\Delta S \approx \left(\hat{\sigma}(\delta\lambda)\,\sqrt{I\,\delta\lambda\,k(\delta\lambda)\,\delta t}\right)^{-1} \tag{1.6}$$

The exposure time determines the temporal resolution of the measurement and should match the characteristic time scale of the studied process. The radiance of the light source is in most atmospheric applications also predefined (e.g. the radiance of skylight). Thus, the instrument light throughput and the spectral resolution basically determine weather a process (characterized by $\hat{\sigma}$ and δt) can be studied. Decreasing $\delta\lambda$ (increasing spectral resolution) in most cases leads to an increasing sensitivity $\hat{\sigma}$ and a decreasing instrument light throughput k. The dependencies of k and $\hat{\sigma}$ on $\delta\lambda$ thus, ultimately determine the detection limit ΔS of the trace gas remote sensing measurement.
Different approaches to spectrally resolving radiance measurements exist. As discussed above (Sect. 1.2.2), in atmospheric remote sensing GS measurements have been very successful and are widely in use. Mobile and cost-efficient GSs have a spectral resolution that is sufficient to resolve absorption structures of many atmospheric gases. There are, however, two basic limitations to GS, particularly with respect to volcanic observations:

1. Parallelised measurements, enabling the implementation in fast imaging schemes, are difficult to implement with GSs. This imposes limits to the spatio-temporal resolution of GS observations (see e.g. Platt et al., 2015, 2021).

2. When increasing the spectral resolution of a GS the light throughput decreases particularly fast ($k_{\mathrm{GS}} \propto \delta\lambda^2$, $k_{\mathrm{FPI}} \propto \delta\lambda$), while at the same time the GSs' mobility advantage is lost (see Kuhn et al., 2021).

The SO_2 camera principle (see Sect. 1.2.2 above) illustrates the benefits of its customisation to the intended measurement of high-resolution SO_2 emission fluxes. While GS (DOAS) measurements require scanning across the volcanic plume in order to calculate the emission flux (see Fig. 1.3c, left panel), the SO_2 camera can record images resolving the SO_2 column density distribution within the plume with high temporal resolution (about 1 Hz, see Fig. 1.3c, right panel). This allows to capture turbulence features and to use the detailed plume movement for the flux quantification.
The rather low dependence of $\hat{\sigma}_{SO_2}$ on the spectral resolution in the UV (see Fig. 1.4) allows one to use a band-pass-filter-based detection of SO_2 (increasing $\delta\lambda$ by about a factor of 10

compared to DOAS measurements). The thereby drastically enhanced light throughput is instantly exploited by massive parallelisation of the measurement, which is implemented straight-forward by placing the band-pass-filter in front of a UV-sensitive imaging device. Thereby, each pixel of the imaging detector provides a SO_2 measurement.
The trade-off is a loss of spectral information so that the extinction of other processes (e.g. scattering at plume aerosol) interfere with the SO_2 detection (see last paragraph of Sect. 1.2.2). The application of band-pass-filter based SO_2 cameras is thus limited to measurement conditions, at which it is a priory known that the SO_2 absorption dominates the extinction of the plume. Influences of aerosol extinction are hard to quantify and spectral modifications of the background sky through clouds render the recorded data unusable. Nevertheless, at volcanoes with high SO_2 emission and on clear-sky days with low plume aerosol, SO_2 cameras deliver data with superior spatio-temporal resolution that provide important insight into volcanic processes.
On the other hand, there are absorbers with a strong dependence of $\hat{\sigma}$ on the spectral resolution of the instrument, for instance when the absorption cross section is composed of separate rovibronic absorption lines (e.g. OH absorption, see below). These lines are much narrower than the spectral interval $\delta\lambda$ that can be resolved by a compact GS. Thus, their measured absorption is strongly attenuated and generally not separable from other atmospheric extinction processes.
In this thesis, two novel spectroscopic techniques for trace gas remote sensing were developed with the aim to improve the named shortcomings of GSs for volcanic studies. Both technique rely on the use of a FPI. Imaging FPI correlation spectroscopy (IFPICS, Sect. 1.3.2) exploits the high light throughput of FPIs to increase spatio-temporal resolution (similar to the SO_2 camera) while maintaining high selectivity of the trace gas detection. FPI spectrographs (Sect. 1.3.3) combine high spectral resolution with high light throughput and preserved instrument mobility.

1.3.2 Imaging FPI correlation spectroscopy (IFPICS)

The IFPICS technique is described in detail in Kuhn et al. (2014); Kuhn (2015); Fuchs (2019); Kuhn et al. (2019); Fuchs et al. (2021).
Figure 1.5a and 1.5b outline the detection scheme for SO_2 in the UV. The periodic FPI transmission spectrum is matched to – in this case – vibro-electronic SO_2 absorption structures, so that only light with wavelength of the absorption peaks is transmitted (drawn yellow line in Fig. 1.5b). By slightly tuning a physical FPI parameter (e.g. the light's incidence angle by tilting the FPI) the transmission spectrum is slightly shifted, so that the transmission peaks now coincide with the minima of the absorption cross section (dashed yellow line in Fig 1.5b). The difference of the optical densities measured with both FPI configurations is then a measure for the trace gas column density.
The major benefits of this technique are:

1. The FPI can be used – similarly to band-pass-filters – in full frame imaging set-ups. That is to say, they can be placed within a camera optics and thereby allow for highly parallelised measurements enabling high spatial resolution and differential evaluation within the image frame (see Fig. 1.3c right panel).

2. The high light throughput of FPIs enables high temporal resolution of such imaging measurements. Co-adding of image pixels further allows to trade for instance spatial resolution against an improved detection limit for a given temporal resolution.

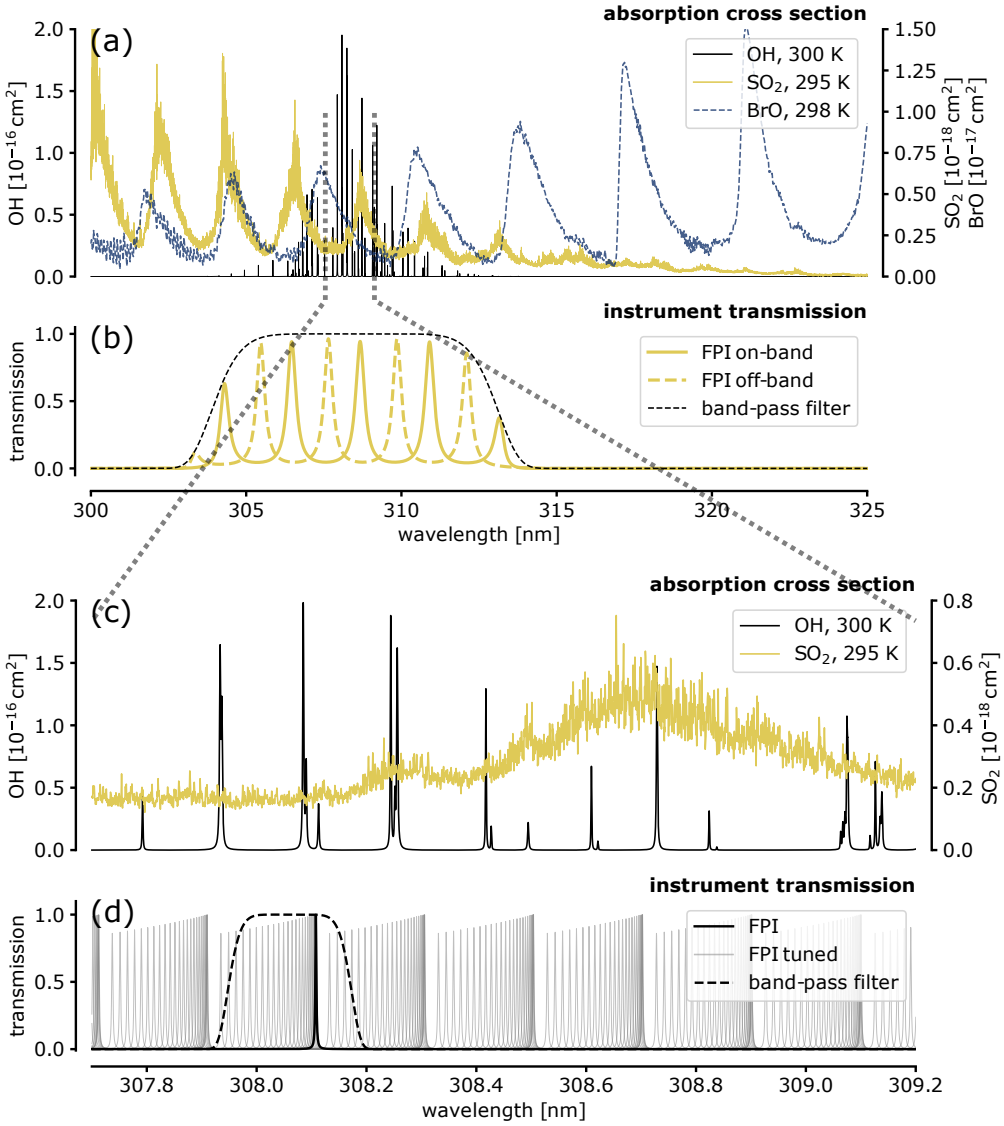

Figure 1.5: Panels (a) and (b) outline the measurement principle of the IFPICS technique. A FPI matched to the spectral absorption (here SO_2, data from Rufus et al. (2003)) is used to separate the trace gas' absorption from other extinction effects. This can be applied to many absorbers with periodic vibronic bands in the UV and visible, e.g. BrO (data from Fleischmann et al., 2004). Panel (c) and (d) illustrate the benefit of high spectral resolution measurements and how they are achieved by high resolution (high finesse) FPIs. In panel (d) the transmission spectrum of a FPI (finesse of about 100) is shown as it scans a short wavelength range to resolve the sharp rovibronic OH absorption peaks (data from Rothman et al., 2013).

3. The spectral detection scheme uses much more trace gas specific spectral information than that of the band-pass-filter-based SO_2 camera. Thus, cross interferences of aerosol or other trace gases, as well as the influence of clouds in the background sky are drastically reduced.

4. Through its higher selectivity IFPICS – unlike the case of the filter-based SO_2 camera – can be applied to gases that do not dominate the plume's absorption in a particular spectral range. Figure 1.5a shows for instance the periodic vibronic structure of BrO.

5. IFPICS can be implemented in mobile instruments.

6. Similarly to DOAS measurements, IFPICS can be calibrated intrinsically with literature absorption cross sections and an instrument model.

IFPICS has the potential to subtantially improve volcanic gas observations. The combination of the advantages of SO_2 camera (high spatial reolution) and DOAS (high selectivity) enables drastic enhancement of the accuracy of volcanic SO_2 flux measurements. Furthermore, imaging measurements of BrO or OClO can be achieved with the IFPICS technique. This would allow unprecedented insight into the yet debated conversion processes of volcanic halogen species in the plume (see Sect. 1.1.4).

1.3.3 FPI spectrographs

FPI spectrographs are described in detail by Kuhn et al. (2021). They rely on the intrinsic light throughput advantage compared to GSs that becomes relevant for measurements with high resolving power (e.g. Jacquinot, 1954, 1960).
Figure 1.5c shows a part of the spectrum of Fig. 1.5a on a finer wavelength scale. The specific quantification of for instance OH based on its rovibronic absorption lines requires to resolve about the spectral width of those lines (i.e. about 2 pm, corresponding to $\frac{\lambda}{\delta\lambda} \approx 150000$). A high resolution FPI (i.e. with a narrow width of an individual transmission peak) can be tuned to scan a certain spectral range to provide high resolution spectra (see Fig. 1.5d). A single FPI transmission order is thereby isolated by e.g. a band-pass-filter. The tuning has been implemented in many different ways during the long history of FPI spectroscopy (see e.g. Perot and Fabry, 1899; Fabry and Buisson, 1908; Burnett and Burnett, 1981; Vaughan, 1989). Advances in photo sensor array technology within the last decades enabled the implementation of FPI spectrographs (i.e. a spectrometer that records all spectral channels simultaneously, similar to a GS). The slightly different incidence angles of a collimated light beam traversing the FPI can be mapped onto a detector array. This allows to instantaneously record full spectra without physical scanning schemes. For environmental observations, this is an essential advantage, since it avoids disturbing effects from variable light sources and allows implementation in mobile instrumentation without moving parts.
The light throughput of a FPI is basically determined by its clear aperture. Nowadays, for high finesse FPIs the surface sphericity, induced by the reflective coating and decreasing for increasing clear aperture, limits the finesse. Nevertheless, the light throughput advantage of high resolution FPI spectrographs over GSs amounts to many orders of magnitude with nowadays available etalons.
The remote detection of OH and other gas species in hot volcanic emissions could open the door to directly study the chemistry of early and hot volcanic gas emissions (see Sect. 1.1.4) and thus, significantly contribute to a better understanding of volcanic degassing processes.

Furthermore, FPI spectrogaphs might extend the range of gases that can be measured by skylight remote sensing techniques and through that enable improved and new volcanic (and atmospheric) studies.

1.4 Scope of the thesis

This cumulative thesis is composed of 3 peer-reviewed and published scientific articles (P1–P3, Creative Commons Attribution 4.0 License, see https://creativecommons.org/licenses/by/4.0/) and one unpublished article manuscript (P4):

P1 Kuhn, J., Platt, U., Bobrowski, N., and Wagner, T.: Towards imaging of atmospheric trace gases using Fabry–Pérot interferometer correlation spectroscopy in the UV and visible spectral range, Atmospheric Measurement Techniques, 12, 735–747, 2019.

P2 Fuchs, C., Kuhn, J., Bobrowski, N., and Platt, U.: Quantitative imaging of volcanic SO2 plumes using Fabry–Pérot interferometer correlation spectroscopy, Atmospheric Measurement Techniques, 14, 295–307, 2021.

P3 Kuhn, J., Bobrowski, N., Wagner, T., and Platt, U.: Mobile and high-spectral-resolution Fabry–Pérot interferometer spectrographs for atmospheric remote sensing, Atmospheric Measurement Techniques, 14, 7873–7892, 2021.

P4 Kuhn, J., Bobrowski, N., and Platt, U.: The interface between magma and Earth's atmosphere, unpublished manuscript, 2022.

The articles cover three major topics related to the analysis of volcanic gases. They are briefly outlined here, together with statements on author contributions.

P1 and P2: A novel trace gas imaging technique for volcanic plumes

P1 summarizes large parts of my work on imaging atmospheric trace gases with FPI correlation spectroscopy, which was also a subject of my undergraduate studies (Kuhn et al., 2014; Kuhn, 2015). The paper presents calculations on the feasibility of quantifying typical amounts of different atmospheric trace gases (including volcanic SO_2 and BrO) with the IFPICS technique. Moreover, it includes a proof-of-concept field measurement of volcanic SO_2 at Mt. Etna with a one-pixel prototype instrument, which I built.
Christopher Fuchs continued the work on IFPICS in his Master's thesis under my supervision (Fuchs, 2019). Together, we figured out how to implement the technique in a field-ready imaging instrument. Christpher Fuchs built and characterized the imaging prototype and evaluated the data relying on my earlier model developments. P2 summarizes this work and presents the first IFPICS measurements of SO_2 taken at Mt. Etna.

P3: A mobile high-resolution spectrograph for volcanic gas remote sensing

During the course of my PhD studies, the idea of using FPI properties to achieve atmospheric observations with high spectral resolution has come up. This idea bases on the manifold high-resolution applications of FPIs in other scientific fields (e.g. Vaughan, 1989). The quantification of volcanic OH radicals was thereby the principal motivation, since TE models predict very high levels (e.g. Gerlach, 2004). After theoretically assessing the feasibility, I built first field-ready prototype instruments. P3 introduces the concept of FPI spectrographs for atmospheric studies and possible implementations thereof. In the scope of this study I thoroughly compare GSs with FPI spectrographs, regarding the light throughput as a function of spectral resolution paired with basic considerations on instrument mobility (and thereby field-applicability). The results of this study indicate major improvements of trace gas spectroscopy in the atmosphere in general. For instance it even suggests that FPI spectrographs can be used to detect the tropospheric OH background (around 0.1ppt)

via skylight absorption spectroscopy (presently only possible with intricate and immobile instrumentation, see Stone et al., 2012, and references therein). Appendix A of this thesis, in extension to P3, describes the first FPI spectrograph measurements of hot gas emissions at a lava flow, which I performed within the crater of Nyiragongo volcano.

P4: Modeling turbulent mixing of hot magmatic gases with air

The contemplation of hot magmatic gas emissions and their direct visual observation during field measurements has led to an emerging doubt concerning the treatment of this process in the recent literature. There, the highly dynamic magma-atmosphere interface is usually described with TE terminology (e.g. Gerlach and Nordlie, 1975; Martin et al., 2006; Oppenheimer et al., 2018b; Moussallam et al., 2019). A first kinetic modeling approach for a time fraction of an eruptive degassing scenario by Roberts et al. (2019) indicated the potentially crucial role of reaction rates within high temperature gas emissions. I developed a kinetic chemistry model that allows comprehensive and flexible simulations of the turbulent atmospheric mixing and associated cooling process in the early and hot volcanic plume. It encompasses the entire cooling process and allows to cover a large range of initial conditions with only a few model runs. Studies of the interaction of chemical kinetics with plume mixing and cooling suggest that volcanic gases, within split seconds after emission, are far from TE and strongly influenced by intermediate species. This is crucial for both, the interpretation of volcanic gas measurements and studies that assess their influence on the atmosphere. P4 describes the model study and discusses its potential broad consequences for volcanic gas studies.

The co-authors Nicole Bobrowski, Thomas Wagner, and Ulrich Platt shared their experience and expertise in extensive discussions on the subjects and reviewed and extended the manuscripts of the articles.

Chapter 2 displays the articles in their originally published or preprint layout. In Chapter 3, the results of the individual studies are further discussed, focusing on their implications for volcanic gas studies and beyond. The conclusions are summarised in Chapter 4.

2 Publications

Atmos. Meas. Tech., 12, 735–747, 2019
https://doi.org/10.5194/amt-12-735-2019

Atmospheric Measurement Techniques
Open Access
EGU

Towards imaging of atmospheric trace gases using Fabry–Pérot interferometer correlation spectroscopy in the UV and visible spectral range

Jonas Kuhn[1,2], **Ulrich Platt**[1,2], **Nicole Bobrowski**[1,2], **and Thomas Wagner**[2]

[1]Institute of Environmental Physics, University of Heidelberg, Heidelberg, Germany
[2]Max Planck Institute for Chemistry, Mainz, Germany

Correspondence: Jonas Kuhn (jkuhn@iup.uni-heidelberg.de)

Received: 3 October 2018 – Discussion started: 15 October 2018
Revised: 21 January 2019 – Accepted: 23 January 2019 – Published: 1 February 2019

Abstract. Many processes in the lower atmosphere including transport, turbulent mixing and chemical conversions happen on timescales of the order of seconds (e.g. at point sources). Remote sensing of atmospheric trace gases in the UV and visible spectral range (UV–Vis) commonly uses dispersive spectroscopy (e.g. differential optical absorption spectroscopy, DOAS). The recorded spectra allow for the direct identification, separation and quantification of narrow-band absorption of trace gases. However, these techniques are typically limited to a single viewing direction and limited by the light throughput of the spectrometer set-up. While two-dimensional imaging is possible by spatial scanning, the temporal resolution remains poor (often several minutes per image). Therefore, processes on timescales of seconds cannot be directly resolved by state-of-the-art dispersive methods.

We investigate the application of Fabry–Pérot interferometers (FPIs) for the optical remote sensing of atmospheric trace gases in the UV–Vis spectral range. By choosing a FPI transmission spectrum, which is optimised to correlate with narrow-band (ideally periodic) absorption structures of the target trace gas, column densities of the trace gas can be determined with a sensitivity and selectivity comparable to dispersive spectroscopy, using only a small number of spectral channels (FPI tuning settings). Different from dispersive optical elements, the FPI can be implemented in full-frame imaging set-ups (cameras), which can reach high spatio-temporal resolution. In principle, FPI correlation spectroscopy can be applied for any trace gas with distinct absorption structures in the UV–Vis range.

We present calculations for the application of FPI correlation spectroscopy to SO_2, BrO and NO_2 for exemplary measurement scenarios. In addition to high sensitivity and selectivity we find that the spatio temporal resolution of FPI correlation spectroscopy can be more than 2 orders of magnitude higher than state-of-the-art DOAS measurements. As proof of concept we built a 1-pixel prototype implementing the technique for SO_2 in the UV. Good agreement with our calculations and conventional measurement techniques is demonstrated and no cross sensitivities to other trace gases are observed.

1 Introduction

Within the last decades, progress in optical remote sensing of atmospheric trace gases has led to a better understanding of many important processes including air pollution, ozone, and halogen chemistry and the evolution of volcanic plumes. Narrow-band structures in the trace gas molecule's absorption spectrum are used to identify and quantify the amount of a trace gas integrated along a line of sight, i.e. its column density (CD, typically in units of molecules per cubic centimetre), and to separate its absorption signal from interfering gas absorptions and scattering processes.

Differential optical absorption spectroscopy (DOAS; see Platt and Stutz, 2008, for details) has become a well established technique for atmospheric trace gas remote sensing in the UV–Vis with high sensitivity (detection limits within the parts per billion to parts per trillion range for atmospheric

light paths of a few kilometres). A spectrometer and a telescope with narrow field of view (FOV) are used to record spectra $I(\lambda)$ of scattered sunlight, which are compared to a reference spectrum $I_0(\lambda)$. The Beer–Lambert law describes the corresponding spectral optical density $\tau(\lambda)$ with $\sigma_i(\lambda)$ and $c_i(l)$ being the absorption cross section and the concentration of trace gas species i along a line of sight L, respectively:

$$\tau(\lambda) = -\log\frac{I(\lambda)}{I_0(\lambda)} = \int_0^{\mathrm{L}} \sum_i \sigma_i(\lambda) c_i(l)\mathrm{d}l + \text{scattering at molecules and aerosols.} \quad (1)$$

Atmospheric UV–Vis optical densities are dominated by trace gas absorption and scattering processes at air molecules or aerosols. The known absorption cross sections of the trace gases together with a polynomial, which accounts for the broad-band absorption and scattering effects, are fitted to the measured spectral optical density. The fit coefficients represent the CDs $S_i = \int_0^{\mathrm{L}} c_i(l)\mathrm{d}l$, i.e. the integrated trace gas concentration along the light path difference of $I(\lambda)$ and the reference $I_0(\lambda)$. In principle, spatial distributions of trace gases (images or height profiles) can be recorded by scanning of viewing angles with a narrow FOV telescope (e.g. multi-axis DOAS; Hönninger et al., 2004). More complicated optical set-ups allow us to record spectra of an entire image column at once by using a two-dimensional detector array (e.g. imaging DOAS; Lohberger et al., 2004). Images can then be recorded by column (push broom) scanning. The acquisition times of these techniques used to be rather large (often several minutes per image or profile for typical trace gas CDs), limiting their application to processes that are spatially homogeneous on that timescale or processes with very high trace gas CDs. Recently, Manago et al. (2018) reported NO_2 measurements with a hyperspectral camera based on the imaging DOAS technique with considerably higher temporal resolution (~ 0.08 Hz).

Determination of two-dimensional atmospheric trace gas distributions with high time resolution at timescales of the order of seconds, i.e. fast imaging, of atmospheric trace gases is possible with techniques recording all spatial pixels of an image at once for a low number of spectral channels (see e.g. Platt et al., 2015). This allows the study of phenomena which are not accessible to conventional scanning methods. With fast trace gas imaging techniques, sources and sinks of trace gases can be identified and quantified on much smaller spatial and temporal scales than with conventional remote-sensing techniques. This allows us to, for instance, gain insight into small-scale mixing processes and to distinguish chemical conversions from transport.

Most of the presently used atmospheric trace gas imaging schemes use either a set of two band pass filters (BPFs) (e.g. SO_2 camera, ~ 1 Hz for volcanic emissions; see e.g. Mori and Burton, 2006; Bluth et al., 2007; Kern et al., 2010; Platt et al., 2018) or a tuneable BPF as a wavelength selective element (e.g. NO_2 camera, ~ 3 min per image for stack emissions of power plants; Dekemper et al., 2016). These techniques either involve intricate optical set-ups with low light throughput or yield a rather coarse spectral resolution, which might result in strong cross interferences (see e.g. Lübcke et al., 2013; Kuhn et al., 2014).

Here we study the application of Fabry–Pérot interferometers (FPIs) as wavelength selective elements for trace gas imaging in the UV–Vis range. The periodic FPI transmission spectrum is matched to the spectral absorption structures of trace gases that often show a similar periodicity. Thanks to the high correlation of the transmission spectrum of the wavelength selective element and the trace gas absorption spectrum, a high sensitivity can be reached and cross interferences with other absorbers are minimised, even if only a small number of spectral channels (FPI tuning settings) is used (see Kuhn et al., 2014, and the discussion in Sect. 3.2 below). Air spaced FPI etalons are very robust devices and allow for simple optical designs that can easily be implemented in imaging sensors. We present a model study on the sensitivity and selectivity of FPI correlation spectroscopy applied to SO_2, BrO and NO_2 (Sect. 3). For exemplary measurement scenarios, we infer the possible spatio-temporal resolution of these measurements for a specific instrument implementation. We find that, for the three gases, imaging with spatio-temporal resolutions about 2 orders of magnitude higher than state-of-the-art methods should be possible. In addition, we present a proof-of-concept study of the technique for volcanic sulfur dioxide (SO_2), validating the expected high accuracy and sensitivity of the technique with a 1-pixel prototype instrument. Further, we show that SO_2 CDs can be accurately retrieved from the recorded data without calibration (Sect. 4).

2 Fabry–Pérot interferometer correlation spectroscopy

2.1 Fabry–Pérot interferometer

The FPI is a fundamentally very simple optical device, known for more than a century (e.g. Perot and Fabry, 1899). In principle, it consists of two plane parallel surfaces each with reflectance R, separated by a distance d (see Fig. 1). The medium between the plates has the index of refraction n. Incident light (angle of incidence α) is split up in partial beams with different optical path lengths between the two surfaces. Due to interference of the transmitted partial beams, the spectral transmission of the FPI is characterised by periodic transmission peaks, referring to constructive interference. For high enough orders of interference, the free spectral range (FSR) Δ_λ between two transmission peaks in units of wavelength λ is approximately given by

$$\Delta_\lambda(\lambda) \approx \frac{\lambda^2}{2nd\cos\alpha}. \quad (2)$$

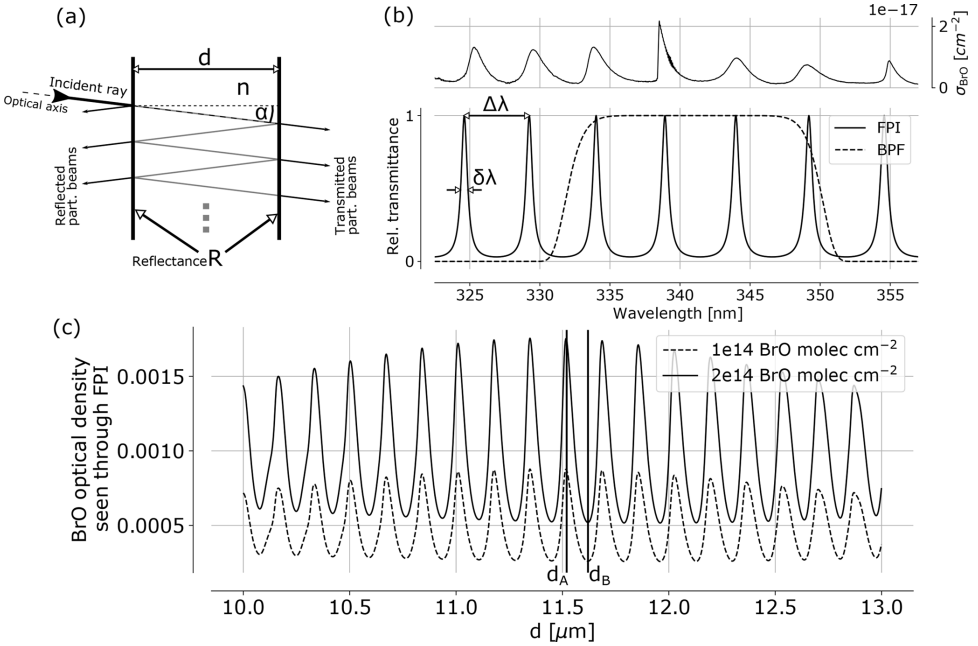

Figure 1. **(a)** FPI schematics indicating the splitting of incident radiation into partial beams that interfere to cause the FPI transmittance spectrum **(b)**, which is characterised by periodic transmission maxima with a FWHM of δ_λ and a FSR of Δ_λ. The BrO absorption cross section (upper panel) shows approximately periodic structures allowing for a high correlation with spectral FPI transmittance. This leads to a modulation of the BrO optical density as seen through the FPI with changing surface displacement d **(c)**. The apparent absorbance is the difference of the optical densities of FPI settings A and B, representing maximum and minimum correlation of FPI transmission and absorption cross section σ.

The finesse F of a FPI represents the ratio of FSR to the full width half maximum (FWHM) δ_λ of a transmission peak:

$$F = \frac{\Delta_\lambda}{\delta_\lambda}. \tag{3}$$

The finesse is a measure for the number of effectively interfering partial beams and therefore increasing with the surface reflectance. However, it also depends on the alignment and quality of the surfaces.

The spectral transmission as a function of λ and the FPI's instrument parameters is given by

$$T_{\mathrm{FPI}}(\lambda) = \left[1 + \frac{4R}{(1-R)^2}\sin^2\left(\frac{2\pi d n \cos\alpha}{\lambda}\right)\right]^{-1}. \tag{4}$$

Despite its simple design, the challenge in manufacturing FPI devices lies in creating set-ups keeping d stable to a fraction of a wavelength across the effective aperture.

2.2 Detection principle

The concept of using FPI correlation to detect atmospheric trace gases is described in Kuhn et al. (2014). The correlation of periodic absorption structures of atmospheric trace gases and the FPI transmission is exploited. An apparent absorbance $\widetilde{\tau}_i$ of a trace gas i is calculated from the optical densities of an on-band τ_A and off-band τ_B channel:

$$\begin{aligned}\widetilde{\tau}_i &= \tau_A - \tau_B = \log\frac{I_{A,0}}{I_A} - \log\frac{I_{B,0}}{I_B} \\ &= (\overline{\sigma}_{A,i} - \overline{\sigma}_{B,i})\, S_i = \Delta\overline{\sigma}_i\, S_i.\end{aligned} \tag{5}$$

S_i denotes the CD of a trace gas i. For the on-band channel, the spectral pattern of the FPI transmittance is chosen to correlate with the absorption band structure of the target trace gas, while for the off-band channel the FPI is tuned to show minimum correlation with the target trace gas absorption (see Fig. 1). The apparent absorbance is – for low trace gas optical densities – proportional to the CD of the trace gas. The proportionality is $\Delta\overline{\sigma}$, representing the difference of the effective absorption cross section seen by channel A and channel B. The optical densities τ_k are calculated from measured radiances I_k transmitted by the FPI in a setting $k = A,\ B$:

$$I_k = \int_{\Delta\lambda} I(\lambda)\cdot T_{\mathrm{FPI},k}(\lambda)\,\mathrm{d}\lambda. \tag{6}$$

$I_{k,0}$ denotes the reference radiance without the target trace gas in the light path. In practice, a wavelength range $\Delta\lambda$ of high correlation of spectral trace gas absorption and FPI transmission is preselected with a BPF. Within this spectral range the FPI physical parameters are optimised. Figure 1c

Table 1. Differential CDs assumed for the different measurement scenarios. The values represent high values for CD variations within a typical imaging FOV. The targeted detection limits are indicated in italic.

	Differential CD across imaging FOV (molec cm^{-2})		
	SO_2: volcanic emission (low) 300–315 nm	BrO: volcanic emission (high) 330–355 nm	NO_2: stack emission 424–445 nm
SO_2	*1×10^{17}* (volcanic)	3×10^{18} (volcanic)	–
BrO	1×10^{14} (volcanic)	*1×10^{14}* (volcanic)	–
NO_2	1×10^{17} (bgr. pollution)	1×10^{16} (bgr. pollution)	*1×10^{16}* (stack plume)
O_3	3×10^{17} (SZA change strat.)	3×10^{17} (SZA change strat.)	3×10^{17} (SZA change strat.)
HCHO	5×10^{15} (background)	5×10^{15} (background)	–
H_2O	–	–	1×10^{23} (background)
OClO	5×10^{13} (volcanic)	5×10^{13} (volcanic)	–
O_4	–	1×10^{43} (O_2 dimer, molec^{2}cm^{-5})	1×10^{43} (O_2 dimer, molec^{2}cm^{-5})

Typical values based on Roscoe et al. (2010), Gliß et al. (2015), Bobrowski and Giuffrida (2012) and Dekemper et al. (2016). Absorption cross sections are based on Vandaele et al. (2009), Fleischmann et al. (2004), Bogumil et al. (2003), Serdyuchenko et al. (2014), Chance and Orphal (2011), Rothman et al. (2013), Kromminga et al. (2003) and Thalman and Volkamer (2013).

shows the optical density of BrO seen through an FPI with varying surface displacement d. The maximum difference between maximum and minimum optical density determines the FPI settings A and B. In addition, the finesse is chosen to maximise the signal-to-noise ratio.

Here we apply FPI correlation spectroscopy for passive imaging of a trace gas in the atmosphere. This means that the light source is scattered sky radiation that is measured within an imaging FOV (e.g. 20° aperture angle). We assume in the following that a reference I_0 (i.e. a part without trace gas) is always present within the image, so that S denotes the differential trace gas CD compared to that reference.

The proportionality $\Delta\overline{\sigma}$ of apparent absorbance $\widetilde{\tau}$ and trace gas CD S (see Eq. 5) can be calculated from literature absorption cross sections of the target trace gas, a background spectrum $I_0(\lambda)$ and a modelled instrument transfer function (see Sects. 3.1 and 4.2). Alternatively, $\Delta\overline{\sigma}$ can be determined through calibration (see e.g. Lübcke et al., 2013; Sihler et al., 2017).

3 Model study for SO_2, NO_2 and BrO

FPI correlation spectroscopy can be applied to every trace gas species that yields sufficiently strong spectral absorption structures in the regarded wavelength range. In this section we present exemplary model studies for imaging of SO_2, NO_2 and BrO. For each target trace gas we regard a typical exemplary measurement scenario (Table 1). For the target species BrO and SO_2 we use typical measurement scenarios of volcanic emissions in the UV spectral range. For SO_2 we assume CDs that are typically measured in volcanic plumes of a comparably weak volcanic emitter or an already highly diluted plume (required detection limit of 1×10^{17} molec cm^{-2}; see Table 1). We additionally chose a high and probably disturbing NO_2 CD (1×10^{17} molec cm^{-2}) in order to make the scenario also applicable to SO_2 measurements at ship or industrial stack emissions. Existing filter-based SO_2 cameras are subject to strong cross interferences in this CD range (see e.g. Lübcke et al., 2013; Kuhn et al., 2014). In the scenario for BrO we assume a relatively strong but not uncommon volcanic emitter, with BrO mixing ratios of tens to hundreds of parts per trillion within the plume (required detection limit of 1×10^{14} molec cm^{-2}; see Table 1) and high SO_2 CDs (3×10^{18} molec cm^{-2}). Gradients in the BrO distributions can give insight into in-plume halogen chemistry (see e.g. Bobrowski et al., 2007; von Glasow, 2010; Roberts et al., 2014). The NO_2 scenario (blue spectral range) is applicable to measurements of stack emissions at, for example, a coal power plant (see e.g. Dekemper et al., 2016) but also to local gradients induced by traffic (required detection limit of 1×10^{16} molec cm^{-2}; see Table 1).

We calculate the sensitivities and study the cross interference of the apparent absorbance with other atmospheric absorbers for typical differential CDs for the respective measurement scenario. Table 1 lists the assumed differential CDs of the trace gases absorbing in the same spectral range as the trace gases under investigation. For these potentially interfering trace gases we chose relatively high values, so that the indicated cross interferences correspond to upper limits. The listed CDs represent differential CDs across a typical image FOV ($\sim 20°$), assuming that within the image a reference region I_0 without the target trace gas is always present.

In a second step, we calculate the corresponding photon budgets in order to infer the approximate achievable spatial and temporal resolution of the respective imaging measurement.

3.1 Description of the model

The apparent absorbance is calculated from radiances I_k (in photons s^{-1} mm^{-2} sr^{-1}) of scattered solar radiation transmit-

ted by the respective spectral channel $k = A,\ B$ (on-band and off-band FPI setting):

$$I_k = \int \mathrm{d}\lambda\, I_0(\lambda) e^{-\sum_i \sigma_i(\lambda) S_i} T_{\mathrm{FPI},\,k}(\lambda) T_{\mathrm{BPF}}(\lambda). \tag{7}$$

A spectrum recorded on a clear day in Heidelberg with a solar zenith angle of 73° (160° relative solar azimuth, 89° viewing zenith angle) was used to approximate the spectral radiance $I_0(\lambda)$. $I_0(\lambda)$ was scaled with scattered sky radiance measurements from Blumthaler et al. (1996). The radiance measurements were performed in Innsbruck in February 1995 with a solar zenith angle of 68°. For our calculations we used the values for a 180° relative solar azimuth and 70° viewing zenith angle. S_i is the CD of an absorbing gas species i with spectral absorption cross section $\sigma_i(\lambda)$. $T_{\mathrm{FPI},\,k}$ is the FPI transmittance in configuration k (see Eq. 4) and T_{BPF} the transmittance of the BPF isolating the measurement wavelength range for the respective target trace gas. T_{BPF} was modelled with a higher-order Gaussian function:

$$T_{\mathrm{BPF}}(\lambda) = P\, e^{-\left(\frac{(\lambda_{\mathrm{BPF}}-\lambda)^2}{2c^2}\right)^p}, \tag{8}$$

with a FWHM of

$$\delta_{\lambda,\,\mathrm{BPF}} = 2c\sqrt{2(\log 2)^{\frac{1}{p}}}. \tag{9}$$

P describes the peak transmission at a central wavelength λ_{BPF}. An order $p = 6$ was used to approximate interference filter transmission profiles.

With Eq. (5) and the intensities I_k from Eq. (7), the apparent absorbance $\widetilde{\tau}_i$ can be calculated, allowing us to study the sensitivity and selectivity of the detection of a trace gas i for given FPI instrument settings.

In addition, we approximate the respective detection limits based on photon shot noise. In order to calculate the number of photons that reach the detector of the imaging device, we need to know the etendue (product of entrance area A and aperture solid angle Ω) of the employed optics. Kuhn et al. (2014) suggest several optical set-ups for FPI correlation spectroscopy imaging implementations. Here, we chose the set-up in which, with help of image space telecentric optics (see Fig. 5), the incident radiation from the imaging FOV is parallelised before traversing the FPI and BPF. In order to avoid strong blurring of the FPI transmission spectrum due to different incidence angles, the divergence Θ of the light beams traversing the FPI should not be much larger than $\Theta = 1°$. With a lens of focal length f this condition limits the maximum aperture radius a to

$$a = f \tan\frac{\Theta}{2}. \tag{10}$$

The FPI clear aperture radius a_{FPI} determines the imaging FOV aperture angle:

$$\gamma_{\mathrm{FOV}} = 2\arctan\frac{a_{\mathrm{FPI}}}{f}. \tag{11}$$

The etendue per pixel E_{pix} is determined by the spatial resolution of the recorded image, which can be varied by binning individual pixels. For n_{pix} being the number of pixels along a column of a square detector array, the approximate etendue per pixel of the instrument is

$$E_{\mathrm{pix}} = A_{\mathrm{pix}}\,\Omega_{\mathrm{pix}} \approx a^2 \sin^2\left(\frac{\gamma_{\mathrm{FOV}}}{2n_{\mathrm{pix}}}\right)\pi^2. \tag{12}$$

The detectors' quantum efficiency and losses within the optics are considered to be not wavelength dependent in the regarded spectral ranges and combined in a loss factor η. We chose a somewhat lower loss factor for the UV range (0.25 for SO_2 and BrO) compared to the visible range (0.5 for NO_2) due to the higher quantum efficiency of commonly used detectors. Each FPI channel (on-band and off-band setting) requires one image acquisition. We assume a measurement limited by photoelectron shot noise, where for an exposure time Δt the number of counted photoelectrons per pixel and image is

$$N_{\mathrm{phe,\,pix}} = I\, E_{\mathrm{pix}} \eta \Delta t, \tag{13}$$

with an uncertainty of $\Delta N_{\mathrm{phe,\,pix}} = \sqrt{N_{\mathrm{phe,\,pix}}}$. The uncertainty in the apparent absorbance $\widetilde{\tau}$ is then

$$\Delta\widetilde{\tau} \approx \sqrt{\frac{2}{N_{\mathrm{phe,\,pix}}}}, \tag{14}$$

assuming the intensities I_k for the two FPI settings $k = A,\ B$ are similar and that the reference intensities $I_{0,\,k}$ have to be recorded only once.

Note that the used sky radiances, loss factors and dimensions of the optics (see Table 2) represent conservative assumptions. For instance the light throughput could be enhanced by more than an order of magnitude by choosing a different optical set-up (see Kuhn et al., 2014). There, the FPI is placed in front of the lens using the full clear aperture and the full aperture angle of the FPI and the optics. Each viewing direction of the FOV, however, will have a different incidence angle onto the FPI and therefore a different FPI transmission spectrum, which has to be accounted for in the data analysis. Alternatively, simply a larger FPI could be used. The results of the following calculations for the image space telecentric optics, therefore, represent lower limits of the performance.

3.2 Results of the simulations

The FPI correlation spectroscopy technique allows for numerous different realisations regarding the used spectral window and FPI instrument parameters that can be chosen according to, for example, measurement conditions or availability of optical components (FPI, BPF). Here, we identified spectral windows in which the target trace gas absorption cross sections exhibit approximately periodic structures

Table 2. Instrument parameters of FPI, BPF and optical set-up used for the simulations. The radiance for the on-band setting I_A at the detector was approximated based on the instrument parameters and sky radiance values from Blumthaler et al. (1996).

	Instrument parameters			
	SO_2	BrO	NO_2	
d_A (µm)	21.60	11.52	23.72	FPI surface displacement setting A
d_B (µm)	21.44	11.62	23.63	FPI surface displacement setting B
R	0.7	0.7	0.7	FPI surface reflectivity
P_{BPF}	0.7	0.7	0.7	BPF peak transmission
λ_{BPF} (nm)	308	342	434	BPF central wavelength
$\delta_{\lambda,\,BPF}$ (nm)	10	20	18	BPF FWHM
f (mm)		50		focal length of imaging optics
Θ (°)		1		required parallelisation
a (mm)		0.44		aperture radius of imaging optics
a_{FPI} (mm)		7.5		aperture radius of FPI
η	0.25		0.5	loss factor
γ_{FOV} (°)		17		imaging FOV of camera
I_A (photons s^{-1} mm^{-2} sr^{-1})	4.51×10^9	$1.48 \times ^{11}$	5.17×10^{11}	

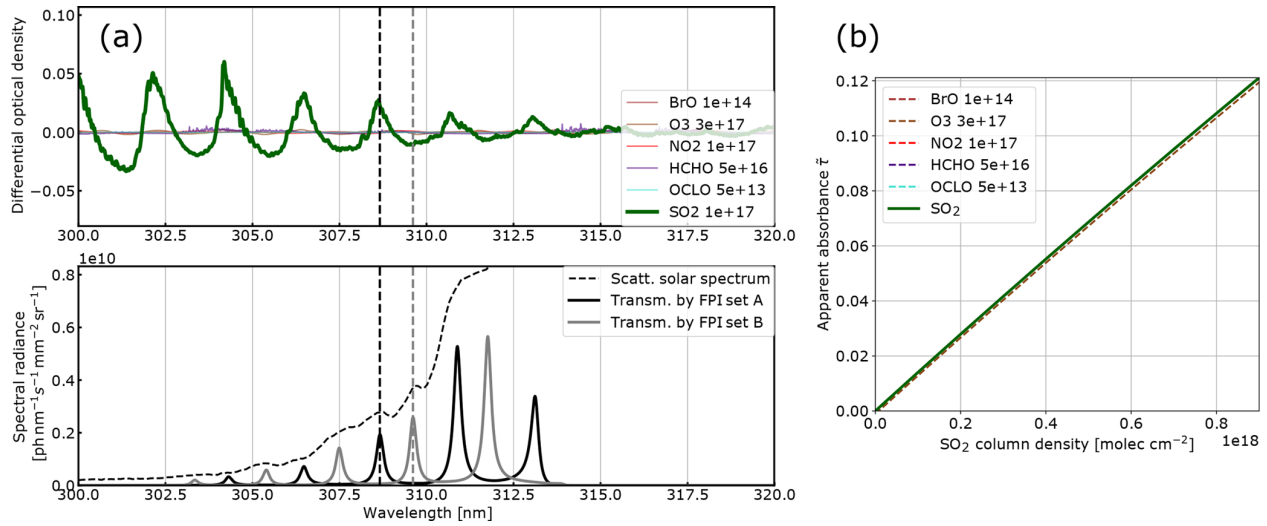

Figure 2. Model results for SO_2: **(a)** the differential optical densities of the assumed differential trace gas CDs are plotted in the upper panel. The lower panel shows the spectral radiance of the sky (dashed line) and the transmitted spectral radiances of the FPI and BPF (drawn lines, on-band in black, off-band in grey). Panel **(b)** shows the calculated calibration curve for SO_2 only (drawn line) and with different interfering species included (dashed lines, CDs in molecules per square centimetre; see legend and Table 1).

and appropriate FPI parameters were determined in order to maximise the correlation of FPI transmission and trace gas absorption according to the procedures described in Kuhn et al. (2014). Table 2 lists the parameters for the exemplary set-ups we use in this work.

The results for SO_2, BrO and NO_2 are summarised in Figs. 2, 3 and 4, which show the differential optical densities of the target trace gas and the potentially interfering trace gases for the respective measurement wavelength ranges (Figs. 2a, 3a, 4a). In the lower panels, the transmitted spectral radiances of the respective FPI spectral channels (on-band, off-band) are plotted. The SO_2 and NO_2 trace gas optical densities clearly dominate the total differential optical density for the targeted detection limits. For BrO the other trace gases exhibit differential optical depths on the same order of magnitude as BrO. In Figs. 2b, 3b and 4b, the respective simulated calibration curves are plotted, where the dashed lines indicate the impact of the individual interfering gases for the assumed amounts. For all three gases these impacts are well below the targeted detection limit. Especially for the case of BrO this illustrates how FPI correlation spectroscopy can effectively separate the absorption structure of

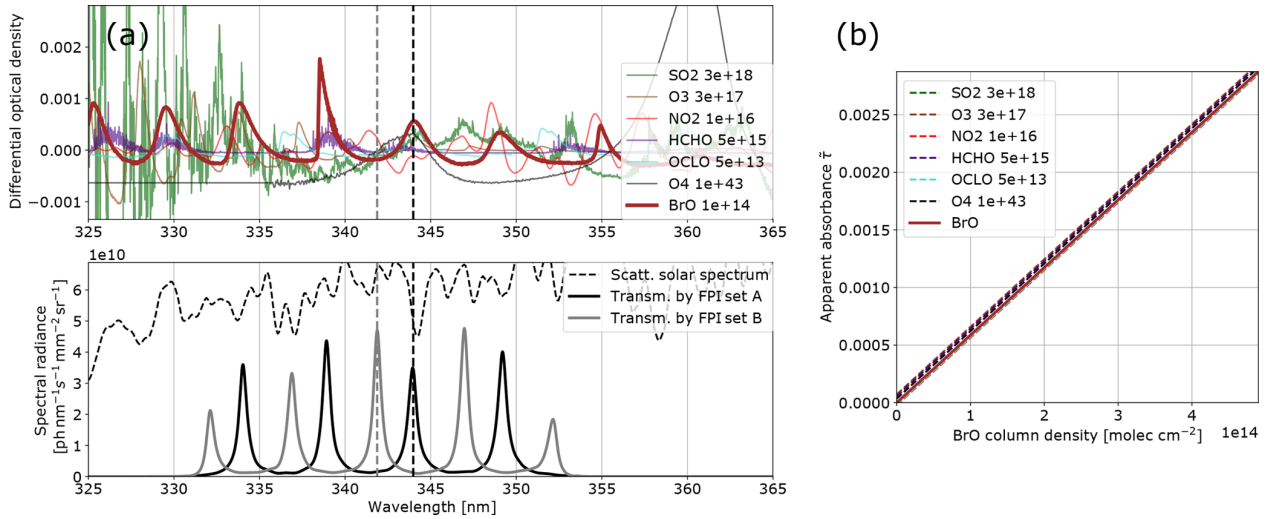

Figure 3. Model results for BrO: **(a)** the differential optical densities of the assumed differential trace gas CDs are plotted in the upper panel. The lower panel shows the spectral radiance of the sky (dashed line) and the transmitted spectral radiances of the FPI and BPF (drawn lines, on-band in black, off-band in grey). Panel **(b)** shows the calculated calibration curve for BrO only (drawn line) and with different interfering species included (dashed lines, CDs in molecules per square centimetre; see legend and Table 1).

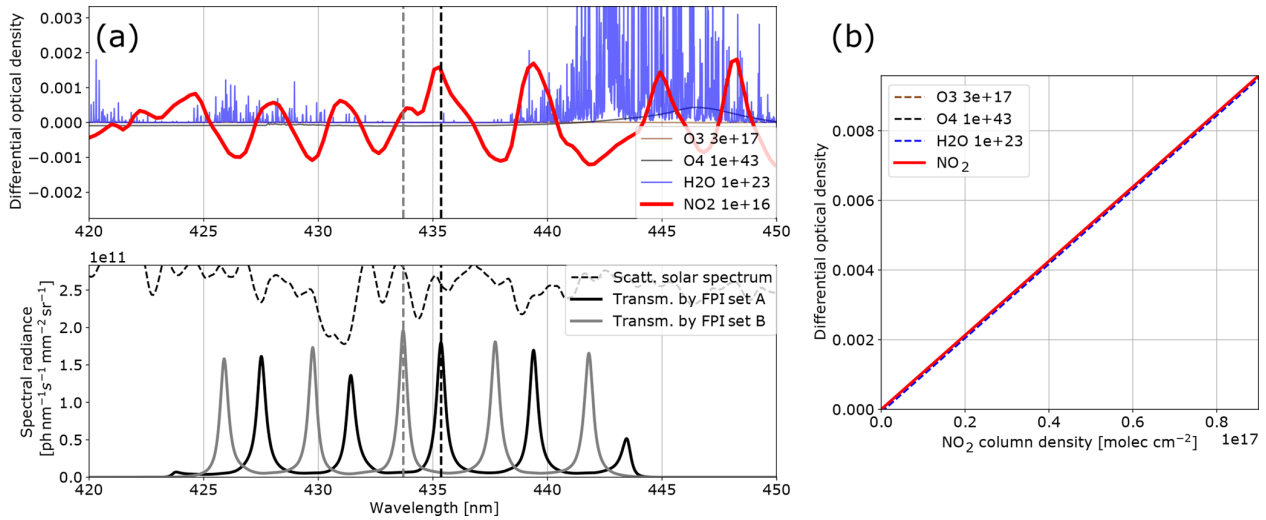

Figure 4. Model results for NO_2: **(a)** the differential optical densities of the assumed differential trace gas CDs are plotted in the upper panel. The lower panel shows the spectral radiance of the sky (dashed line) and the transmitted spectral radiances of the FPI and BPF (drawn lines, on-band in black, off-band in grey). Panel **(b)** shows the calculated calibration curve for NO_2 only (drawn line) and with different interfering species included (dashed lines, CDs in molecules per square centimetre; see legend and Table 1).

a single trace gas from a multitude of trace gas optical densities of the same order of magnitude. By using more than two FPI settings, the selectivity can be enhanced even further.

The absorption bands of NO_2 are not ideally periodic in the chosen wavelength window. Therefore, at first glance they appear to be non-ideal for FPI correlation. The apparent absorbance, however, is still reasonably high with extremely low cross interferences to water vapour and O_4. This demonstrates that periodical absorption structures are ideal but not necessary for FPI correlation spectroscopy. For a different measurement scenario (here we optimised for stack and ship emissions; see above) there might also be a better choice for instrument parameters. For instance for a high-radiance and low-NO_2 scenario one might use a single FPI transmission peak on the NO_2 absorption band at ~ 435 nm (as setting A)

Table 3. Simulation results: the spatial resolution of a FPI correlation spectroscopy measurement was calculated for an exposure time of 10 s and the target detection limits, shown in Table 1.

	Simulation results		
	SO_2	BrO	NO_2
$\Delta\overline{\sigma}$ (cm^{-2})	1.5×10^{-19}	6×10^{-18}	1.1×10^{-19}
Target det. lim. (molec cm^{-2})	1×10^{17}	1×10^{14}	1×10^{16}
Target det. lim $\widetilde{\tau}$	0.015	0.0006	0.0011
Required $N_{\text{phe, pix}}$	8.9×10^{3}	5.6×10^{6}	1.7×10^{6}
Required E_{pix} (mm^2 sr)	7.9×10^{-7}	1.5×10^{-5}	6.6×10^{-7}
Max. spatial resolution ($n_{\text{pix}} \times n_{\text{pix}}$)	226×226	51×51	252×252

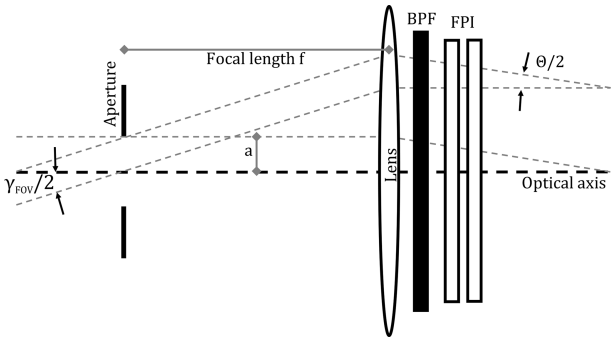

Figure 5. Image space telecentric optical set-up for parallelising light from the imaging FOV before traversing the FPI and BPF.

and at ∼ 438 nm (as setting B) in order to increase the sensitivity (see Fig. 4).

Table 3 summarises the results of the photon budget calculations. We calculated the maximum possible spatial resolution of the imaging measurement for a 10 s exposure time and the instrument parameters listed in Table 2. For this, spatial pixels are co-added until the targeted detection limit was reached. We find that for the targeted detection limits the spatial resolutions of the imaging measurements for the chosen parameters are 226 by 226 pixels for SO_2, 51 by 51 pixels for BrO and 252 by 252 pixels for NO_2 for a temporal resolution of 10 s. The temporal resolution could be enhanced at the expense of the spatial resolution or vice versa. For instance, cutting the linear spatial resolution in half (e.g. from 226 by 226 to 113 by 113 pixels for SO_2), would reduce the temporal resolution to 5 s for the same detection limit.

When comparing to corresponding DOAS measurements the increase in spatio-temporal resolution becomes evident. A state-of-the-art DOAS measurement takes around 1 s to reach a detection limit of 1×10^{14} molec cm^{-2} BrO for one spatial pixel. To scan the ca. 2600 pixels of the assumed BrO image would take 2600 s. This is, however, a comparison with an instrument that is not optimised for these kinds of imaging measurements. Manago et al. (2018) recently recorded NO_2 images with a hyperspectral camera, based on imaging DOAS. A detection limit of around 1×10^{16} molec cm^{-2} NO_2 is reached with a spatial resolution of 480 by 640 pixels and 3 by 3 pixel binning with 12 s $frame^{-1}$. This is only a factor of 2.2 slower than our calculation for the telecentric set-up. By applying the standard optics introduced in Kuhn et al. (2014), the light throughput is increased by another factor of 32. Therefore, theoretically, the FPI technique can be a factor of ∼ 70 times faster. Of course these values always depend on the size of the assumed instrument optics. Our results show that FPI correlation spectroscopy can be about 2 orders of magnitude faster than conventional DOAS measurements while maintaining a similar degree of selectivity and interference suppression.

The presented results of the exemplary calculations for SO_2, BrO and NO_2 suggest that FPI correlation spectroscopy can also be implemented for other trace gases with similarly strong and structured absorption, such as, for example, O_3, HCHO, IO or OClO.

4 Proof of concept: field measurements of volcanic SO_2

4.1 Sensitivity and ozone interference

The above model study on trace gas detection with FPI correlation spectroscopy was validated in a proof-of-concept field study for volcanic SO_2. In a 1-pixel prototype a single photodiode was used as a detector. A BPF ($\lambda_{\text{BPF}} \approx 310$ nm, $\delta_{\lambda,\,\text{BPF}} \approx 10$ nm) was used for the preselection of a wavelength range, for which the SO_2 differential absorption is strong and approximately periodic (see Fig. 2). A FPI (air-spaced etalon from SLS Optics Ltd.) with a FSR of 2.1 nm and a finesse of 7 across a clear aperture of 20 mm was tilted by a servomotor in order to tune it to the on-band and off-band transmission settings. The individual plates of the FPI have a finite thickness and two surfaces; the outer surfaces have an anti-reflective coating and are slightly wedged from the inner surfaces of the plates, so their influence can be neglected here. The optical set-up behind FPI and BPF consists

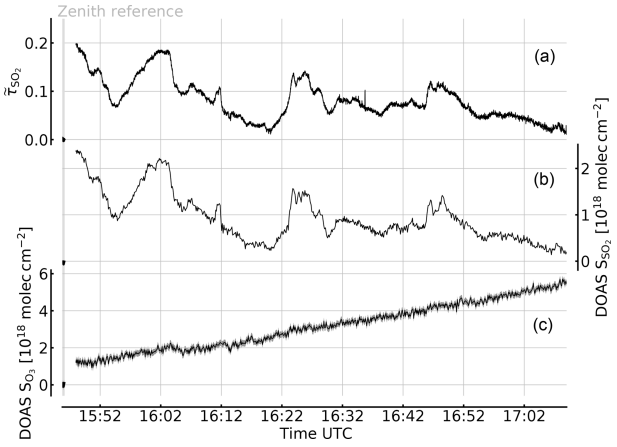

Figure 6. Time series of the apparent absorbance of the 1-pixel FPI correlation spectroscopy prototype for SO_2 detection (top trace, left scale) recorded at Etna, Sicily, on 30 July 2017. A co-aligned telescope was used to simultaneously record spectra for DOAS evaluation of SO_2 and O_3 (centre and bottom traces and right and bottom left scales, respectively). The apparent absorbance nicely correlates with the SO_2 CD (see Fig. 7), while no O_3 impact is observable. The growth of the retrieved O_3 differential CD is expected due to the increasing stratospheric O_3 column for increasing solar zenith angle (see text).

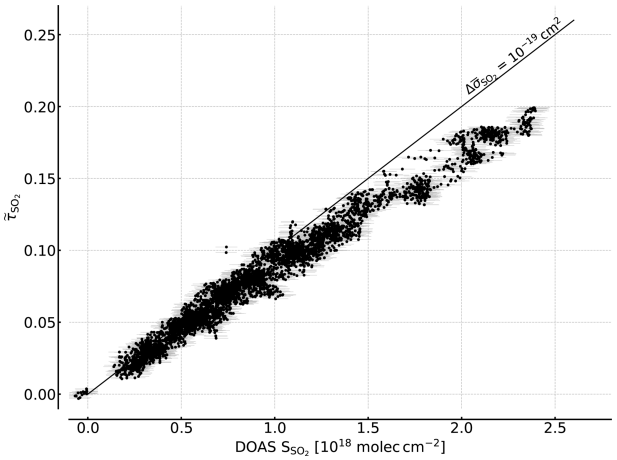

Figure 7. Correlation plot of the recorded FPI correlation spectroscopy apparent absorbance and the SO_2 CD retrieved by DOAS. A sensitivity of about $\Delta\overline{\sigma}_{SO_2}$ of 10^{-19} cm^2 is reached for lower SO_2 CDs. For higher CDs a flattening of the curve is observed that is induced by saturation effects due to the high SO_2 optical densities at the absorption peaks.

of a fused silica lens ($f \approx 50$ mm), which projects light from a narrow FOV ($\sim 0.8°$ aperture angle) onto the photodiode.

Radiances for the on-band and off-band channels were recorded, delivering an apparent absorbance measurement with 0.42 Hz. A telescope ($\sim 0.5°$ aperture angle) was co-aligned with the 1-pixel FPI set-up and connected to a temperature-stabilised spectrometer (spectral resolution ~ 0.8 nm). The recorded spectra (~ 0.13 Hz) were evaluated with the DOAS algorithm.

The measurement was performed at the Osservatorio Vulcanologico Pizzi Deneri (lat 37.766, long 15.017, 2800 m a.s.l.) at Mt Etna on Sicily on 30 July 2017. The device was pointed towards the volcanic plume of Mt Etna with a constant viewing angle (8° viewing elevation, azimuth 280° N). A plume-free part of the sky (zenith viewing direction) was used for reference measurements and recorded prior to the plume measurement. Figure 6 shows the time series of the apparent absorbance of the FPI correlation spectroscopy prototype together with the SO_2 CD retrieved from the co-recorded spectra. The apparent absorbance shows high correlation with the retrieved SO_2 CD. In Fig. 7 the correlation plot is shown. For high SO_2 CDs the sensitivity of $\widetilde{\tau}_{SO_2}$ decreases slightly due to saturation effects. The scatter of the values mainly originates from slight misalignment and the difference of the two narrow FOVs.

The recorded UV spectra also allow for evaluation of the O_3 absorption. The lower panel of Fig. 6c shows the change of the differential O_3 CD during the measurement with respect to the reference. The observed increase in the O_3 CD by more than 4×10^{18} molec cm^{-2} during the plume measurement is due to the increasing stratospheric light path with increasing solar zenith angle (63.58 to 79.31° during the measurement sequence). Within an imaging FOV (of 17°, for example) much lower differential O_3 CDs are expected (see Table 2), since all pixels are similarly affected by the change in O_3 background. Even with this extreme change in O_3 CD no impact on the recorded SO_2 apparent absorbances is observed.

The presented data also indicate the potential of using an additional DOAS measurement for the calibration of the apparent absorbance of an FPI imaging device. The position of the narrow FOV of a DOAS telescope pointing into the wide imaging FOV can be retrieved from time series and used for an in-operation calibration (see e.g. Lübcke et al., 2013; Sihler et al., 2017).

4.2 Calculation of SO_2 CDs by modelling effective absorption cross sections

As stated in Sect 2.2 we can also directly calculate the SO_2 CDs from the apparent absorbance $\widetilde{\tau}$ by modelling the effective absorption cross sections and thereby $\Delta\overline{\sigma}_{SO_2}$. This requires knowledge about the instrument spectral transmission, the background scattered light spectrum and the SO_2 absorption cross section.

We modelled the instrument transfer function with the transmission spectrum of the used BPF, the calculated FPI transmission spectrum (see Sect. 3.1) and the quantum efficiency of the photodiode. The background scattered sunlight spectrum was modelled using a high-resolution solar atlas

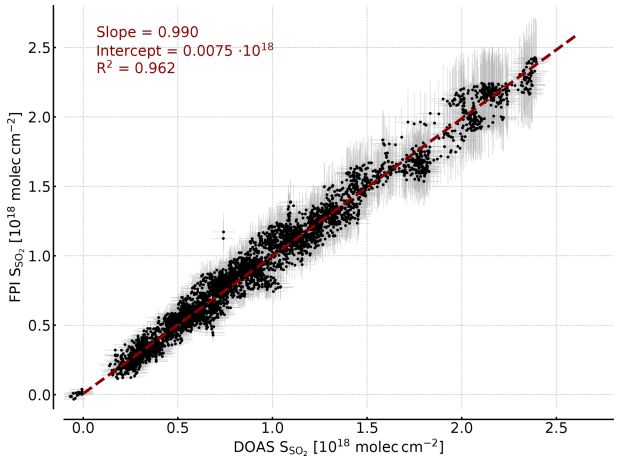

Figure 8. Correlation plot of the SO_2 CDs retrieved by modelling and the SO_2 CDs retrieved by DOAS. The error bars indicate the uncertainty of the FPI finesse (±3 %) and the background spectral radiance in the model (±10 %) and the DOAS retrieval error. A high correlation is observed and the saturation effect is accounted for by the model as well.

spectrum according to Chance and Kurucz (2010), scaled by the wavelength to the fourth power (assuming Rayleigh scattering) and multiplied with the transmission of the total slant atmospheric ozone column. The ozone column was estimated to 2.5×10^{19} molec cm^{-2} using the vertical ozone column (for the measurement day according to satellite measurements, TEMIS database; Veefkind et al., 2006) multiplied with a geometric air mass factor for the average solar zenith angle during the measurement. The SO_2 absorption cross section of Vandaele et al. (2009) was used.

The largest uncertainties are the finesse of the FPI and the modelled background spectrum, in which Rayleigh scattering approximation and the assumed ozone column introduce uncertainties. A finesse of about 7 is reported by the manufacturer for perpendicularly incident radiation. For the instrument model we have to calculate the effective finesse for a divergent light ray (∼ 0.8° aperture angle) for the two FPI tilt positions (around 0° for setting *B* and 5° for setting A, corresponding to a finesse of around 7 and 5, respectively). Since the divergent light ray reaching the detector is dependent on focal length, detector area and the alignment of the optical components and due to the uncertainty in the reflectance of the FPI, we can determine the finesse only with an uncertainty of ±3 %. Further, we estimate an uncertainty in the background spectrum by ±10 % in our calculation, accounting for uncertainties in atmospheric radiative transfer and ozone column.

Figure 8 shows the SO_2 CDs calculated with the described FPI model as a function of the SO_2 CDs retrieved from the DOAS spectra. We observe an excellent agreement with a slope of 0.99, an intercept of 7.5×10^{15} molec cm^{-2} and $R^2 = 0.96$. The uncertainties in background spectral radiance and finesse result in a uncertainty in the SO_2 sensitivity $\Delta\overline{\sigma}_{SO_2}$ of around ±10 % and therefore a relative uncertainty of ±10 % in the retrieved SO_2 CD. Here, it is important to highlight the difference between ozone interference with the apparent absorbance and the influence of an uncertainty in the total ozone column assumed in the model. The former seems to be negligible as shown by the measurements (Fig. 6) and in the model study (Sect. 3.2). The latter influences the modelled sensitivity of the measurement. This means it introduces a small relative uncertainty to the retrieved CDs, which has almost no influence on the detection limit. The saturation effects observed for high CDs in the apparent absorbances (see Fig. 7), meaning the CD dependency of $\Delta\overline{\sigma}_{SO_2}$, are accounted for by the model as well. This is a very promising result, pointing towards the possibility of calibration-free measurements, which would be another major advantage of the FPI correlation spectroscopy compared to, for example, filter-based SO_2 cameras.

4.3 Imaging

The 1-pixel FPI correlation spectroscopy prototype, introduced in this study, can be implemented in a full-frame imaging instrument. This is the major advantage of the technique compared with the DOAS technique. The imaging implementation can be achieved with, for example, the image space telecentric optical set-up, used for the above calculations and shown in Fig. 5. In principle, the single-pixel detector (photodiode) is replaced by a two-dimensional detector array (UV sensitive for SO_2 and BrO) and an aperture stop is added in the focal plane in front of the lens. This would, however, reduce the light throughput per pixel of the imaging set-up compared to the 1-pixel prototype. Alternatively, the FPI could be placed in front of the lens using the full clear aperture and the full aperture angle of the FPI and the optics, increasing the light throughput by a factor of 32 (see Kuhn et al., 2014). This leads to a much higher light throughput; however, the incidence angle of the incident light onto the FPI and thereby the FPI transmission spectrum becomes dependent on the pixel (i.e. the viewing direction within the imaging FOV) and has to be accounted for in the data evaluation.

5 Conclusions

Many locally variable atmospheric processes are difficult to quantify with state-of-the-art UV–Vis remote-sensing methods (e.g. DOAS) due to the limited spatio-temporal resolution. This makes it difficult to, for example, study the emission of point sources or to separate the effects of transport and chemical conversion on local scales. Kuhn et al. (2014) proposed the FPI correlation spectroscopy for SO_2 in the UV wavelength range after similar approaches have been stud-

ied in infrared wavelength ranges (e.g. Wilson et al., 2007; Vargas-Rodríguez and Rutt, 2009). The major motivation is to reduce the number of spectral channels used for the trace gas detection in order to increase the spatio-temporal resolution of the measurement while maintaining its selectivity.

In a model study we investigated the sensitivity and determined the photon budget of FPI correlation spectroscopy for three measurement scenarios for SO_2, BrO and NO_2. For SO_2 we assumed a scenario with rather low volcanic emissions, which is also representative for industrial stack or ship emissions. For BrO a scenario with stronger volcanic emissions was assumed, with BrO mixing ratios of 10 to 100 ppt within the volcanic plume and high SO_2 CDs. The NO_2 measurement scenario represents typical stack emissions of power plants and gradients of local air pollution induced by traffic, for example.

For all three investigated gases, cross interferences with other trace gases absorbing in the preselected spectral ranges were found to be very low, meaning that the selectivity of FPI correlation spectroscopy can be similar to the selectivity of conventional techniques (e.g. DOAS). In this study, we only used two FPI settings. A larger number of FPI settings could be used to further reduce possible cross interferences.

Using rather conservative assumptions regarding the intensity of the incoming radiation and the size of the instrument optics, we calculated the highest possible spatio-temporal resolution of the FPI correlation spectroscopy measurements for the different scenarios and found that they can be more than 2 orders of magnitude higher compared to state-of-the-art DOAS measurements for the same trace gas CD. This means that in the same time period a conventional dispersive technique records a single viewing direction (i.e. a single spatial pixel), almost an entire image can be recorded with the FPI correlation spectroscopy. This strongly indicates that future instruments based on FPI correlation spectroscopy can provide unprecedented insight into short time or small-scale processes in the atmosphere.

In the second part, we presented a proof-of-concept field study for FPI correlation spectroscopy applied to volcanic SO_2, which confirms the model simulations by comparing the measured apparent absorbance to SO_2 CDs retrieved by a co-aligned DOAS measurement. One particularly important finding is that, as expected from the model study, no O_3 cross interference can be observed over a large O_3 CD range. Further, SO_2 CDs could be directly calculated from the instrument model and a very simple radiative transfer model very accurately and with a $\sim 10\,\%$ uncertainty of the sensitivity. This indicates that CDs can be retrieved directly from the FPI radiance data without calibration.

The extension of the 1-pixel prototype to a camera can be accomplished comparably easily by minor modifications of the optics and by using a UV-sensitive detector array and should be the aim of future studies. By replacing the FPI and the BPF, the instrument is adjusted to measure different trace gases, e.g. BrO and NO_2, according to the model calculations performed in Sect. 3.

The applications of UV–Vis FPI correlation spectroscopy mentioned in this work represent only some examples for trace gases and phenomena that could be studied. Beyond the volcanological application, FPI imaging can for instance be used to study SO_2 in air pollution or BrO in salt pans (see e.g. Holla et al., 2015). The technique can also be applied to other trace gases with similarly strong and structured absorption, such as, for example, O_3, HCHO, IO or OClO.

Data availability. The data used for the proof-of-concept study can be obtained from the authors upon request.

Author contributions. All authors contributed to the conception and design of the study and substantially worked on several rounds of paper extension and revision. NB helped with the field measurements. JK developed the model, designed and built the instrument, performed and evaluated the measurements, and wrote the draft of the paper.

Competing interests. The authors declare that they have no conflict of interest.

Acknowledgements. We would like to thank SLS Optics Ltd. for sharing their expertise in designing and manufacturing etalons. We also thank Jan-Lukas Tirpitz and Denis Pöhler for their help with instrument design and electronics. We gratefully acknowledge financial support from the Deutsche Forschungsgemeinschaft (project DFG PL 193/23-1) and the Heidelberg Graduate School of Fundamental Physics.

The article processing charges for this open-access publication were covered by the Max Planck Society.

Edited by: Andreas Hofzumahaus
Reviewed by: Emmanuel Dekemper and one anonymous referee

References

Blumthaler, M., Gröbner, J., Huber, M., and Ambach, W.: Measuring spectral and spatial variations of UVA and UVB sky radiance, Geophys. Res. Lett., 23, 547–550, https://doi.org/10.1029/96gl00248, 1996.

Bluth, G., Shannon, J., Watson, I., Prata, A., and Realmuto, V.: Development of an ultra-violet digital camera for volcanic SO2 imaging, J. Volcanol. Geotherm. Res., 161, 47–56, https://doi.org/10.1016/j.jvolgeores.2006.11.004, 2007.

Bobrowski, N. and Giuffrida, G.: Bromine monoxide/sulphur dioxide ratios in relation to volcanological observations at Mt. Etna 2006–2009, Solid Earth, 3, 433–445, https://doi.org/10.5194/se-3-433-2012, 2012.

Bobrowski, N., von Glasow, R., Aiuppa, A., Inguaggiato, S., Louban, I., Ibrahim, O. W., and Platt, U.: Reactive halogen chemistry in volcanic plumes, J. Geophys. Res., 112, D06311, https://doi.org/10.1029/2006JD007206, 2007.

Bogumil, K., Orphal, J., Homann, T., Voigt, S., Spietz, P., Fleischmann, O., Vogel, A., Hartmann, M., Kromminga, H., Bovensmann, H., Frerick, J., and Burrows, J.: Measurements of molecular absorption spectra with the {SCIAMACHY} pre-flight model: instrument characterization and reference data for atmospheric remote-sensing in the 230–2380 nm region, J. Photoch. Photobio. A, 157, 167–184, https://doi.org/10.1016/S1010-6030(03)00062-5, 2003.

Chance, K. and Kurucz, R.: An improved high-resolution solar reference spectrum for earth's atmosphere measurements in the ultraviolet, visible, and near infrared, J. Quant. Spec. Rad. Trans., 111, 1289–1295, https://doi.org/10.1016/j.jqsrt.2010.01.036, 2010.

Chance, K. and Orphal, J.: Revised ultraviolet absorption cross sections of H_2CO for the HITRAN database, J. Quant. Spec. Rad. Trans., 112, 1509–1510, https://doi.org/10.1016/j.jqsrt.2011.02.002, 2011.

Dekemper, E., Vanhamel, J., Van Opstal, B., and Fussen, D.: The AOTF-based NO_2 camera, Atmos. Meas. Tech., 9, 6025–6034, https://doi.org/10.5194/amt-9-6025-2016, 2016.

Fleischmann, O. C., Hartmann, M., Burrows, J. P., and Orphal, J.: New ultraviolet absorption cross-sections of BrO at atmospheric temperatures measured by time-windowing Fourier transform spectroscopy, J. Photoch. Photobio. A, 168, 117–132, https://doi.org/10.1016/j.jphotochem.2004.03.026, 2004.

Gliß, J., Bobrowski, N., Vogel, L., Pöhler, D., and Platt, U.: OClO and BrO observations in the volcanic plume of Mt. Etna – implications on the chemistry of chlorine and bromine species in volcanic plumes, Atmos. Chem. Phys., 15, 5659–5681, https://doi.org/10.5194/acp-15-5659-2015, 2015.

Holla, R., Schmitt, S., Frieß, U., Pöhler, D., Zingler, J., Corsmeier, U., and Platt, U.: Vertical distribution of BrO in the boundary layer at the Dead Sea, Environ. Chem., 12, 438–460, https://doi.org/10.1071/EN14224, 2015.

Hönninger, G., von Friedeburg, C., and Platt, U.: Multi axis differential optical absorption spectroscopy (MAX-DOAS), Atmos. Chem. Phys., 4, 231–254, https://doi.org/10.5194/acp-4-231-2004, 2004.

Kern, C., Kick, F., Lübcke, P., Vogel, L., Wöhrbach, M., and Platt, U.: Theoretical description of functionality, applications, and limitations of SO_2 cameras for the remote sensing of volcanic plumes, Atmos. Meas. Tech., 3, 733–749, https://doi.org/10.5194/amt-3-733-2010, 2010.

Kromminga, H., Orphal, J., Spietz, P., Voigt, S., and Burrows, J. P.: New measurements of OClO absorption cross-sections in the 325–435 nm region and their temperature dependence between 213 and 293 K, J. Photoch. Photobio. A, 157, 149–160, https://doi.org/10.1016/S1010-6030(03)00071-6, 2003.

Kuhn, J., Bobrowski, N., Lübcke, P., Vogel, L., and Platt, U.: A Fabry–Perot interferometer-based camera for two-dimensional mapping of SO_2 distributions, Atmos. Meas. Tech., 7, 3705–3715, https://doi.org/10.5194/amt-7-3705-2014, 2014.

Lohberger, F., Hönninger, G., and Platt, U.: Ground-Based Imaging Differential Optical Absorption Spectroscopy of Atmospheric Gases, Appl. Opt., 43, 4711–4717, https://doi.org/10.1364/AO.43.004711, 2004.

Lübcke, P., Bobrowski, N., Illing, S., Kern, C., Alvarez Nieves, J. M., Vogel, L., Zielcke, J., Delgado Granados, H., and Platt, U.: On the absolute calibration of SO_2 cameras, Atmos. Meas. Tech., 6, 677–696, https://doi.org/10.5194/amt-6-677-2013, 2013.

Manago, N., Takara, Y., Ando, F., Noro, N., Suzuki, M., Irie, H., and Kuze, H.: Visualizing spatial distribution of atmospheric nitrogen dioxide by means of hyperspectral imaging, Appl. Opt., 57, 5970, https://doi.org/10.1364/ao.57.005970, 2018.

Mori, T. and Burton, M.: The SO_2 camera: A simple, fast and cheap method for ground-based imaging of SO_2 in volcanic plumes, Geophys. Res. Lett., 33, L24804, https://doi.org/10.1029/2006GL027916, 2006.

Perot, A. and Fabry, C.: On the Application of Interference Phenomena to the Solution of Various Problems of Spectroscopy and Metrology, Astrophys. J., 9, 87–115, https://doi.org/10.1086/140557, 1899.

Platt, U. and Stutz, J.: Differential optical absorption spectroscopy, Springer, Berlin, Heidelberg, Germany, 2008.

Platt, U., Lübcke, P., Kuhn, J., Bobrowski, N., Prata, F., Burton, M., and Kern, C.: Quantitative imaging of volcanic plumes – Results, needs, and future trends, J. Volcanol. Geotherm. Res., 300, 7–21, 2015.

Platt, U., Bobrowski, N., and Butz, A.: Ground-Based Remote Sensing and Imaging of Volcanic Gases and Quantitative Determination of Multi-Species Emission Fluxes, Geosciences, 8, 44, https://doi.org/10.3390/geosciences8020044, 2018.

Roberts, T. J., Martin, R. S., and Jourdain, L.: Reactive bromine chemistry in Mount Etna's volcanic plume: the influence of total Br, high-temperature processing, aerosol loading and plume-air mixing, Atmos. Chem. Phys., 14, 11201–11219, https://doi.org/10.5194/acp-14-11201-2014, 2014.

Roscoe, H. K., Van Roozendael, M., Fayt, C., du Piesanie, A., Abuhassan, N., Adams, C., Akrami, M., Cede, A., Chong, J., Clémer, K., Friess, U., Gil Ojeda, M., Goutail, F., Graves, R., Griesfeller, A., Grossmann, K., Hemerijckx, G., Hendrick, F., Herman, J., Hermans, C., Irie, H., Johnston, P. V., Kanaya, Y., Kreher, K., Leigh, R., Merlaud, A., Mount, G. H., Navarro, M., Oetjen, H., Pazmino, A., Perez-Camacho, M., Peters, E., Pinardi, G., Puentedura, O., Richter, A., Schönhardt, A., Shaiganfar, R., Spinei, E., Strong, K., Takashima, H., Vlemmix, T., Vrekoussis, M., Wagner, T., Wittrock, F., Yela, M., Yilmaz, S., Boersma, F., Hains, J., Kroon, M., Piters, A., and Kim, Y. J.: Intercomparison of slant column measurements of NO_2 and O_4 by MAX-DOAS and zenith-sky UV and visible spectrometers, Atmos. Meas. Tech., 3, 1629–1646, https://doi.org/10.5194/amt-3-1629-2010, 2010.

Rothman, L., Gordon, I., Babikov, Y., Barbe, A., Benner, D. C., Bernath, P., Birk, M., Bizzocchi, L., Boudon, V., Brown, L., Campargue, A., Chance, K., Cohen, E., Coudert, L., Devi, V., Drouin, B., Fayt, A., Flaud, J.-M., Gamache, R., Harrison, J., Hartmann, J.-M., Hill, C., Hodges, J., Jacquemart, D., Jolly, A., Lamouroux, J., Roy, R. L., Li, G., Long, D., Lyulin, O., Mackie, C., Massie, S., Mikhailenko, S., Müller, H., Naumenko, O., Nikitin, A., Orphal, J., Perevalov, V., Perrin, A., Polovtseva, E., Richard, C., Smith, M., Starikova, E., Sung, K., Tashkun, S., Tennyson, J., Toon, G., Tyuterev, V., and Wagner, G.: The HITRAN2012 molecular spectro-

scopic database, J. Quant. Spec. Rad. Trans., 130, 4–50, https://doi.org/10.1016/j.jqsrt.2013.07.002, 2013.

Serdyuchenko, A., Gorshelev, V., Weber, M., Chehade, W., and Burrows, J. P.: High spectral resolution ozone absorption cross-sections – Part 2: Temperature dependence, Atmos. Meas. Tech., 7, 625–636, https://doi.org/10.5194/amt-7-625-2014, 2014.

Sihler, H., Lübcke, P., Lang, R., Beirle, S., de Graaf, M., Hörmann, C., Lampel, J., Penning de Vries, M., Remmers, J., Trollope, E., Wang, Y., and Wagner, T.: In-operation field-of-view retrieval (IFR) for satellite and ground-based DOAS-type instruments applying coincident high-resolution imager data, Atmos. Meas. Tech., 10, 881–903, https://doi.org/10.5194/amt-10-881-2017, 2017.

Thalman, R. and Volkamer, R.: Temperature dependent absorption cross-sections of O_2-O_2 collision pairs between 340 and 630 nm and at atmospherically relevant pressure, Phys. Chem. Chem. Phys., 15, 15371–15381, https://doi.org/10.1039/C3CP50968K, 2013.

Vandaele, A. C., Hermans, C., and Fally, S.: Fourier transform measurements of SO_2 absorption cross sections: II.: Temperature dependence in the 29 000–44 000 cm^{-1} (227–345 nm) region, J. Quant. Spec. Rad. Trans., 110, 2115–2126, 2009.

Vargas-Rodríguez, E. and Rutt, H.: Design of CO, CO_2 and CH_4 gas sensors based on correlation spectroscopy using a Fabry–Perot interferometer, Sensor. Actuat. B Chem., 137, 410–419, https://doi.org/10.1016/j.snb.2009.01.013, 2009.

Veefkind, J., de Haan, J., Brinksma, E., Kroon, M., and Levelt, P.: Total ozone from the ozone monitoring instrument (OMI) using the DOAS technique, IEEE T. Geosci. Remote., 44, 1239–1244, https://doi.org/10.1109/tgrs.2006.871204, 2006.

von Glasow, R.: Atmospheric chemistry in volcanic plumes, P. Natl. Acad. Sci. USA, 107, 6594–6599, 2010.

Wilson, E. L., Georgieva, E. M., and Heaps, W. S.: Development of a Fabry–Perot interferometer for ultra-precise measurements of column CO_2, Meas. Sci. Technol., 18, 1495–1502, https://doi.org/10.1088/0957-0233/18/5/040, 2007.

Atmos. Meas. Tech., 14, 295–307, 2021
https://doi.org/10.5194/amt-14-295-2021

Atmospheric Measurement Techniques
Open Access
EGU

Quantitative imaging of volcanic SO_2 plumes using Fabry–Pérot interferometer correlation spectroscopy

Christopher Fuchs[1], **Jonas Kuhn**[1,2], **Nicole Bobrowski**[1,2], **and Ulrich Platt**[1,2]

[1]Institute of Environmental Physics, University of Heidelberg, Heidelberg, Germany
[2]Max Planck Institute for Chemistry, Mainz, Germany

Correspondence: Christopher Fuchs (cfuchs@iup.uni-heidelberg.de) and Jonas Kuhn (jkuhn@iup.uni-heidelberg.de)

Received: 29 June 2020 – Discussion started: 21 July 2020
Revised: 17 November 2020 – Accepted: 23 November 2020 – Published: 14 January 2021

Abstract. We present first measurements with a novel imaging technique for atmospheric trace gases in the UV spectral range. Imaging Fabry–Pérot interferometer correlation spectroscopy (IFPICS) employs a Fabry–Pérot interferometer (FPI) as the wavelength-selective element. Matching the FPI's distinct, periodic transmission features to the characteristic differential absorption structures of the investigated trace gas allows us to measure differential atmospheric column density (CD) distributions of numerous trace gases with high spatial and temporal resolution. Here we demonstrate measurements of sulfur dioxide (SO_2), while earlier model calculations show that bromine monoxide (BrO) and nitrogen dioxide (NO_2) are also possible. The high specificity in the spectral detection of IFPICS minimises cross-interferences to other trace gases and aerosol extinction, allowing precise determination of gas fluxes. Furthermore, the instrument response can be modelled using absorption cross sections and a solar atlas spectrum from the literature, thereby avoiding additional calibration procedures, e.g. using gas cells. In a field campaign, we recorded the temporal CD evolution of SO_2 in the volcanic plume of Mt. Etna, with an exposure time of 1 s and 400×400 pixel spatial resolution. The temporal resolution of the time series was limited by the available non-ideal prototype hardware to about 5.5 s. Nevertheless, a detection limit of 2.1×10^{17} molec cm^{-2} could be reached, which is comparable to traditional and much less selective volcanic SO_2 imaging techniques.

1 Introduction

Ground-based imaging of atmospheric trace gas distributions has a great potential to give new insights into mixing processes and chemical conversion of atmospheric trace gases by allowing their observation at high spatio-temporal resolution. Whereas present space-borne trace gas imaging provides daily global coverage with a spatial resolution of a few kilometres (e.g. Veefkind et al., 2012), ground-based observation can potentially reach a spatial resolution in the order of metres and a temporal resolution in the single digit Hz range. Such techniques in particular allow the investigation of trace gas distributions with strong gradients and short timescale chemical conversions.

There are several approaches for imaging trace gas distributions using scattered sunlight in the UV–Vis wavelength range (see, for example, Platt and Stutz, 2008; Platt et al., 2015): an image can be scanned pixel by pixel with a telescope, and recorded spectra are evaluated to determine the trace gas column density (whiskbroom approach). Alternatively, with a more complex optics and a two-dimensional detector, one detector dimension of the spectrograph can be used for spatially resolving an image column. Column by column (or pushbroom) scanning then resolves an image. The high spectral resolution of the spectrograph-based techniques allows the accurate and simultaneous identification of several trace gases; however, the light throughput and the scanning process severely limit the temporal resolution. A third approach applies tunable filters to resolve the trace gas spectral features, e.g. acousto-optical tunable filters (Dekemper et al., 2016), as wavelength-selective elements for an entire image frame. The application of tunable filters can have

high spectral resolution and hence high trace gas selectivity; however, due to limited light throughput the temporal resolution lies in the order of minutes. A fourth imaging technique uses a small number (typically two) of wavelength channels selected by static filters, e.g. interference filters (Mori and Burton, 2006). This approach can be quite fast with a temporal resolution in the order of seconds; the trace gas selectivity, however, strongly depends on the correlation of trace gas absorption with the wavelength-selective elements and usually is rather marginal.

Fabry–Pérot interferometers (FPIs) exhibit a periodic spectral transmission pattern which can be matched to periodic spectral features (typically due to rotational or vibrational structures of electronic transitions) of the trace gas absorption, thereby yielding very high correlation for some trace gases. Imaging Fabry–Pérot interferometer correlation spectroscopy (IFPICS) thus essentially combines the advantage of fast image acquisition with selective spectral identification of the target trace gas. IFPICS was proposed by Kuhn et al. (2014) and discussed in Platt et al. (2015) for volcanic SO_2. Kuhn et al. (2019) demonstrated the feasibility with a 1 pixel prototype for volcanic SO_2 and evaluated its applicability to other trace gases.

Here we present first imaging measurements (at a resolution of 400×400 pixels, 1 s exposure time) performed with IFPICS and confirm its high selectivity and sensitivity. A prototype instrument for SO_2 was tested at Mt. Etna volcano, Italy, showing a noise-equivalent signal between 2.1×10^{17}–5.5×10^{17} molec cm^{-2} s$^{-1/2}$. Furthermore, we show that the instrument response can be modelled and thereby intrinsically calibrated, using a solar atlas spectrum and literature trace gas absorption cross sections.

Existing interference-filter-based SO_2 cameras used, for example, for the quantification of volcanic trace gas emission fluxes into the atmosphere (Mori and Burton, 2006; Bluth et al., 2007; Kern et al., 2015a), exhibit strong cross-interferences to aerosol scattering extinction and other trace gases (Lübcke et al., 2013; Kuhn et al., 2014). Furthermore, these techniques require in-field calibration. Besides the thereby induced systematic errors that propagate into the emission flux quantification, the detection limit is mostly determined by these cross-interferences. Thus, the applicability of the technique is limited to strong emitters with respective plume and weather conditions. The much higher selectivity of IFPICS largely extends the range of applicable conditions (e.g. to ship emissions and weaker emitting volcanoes) and significantly reduces the systematic errors. Furthermore, the extension of the technique to other trace gases, e.g. bromine monoxide (BrO), formaldehyde (HCHO), or nitrogen dioxide (NO_2), can give new important insights into short-scale chemical conversion processes in the atmosphere.

2 Imaging Fabry–Pérot interferometer correlation spectroscopy (IFPICS)

Similarly to the SO_2 camera principle (e.g. Mori and Burton, 2006; Bluth et al., 2007), IFPICS uses an apparent absorbance (AA) $\tilde{\tau} = \tau_A - \tau_B$, i.e. the difference between two measured optical densities τ_A and τ_B, to quantify the column density (CD) $S = \int_0^L c(l)\,\mathrm{d}l$, i.e. the integrated concentration c of the measured gas along a light path L for each pixel of the image. The AA is calculated from two (or more) spectral settings that yield a maximum correlation difference to the gas absorption spectrum. Ideally the periodicity of the FPI fringes is matched to periodic spectral absorption features as shown in Fig. 1 for SO_2. For IFPICS we use two spectral settings A and B. Setting A exhibits on-band absorption, where the FPI transmission maxima coincide with the SO_2 absorption maxima and hence correlate with the differential absorption structures of SO_2. Setting B uses an off-band position, where the FPI transmission maxima anti-correlate with the differential SO_2 absorption structures (see Fig. 1). The spectral separation between setting A and B is thereby reduced by a factor of ≈ 30 (in the case of SO_2) to only ≈ 0.5 nm in contrast to ≈ 10–15 nm for traditional SO_2 cameras (see Lübcke et al., 2013; Kern et al., 2015a), which minimises broadband interferences due to, for example, scattering and extinction by aerosols or other absorbing gases. This application of an FPI is similar to approaches reported by Wilson et al. (2007) and Vargas-Rodríguez and Rutt (2009), for the detection of carbon monoxide, carbon dioxide, and methane in the infrared spectral range.

By measuring the optical density $\tau_A = \ln(I_A/I_{0,A})$ and $\tau_B = \ln(I_B/I_{0,B})$ in both spectral settings A and B respectively, the relation between the AA $\tilde{\tau}(S)$ with the CD S is given by

$$\tilde{\tau}(S) = \tau_A - \tau_B = -\log\frac{I_A}{I_{0,A}} + \log\frac{I_B}{I_{0,B}} = k(S) = \Delta\tilde{\sigma}(S)\cdot S, \quad (1)$$

where I_A and I_B denote the radiances with the presence of the target trace gas in the absorption light path and $I_{0,A}$ and $I_{0,B}$ the radiance without. The absorber-free reference radiances $I_{0,A}$ and $I_{0,B}$ can be determined from, for example, a reference region within the image. The differential weighted effective trace gas absorption cross section $\Delta\tilde{\sigma}(S)$ becomes independent of S for small AAs ($\tilde{\tau} \ll 1$). At higher AAs, saturation effects occur due to the non-linearity of Lambert–Beer's law; however knowledge of the absorption cross sections, the background radiation spectrum, and the instrument transmission allows $\tilde{\tau}$ to be calculated for arbitrary CDs S using a numerical model.

2.1 Instrument model

The AA $\tilde{\tau}$ is modelled for given target trace gas CDs S by simulating the incoming radiances I_A and I_B and $I_{0,A}$

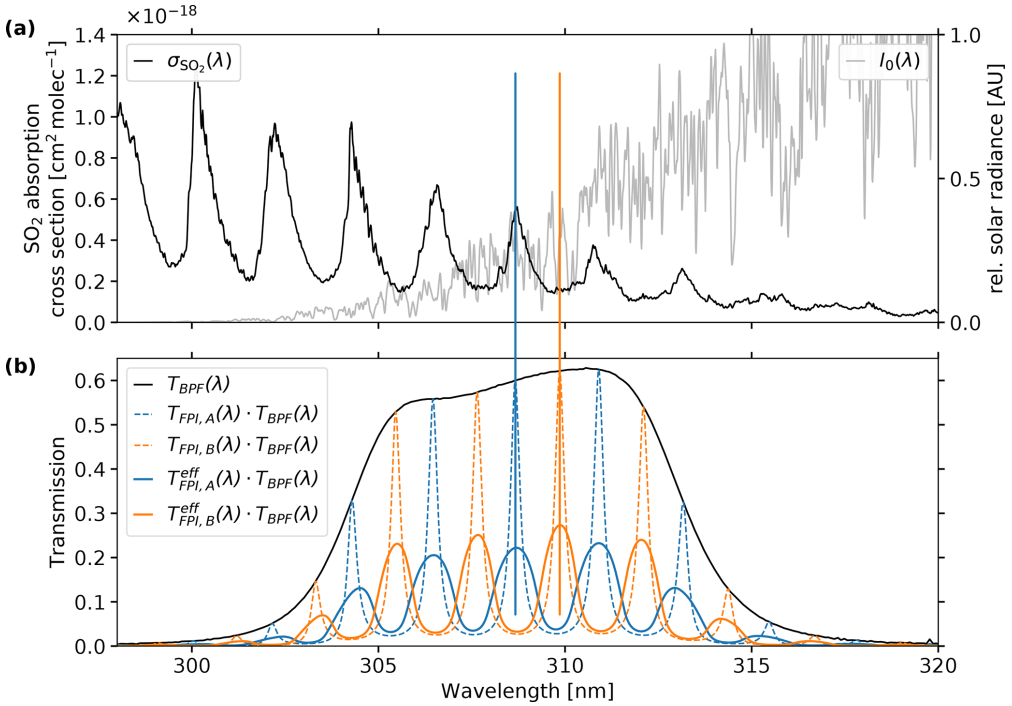

Figure 1. Spectral variation of **(a)** the SO_2 absorption cross section σ_{SO_2} (black drawn, left axis, according to Bogumil et al., 2003) and the scattered skylight radiance $I_0(\lambda)$ (grey drawn, right axis in relative units), given by Eq. (2). **(b)** The FPI transmissions in settings A and B yielding the maximum AA detectable (best correlation/anti-correlation to σ_{SO_2}) in the spectral range specified by the band pass filter used (BPF). The BPF transmission $T_{BPF}(\lambda)$ (black) and the FPI transmission spectrum for a single-beam approach are shown according to Eq. (6) in on-band $T_{FPI,A}(\lambda)$ (dashed blue, correlation with σ_{SO_2}) and off-band $T_{FPI,B}(\lambda)$ setting (dashed orange, anti-correlation with σ_{SO_2}). The effective FPI transmission spectrum including an incident angle distribution is shown according to Eq. (7) in on-band $T^{eff}_{FPI,A}(\lambda)$ (drawn blue) and off-band $T^{eff}_{FPI,B}(\lambda)$ setting (drawn orange).

and $I_{0,B}$. As incident radiation, a high-resolution, top of atmosphere (TOA) solar atlas spectrum $I_{0,TOA}(\lambda)$ is used according to Chance and Kurucz (2010). The TOA spectrum is scaled by the wavelength λ^{-4} approximating a Rayleigh scattering atmosphere. Since our measurement wavelength range, of 304–313 nm for SO_2, overlaps with absorption of ozone (O_3), the TOA spectrum is corrected for the stratospheric O_3 absorption by multiplying all intensities by Lambert–Beer's term $e^{-\sigma_{O_3}(\lambda)\cdot S_{O_3}}$, where S_{O_3} denotes the total atmospheric ozone slant column density, e.g. according to the TEMIS database (Veefkind et al., 2006), and σ_{O_3} the O_3 absorption cross section according to Serdyuchenko et al. (2014). This yields the scattered skylight radiance $I_0(\lambda)$ as follows:

$$I_0(\lambda) = I_{0,TOA}(\lambda) \cdot e^{-\sigma_{O_3}(\lambda)\cdot S_{O_3}} \cdot f(\lambda^{-4}), \tag{2}$$

indicated in Fig. 2. Based on $I_0(\lambda)$, the radiances measured by the instrument for the two respective spectral settings are calculated with the absorption of trace gases and the spectral instrument transfer function $T_{instr}(\lambda)$. The investigated target trace gas j (in this work SO_2) and potentially interfering trace gas species k (in this work O_3) are added according to Lambert–Beer's law. In the following we use the index i, denoting the FPI settings A and B, respectively. The quantity $I_{0,i}$ thereby denotes the reference radiance excluding the target trace gas j from the light path (see Fig. 2).

$$I_i = \int \mathrm{d}\lambda\, I_0(\lambda) \cdot \exp\left(-\sigma_j(\lambda)\, S_j - \sum_k \sigma_k(\lambda)\, S_k\right) \cdot T_{instr,i}(\lambda) \tag{3}$$

$$I_{0,i} = \int \mathrm{d}\lambda\, I_0(\lambda) \cdot \exp\left(-\sum_k \sigma_k(\lambda)\, S_k\right) \cdot T_{instr,i}(\lambda) \tag{4}$$

The spectral instrument transfer functions $T_{instr,i}(\lambda)$ for the two spectral settings,

$$T_{instr,i}(\lambda) = T^{eff}_{FPI,i}(\lambda) \cdot T_{BPF}(\lambda) \cdot Q(\lambda) \cdot \eta(\lambda), \tag{5}$$

consists of the measured band pass filter (BPF) transmission spectrum $T_{BPF}(\lambda)$, the spectral (i.e. wavelength-dependent) quantum efficiency $Q(\lambda)$ of the detector, and a spectral loss factor $\eta(\lambda)$ of the employed optical components (e.g. by reflections). Considering only a single, parallel beam of light

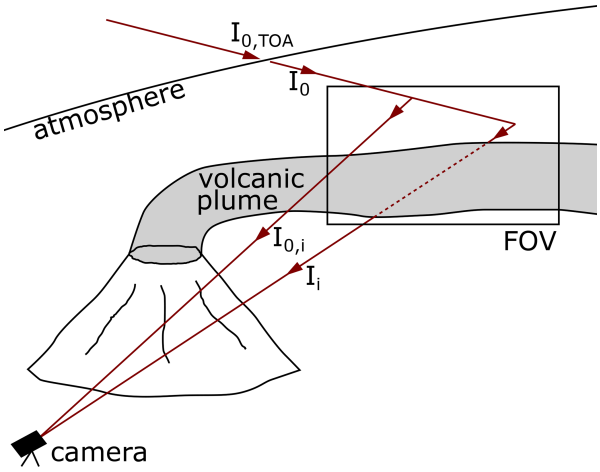

Figure 2. Schematic of the IFPICS measurement geometry, including the simulated radiances used in the instrument model. The incident top of atmosphere (TOA) radiation $I_{0,\mathrm{TOA}}$ is propagating through the atmosphere and is potentially scattered into the IFPICS camera field of view (FOV), yielding the scattered skylight radiance I_0. The camera records radiation in the respective FPI settings $i = A$ and B that either traverses the volcanic plume I_i or originates from a plume-free area within the FOV $I_{0,i}$.

traversing the instrument, the FPI transmission spectrum $T_{\mathrm{FPI},i}(\lambda)$ is defined by the Airy function (Perot and Fabry, 1899)

$$T_{\mathrm{FPI},i}(\lambda;\alpha_i,d,n,R) = \left[1+\frac{4\cdot R}{(1-R)^2}\cdot\sin^2\left(\frac{2\pi\cdot d\cdot n\cdot\cos\alpha_i}{\lambda}\right)\right]^{-1} \quad (6)$$

with the light beam incidence angle α_i for the two spectral settings onto the FPI, the FPI mirror separation d, the refractive index n of the medium inside the FPI, and the FPI reflectivity R (see Table 1, Figs. 1 and 3d). The FPI used in this work is static and air-spaced, meaning d, n, and R are fixed. Hence, the incidence angle α_i is the exclusive free parameter available to tune the FPIs transmission spectrum $T_{\mathrm{FPI},i}$ between settings $i = A$ and $i = B$ respectively. The change in α_i is achieved by tilting the FPI optical axis with respect to the imaging optical axis (see Sect. 2.2).

However, in reality a spectral setting will always impinge with a range of incidence angles onto the FPI. In this work we assume cone-shaped light beams, with half cone opening angles ω_c, where the entire cone can be tilted by α_i relative to the normal of the FPI mirrors (see Fig. 3d). From this assumption, it follows that the incidence angles α_i are distributed over a cone with the incidence angle distribution $\gamma(\alpha_i,\omega_\mathrm{c},\vartheta,\varphi)$, where ϑ and φ are the polar and azimuth angles, respectively. Hence, the single-beam FPI transmission spectrum $T_{\mathrm{FPI},i}(\lambda)$ of Eq. (6) is extended by a weighted average over $T_{\mathrm{FPI},i}(\lambda;\gamma(\alpha_i,\omega_\mathrm{c},\vartheta,\varphi),d,n,R)$, giving the effective FPI transmission spectrum $T^{\mathrm{eff}}_{\mathrm{FPI},i}(\lambda)$:

$$T^{\mathrm{eff}}_{\mathrm{FPI},i}(\lambda;\gamma(\alpha_i,\omega_\mathrm{c}),d,n,R) = \frac{1}{N(\gamma(\alpha_i,\omega_\mathrm{c}))} \times \int_0^{\varphi_{\max}}\int_{\vartheta_{\min}}^{\vartheta_{\max}} T_{\mathrm{FPI},i}(\lambda;\gamma(\alpha_i,\omega_\mathrm{c},\vartheta,\varphi),d,n,R)\sin\vartheta\,\mathrm{d}\vartheta\,\mathrm{d}\varphi. \quad (7)$$

Thereby, $N(\gamma(\alpha_i,\omega_\mathrm{c}))$ denotes the weighting function with $N(\gamma(\alpha_i,\omega_\mathrm{c})) = \int_0^{\varphi_{\max}}\int_{\vartheta_{\min}}^{\vartheta_{\max}}\sin\vartheta\,\mathrm{d}\vartheta\,\mathrm{d}\varphi$ given by the integral in Eq. (7), excluding the integrand $T_{\mathrm{FPI},i}$ itself, ϑ the polar angle, and φ the azimuth angle of the spherical integration within boundaries defined by the tilted cone-shaped light beams. For example, for a non-tilted FPI ($\alpha_i = 0$) the integration boundaries are $\vartheta \in [0,\omega_\mathrm{c}]$ and $\varphi \in [0,2\pi]$; for a tilted FPI, however, the transformation of $\gamma(\alpha_i,\omega_\mathrm{c},\vartheta,\varphi)$ is more complex and requires several case analyses.

The incidence angle distribution $\gamma(\alpha_i,\omega_\mathrm{c})$ will affect the shape of the FPI transmission spectrum by decreasing the effective finesse F of the FPI, leading to a blurring of the FPI fringes (see Fig. 1).

2.2 The IFPICS prototype

The IFPICS prototype is a newly developed instrument, designed to function under harsh environmental conditions in remote locations like, for example, in proximity to volcanoes. Hence, the prototype is designed to be small, with dimensions of 200 mm × 350 mm × 130 mm, lightweight at 4.8 kg (see Fig. 3a), and a power consumption < 10 W; thus it can be battery-operated for several hours. A 2D UV-sensitive CMOS sensor with 2048 × 2048 pixel resolution (SCM2020-UV provided by EHD imaging) is used to acquire images. The sensor is operated in 4 × 4 binning mode, yielding a final image resolution of 512 × 512 pixels. However, we found that the software of the SCM2020-UV image sensor does not allow sufficiently precise triggering. Therefore ≈ 0.6 s is lost in each image acquisition, which severely limits the operation of the IFPICS camera. Replacement of the sensor by a scientific-grade UV detector array will solve this problem in future studies.

The internal camera optics is highly modular and easily adjustable. The IFPICS prototype employs an image side telecentric optical setup as proposed in Kuhn et al. (2014, 2019). A photograph and a schematic drawing are shown in Fig. 3. An aperture and a lens (lens 1) parallelise incoming light from the imaging field of view (FOV) before it traverses the FPI and the BPF. A second lens (lens 2) focusses the light onto the 2D UV-sensitive sensor. Thereby, in good approximation, all the pixels of the image experience the same spectral instrument transfer function $T_{\mathrm{instr},i}(\lambda)$ for the two wavelength settings.

The FPI is the central optical element of the IFPICS prototype and is implemented as static air-spaced etalon with fixed

d, n, and R (provided by SLS Optics Ltd.). The mirrors are separated using ultra-low expansion glass spacers to maintain a constant mirror separation d and parallelism over the large clear aperture of 20 mm, even in variable environmental conditions. In order to tune the spectral transmission $T^{\text{eff}}_{\text{FPI}}$ between setting A and B, a variation of the incidence angle α is applied. The FPI can be tilted within the parallelised light path using a stepper motor. The stepper motor has a resolution of 0.9° per step, is equipped with a planetary gearbox (reduction rate 1/9), and is operated in micro-stepping mode (1/16), resulting in a resolution of 0.00625° per motor step. The time required for tilting between our settings A and B is ≈ 0.15 s. We favour the approach of tilting the FPI over changing internal physical properties like, for example, the mirror separation d by piezoelectric actuators, as it keeps simplicity, robustness, and accuracy high for measurements under non-laboratory conditions. However it needs to be considered that the tilting of the FPI will generate a linear shift between the respective images acquired in setting A and B, requiring an alignment in the evaluation process.

The half cone opening angle ω_c is determined by the entrance aperture a and the focal length f of lens 1 and can be calculated by $\omega_c = \arctan(a/2f)$. The physical properties of the optical components and the instrument are listed in Table 1 and were mostly chosen according to the dimensioning assumed in the calculations of Kuhn et al. (2019).

The FPI design with fixed d, n, and R (see Fig. 3c) in particular is chosen to inherently generate a transmission spectrum matching the differential absorption structures of SO_2. This includes the basic idea that the untilted FPI ($\alpha_i = 0°$) already matches the on-band position A. In our case, however, the manufacturing accuracy of d lies within one free spectral range (≈ 2 nm for SO_2) so that $\alpha_B = 0°$ corresponds to an off-band (B) position ($T^{\text{eff}}_{\text{FPI},B}$), and the on-band ($A$) position ($T^{\text{eff}}_{\text{FPI},A}$) is reached by a small tilt of $\alpha_A = 4.5°$. The basic advantages of using small incident angles α_i are that they keep the spread of the incidence angle distribution $\gamma(\alpha_i, \omega_c)$ (see Sect. 2.1) low and thereby retain the FPI's effective finesse F high (since the reflectivity R of the FPI mirror coating is somewhat dependent on the angle of incidence so is the finesse F). This leads to a much weaker blurring of the FPI fringes in the FPI transmission spectrum $T^{\text{eff}}_{\text{FPI},i}$ resulting in a higher sensitivity of the instrument (see Fig. 1). With the prototype setup, however, we encountered disturbing reflections for low FPI incidence angles. For that reason we used the subsequent correlating order of the FPI transmission with $\alpha_A = 8.17°$ for an on-band and $\alpha_B = 6.45°$ for an off-band setting (see Table 1), thereby making a compromise between sensitivity and accurate evaluable images.

3 Proof of concept study

3.1 Measurements at Mt. Etna, Italy

First measurements with the prototype described above were performed at the Osservatorio Vulcanologico Pizzi Deneri (lat. 37.766, long. 15.017; 2800 m a.s.l.) at Mt. Etna, on 21 and 22 July 2019. The physical properties of the IFPICS prototype and the FPI tilt angles α_i for tuning $T^{\text{eff}}_{\text{FPI},i}(\lambda)$ between on-band $i = A$ and off-band setting $i = B$ were selected according to Table 1. The tilt of the FPI generates a linear shift between the recorded on-band and off-band images on the detector and accounts for 6 pixels using tilt angles α_i. This shift needs to be corrected before cross-evaluating images recorded in setting A and B. The exposure time was set to 1 s for all measurements, and 4×4 binning (total spatial resolution of 512×512 pixels) was applied for all acquired images.

3.2 Validation of the instrument model

To quantify the accuracy of our model, two SO_2 gas cells were measured with the IFPICS prototype and by differential optical absorption spectroscopy (DOAS; see Platt and Stutz, 2008), on 21 July 2019, 11:10–11:20 CET. The sky was used as light source with a constant viewing angle (10° elevation, 270° N azimuth) in a plume-free part of the sky. To enhance the image quality, a flat-field correction is used, compensating pixel-to-pixel variations in sensitivity. The flat-field correction requires the acquisition of dark and flat-field images. The dark images are determined by the arithmetic mean over five images with no light entering the IFPICS instrument, and the flat-field images are obtained by the arithmetic mean over five images acquired in a plume-free sky region. The flat-field images thereby directly include the reference measurement $I_{0,i}$, making a later correction for the atmospheric background unnecessary. In the same viewing direction, I_i is measured for each gas cell and FPI setting i in order to calculate the AA according to Eq. (1). Figure 4 shows the gas cell measurements (red) including uncertainties (error bars, 1σ). The uncertainties directly arise from the errors of the DOAS measurement and due to variations in optomechanical settings of the IFPICS prototype.

The instrument model (Eqs. 2–7) was used to calculate the IFPICS AA $\tilde{\tau}_{SO_2}(S_{SO_2})$ from a given SO_2 CD S_{SO_2}. The model parameters are mostly fixed by the IFPICS prototype optics, as given in Table 1. The remaining parameter, the atmospheric O_3 slant column density S_{O_3} (see Eq. 2), is calculated in a geometric approximation $S_{O_3} = \text{VCD}_{O_3}/\cos(\text{SZA})$ using the solar zenith angle (SZA) and vertical O_3 column density (VCD_{O_3}), which both are location-, date-, and time-dependent. They were $\text{SZA} = (53 \pm 3)°$ (according to the solar geometry calculator by NOAA, 2020) and $\text{VCD}_{O_3} = (335 \pm 5)$ DU (according to the TEMIS database; Veefkind et al., 2006). The VCD_{O_3} can be treated to be approximately constant over the period of a day.

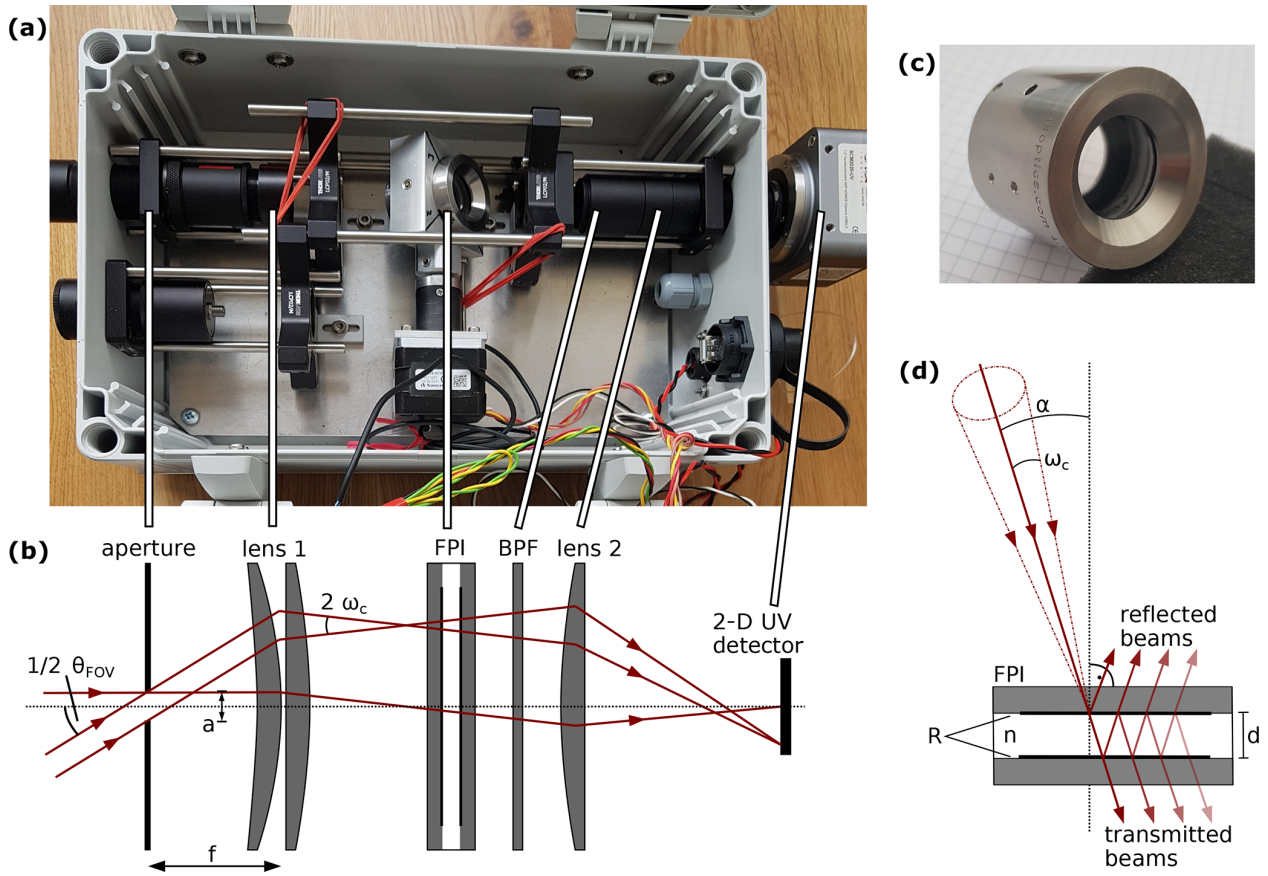

Figure 3. **(a)** Photograph of the IFPICS instrument. The physical dimensions are 200 mm × 350 mm × 130 mm ($w \times l \times h$) and 4.8 kg. **(b)** Sketch of the image side telecentric optical setup of the IFPICS prototype. Incident radiation is parallelised by an entrance aperture and lens 1 before traversing the FPI and the band pass filter (BPF). The maximum half cone opening angle ω_c is dependent on the aperture diameter a and the focal length f of lens 1. The camera field of view is $\theta_{FOV} = 18°$. A second lens maps the image onto a 2D UV-sensitive CMOS detector. **(c)** Photograph of the static air-spaced etalon (FPI) provided by SLS Optics Ltd. **(d)** Sketch of the FPI. An incoming single beam (drawn red) with incidence angle α is reflected multiple times between the FPI mirrors with reflectance R and separation d. Visualisation of an incoming cone-shaped beam (red dashed–dotted lines), with half cone opening angle ω_c and incidence angle α of the cone axis.

The output of the instrument model (drawn, black) for an SZA of 53° is shown in Fig. 4. The model uncertainty (shaded grey) is determined by a root mean square over the errors in the output by individually varying the input parameters within their stated uncertainties. The thus calculated calibration function using the instrument model matches the SO_2 gas cells' validation measurement within the range of confidence. The model nicely describes the flattening of the AA–CD relation for high CDs (up to $\approx 2.5 \times 10^{18}$ molec cm^{-2}), which originates from the CD dependence of $\Delta\tilde{\sigma}(S)$ (see Eq. 1).

To show the impacts of the SZA on the instrument model, the model output is also calculated for three other SZAs while keeping the other parameters constant. The model output is shown in Fig. 4 for an SZA of 80° (dashed–dotted black) for early morning and late afternoon conditions, an SZA of 70° (dashed black) for morning and afternoon conditions, and an SZA of 25° (dotted black) for noon conditions. High SZAs lead to an increase of stratospheric O_3 absorption, which alters the spectral shape of the scattered skylight radiance $I_0(\lambda)$ (see Eq. 2) which is used in the forward model. In other words, for high O_3 absorption, lower wavelength radiance, where the differential SO_2 absorption features are stronger, will contribute less to the integrated radiances I_i, $I_{0,i}$ (Eqs. 3, 4). The thereby induced SZA dependence of the sensitivity can easily be accounted for in the model. Note that this influence of strong O_3 absorption only occurs at our chosen wavelength range for the SO_2 measurement. When applying IFPICS to other trace gases, e.g. BrO or NO_2, at higher wavelength, this effect will be negligible.

Table 1. Parameters of the optical components installed in the IFPICS prototype and used in the calibration model. The uncertainties of the model input parameters are shown.

Parameter	Value	Uncertainties	Description
d (µm)	21.666	±0.002	FPI plate separation
R	0.65		FPI reflectivity
F	7.15		FPI finesse
n	1.0003		refractive index (air)
α_A (°)	8.17[a]	±0.02	FPI tilt, on-band
α_B (°)	6.45[a]	±0.02	FPI tilt, off-band
$T_{\mathrm{BPF,max}}$	0.63		BPF peak transmission
λ_{BPF} (nm)	308.5		BPF central wavelength
δ_{BPF} (nm)	9.0		BPF FWHM
f (mm)	47[b]	±2	lens 1 focal length
a (mm)	1.55	±0.05	aperture diameter
ω_c (°)	0.945		half cone opening angle
θ_{FOV} (°)	18		imaging FOV

[a] Used in units of radian in the instrument model (Eqs. 6 and 7).
[b] Two lenses: $f = \frac{f_1 \cdot f_2}{f_1 + f_2}$ with $f_1 = f_2 \approx 94$ mm and $\lambda = 310$ nm.

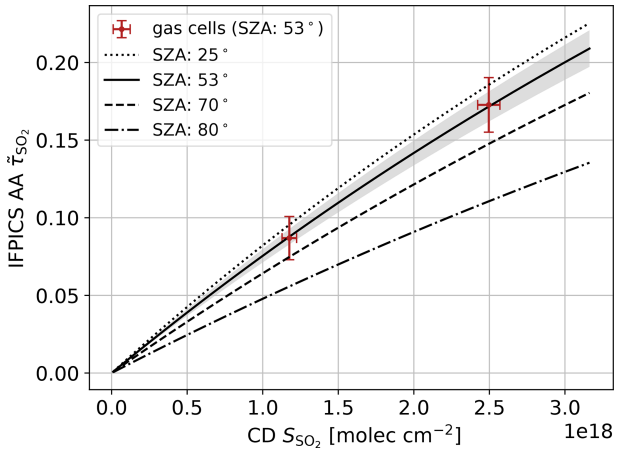

Figure 4. The validation measurement with two SO_2 gas cells (red, with 1σ error) with the IFPICS prototype and by DOAS on 21 July 2019, 11:10–11:20 CET, with a solar zenith angle (SZA) of 53°. The instrument forward model (Eqs. 2–7) is used to calculate the IFPICS AA $\tilde{\tau}_{SO_2}$ for a given CD S_{SO_2} range. The model input parameters are shown in Table 1, and (335±5) DU is used as VCD_{O_3}. The calculated model output (black) is shown for four different SZAs (25°, dotted; 53°, drawn; 70°, dashed and 80°, dashed–dotted). The model output and the validation measurement are in good agreement if a model SZA of 53° is used, which is equivalent to the SZA during the measurement time. The model uncertainty is shown by the grey shading.

3.3 Results of the field measurements

Volcanic plume measurements were performed on 22 July 2019 at 08:50–09:10 CET. The instrument was pointing towards the plume of Mt. Etna's South-East Crater with a constant viewing direction (azimuth 204° N, elevation 5°; see Fig. 5). The wind direction was ≈ 5° N, with a velocity of ≈ 6 m s^{-1} (wind data from UWYO, 2020). Hence, the plume was partly covered by the crater flank. The frame rate during the measurement was 0.2 Hz for a pair (I_A and I_B) of images.

The flat-field correction was performed as described in Sect. 3.2, using the arithmetic mean over 10 dark images and five flat-field images, obtained in a plume-free sky region. An exemplary set of volcanic plume SO_2 images, obtained with the IFPICS instrument in on-band setting I_A and off-band setting I_B, are shown in Fig. 6. Further images of I_A and I_B are shown in Appendix A. The circular shape of the retrieved image arises from the FPI's circular clear aperture limiting the imaging FOV.

The IFPICS SO_2 AA $\tilde{\tau}_{SO_2}$ is calculated pixel-wise according to Eq. (1) from I_A and I_B. For the conversion into SO_2 CD S_{SO_2}, the forward instrument model (Eqs. 2–7) is inverted by least-squares fitting of a fourth-order polynomial to the calculated CD relation $S_{SO_2}(\tilde{\tau}_{SO_2})$. The model input parameters of the instrument are shown in Table 1. The SZA during the time of the measurement is (78 ± 3)° (NOAA, 2020), with a VCD_{O_3} of 335±5 DU (according to the TEMIS database; Veefkind et al., 2006). The retrieved calibration function $S_{SO_2}(\tilde{\tau}_{SO_2})$ is

$$S_{SO_2}(\tilde{\tau}_{SO_2}) = \sum_0^4 x_i \cdot \tilde{\tau}^i_{SO_2}, \tag{8}$$

with $x_0 \stackrel{!}{=} 0$, $x_1 = 1.8 \times 10^{19}$, $x_2 = 1.7 \times 10^{19}$, $x_3 = 1.7 \times 10^{19}$, and $x_4 = 6.6 \times 10^{19}$ in units of molec cm^{-2} respectively, with x_0 fixed to zero. This approximation yields an average relative deviation of 0.007 % for S_{SO_2} from the mod-

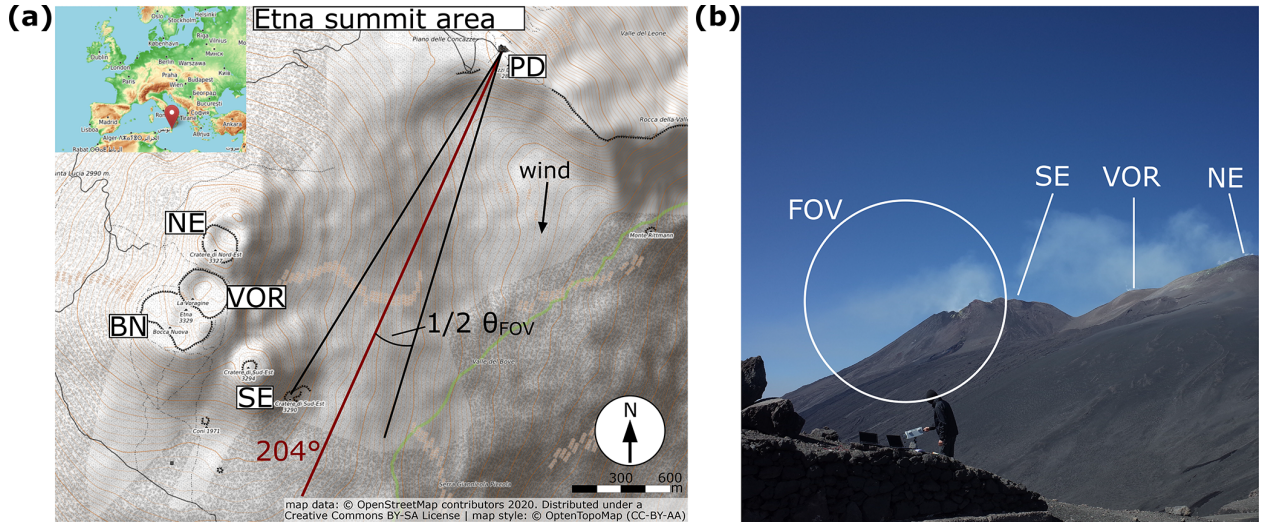

Figure 5. (a) Topographic map of the Mt. Etna summit area: North-East Crater (NE), Voragine (VOR), Bocca Nuova (BN), South-East Crater (SE), and measurement location at the Osservatorio Vulcanologico Pizzi Deneri (PD) are indicated. The viewing direction on 22 July 2019 is 204° (red drawn) with a FOV of $\theta_{FOV} = 18°$ (black drawn) and an elevation of 5°. The FOV is partly covering the plume emanating from SE crater. The average wind direction is $\approx 5°$ with a speed of $\approx 6\,m\,s^{-1}$ (wind data from UWYO, 2020). **(b)** Visual image of the volcanic plume on 22 July 2019 with camera field of view (FOV) indicated.

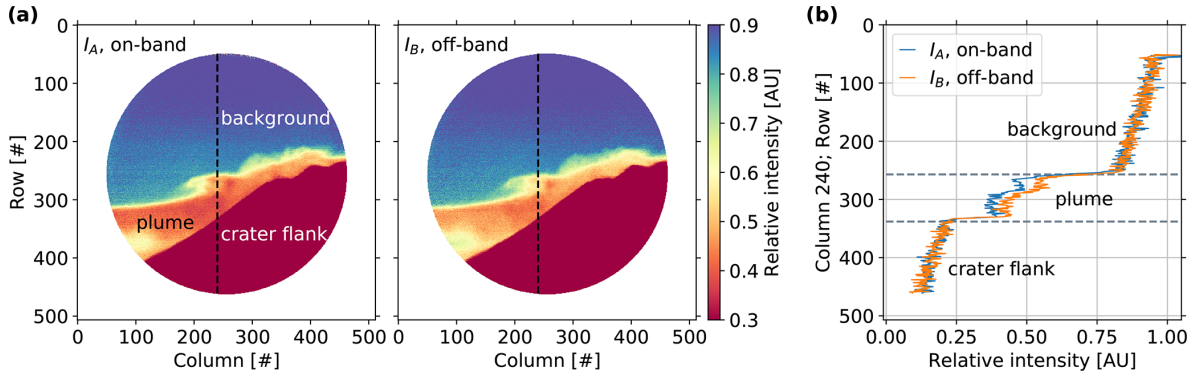

Figure 6. (a) Flat-field-corrected intensity images (400 × 400 pixels) acquired with the IFPICS prototype in on-band I_A and off-band setting I_B. The I_A image shows the expected higher SO_2 absorption in comparison with I_B ($I_A < I_B$ in plume region). The plume is visible in both images due to the broadband SO_2 absorption and other extinction in the measurement spectral range. The circular image shape arise from the FPI's circular clear aperture. **(b)** Intensity column 240 (dashed black lines in **a**) for I_A (blue) and I_B (orange). The enhanced absorption (reduced intensity) is clearly visible in the plume section with $I_A < I_B$, whereas in the background sky and crater flank sections, the intensities are equal: $I_A = I_B$.

elled value, with a maximum relative deviation of 0.08 % for small SO_2 CDs.

An evaluated image of the volcanic plume SO_2 CD distribution corresponding to the intensities shown in Fig. 6 is shown in Fig. 7. Further evaluated CD distribution images of the same time series are presented in Appendix A. A time series of the plume evolution is visualised in a flip-book in the Supplement.

The volcanic plume of Mt. Etna's South-East Crater is clearly visibly and reaches SO_2 CDs higher than $3 \times 10^{18}\,molec\,cm^{-2}$. The atmospheric background is $S_{SO_2,bg} = 4.3 \times 10^{16}\,molec\,cm^{-2}$ and was determined by the arithmetic mean over a plume-free area within the evaluated image (white square, 100 × 100 pixels, in Fig. 7a). Since the $S_{SO_2,bg}$ is determined from an evaluated CD distribution image, it accounts for the residual signal in S_{SO_2} between the direction of the volcanic plume and the direction of the flat-field images used in the evaluation. The $S_{SO_2,bg}$ was subtracted from the displayed image in the final step of the evaluation. The similar plume-free area (white square, 100 × 100 pixels, in

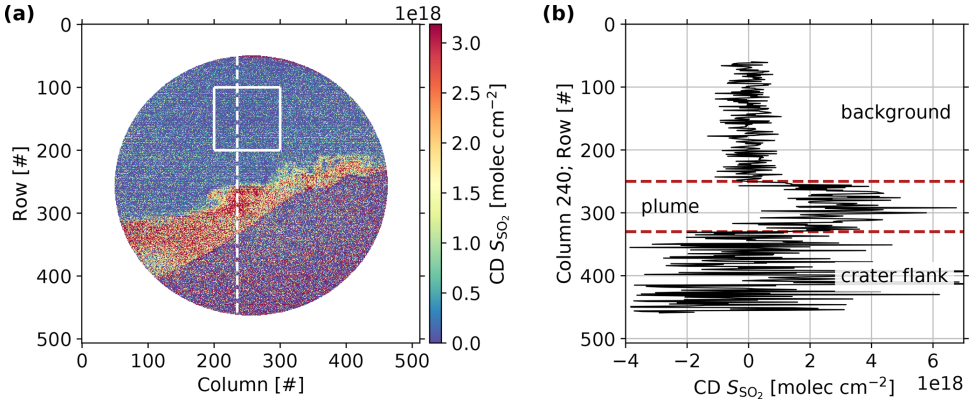

Figure 7. (a) Volcanic plume SO_2 CD distribution calculated from images acquired with the IFPICS prototype and using the instrument forward model conversion function $S_{SO_2}(\tilde{\tau}_{SO_2})$ (see Eq. 8). The plume-free area indicated by a white square (100×100 pixels) is used to correct for atmospheric background and to obtain an estimation for the detection limit. **(b)** Individual SO_2 CD column 240 (indicated by dashed white line in **a**) showing that the background, plume, and crater flank region are clearly distinguishable. High scattering in the crater flank region is induced by low radiance.

Fig. 7a) is further used to give an estimation for the SO_2 detection limit of the IFPICS prototype by calculating the 1σ pixel–pixel standard deviation. The obtained detection limit for an exposure time of 1 s is 5.5×10^{17} molec cm^{-2}, given by the noise-equivalent signal. The measurements were performed in the morning with an SZA of 78° and therefore reduced sensitivity and under relatively low light conditions. For decreasing SZA, the sensitivity will increase according to Fig. 4, and the increasing sky radiance will reduce the photon shot noise. In other words, the gas cell measurements (taken at SZA of 53°, with approximately twice the sky radiance compared to SZA of 78°) show a detection limit of 2.1×10^{17} molec cm^{-2} for an exposure time of 1 s. For ideal measurement conditions (lowest SZA, highest sky radiance), the detection limit will be further improved.

After the proof of concept, showing the capability of IFPICS to determine SO_2 CD images, it is possible to determine fluxes from a CD image time series. In particular, if the series allows us to trace back individual features in consecutively recorded images, it can be used to directly determine the plume velocity using the approach of cross-correlation (e.g. McGonigle et al., 2005; Mori and Burton, 2006; Dekemper et al., 2016) or optical flow algorithms (e.g. Kern et al., 2015b) and to determine the plume propagation direction (e.g. Klein et al., 2017). However, the viewing geometry on the day of our measurement was unfavourable as it was not possible to reach another measurement location due to a lack of infrastructure. The plume propagation direction and central line of sight show an inclination of 19° only, resulting in high pixel contortions, especially for pixels close to the edges of the FOV. Further, significant parts of the plume are covered by the crater flank due to its propagation direction. For the sake of completeness, we would like to give a rough estimate of the SO_2 flux obtained from our data.

The SO_2 flux Φ_{SO_2} is determined by integrating the SO_2 CD along a transect through the volcanic plume and subsequent multiplication by the wind velocity perpendicular to the FOV direction; however due to the viewing geometry issues, we will use external wind data (direction: 5°; velocity $v_{wind} \approx 6\,\mathrm{m\,s^{-1}}$ data from UWYO, 2020) for the calculation. As the camera pixel size is finite, the integral is replaced by a discrete summation over the pixel n:

$$\Phi_{SO_2} = v_\perp \sum_n S_{SO_2,n} \cdot h_n, \tag{9}$$

including the perpendicular wind velocity $v_\perp$, the SO_2 CD $S_{SO_2,n}$, and the pixel extent h_n. The perpendicular wind velocity can directly be calculated from geometric considerations (see Fig. 5a), accounting to $v_\perp \approx \sin(19°) \cdot v_{wind} \approx 2\,\mathrm{m\,s^{-1}}$. To determine the pixel extent, the distance between the volcanic plume and the location of measurement is required. In the centre of the FOV, this distance is $\approx 3500\,\mathrm{m}$, yielding $h_n \approx 2.7\,\mathrm{m}$. To keep the impact of pixel contortions low, the plume transect is located centrally in the FOV at column 250 and ranges from rows $n = 230$ to 330. Using these quantities, we retrieve a mean SO_2 mass flux for the measurement of $\Phi_{SO_2} = (84 \pm 11)\,\mathrm{t\,d^{-1}}$ for the investigated plume of the South-East Crater, which is comparable to previous flux measurements of the South-East Crater (Aiuppa et al., 2008; D'Aleo et al., 2016). Nevertheless, the flux should be regarded as a lower limit, since the plume was covered by the crater flank to an unknown extent.

4 Conclusions

By imaging and quantifying the SO_2 distribution in the volcanic plume of Mt. Etna, we successfully demonstrate the feasibility of the IFPICS technique proposed by Kuhn et al.

(2014). We were able to unequivocally resolve the dynamical evolution of SO_2 in a volcanic plume with a high spatial and temporal resolution (400×400 pixels, 1 s integration time, 4×4 binning). The retrieved detection limit for the SO_2 measurement is 5.5×10^{17} molec cm^{-2} s$^{-1/2}$. The detection limit however varies with the SZA and can reach values below 2×10^{17} molec cm^{-2} s$^{-1/2}$ under ideal conditions, comparable to traditional SO_2 imaging techniques (see Kern et al., 2015a). Also, the imaging technique lends itself to the determination of gas fluxes, and we obtained an SO_2 mass flux of $\Phi_{SO_2} = (84 \pm 11)$ t d^{-1} for Mt. Etna's South-East Crater plume. However, due to unfavourable conditions in the viewing geometry, the retrieved flux should be treated as a lower limit. In general, it is possible to apply optical flow algorithms on image series acquired under more ideal viewing geometry conditions (e.g. Kern et al., 2015b). These allow the plume velocity and angle to be determined between the observation direction and plume propagation direction in order to retrieve accurate SO_2 fluxes (e.g. Klein et al., 2017).

The specific spectral detection scheme of IFPICS allows a numerical instrument model to be used to directly convert the measured AA $\tilde{\tau}$ into CD S distributions. This inherent calibration method makes in-field calibrations methods, e.g. by gas cells, unnecessary. The accuracy of the instrument model could be demonstrated using SO_2 cells with a known CD, determined by simultaneous DOAS measurements.

Our IFPICS instrument is still an early stage prototype. The optics employed is highly modular, allowing easy adjustments even outside a laboratory. The physical dimensions of < 10 L and < 5 kg and the low power consumption of < 10 W, combined with the fact that no maintenance and in-field calibration are needed, make it already a close to ideal field instrument. Furthermore, the temporal resolution of the instrument can further be increased by replacing the sensor employed as it does not allow for time-optimised control of image acquisition.

Compared to traditional SO_2 cameras, the minimised cross-interferences to broadband plume extinction increase the selectivity and thus should allow to apply the IFPICS technique to much weaker SO_2 sources. Furthermore, the expected smaller interference to broadband effects in comparison to traditional SO_2 imaging techniques should allow the range of meteorological conditions acceptable for field measurement to be extended (see Kuhn et al., 2014).

The demonstrated IFPICS technique is not limited to the detection of SO_2. In general the technique is applicable to numerous further trace gases which show a distinct pattern (ideally periodic) in their absorption spectrum (see Kuhn et al., 2019). In the case of volcanic emissions, detectable trace species are, for example, bromine monoxide (BrO) or chlorine dioxide (OClO). Beyond volcanic applications IFPICS could be used to investigate, for example, air pollution by measuring nitrogen dioxide (NO_2) or formaldehyde (HCHO).

Appendix A:

Further evaluated images of the time series acquired on 22 July 2019 at 08:50–09:10 CET at Mt. Etna, Italy, are shown in Fig. A1. The evaluation procedure is analogous to the routine explained in Sect. 3.3. The time difference between a set (1–4) of images accounts for ≈ 120 s and allows us to trace back plume dynamics.

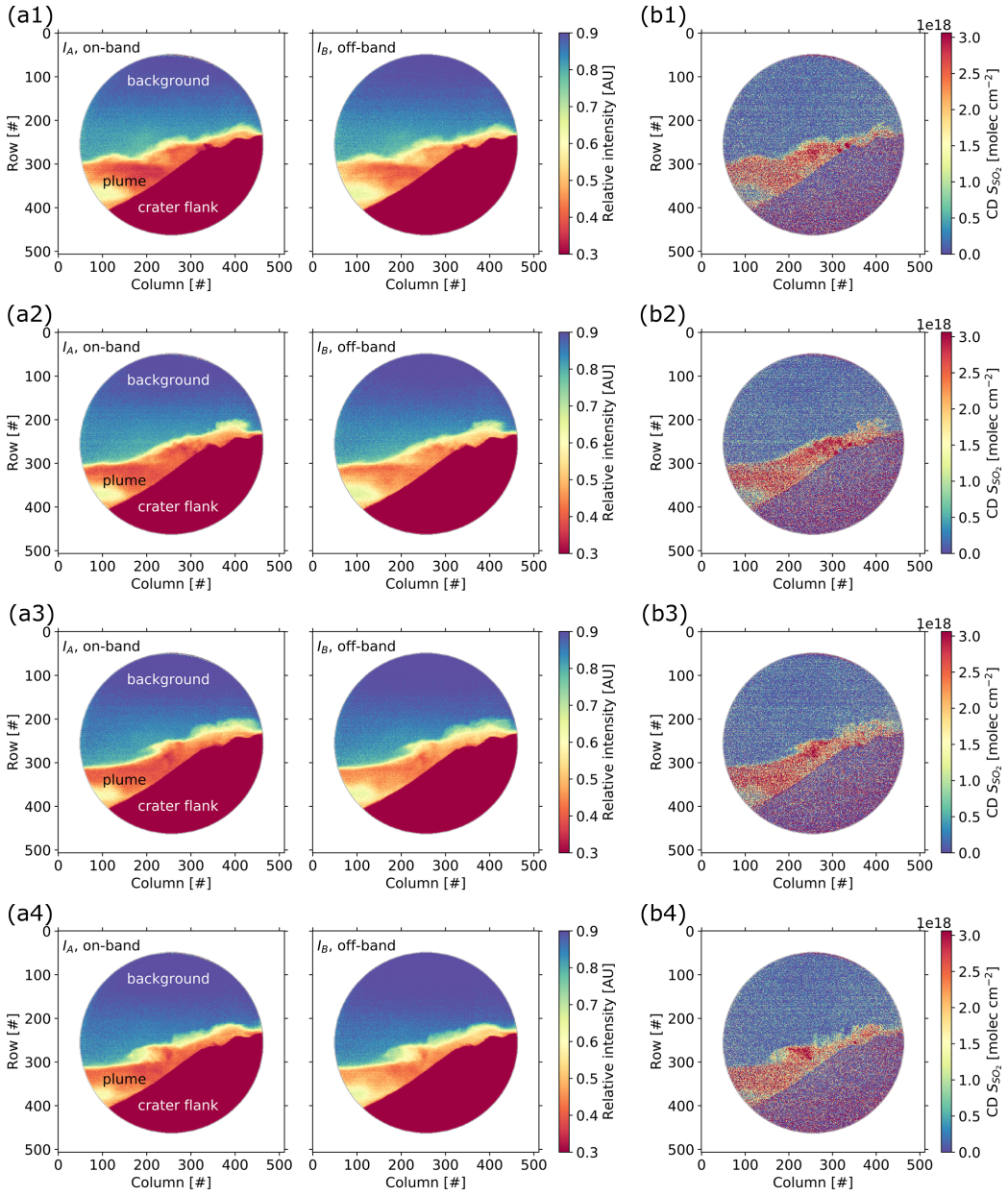

Figure A1. Exemplary set of evaluated images (400 × 400 pixels) acquired with the IFPICS prototype on 22 July 2019 at 08:50–09:10 CET at Mt. Etna, Italy. The time difference between each set of images (1–4) accounts for ≈ 120 s, allowing us to trace back plume dynamics. **(a)** Flat-field-corrected intensity images I_A and I_B. **(b)** Volcanic plume SO_2 CD S_{SO_2} distribution calculated with the conversion function shown in Eq. (8).

Data availability. The data can be obtained from the authors upon request.

Supplement. The supplement related to this article is available online at: https://doi.org/10.5194/amt-14-295-2021-supplement.

Author contributions. JK, NB, and UP developed the question of research. JK, NB, and CF conducted the field campaign. JK and CF developed the instrument model. CF designed, constructed, and characterised the instrument, evaluated the data, and wrote the manuscript, with all authors contributing by revising it within several iterations.

Competing interests. The authors declare that they have no conflict of interest.

Acknowledgements. We would like to thank SLS Optics Ltd. for sharing their expertise in designing and manufacturing the etalons. Support from the Deutsche Forschungsgemeinschaft (project DFG PL 193/23-1) is gratefully acknowledged. We also thank Emmanuel Dekemper and Toshiya Mori for their valuable and constructive reviews.

Financial support. The article processing charges for this open-access publication were covered by the Max Planck Society.

Review statement. This paper was edited by Andreas Hofzumahaus and reviewed by Emmanuel Dekemper and Toshiya MORI.

References

Aiuppa, A., Giudice, G., Gurrieri, S., Liuzzo, M., Burton, M., Caltabiano, T., McGonigle, A. J. S., Salerno, G., Shinohara, H., and Valenza, M.: Total volatile flux from Mount Etna, Geophys. Res. Lett., 35, L24302, https://doi.org/10.1029/2008gl035871, 2008.

Bluth, G., Shannon, J., Watson, I., Prata, A., and Realmuto, V.: Development of an ultra-violet digital camera for volcanic SO_2 imaging, Journal of Volcanol. Geoth. Res., 161, 47–56, 2007.

Bogumil, K., Orphal, J., Homann, T., Voigt, S., Spietz, P., Fleischmann, O., Vogel, A., Hartmann, M., Kromminga, H., Bovensmann, H., Frerick, J., and Burrows, J.: Measurements of molecular absorption spectra with the {SCIAMACHY} pre-flight model: instrument characterization and reference data for atmospheric remote-sensing in the 230–2380 nm region, J. Photoch. Photobio. A, 157, 167–184, https://doi.org/10.1016/S1010-6030(03)00062-5, 2003.

Chance, K. and Kurucz, R.: An improved high-resolution solar reference spectrum for earth's atmosphere measurements in the ultraviolet, visible, and near infrared, J. Quant. Spectrosc. Ra., 111, 1289–1295, https://doi.org/10.1016/j.jqsrt.2010.01.036, 2010.

D'Aleo, R., Bitetto, M., Donne, D. D., Tamburello, G., Battaglia, A., Coltelli, M., Patanè, D., Prestifilippo, M., Sciotto, M., and Aiuppa, A.: Spatially resolved SO_2 flux emissions from Mt Etna, Geophys. Res. Lett., 43, 7511–7519, https://doi.org/10.1002/2016gl069938, 2016.

Dekemper, E., Vanhamel, J., Van Opstal, B., and Fussen, D.: The AOTF-based NO_2 camera, Atmos. Meas. Tech., 9, 6025–6034, https://doi.org/10.5194/amt-9-6025-2016, 2016.

Kern, C., Lübcke, P., Bobrowski, N., Campion, R., Mori, T., Smekens, J.-F., Stebel, K., Tamburello, G., Burton, M., Platt, U., and Prata, F.: Intercomparison of SO_2 camera systems for imaging volcanic gas plumes, J. Volcanol. Geoth. Res., 300, 22–36, https://doi.org/10.1016/j.jvolgeores.2014.08.026, 2015a.

Kern, C., Sutton, J., Elias, T., Lee, L., Kamibayashi, K., Antolik, L., and Werner, C.: An automated SO_2 camera system for continuous, real-time monitoring of gas emissions from Kīlauea Volcano's summit Overlook Crater, J. Volcanol. Geoth. Res., 300, 81–94, https://doi.org/10.1016/j.jvolgeores.2014.12.004, 2015b.

Klein, A., Lübcke, P., Bobrowski, N., Kuhn, J., and Platt, U.: Plume propagation direction determination with SO_2 cameras, Atmos. Meas. Tech., 10, 979–987, https://doi.org/10.5194/amt-10-979-2017, 2017.

Kuhn, J., Bobrowski, N., Lübcke, P., Vogel, L., and Platt, U.: A Fabry–Perot interferometer-based camera for two-dimensional mapping of SO_2 distributions, Atmos. Meas. Tech., 7, 3705–3715, https://doi.org/10.5194/amt-7-3705-2014, 2014.

Kuhn, J., Platt, U., Bobrowski, N., and Wagner, T.: Towards imaging of atmospheric trace gases using Fabry–Pérot interferometer correlation spectroscopy in the UV and visible spectral range, Atmos. Meas. Tech., 12, 735–747, https://doi.org/10.5194/amt-12-735-2019, 2019.

Lübcke, P., Bobrowski, N., Illing, S., Kern, C., Alvarez Nieves, J. M., Vogel, L., Zielcke, J., Delgado Granados, H., and Platt, U.: On the absolute calibration of SO_2 cameras, Atmos. Meas. Tech., 6, 677–696, https://doi.org/10.5194/amt-6-677-2013, 2013.

McGonigle, A. J. S., Hilton, D. R., Fischer, T. P., and Oppenheimer, C.: Plume velocity determination for volcanic SO_2 flux measurements, Geophys. Res. Lett., 32, L11302, https://doi.org/10.1029/2005GL022470, 2005.

Mori, T. and Burton, M.: The SO_2 camera: A simple, fast and cheap method for ground-based imaging of SO_2 in volcanic plumes, Geophys. Res. Lett., 33, L24804, https://doi.org/10.1029/2006GL027916, 2006.

NOAA: NOAA, Global Monitoring Division, Solar Geometry Calculator, available at: https://www.esrl.noaa.gov/gmd/grad/antuv/SolarCalc.jsp, last access: April 2020.

Perot, A. and Fabry, C.: On the Application of Interference Phenomena to the Solution of Various Problems of Spectroscopy and Metrology, Astrophys. J., 9, 87, https://doi.org/10.1086/140557, 1899.

Platt, U. and Stutz, J.: Differential optical absorption spectroscopy, Springer Verlag, Berlin, Heidelberg, 2008.

Platt, U., Lübcke, P., Kuhn, J., Bobrowski, N., Prata, F., Burton, M., and Kern, C.: Quantitative imaging of volcanic plumes – Results, needs, and future trends, J. Volcanol. Geoth. Res., 300, 7–21, https://doi.org/10.1016/j.jvolgeores.2014.10.006, 2015.

Serdyuchenko, A., Gorshelev, V., Weber, M., Chehade, W., and Burrows, J. P.: High spectral resolution ozone absorption cross-

sections – Part 2: Temperature dependence, Atmos. Meas. Tech., 7, 625–636, https://doi.org/10.5194/amt-7-625-2014, 2014.

UWYO: University of Wyoming, Department of Atmopsheric Science, atmospheric soundings; Station data: Trapani (LICT), Italy 2019-07-22 12:00, available at: http://weather.uwyo.edu/upperair/sounding.html, last access: April 2020.

Vargas-Rodríguez, E. and Rutt, H.: Design of CO, CO_2 and CH_4 gas sensors based on correlation spectroscopy using a Fabry–Perot interferometer, Sensor. Actuat. B-Chem., 137, 410–419, https://doi.org/10.1016/j.snb.2009.01.013, 2009.

Veefkind, J., de Haan, J., Brinksma, E., Kroon, M., and Levelt, P.: Total ozone from the ozone monitoring instrument (OMI) using the DOAS technique, IEEE T. Geosci. Remote, 44, 1239–1244, https://doi.org/10.1109/tgrs.2006.871204, 2006.

Veefkind, J., Aben, I., McMullan, K., Förster, H., de Vries, J., Otter, G., Claas, J., Eskes, H., de Haan, J., Kleipool, Q., van Weele, M., Hasekamp, O., Hoogeveen, R., Landgraf, J., Snel, R., Tol, P., Ingmann, P., Voors, R., Kruizinga, B., Vink, R., Visser, H., and Levelt, P.: TROPOMI on the ESA Sentinel-5 Precursor: A GMES mission for global observations of the atmospheric composition for climate, air quality and ozone layer applications, Remote Sens. Environ., 120, 70–83, https://doi.org/10.1016/j.rse.2011.09.027, 2012.

Wilson, E. L., Georgieva, E. M., and Heaps, W. S.: Development of a Fabry–Perot interferometer for ultra-precise measurements of column CO_2, Meas. Sci. Technol., 18, 1495–1502, https://doi.org/10.1088/0957-0233/18/5/040, 2007.

Atmos. Meas. Tech., 14, 7873–7892, 2021
https://doi.org/10.5194/amt-14-7873-2021

Atmospheric Measurement Techniques
Open Access
EGU

Mobile and high-spectral-resolution Fabry–Pérot interferometer spectrographs for atmospheric remote sensing

Jonas Kuhn[1,2], **Nicole Bobrowski**[1,2], **Thomas Wagner**[2], **and Ulrich Platt**[1,2]

[1]Institute of Environmental Physics, University of Heidelberg, Heidelberg, Germany
[2]Max Planck Institute for Chemistry, Mainz, Germany

Correspondence: Jonas Kuhn (jkuhn@iup.uni-heidelberg.de)

Received: 6 May 2021 – Discussion started: 10 August 2021
Revised: 27 September 2021 – Accepted: 10 November 2021 – Published: 17 December 2021

Abstract. Grating spectrographs (GS) are presently widely in use for atmospheric trace gas remote sensing in the ultraviolet (UV) and visible spectral range (e.g. differential optical absorption spectroscopy, DOAS). For typical DOAS applications, GSs have a spectral resolution of about 0.5 nm, corresponding to a resolving power R (ratio of operating wavelength to spectral resolution) of approximately 1000. This is sufficient to quantify the vibro-electronic spectral structure of the absorption of many trace gases with good accuracy and further allows for mobile (i.e. compact and stable) instrumentation.

However, a much higher resolving power ($R \approx 10^5$, i.e. a spectral resolution of about the width of an individual rotational absorption line) would facilitate the measurement of further trace gases (e.g. OH radicals), significantly reduce cross interferences due to other absorption and scattering processes, and provide enhanced sensitivity. Despite these major advantages, only very few atmospheric studies with high-resolution GSs are reported, mostly because increasing the resolving power of a GS leads to largely reduced light throughput and mobility. However, for many environmental studies, light throughput and mobility of measurement equipment are central limiting factors, for instance when absorption spectroscopy is applied to quantify reactive trace gases in remote areas (e.g. volcanoes) or from airborne or spaceborne platforms.

For more than a century, Fabry–Pérot interferometers (FPIs) have been successfully used for high-resolution spectroscopy in many scientific fields where they are known for their superior light throughput. However, except for a few studies, FPIs have hardly received any attention in atmospheric trace gas remote sensing, despite their advantages. We propose different high-resolution FPI spectrograph implementations and compare their light throughput and mobility to GSs with the same resolving power. We find that nowadays mobile high-resolution FPI spectrographs can have a more than 2 orders of magnitude higher light throughput than their immobile high-resolution GS counterparts. Compared with moderate-resolution GSs (as routinely used for DOAS), an FPI spectrograph reaches a 250 times higher spectral resolution while the signal-to-noise ratio (SNR) is reduced by only a factor of 10. Using a first compact prototype of a high-resolution FPI spectrograph ($R \approx 148\,000$, < 8 L, < 5 kg), we demonstrate that these expectations are realistic.

Using mobile and high-resolution FPI spectrographs could have a large impact on atmospheric near-UV to near-infrared (NIR) remote sensing. Applications include the enhancement of the sensitivity and selectivity of absorption measurements of many atmospheric trace gases and their isotopologues, the direct quantification of OH radicals in the troposphere, high-resolution O_2 measurements for radiative transfer and aerosol studies, and solar-induced chlorophyll fluorescence quantification using Fraunhofer lines.

1 Introduction

The Fabry–Pérot interferometer (FPI) was introduced at the end of the 19th century and has since led to tremendous progress in many areas of spectroscopy (as summarized in studies such as Vaughan, 1989). For resolving powers ($R = \frac{\lambda}{\delta\lambda}$) higher than a few thousand, Jacquinot (1954, 1960) showed that the FPI exhibits a fundamental luminosity (or light throughput) advantage over gratings, which, in turn,

outperform prisms in all relevant wavelength ranges. Until the 1970s, most spectrometers were implemented as a scanning monochromator using a one-pixel detector (e.g. a photomultiplier tube). The luminosity advantages were, however, also found for the – in that time so-called – "photographic use" of a spectrometer (i.e. a spectrograph), where photographical plates were used as the focal plane detector.

Nowadays, grating spectrographs (GSs) with one- or two-dimensional detector arrays (e.g. charge-coupled device, CCD, or complementary metal oxide semiconductor, CMOS, detectors) are widely used for atmospheric remote sensing of trace gases in the near-ultraviolet (near-UV) to near-infrared (NIR) spectral region (see Platt and Stutz, 2008). Even when scattered sunlight is used as a light source, they offer sufficient signal-to-noise ratios (SNRs) for moderate resolving powers ($R \approx 1000$) as well as compact and stable (i.e. mobile) instrumentation without moving parts.

Despite the substantial benefits of increased spectral resolution for numerous atmospheric remote sensing applications (see below), the advantages of FPIs are widely ignored, likely for the following major reasons: (1) many trace gases can be detected with moderate resolving power due to moderate-resolution (vibro-electronic) absorption structures in the UV and visible spectral range; (2) in contrast to FPI spectrographs, GSs are commercially readily available and relatively affordable; (3) for broadband light sources (as is the case in many atmospheric measurements) FPIs require further optical components for order sorting; and (4) as concluded by Jacquinot (1960), FPIs "will probably always suffer from the fact that the dispersion is not linear".

In this work, we show that it is worthwhile considering the use of FPIs in spectrographs for remote sensing measurements in the atmosphere. Detection limits of many trace gases can be lowered by orders of magnitude while also maintaining instrument mobility.

First, we discuss the benefits of high-resolution atmospheric trace gas remote sensing and introduce some past applications and their limitations (Sect. 1.2). Basic aspects of mobility are then briefly introduced (Sect. 1.3). In Sect. 2, we sketch high-resolution FPI spectrograph designs that can be implemented in mobile and stable instruments. In Sect. 3, the luminosity and physical size of the proposed FPI spectrograph implementations are compared to a GS with the same resolving power. By scaling the GSs performance, the SNRs of known moderate-resolution atmospheric measurements are used to anticipate the SNRs for the proposed FPI spectrographs. Extensive details of those calculations as well as lists of symbols and abbreviations are presented in the Appendices. In Sect. 4, we discuss the results regarding the potential impact of FPI spectrograph technology on atmospheric sciences and, finally, introduce a first prototype of an FPI spectrograph.

1.1 Definitions and conventions

Throughout the paper, we use spectroscopic terminology that might have slightly varying meanings in different fields of spectroscopy. To avoid confusion, the terms are briefly explained here.

A spectrograph is a spectrometer where the components of the spectrum are separated in space and recorded simultaneously with a detector array. The instrument line function (ILF) H describes the response of a spectrograph to an input of spectrally infinitesimal width (i.e. monochromatic radiation). The ILF determines the spectral interval that can be resolved by the spectrograph. In the following, this interval is called a spectral channel of the spectrograph (not to be confused with the spectral range covered by a pixel of the spectrograph's detector). Its full width at half maximum (FWHM, denoted by $\delta\lambda$) can be used (amongst other and rather similar definitions) to quantify the spectral resolution. What we call high spectral resolution corresponds to a narrow width of a spectral channel (i.e. a low value of $\delta\lambda$). The spectral range covered by all spectral channels of the spectrograph describes its spectral coverage. The resolving power R of the spectrograph is the ratio of the operating wavelength λ to the spectral resolution $\delta\lambda$. Investigating the light throughput of spectrographs on a spectral channel basis allows the direct comparison of their noise-limited detection limits for trace gas absorption (see Sect. 3).

In spectroscopic atmospheric trace gas remote sensing, the column density S of the gas is directly quantified. The column density denotes the concentration of the trace gas integrated along the respective measurement light path. According to different experiment designs and applications, the light path differs and ultimately determines the detection limit in terms of concentration (see e.g. Platt and Stutz, 2008, for details).

1.2 Atmospheric trace gas remote sensing with high spectral resolution

The width of rovibronic absorption lines of atmospheric trace gas molecules in the near-UV to NIR spectral range as well as that of many Fraunhofer lines are of the order of some picometres. In order to observe the corresponding spectral structures (in particular individual rotational lines), resolving powers in the range of $R \approx 10^5$ are required. This defines what we refer to in the following as "high spectral resolution".

In the UV and visible spectral range many trace gas molecules show "bands" of absorption lines composed of many, partially overlapping rotational lines of a vibrational transition, resulting in structured absorption cross sections, even when observed with moderate spectral resolution ($R \approx 1000$). These trace gas molecules can be quantified along light paths inside Earth's atmosphere by differential optical absorption spectroscopy (DOAS; see Platt and Stutz,

2008). Compact moderate-spectral-resolution GSs are used to record spectra of direct or scattered sunlight or artificial light sources from ground-based to space-borne platforms and, thus, allow for spatially and temporally resolved measurements of (also very reactive) trace gases.

However, a higher spectral resolution is desirable in many cases. There are atmospheric trace gases that are more difficult or even impossible to measure with moderate resolution. For instance, hydroxyl radicals (OH) exhibit distinct and narrow absorption lines (widths of 1–2 pm at 308 nm; see Fig. 1). Due to the low atmospheric concentrations of this species, its absorption can not be separated from overlaying effects (e.g. other absorbing gases) with spectral resolutions that are much lower than the width of the individual lines. Tropospheric OH concentrations have been measured with high-resolution absorption spectroscopy by studies such as Perner et al. (1976), Platt et al. (1988), and Dorn et al. (1996) using large GS set-ups (850–1500 mm focal length) and an intricate broadband laser system as a light source (as described in Hübler et al., 1984). Direct sunlight measurements of OH have been performed with Fourier transform spectrometers (FTSs; e.g. Notholt et al., 1997), a high-resolution GS (1500 mm focal length; Iwagami et al., 1995), and rather delicate systems employing series of pressure-tuned FPIs (e.g. Burnett and Burnett, 1981). Furthermore, high-resolution O_2 measurements have been performed in the atmosphere (e.g. Pfeilsticker et al., 1998) using a GS (1500 mm focal length). The high spectral resolution allows one to quantify the absorption of individual lines of different strength and, therefore, to infer, for instance, the light path length distributions in clouds. The rather complex and immobile hardware of the named measurements limited their application to a few and locally restricted atmospheric studies.

Many other atmospheric trace gases show strong and structured absorption on the picometre scale. Besides sulfur dioxide (SO_2; e.g. Rufus et al., 2003), formaldehyde (HCHO; e.g. Ernest et al., 2012), water (Rothman et al., 2013), and chlorine monoxide (ClO; Barton et al., 1984), Neuroth et al. (1991) found strong, discrete, and narrow bromine monoxide (BrO) absorption lines in the UV region. Using these much more detailed and specific spectral features of the trace gases could not only substantially increase the selectivity but also, in many cases, increase the sensitivity of DOAS measurements. Additionally, the absorption cross sections of isotopologues of some trace gases could be distinguished, similarly to the moderate-spectral-resolution measurements of water vapour isotopologues (e.g. Frankenberg et al., 2009). Figure 1a illustrates the addressed difference in spectral resolution by showing the high-resolution absorption cross section of SO_2 (Rufus et al., 2003) as well as a convolution representing the absorption cross section as seen by a compact GS with a 0.4 nm spectral resolution.

Moderate-resolution scattered sunlight DOAS measurements largely undersample solar Fraunhofer lines (the width of which can also be in the picometre range). On the one hand, this introduces uncertainties in the effective spectral absorption of the trace gases (see e.g. Lampel et al., 2017); on the other hand, in most cases, it implies the need for a Fraunhofer reference spectrum. High-resolution spectra would allow a direct separation of Fraunhofer structures from narrow trace gas absorption structures; moreover, absolute atmospheric column densities of trace gases could be determined (rather than the column density relative to a reference spectrum).

1.3 Instrument mobility

A key point in the success of moderate-spectral-resolution DOAS measurements in the atmosphere is the use of compact and stable (i.e. mobile) spectrographs (volume of the order of 1 L, a focal length f of about 10 cm, and no moving parts). As mentioned above, they typically yield a resolving power of approximately 1000 and a light throughput that allows for the recording of scattered sunlight spectra in the UV and visible spectral range with a SNR of several thousand within less than a minute (e.g. Lauster et al., 2021). This is sufficient to retrieve many of the weakly absorbing atmospheric trace gases in the UV and visible spectral range (optical densities of ca. 0.01–0.0001) and to study their dynamics and chemistry.

The mobility of measurement equipment provides substantial advantages for practical field applications, including the following: (1) deployment on mobile platforms (e.g. cars, camels, drones, balloons, aircraft, and miniature satellites); (2) the significant reduction of costs for field campaigns due to reduced infrastructure and human resource requirements; (3) remote locations (e.g. deserts or volcanic craters) are made accessible (e.g. with backpack sized instruments); and (4) instruments can be employed in autonomous, remote, and low-maintenance measurement networks (see e.g. Galle et al., 2010; Arellano et al., 2021). In practice, these points are substantial factors making scientific environmental observations feasible.

As will be shown below, increasing the resolving power of a GS also requires a larger instrument size. Thus, the mobility advantages are largely lost. The use of FPIs in spectrograph set-ups can yield high resolving power while maintaining a high instrument mobility.

1.4 Fourier transform spectroscopy

This work focusses on spectrograph set-ups (GSs, FPI spectrographs) because of their high stability (no movable parts) and low sensitivity to fluctuations in light intensity. FTSs (i.e. Michelson interferometers) do not fulfil these requirements. A one-pixel detector records interferograms in a temporal sequence while mechanical changes in the optics (i.e. the interferometer path length) are conducted. This already imposes limitations on the mobility of the FTS as well as

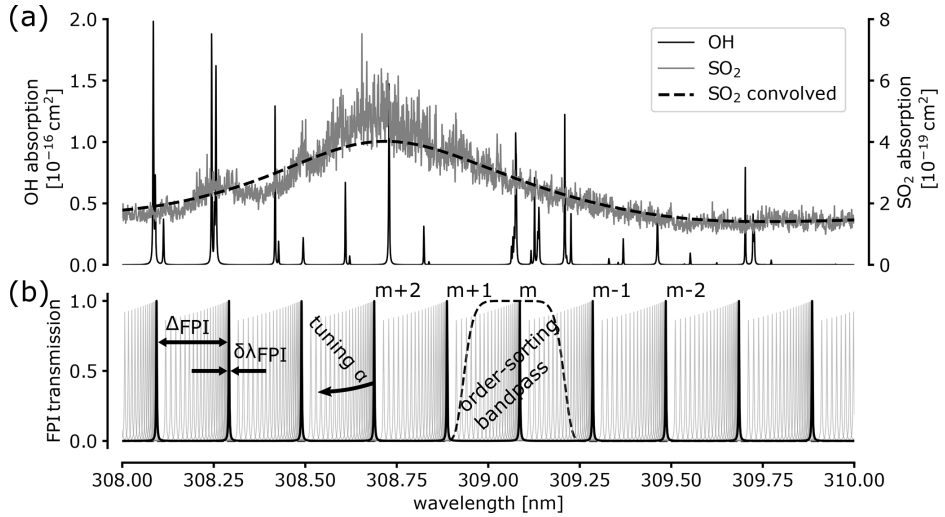

Figure 1. (a) OH absorption cross section (left ordinate axis; Rothman et al., 2013) and SO_2 absorption cross section (right ordinate axis; Rufus et al., 2003). The dashed line shows a convolution of the SO_2 absorption with a Gaussian of 0.4 nm width. **(b)** An FPI transmission spectrum (black drawn line) as it is scanning across a short wavelength range (indicated by the grey lines) obtained by tuning an instrument parameter (here, the incidence angle α is tuned from 0 to 2° in 0.05° steps). The decrease in peak transmission is due to an assumed small beam divergence (0.005° half opening angle). An order-sorting bandpass is indicated by the dashed line isolating the FPI peak of order m.

its applicability under more dynamical measurement conditions (e.g. cloudy skies). As (in addition to GSs) FTSs are in broader use in atmospheric remote sensing (mostly towards longer wavelengths, where the well-established and cost effective technology of silicon detector arrays can not be used anymore, i.e. above ca. 1100 nm), they shall nevertheless be briefly mentioned here.

In contrast to GSs and FPI spectrographs FTSs reach a large spectral coverage with very high and adjustable spectral resolution. This can be an important advantage for many atmospheric studies.

Notholt et al. (1997) compared the SNR of high-resolution ($R \approx 300\,000$) FTS measurements to the SNR of GS measurements with a similar resolving power (Iwagami et al., 1995) for direct sunlight measurements at around 308 nm. It was found that the SNRs of the FTS and GS were similar for clear-sky conditions and worse for the FTS under hazy or slightly cloudy conditions. Thus, the advantages of FPI spectrographs regarding the SNR found below (see Sect. 3.2.3) are expected to similarly hold for an FPI spectrograph to FTS comparison. While the spectral coverage for the high resolution of FTSs is superior, mobility aspects (movable parts and large focal lengths in FTSs) clearly favour FPI spectrographs.

2 High-resolution spectroscopy with Fabry–Pérot interferometers

FPIs are very simple optical instruments that have been known for a long time. However, progress in manufacturing processes has led to largely improved instrument properties over the last few decades. An FPI consists of two plane-parallel reflective surfaces (mirrors; see Fig. 2a). As incident light is reflected back and fourth between these surfaces, the interference of transmitted and reflected partial beams leads to spectral transmission patterns determined by the optical path length between the two surfaces (see e.g. Perot and Fabry, 1899, and Vaughan, 1989, for details). This optical path length and the optical path difference Γ is determined by the physical separation of the reflective surfaces d, the refractive index n of the medium between the surfaces, and the angle of incidence α of the incoming light:

$$\Gamma = 2\,d\,n\,\cos\alpha. \tag{1}$$

Thus, the transmission maximum (constructive interference) with the order m is centred at the wavelength

$$\lambda_m = \frac{\Gamma}{m}. \tag{2}$$

The free spectral range (FSR) $\Delta\lambda_{\mathrm{FPI}}$ describes the spectral separation of two neighbouring transmission peaks (or fringes) and is related to a transmission peak's FWHM $\delta\lambda_{\mathrm{FPI}}$ via the finesse $\mathcal{F}$ (see Fig. 1b):

$$\Delta\lambda_{\mathrm{FPI}} = \mathcal{F}\,\delta\lambda_{\mathrm{FPI}} \approx \frac{\lambda^2}{\Gamma}. \tag{3}$$

Thus, the spectral resolution of an FPI transmission order (i.e. the spectral width of its ILF) is given by $\delta\lambda_{\mathrm{FPI}}$. The isolation of a single FPI peak is desired for broadband light sources, unless the correlation of the FPI transmission

spectrum with the trace gas spectrum can be exploited (as in e.g. Vargas-Rodríguez and Rutt, 2009, and Kuhn et al., 2014, 2019). An order-sorting bandpass (i.e. the isolation of a wavelength range containing a single FPI fringe; see Fig. 1b) can be achieved by a bandpass filter, further FPIs (or a combination of both; see e.g. Mack et al., 1963), or dispersive elements like a grating or a prism (e.g. Fabry and Buisson, 1908). The order-sorting bandpass needs to be in the range of the FSR of the FPI. Through Eq. (3), the spectral resolution $\delta\lambda_{\mathrm{FPI}}$ of an FPI spectrograph is thus limited by the FPI instrument's finesse and the order-sorting bandpass. The finesse of an FPI indicates the number of interfering partial beams and, thus, depends on the reflectivity, the alignment, and the quality of the FPI mirror surfaces across its clear aperture (CA; e.g. the diameter of usable circular aperture). Therefore, it is limited by the manufacturing process to a large extent. Nowadays, high finesse across larger CAs is reached by static, air-spaced FPI set-ups (i.e. FPIs with fixed d and low-thermal-expansion glass spacers). The spectral width of bandpass filters, which in principle also consist of a sequence of interference layers, is limited by manufacturing processes in a similar way. Thus, the measurement application and the available optical components determine the appropriate order-sorting technique.

In order to resolve different wavelengths, the FPI has to be operated within a range of varied physical parameters (d, n, or α), resulting in a spectral shift of the FPI transmission (as indicated in Fig. 1b). This can be implemented in different ways (see e.g. Vaughan, 1989). For high-finesse FPIs, pressure or temperature tuning (i.e. changing the refractive index n of the medium between the mirrors) or using the dependence on the incidence angle α is preferred. The variation in the mirror separation d across the FPI instrument's CA often limits the finesse by impacting the parallelism of the mirrors. An extremely precise tuning of d would be required. Pressure tuning requires one, for instance, to ramp the pressure inside the FPI. While this can only be done in a time sequence, the use of detector arrays allows one to observe different incidence angles α simultaneously in spectrograph implementations without moving parts. For the study of dynamic processes in the atmosphere, a static spectrograph set-up is highly preferred.

Generally, a static set-up (i.e. without moving parts) has a high mechanical stability and low maintenance requirements. This is demonstrated by moderate-resolution GS applications. Spectrographs using FPIs implemented with low-thermal-expansion glass (linear expansion coefficient $\gamma \approx 10^{-8}\,\mathrm{K}^{-1}$) spacers further yield superior thermal stability. From Eqs. (1) and (2), it follows that $\frac{\mathrm{d}\lambda}{\lambda} \approx \gamma\,\mathrm{d}T$. A rather extreme temperature change of 10 K then induces a shift of the transmission spectrum by $10^{-7}\,\lambda$. Even for a high resolving power of 10^5, the effect on the measurement would be negligible in most cases. The issue of potentially varying air density within the etalon impacting the refractive index is solved by hermetically sealing the etalon. Furthermore, the temperature impacts on FPIs, as well as the impact on the simple optics, can be accounted for in models of the instrument transmission. This is much more difficult for GSs, as temperature also significantly affects the rather non-linear imaging of the slit for these instruments. Thus, while GSs often require active temperature stabilisation (see e.g. Platt and Stutz, 2008), this might be redundant for most FPI spectrograph applications. This further substantially enhances their mobility through a simpler and smaller set-up with lower power consumption.

In the following, sample calculations are mostly made for short wavelengths ($\approx 300\,\mathrm{nm}$), where FPI manufacturing is most challenging. For increasing wavelengths, the inferred performance tends to improve because the absolute finesse-limiting requirements concerning the roughness, parallelism, or sphericity of the mirror surfaces (often given as fraction of wavelength, e.g. $\lambda/100$) are higher for lower wavelengths.

FPI spectrograph implementation for atmospheric remote sensing

A simple and compact FPI spectrograph can be implemented with a static FPI as well as optics that image the different FPI incidence angles of the traversing light beam to concentric rings of equal FPI transmission on the focal plane (see Fig. 2a). There, a detector array records the intensities of the different spectral channels simultaneously. The spectral shift of the FPI transmission due to a small change in the small incidence angle α (i.e. a few hundredths of a radian, $\alpha \approx \sin\alpha \approx \tan\alpha$, $\cos\alpha \approx 1$) is dependent on the wavelength λ_m of the transmission peak of the order m and α itself (see Eqs. 1 and 2):

$$\frac{\mathrm{d}\lambda_m}{\mathrm{d}\alpha} = \frac{2\,d\,n}{m}\frac{\mathrm{d}}{\mathrm{d}\alpha}\cos\alpha = \frac{-2\,d\,n}{m}\sin\alpha \approx -\lambda_m\,\alpha. \tag{4}$$

This demonstrates the non-linearity of the dispersion, which, however, leads to a constant light throughput for all spectral channels (as described in detail below). The wavelength range Λ_m covered by a particular transmission order (i.e. the FPI's spectral tuning range) is determined by the angle range covered by the parallelised light beam traversing the FPI:

$$\Lambda_m = -\lambda_m \int_{|\alpha_{\min}|}^{|\alpha_{\max}|} \mathrm{d}\alpha\,\alpha. \tag{5}$$

The maximum and minimum incidence angles, $\alpha_{\max}$ and $\alpha_{\min}$ respectively, are determined by the illuminated entrance aperture B and the focal length of the collimating lens of the FPI spectrograph's imaging optics (lens 1; see Fig. 2a). For the imaging axis centred at the optical axis ($\alpha_{\min} = 0$), the maximum incidence angle is

$$\alpha_{\max} \approx \frac{B}{2\,f_1}. \tag{6}$$

Assuming, for instance, an entrance aperture of $B = 3\,\mathrm{mm}$ and a focal length $f_1 = 50\,\mathrm{mm}$, the maximum FPI incidence angle would be $\alpha_{\max} = 0.03$ (or 1.72°) and the spectral coverage would be about 0.135 nm at 300 nm. The practical incidence angle range that can be imaged onto the focal plane is in the range of a few degrees; therefore, the wavelength coverage can typically reach some hundreds of picometres in the near-UV. A moderate-resolution FPI spectrograph (with $R \approx 1000$, i.e. a spectral resolution of some hundreds of picometres at 300 nm) of the proposed implementation would exhibit a spectral coverage of the order of its spectral resolution, which would render it rather useless. This problem could be solved by tilting the FPI with respect to the imaging optical axis. Moderate-resolution FPI spectrographs are, however, not addressed in this study. For a resolving power of about 10^5, the 0.135 nm wavelength range at 300 nm would be divided into about 45 spectral channels with a 3 pm spectral resolution. This is about the number of spectral channels used in a typical moderate-resolution DOAS fitting window.

The sampling of the different spectral channels can be adjusted via the detector pixel size and the focal length of lens 2. Due to the non-linear dispersion, the sampling needs to be adjusted to the outermost ring corresponding to the spectral channel with the lowest wavelength of an FPI order (when assuming equally sized pixels). For the above example ($B = 3\,\mathrm{mm}$, $f_1 = 50\,\mathrm{mm}$) and $f_2 = 50\,\mathrm{mm}$, the radial extension of the outermost spectral channel is about $\frac{\delta\lambda_{\mathrm{FPI}}}{\lambda\,\alpha} f_2 \approx 17\,\mu\mathrm{m}$ (see Eq. 4). Nowadays, detector pixels with a 1–5 µm pitch are common. This would facilitate sufficient sampling (> 3.4 pixels per spectral channel width) for all spectral channels. The spectral sampling can further be adjusted via the focal length of lens 2. As the intensities of all pixels with the same wavelength are co-added, this does not affect the light throughput.

The above-mentioned order-sorting mechanisms (OSMs) allow two basic FPI spectrograph implementations:

1. Using a grating as the OSM in an FPI spectrograph results in a superposition of the linear grating dispersion with the radially symmetrical FPI transmission on the detector (see Fig. 2c). This allows one to record several FPI transmission orders at once, thereby increasing the total spectral coverage of the FPI spectrograph. This OSM is referred to as a grating OSM in the following.

2. Using a combination of further FPIs and filters as the OSM leads to an optimised étendue for a wavelength coverage of a single transmission order but also to a reduced total wavelength coverage (only a single FPI order). This OSM is referred to as interferometric OSM in the following.

As already mentioned above, the choice of the OSM depends on the measurement application, particularly the radiance of the light source, the desired SNR, the required spectral coverage, and the manufacturability of optical components.

An optical fibre and, as the case requires, relay optics direct the light collected by a telescope to the entrance aperture B (see Fig. 2a). From there, it traverses the imaging optics, containing the FPI and the OSM (certainly, the OSM can also be in front or behind the FPI imaging optics, for instance, the focal plane of an order-sorting GS could be re-imaged).

Both OSM implementations allow for simple, stable, and mobile set-ups with no moving parts. Therefore, they can be applied similarly to moderate-resolution compact grating spectrographs in field measurement campaigns, autonomous measurement networks in remote areas, and in airborne or satellite applications.

3 Comparison of the FPI spectrograph and GS

In this section, we compare the FPI spectrograph with the GS. First, size scaling considerations illustrate intrinsic mobility differences between FPI and grating instruments. Second, the light throughput per individual spectral channel is calculated and compared for different spectrograph implementations. Finally, from known SNRs of atmospheric measurements with moderate-resolution GSs, the SNRs of the high-resolution spectrographs are approximated.

3.1 Fundamental differences and size considerations

When examining spectroscopic methods, a basic question is how a physical parameter changes as a function of the wavelength λ. For spectrographs, this physical parameter is most often a deflection angle $\theta(\lambda)$ of a light beam. The angular dispersion describes the dependence of the deflection angle $\theta_{\mathrm{g}}(\lambda)$ on the wavelength for the grating. For the FPI spectrograph, the incidence angle dependence of the FPI transmission spectrum is used to separate the different spectral channels (see Sect. 2). Therefore, we regard the incidence angle α as equivalent to the deflection angle $\theta_{\mathrm{fp}}(\lambda)$ for the FPI.

For a blazed grating with a given ruling distance r_{g} operated in the mth order and a Littrow-type spectrograph set-up (incidence angle and dispersion angle are as equal as possible), the relation of the wavelength and deflection angle θ_{g} (which equals the gratings blaze angle in this case) is given by (see e.g. Jacquinot, 1954)

$$m\,\lambda = 2\,r_{\mathrm{g}}\,\sin\theta_{\mathrm{g}}; \tag{7}$$

consequently,

$$\frac{\mathrm{d}\lambda}{\mathrm{d}\theta_{\mathrm{g}}} = \frac{2\,r_{\mathrm{g}}}{m}\cos\theta_{\mathrm{g}}. \tag{8}$$

A close to ideal choice of the ruling distance of the grating for a given wavelength is $r_{\mathrm{g}} \approx m\,\lambda$. For a typical value of $\theta_{\mathrm{g}} = 30°$, a small wavelength shift by the width $\delta\lambda$ of one ILF (or one spectral channel) changes θ_{g} by

$$\delta\theta_{\mathrm{g}} \approx 0.58\,\frac{\delta\lambda}{\lambda}. \tag{9}$$

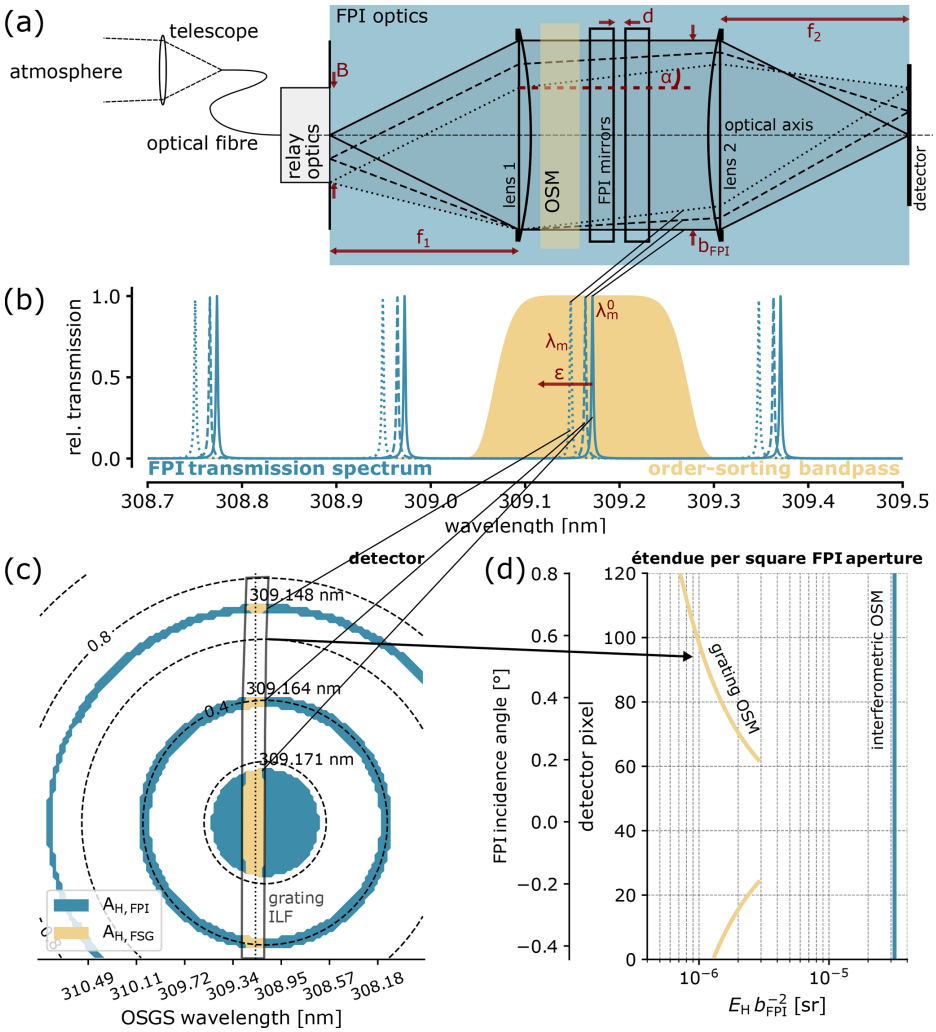

Figure 2. Schematic optical set-up of an FPI spectrograph: **(a)** light from the atmosphere is directed to the spectrograph entrance via a telescope, an optical fibre, and, if needed, relay optics. The order-sorting mechanism (OSM), depending on its implementation, can be at different locations within the optical path. Lens 2 images the different FPI incidence angles onto the image plane; thus, different spectral FPI transmission spectra **(b)** are separated on the focal plane detector **(c)**. The dashed circles in panel **(c)** indicate the corresponding FPI incidence angle α (in degrees). The OSM isolates a single FPI transmission order, either via filters (interferometric) or via a grating (see grating ILF in **c**). Panel **(d)** shows the étendue per square FPI aperture for the two OSMs and the instrument parameters in Table 1.

For the FPI, the angle dependence (for a small incidence angles) is given by Eq. (4):

$$\frac{\mathrm{d}\lambda}{\mathrm{d}\theta_{\mathrm{fp}}} = -\lambda\,\theta_{\mathrm{fp}}. \tag{10}$$

The same small wavelength shift by one spectral channel $\delta\lambda$ changes θ_{fp} by

$$\delta\theta_{\mathrm{fp}} \approx \frac{1}{\theta_{\mathrm{fp}}}\frac{\delta\lambda}{\lambda}. \tag{11}$$

This means that the angular change $\delta\theta_{\mathrm{g}}$ for a single spectral channel of the GS is approximately given by its inverse resolving power, whereas for low FPI incidence angles, the angular change $\delta\theta_{\mathrm{fp}}$ for a wavelength change of $\delta\lambda$ can easily be 2 orders of magnitude larger than its inverse resolving power (e.g. factor of 100 for $\theta_{\mathrm{fp}} \approx 0.6°$).

In either type of spectrograph, the angular deflection is translated to a spatial separation δx on a detector array via the imaging optics with focal length f (see Fig. 3b or f_2 in Fig. 2a):

$$\delta x \approx f\,\delta\theta. \tag{12}$$

The desired spatial interval per spectral channel on the detector depends on the pixel size and the spectral sampling.

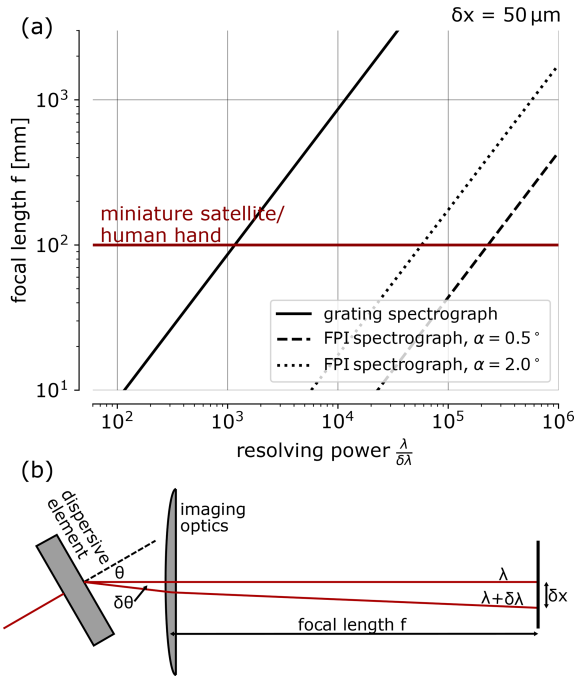

Figure 3. (a) Relationship between size (represented by the focal length) and resolving power of GS and FPI spectrographs for an ILF spatial dimension of $\delta x = 50\,\mu m$. The size of a human hand or a miniature satellite is about 10 cm (red line); this size determines the favourable resolving power of the respective GS or FPI spectrograph for many applications. **(b)** Schematic of a spectrograph illustrating the fundamental aspects that determine the values in panel **(a)**. The focal length f mainly determines the overall spectrograph size.

Assuming that the ILF is sampled by five pixels of 10 µm pitch, this interval would be $\delta x = 50\,\mu m$. Given that the size of a spectrograph is of the order of its focal length and its volume and mass scale with its third power (see e.g. Platt et al., 2021), the above relations reveal the principal difference between the GS and FPI spectrograph in terms of size and resolving power (see Fig. 3a). For instance, one could argue that easily portable tools for humans have the size of a human hand (i.e. ca. 10 cm), which is about the size of a CubeSat miniature satellite (see e.g. Poghosyan and Golkar, 2017). The resolving power of the corresponding GS is about 1000 and, thus, quite close to that used by moderate-resolution DOAS measurements. The resolving power of the corresponding ($f = 10\,cm$) FPI spectrograph is in the range of 10^5 and, therefore, capable of resolving individual rovibronic absorption lines of trace gases in the UV and visible spectral range.

These considerations point towards the advantages of FPIs for high-resolution spectroscopy, where they have been widely in use for more than a century (see Vaughan, 1989). Moreover, we have illustrated that the fundamental differences between grating and FPI result in different instrument sizes (or levels of mobility) for a given resolving power. However, these considerations do not yet include the spectrograph's light throughput and, hence, the maximum achievable SNR, which is also decisive for most atmospheric remote sensing applications.

3.2 Light throughput

In the following, we derive the general relationship between the sensitivity of a spectroscopic measurement and the light throughput of a spectroscopic instrument. The light throughput k_H of a spectrograph defines the conversion of incoming spectral radiance I (in units of $[\text{photons}\,s^{-1}\,mm^{-2}\,sr^{-1}\,nm^{-1}]$) to a flux $J_{ph,H}$ of photons with energies (or wavelengths) from within a single spectral channel of the spectrograph (see Eq. 16 below).

The upper limit for the SNR of an atmospheric remote sensing measurement is often determined by photoelectron shot noise, i.e. by the number $N_{ph} = J_{ph,H} \cdot \delta t$ of photons detected within an exposure time period δt (defining the measurement interval). The noise of such a spectrum is given by $\sqrt{N_{ph}}$; thus, the photon SNR Θ of a spectrum can be approximated by

$$\Theta \approx \frac{N_{ph}}{\sqrt{N_{ph}}} = \sqrt{I\,k_H(\delta\lambda)\,\delta t}. \tag{13}$$

This can be translated to the corresponding limits ΔS for the detection of trace gas column densities using the effective differential absorption cross sections $\overline{\sigma}(\delta\lambda)$, which, in many cases, are a function of spectral resolution (compare Fig. 1):

$$\Delta S \approx \frac{1}{\overline{\sigma}(\delta\lambda)\,\Theta} = \frac{1}{\overline{\sigma}(\delta\lambda)\,\sqrt{I\,k_H(\delta\lambda)\,\delta t}}. \tag{14}$$

Here, the crucial role of the light throughput of the instrument becomes obvious, especially when the radiance of the light source (e.g. scattered sunlight) and the exposure time (e.g. time constant of the process to be studied) are fixed. Moreover, the choice of $\delta\lambda$ is a compromise between optimal sensitivity (i.e. $\overline{\sigma}$, typically decreasing with increasing $\delta\lambda$) and optimal light throughput (typically increasing with increasing $\delta\lambda$; see below). Particularly for trace gases with absorption cross sections consisting of discrete lines (e.g. OH, water vapour, or O_2), the sensitivity increases almost linearly with the spectral resolution as long as it is much lower than the line width (see Appendix B).

When broadband light sources are used, a linear dependency of the light throughput on $\delta\lambda$ is introduced. For line emitters where the spectral width of the emitted line is smaller than $\delta\lambda$ (e.g. atomic emission lines), this is not the case (compare e.g. Jacquinot, 1954). Here, we regard light sources that are broadband compared to $\delta\lambda$ (scattered or direct sunlight or incoherent artificial light sources); therefore, we include the factor $\delta\lambda$ in the light throughput quantifica-

tion. Furthermore, the light throughput depends on the geometric beam acceptance of the optics (i.e. its étendue E_H), which often introduces a further $\delta\lambda$ dependency (see the following subsections). The spectrograph's étendue for a given spectral channel is approximated by the product of surface area A_H and the solid angle Ω_H of the corresponding light beam:

$$E_\mathrm{H} \approx A_\mathrm{H} \cdot \Omega_\mathrm{H}. \tag{15}$$

Losses at the optical components are accounted for by a factor μ. From these effects, the light throughput can then be calculated as follows:

$$k_\mathrm{H} = \frac{J_\mathrm{ph,H}}{I} = \mu\,\delta\lambda\,E_\mathrm{H}(\delta\lambda). \tag{16}$$

In the following, we compare the light throughput of FPI spectrographs with that of GSs for a given spectral resolution $\delta\lambda$. The losses at the optical components depend on their number, type, and quality. We assume that μ (accounting for these losses) is always optimised and that, apart from the OSM (introducing about a factor of 2 difference), there is no substantial difference in μ for the FPI spectrograph and GS. Thus, the light throughput is essentially determined by the étendue E_H of an individual spectral channel.

We derive the étendue E_H of GS and FPI spectrograph by approximating the surface area on the focal plane detector that is illuminated by light from a single spectral channel. The spectrograph's imaging optics determines the corresponding beam solid angle.

Imaging magnification does not affect the étendue (which is one of the reasons why the étendue is a universal measure of a spectrograph's quality), as it only converts a solid angle into surface area and vice versa. Therefore, for a light throughput comparison, we can ignore magnification and always assume ideal 1 : 1 imaging (i.e. collimating and focusing optics with the same focal length).

Investigating the light throughput per wavelength interval $\delta\lambda$ allows the comparison of spectrograph set-ups with respect to their photon shot noise-limited SNR.

3.2.1 Étendue of a grating spectrograph

For a simple GS, as typically used for DOAS measurements, the above definition of E_H might seem a bit artificial, as the étendue per spectral channel $\delta\lambda_\mathrm{GS}$ equals the étendue of the entrance optics. Assuming ideal 1 : 1 imaging, the surface area $A_\mathrm{H,GS}$ on the detector that is illuminated by light from within $\delta\lambda_\mathrm{GS}$ is determined by the illuminated slit area (i.e. by the illuminated slit height h_S and width w_S). The slit width determines the spectral resolution via the GS's linear dispersion $D_\mathrm{GS} := \frac{\mathrm{d}x}{\mathrm{d}\lambda}$ along the dispersion direction x. Because of the 1 : 1 imaging, $A_\mathrm{H,GS}$ at the detector is given by

$$A_\mathrm{H,GS} = w_\mathrm{S}\,h_\mathrm{S} = \delta\lambda_\mathrm{GS}\,D_\mathrm{GS}\,h_\mathrm{S}. \tag{17}$$

The corresponding imaging beam solid angle Ω_H can be calculated from the F number $F_\mathrm{GS} = \frac{f}{b}$ of the GS's imaging optics, according to the approximation for higher F numbers:

$$\Omega_\mathrm{H,GS} \approx \frac{\pi}{4\,F_\mathrm{GS}^2} = \frac{\pi\,b^2}{4\,f^2}, \tag{18}$$

with the imaging optics' (or the grating's) circular CA b and its focal length f. The étendue of a GS is then

$$\begin{aligned} E_\mathrm{H,GS} &\approx A_\mathrm{H,GS} \cdot \Omega_\mathrm{H,GS} \approx \frac{\pi}{4\,F_\mathrm{GS}^2} w_\mathrm{S}\,h_\mathrm{S} \\ &= \frac{\pi}{4\,F_\mathrm{GS}^2} \delta\lambda_\mathrm{GS}\,D_\mathrm{GS}\,h_\mathrm{S}. \end{aligned} \tag{19}$$

In the spectral ranges regarded in this study, due to the availability of appropriate gratings, the GS resolving power is basically determined by slit imaging. When the grating is optimised to the operating wavelength (i.e. $r_\mathrm{g} \approx m\,\lambda$, see above, or $\kappa\,r_\mathrm{g} = m\,\lambda$ with $\kappa \approx 1$), the GS resolving power is determined by the slit width and focal length (see Appendix C for details):

$$\frac{\lambda}{\delta\lambda_\mathrm{GS}} = \kappa\,\frac{f}{w_\mathrm{S}}. \tag{20}$$

Without exact knowledge of the factor κ (which is around unity and accounts for slight inaccuracies in the assumptions made) this relation allows one to evaluate how the size and the étendue of a particular GS change with its slit width and focal length for constant resolving power (see Fig. 4). As a measure of the spectrograph's size scaling, a minimum "beam volume" V_GS is determined by the light cone constrained by the F number and the focal length:

$$V_\mathrm{GS} = \frac{1}{12}\,\pi\,f\,b^2 = \frac{1}{12}\,\pi\,\frac{f^3}{F_\mathrm{GS}^2}. \tag{21}$$

While representing the lowest boundary for the absolute size of the spectrograph's optical set-up, it describes the scaling of a GS's volume and mass with the third power of its focal length for a constant F number (see also Platt et al., 2021).

The resolving power of such an idealised GS can now be increased by either increasing the focal length or by narrowing the entrance slit (see Fig. 4). Increasing the focal length leads to a larger and heavier instrument and is, therefore, limited by mobility requirements. Narrowing the entrance slit reduces the étendue of the GS. The theoretical lower bound is given by diffraction at the entrance slit, i.e.

$$w_\mathrm{S,min} \approx 1.22\,F_\mathrm{GS}\,\lambda. \tag{22}$$

In practice, imaging aberrations limit the resolving power for narrow slit widths. In particular, aberrations will limit the slit height of the GS, which substantially influences the GS étendue (see Eq. 4). Approximating the maximum possible slit

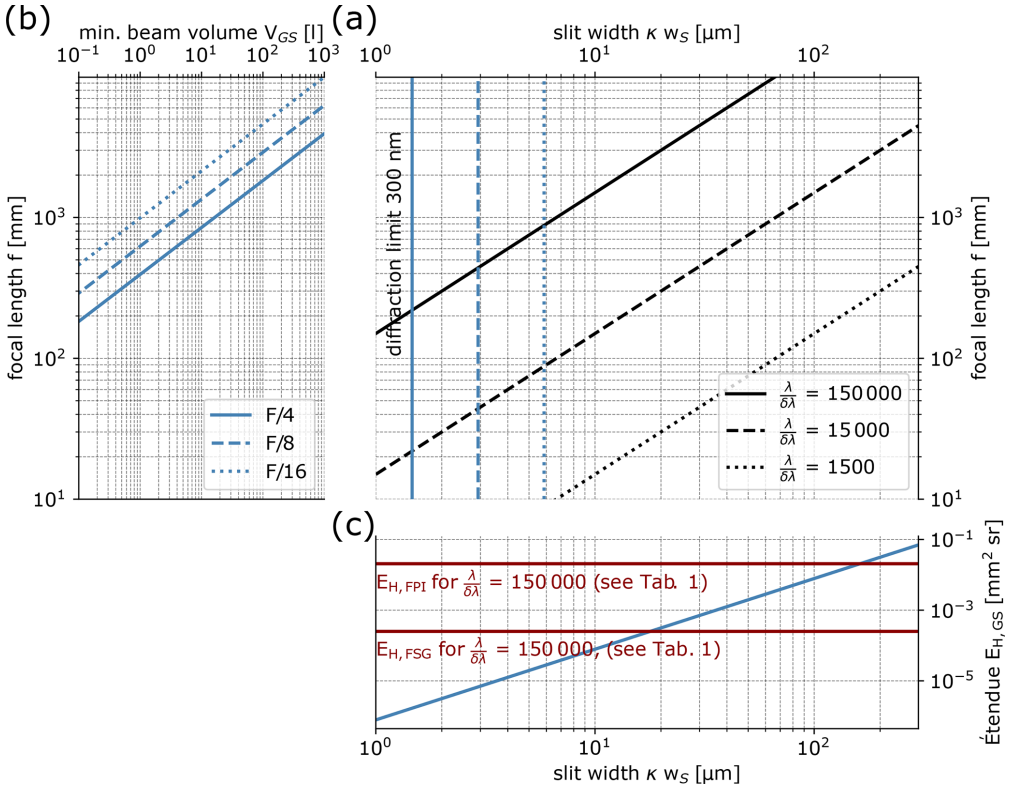

Figure 4. Combined visualisation of Eqs. (20)–(22) and (24). **(a)** For three exemplary resolving powers (1500, 15 000, and 150 000), the possible slit-width-to-focal-length ratios are shown. The focal length determines the spectrograph's size scaling **(b)**, whereas the slit width determines its étendue (blue line in **c**). The étendue of the FPI spectrograph with the grating OSM (for an incidence angle of 0.5°) and the total étendue of the FPI (i.e. the FPI spectrograph with an interferometric OSM) with the specifications given in Table 1 are shown in red.

height based on an empirical quantification of the astigmatism of GSs by Fastie (1952) leads to the following simple expression (see Appendix D):

$$h_S \approx w_S F_{GS}^2. \tag{23}$$

By inserting this relationship into Eq. (19), the expression for the GS étendue is further simplified to

$$E_{H,GS} \approx \frac{\pi}{4} w_S^2 \propto \delta\lambda_{GS}^2. \tag{24}$$

Surprisingly, the F number cancels, which is because small F numbers increase the accepted beam solid angle of the GS while also reducing the allowed slit height through imaging aberrations (at the same time and by the same amount). In principle, this introduces a dependence of the GS étendue on the square of $\delta\lambda_{GS}$, which further stresses the problems of high-resolution GS. This does not mean that the F number can be chosen arbitrarily. To avoid further distortions, the slit height must remain much smaller than the CA of the imaging optics.

Correcting aberrations (like the astigmatism) is possible but onerous. Large imaging spectrographs can reach large slit heights with a low F number, for instance, by using lens optics to avoid off-axis imaging and, thus, largely reducing aberration (see e.g. Crisp et al., 2017). This will not be considered in this study, as we focus on mobile spectrographs.

3.2.2 Étendue of the FPI spectrographs

In order to assess the étendue of the FPI spectrographs, it is useful to first regard the étendue of a single FPI order, ignoring the influence of the OSM for the moment. For instance, an idealised bandpass filter or a FSR much larger than the spectral band of the light source could be assumed. By assessing the transmission solid angles $\Omega_{H,FPI}$ of an FPI order (see Appendix E), we find the étendue of the FPI, which is (for a given resolving power) only dependent on the FPI CA b_{FPI}:

$$E_{H,FPI} \approx \frac{\pi^2}{2} b_{FPI}^2 \frac{\delta\lambda_{FPI}}{\lambda}. \tag{25}$$

Consequently, in the focal plane of a lens that is placed behind the FPI (lens 2 in Fig. 2a), the appearing rings corresponding to a wavelength interval $\delta\lambda_{FPI}$ (Fig. 2c, d) have the same surface area and the étendue of all spectral channels is

the same. For a given FPI CA and resolving power, $E_{\mathrm{H,FPI}}$ (as given by Eq. 25) states an upper limit for the étendue of an FPI spectrograph.

For an FPI spectrograph with an interferometric OSM, this étendue can be reached if the étendue of all of the respective OSM components is equal or larger than $E_{\mathrm{H,FPI}}$. This should not be a problem, as the interferometric OSM components are FPIs or interference filters with similar or lower resolving powers and, therefore, higher étendue for the same CA (see Appendix G for details).

For the grating OSM, things are a bit more complicated. We assume an order-sorting GS (OSGS) with a spectral resolution of about the FPI's FSR (i.e. $R_{\mathrm{FPI}} = R_{\mathrm{OSGS}} \cdot \mathcal{F}$). The spectrum of the OSGS can, for instance, be re-imaged by the FPI imaging optics (Fig. 2a). Therefore, the radially symmetric FPI spectral transmission overlaps with the OSGS spectrum, resulting in stripes (along the OSGS slit dimension) that isolate individual FPI transmission orders. Specifically, this will introduce an FPI incidence angle dependence to the étendue. The étendue of the FPI spectrograph with a grating OSM $E_{\mathrm{H,\,FSG}}$ can be approximated by the following expression (see Appendix F):

$$E_{\mathrm{H,FSG}} \approx \frac{\pi}{4\,F^2}\, w_{\mathrm{S}}\, \frac{f_2}{\alpha}\, \frac{\delta\lambda_{\mathrm{FPI}}}{\lambda} \approx \frac{w_{\mathrm{S}}}{2\,\pi\, f_2\, \alpha}\, E_{\mathrm{H,FPI}}. \tag{26}$$

As expected, the étendue equals the étendue of the OSGS with the slit height replaced by the radial extent of an FPI transmission ring with the spectral width of $\delta\lambda_{\mathrm{FPI}}$. Furthermore, it can be expressed as a fraction of the total étendue (Eq. 25) of the used FPI. The expression approximates only a part of the total spectrum recorded with such an FPI spectrograph (i.e. where grating dispersion and FPI dispersion are approximately perpendicular). It is, however, representative for large parts of the spectrum.

The OSGS resolution $\delta\lambda_{\mathrm{OSGS}}$ needs to approximately equal the FSR $\Delta\lambda_{\mathrm{FPI}}$ of the FPI. This means that the slit width w_{S} of the OSGS (and, thus, $E_{\mathrm{H,FSG}}$) can be increased if the FSR of the FPI is increased. In order to keep the spectral resolution $\delta\lambda_{\mathrm{FPI}}$ constant, the same increase is required for the finesse. For increasing slit width, FSR, and finesse, $E_{\mathrm{H,FSG}}$ converges to $E_{\mathrm{H,FPI}}$. As less FPI orders are then sampled, the total wavelength coverage decreases. This allows one, for instance, to adjust the spectral coverage and the étendue according to a specific application.

For Eq. (26) to hold, the F numbers of the OSGS and FPI imaging optics need to be matched. Thus, the focal length f_2 is determined by the FPI's CA and the OSGS's F number. Figure 2c and d illustrate the étendue differences of the interferometric and grating OSM.

3.2.3 Comparison of FPI spectrographs and GSs

With the above evaluation of the étendue, we can compare the light throughput and SNR of FPI spectrographs with a GS for a given resolving power. Furthermore, we can relate the results to moderate-resolution GSs with a known absolute SNR. This allows one to approximate the absolute SNR of high-resolution FPI spectrographs for atmospheric remote sensing applications. Table 1 summarises the results.

In order to reach spectral resolutions of the order of single rotational trace gas absorption lines, a resolving power of 150 000 is assumed, which corresponds to a 2 pm spectral resolution at 300 nm. A 100 mm focal length facilitates the mobility of the spectrograph (Sect. 3.1). As found in Sect. 3.2.1 (see Fig. 4), the high-resolution GS can not be implemented with a 100 mm focal length (due to diffraction at the entrance slit) and, therefore, uses optics with a focal length of 1 m. We also assume the same F number of $F = 4$ for all spectrographs. These assumptions mainly determine the étendue of the spectrographs.

For the FPI spectrograph with an interferometric OSM, we assume here that the element with the highest resolving power (i.e. the FPI with $R = 150\,000$) limits the étendue (see Eq. 25 and, for further details, Appendix G). The FPI spectrograph with a grating OSM requires the FSR of the FPI to be matched with the OSGS spectral resolution. We assume an FPI with a finesse of 100 and, therefore, need a OSGS with $R = 1500$. A finesse of 100 for the given FPI dimensions is challenging but possible to manufacture for the UV. For larger wavelengths, even higher finesses (i.e. higher spectrograph light throughputs) can be reached. The étendue of the FPI spectrograph with a grating OSM was calculated for a representative FPI incidence angle of $\alpha = 0.5°$. For the light throughput comparison, the OSMs are accounted for by a loss factor of 0.5.

In practice, a moderate-resolution DOAS GS with $f =$ 75 mm typically has a resolving power of 600 (i.e. a spectral resolution of 0.5 nm at 300 nm), and a 100 µm wide slit is used with, for instance, a 400 µm optical fibre, determining the illuminated slit height (see e.g. Platt and Stutz, 2008). Such set-ups are able to record spectra of scattered sky light with SNRs of several thousand in the UV spectral range within about a 1 min integration time (see e.g. Lauster et al., 2021). In addition, we determined the light throughput of an (with respect to our formalism) optimised GS with the same moderate resolving power and a 100 mm focal length. Its light throughput is about an order of magnitude higher than that of moderate-resolution GSs presently in use.

Compared with compact moderate-resolution GSs that are in use for DOAS measurements, the FPI spectrograph with an interferometric OSM exhibits light throughput that is a factor of 100 lower with a 250 times higher spectral resolution. Consequently, for a given integration time, the photon SNR of the high-resolution spectrum of the FPI spectrograph is only about 10 times lower than that of a compact moderate-resolution GS. For the spectrum of a grating OSM FPI spectrograph, the corresponding SNR is 100 times lower for the same gain in spectral resolution. However, a considerably larger wavelength range is covered compared with the interferometric OSM version.

Table 1. Comparison of an FPI spectrograph and a GS. All spectrographs have an F number of 4 and, to ensure mobility, a focal length of 100 mm, except for the high-resolution GS (see Sect. 3.2.1 for details). The light throughput and SNR are calculated relative to that of a moderate-resolution GS, commonly used for DOAS measurements and, thus, with a known SNR.

Quantity	Symbol	Unit	FPI spectrograph			Grating spectrograph		
			Interferometric OSM	Grating OSM		High resolution	Moderate resolution	
					OSGS		Optimised	Common DOAS
				$\alpha = 0.5°$				
Resolving power	R		150 000	150 000	1500	150 000	600	ca. 600
Spectral resolution at 300 nm	$\delta\lambda$	nm	0.002	0.002	0.2	0.002	0.5	ca. 0.5
Principal focal length	f	mm	100	100	100	1000	100	75
F number	F		4	4	4	4	4	4
Slit width	w_S	µm	–	–	67	6.7	167	100
Slit height	h_S	µm	–	–	268	26.8	668	400
Grating/FPI CA	b	mm	25	25	25	250	25	18.75
Étendue	E_H	mm^2 sr	2.06×10^{-2}	2.51×10^{-4}		3.54×10^{-5}	2.19×10^{-2}	1.96×10^{-3}
Relative loss	$\frac{\mu}{\mu_0}$		0.5	0.5		1	1	1
Relative light throughput	$\frac{k_H}{k_{H,0}}$		1.05×10^{-2}	1.28×10^{-4}		3.61×10^{-5}	11.15	1
Relative SNR	$\frac{\Theta}{\Theta_0}$		1.02×10^{-1}	1.13×10^{-2}		6.00×10^{-3}	3.34	1
Relative volume and mass	$\frac{V}{V_0}$		1–2	1–2		1000	1	1
Relative resolving power $\sqrt{\text{light throughput}}$ product per instrument volume	$\frac{R}{V}\frac{V_0}{}\sqrt{\frac{k_H}{k_{H,0}}}$		7685–15 370	849–1697		1	2003	600

The high-resolution GS, despite its volume that is already about 1000 times the volume of the other spectrographs, yields even only about half the SNR of the grating OSM FPI spectrograph.

Extending the FPI's CA to 250 mm would yield a 250-fold increase in spectral resolution with the same SNR as a compact moderate-resolution DOAS spectrograph. If such an FPI could be manufactured, the corresponding spectrograph would have a focal length of about 1 m. The corresponding high-resolution GS with the same SNR would need a focal length of about 15 m.

4 Implications for atmospheric remote sensing, and the FPI spectrograph prototype developed in this study

4.1 Implications for atmospheric remote sensing

FPI spectrographs offer a way to reach large resolving powers with a largely reduced impact on the SNR (compared with GSs) while maintaining a mobile instrument set-up. This might allow substantially lower detection limits for trace gas measurements in the near-UV to NIR spectral range or may increase the measurements' spatial or temporal resolution.

When regarding noise-limited trace gas detection limits (as introduced in Eq. 14), we find that the effective differential absorption cross section (and, thus, the sensitivity of the measurement) increases with spectral resolution for many gases in the near-UV to NIR regions. For absorbers with discrete lines (e.g. OH, water vapour, or O_2), the sensitivity increase will be almost linear to the increase in spectral resolution (see Appendix B, i.e. for our example a factor of ca. 250). For such gases, this effect outweighs the effect of reduced light throughput (0.01 compared with moderate-resolution GSs; Table 1), and the corresponding noise-limited detection limits of the FPI spectrograph with interferometric OSM will be reduced by a factor of $(250 \cdot \sqrt{0.01})^{-1} = 0.04$ (0.4 for a grating OSM) compared with that of common, moderate-spectral-resolution DOAS measurements. By reducing the temporal resolution of FPI spectrograph measurements by a factor of 100 (i.e. increasing the exposure time, e.g. from 30 s to 50 min), the same photon SNR as that of moderate-resolution DOAS measurements (with 30 s exposure time) can be reached, reducing the detection limits by another order of magnitude.

In addition, the increase in sensitivity comes with a massive increase in selectivity for the following reason: on the one hand, the high spectral resolution allows one to use much more specific absorption structures for gas detection; on the other hand, the high spectral resolution reduces or removes the influence of undersampled Fraunhofer lines for sunlight measurements. Thus, detection limits can further be significantly lowered with respect to moderate-resolution measurements, which are, in many cases, also limited by cross in-

terferences (see e.g. Vogel et al., 2013). Consequently, line broadening effects could also add valuable information to retrievals of vertical atmospheric trace gas distributions, and the feasibility of distinguishing trace gas isotopologues is strongly improved. Besides improving water vapour isotopologue quantification (see e.g. Frankenberg et al., 2009), the separation of $^{34}SO_2$ in volcanic emissions could also be possible using the differences in the absorption cross section, which are on a sub-nanometre scale (e.g. Danielache et al., 2008) and, thus, impossible to resolve with moderate spectral resolution.

Similar advantages are expected for the passive quantification of solar-induced fluorescence of chlorophyll by in-filling of narrow solar Fraunhofer lines with increased spectral resolution (see e.g. Plascyk and Gabriel, 1975; Grossmann et al., 2018).

The following simple example outlines the impact that FPI spectrographs might have on atmospheric sciences. According to the above assessment, a high-resolution FPI spectrograph records a spectrum with a SNR Θ of 3333 with about a 1 h integration time. For scattered sunlight measurements in the UV, the tropospheric light path L can reach about 10 km. The absorption cross section of OH $\overline{\sigma}_{\mathrm{OH}}$ at around 308 nm reaches about $1.5 \times 10^{-16}\,\mathrm{cm}^2$ per molecule (see Rothman et al., 2013). The detection limit of OH concentrations Δc_{OH} (see Eq. 14) would then be

$$\Delta c_{\mathrm{OH}} \approx \frac{\Delta S_{\mathrm{OH}}}{L} = \frac{1}{\Theta\,\overline{\sigma}_{\mathrm{OH}}\,L} = 2 \times 10^{6}\,\mathrm{molec.\,cm}^{-3}. \quad (27)$$

This is already in the range of tropospheric background OH concentrations (see e.g. Stone et al., 2012). This detection limit can be lowered further by using active light sources like light-emitting diodes (LEDs) or Xe lamps instead of scattered sunlight or by using larger FPIs or arrays of parallel FPI spectrographs.

Furthermore, as assessed in Sect. 1.4, FPI spectrographs are expected to have similar advantages over FTS and GS measurements in the NIR. Thus, FPI spectrographs could also substantially improve remote sensing measurements of greenhouse gases (e.g. CO_2 or CH_4) or CO in Earth's atmosphere. Instead of the large spectral coverage with high resolution reached by FTS, several FPI spectrographs could record spectra in different spectral windows that are relevant for the trace gas retrieval (e.g. an additional spectral window for O_2 light path information; see e.g. Crisp et al., 2017).

An important aspect with respect to the named and quantified benefits of FPI spectrographs is that the low level of complexity and the high mobility of presently used moderate-resolution GS measurements is maintained.

4.2 FPI spectrograph prototype

As a proof of concept, we built a prototype of an FPI spectrograph with a grating OSM at the Institute of Environmental Physics in Heidelberg (see Fig. 5a). It operates at around 308 nm. An FPI with high finesse (ca. 95) across a CA of 5 mm and a resolving power of ca. 148 000 (supplied by SLS Optics Ltd) was used with a compact OSGS. We recorded a spectrum of light from a UV LED that traversed a burner flame (see Fig. 5a) containing large amounts of OH (typically several thousand parts per million; see e.g. Cattolica et al., 1982). For a light path of about 1 cm, this leads to optical densities > 1 for many OH lines (see the OH absorption spectrum in Fig. 1, which is slightly altered due to the high temperature; see Rothman et al., 2013). Figure 5b shows the corresponding spectrum recorded by the FPI spectrograph prototype. The bright vertical stripes originate from a slight overlap of the individual FPI orders and, thus, also indicate their boundaries (compare Fig. 2b and c). The dark spots correspond to individual OH absorption lines. This is verified by calculating the intensity distribution using an instrument model and OH absorption data from Rothman et al. (2013). The orange box in Fig. 5b shows the region of the spectrum that is modelled in Fig. 5c. The locations of the individual OH absorption lines (dark spots) are clearly reproduced by the model, confirming the high resolving power.

Compared with the FPI spectrograph assumed in Sect. 3.2.3, the light throughput of this prototype instrument is reduced due to its smaller CA (i.e. by a factor of about 25; see Eq. 25). The mobility advantages of FPI spectrographs as derived in Sect. 3.1 are already demonstrated by this still rudimentary prototype. Its volume is below 8 L, and it weighs less than 5 kg. The FPI can be replaced by an FPI with a larger CA without significantly impacting the instrument size.

A comprehensive description of this and further prototype instruments as well as the instrument models would go beyond the scope of this work and will be the topic of future publications.

5 Conclusions

We compared the performance of high-resolution spectrographs using gratings or FPIs. Increasing the spectral resolution of a GS results in the loss of its mobility and light throughput advantages and, thus, its applicability to many atmospheric studies. In contrast, the implementation of mobile FPI spectrographs with high resolving power is possible (as shown by the presented prototype) and can yield a much larger light throughput than a GS with the same (high) resolving power. Compared with moderate-resolution GSs (as used in conventional DOAS measurements), FPI spectrographs with the currently available optical components and a 250-fold spectral resolution (e.g. 2 pm instead of 0.5 nm at 300 nm) yield a light throughput that is only a factor of 100 smaller for an instrument of the same size. In contrast, the corresponding high-resolution GS, which can only be implemented with about a 1000-fold volume, yields only ap-

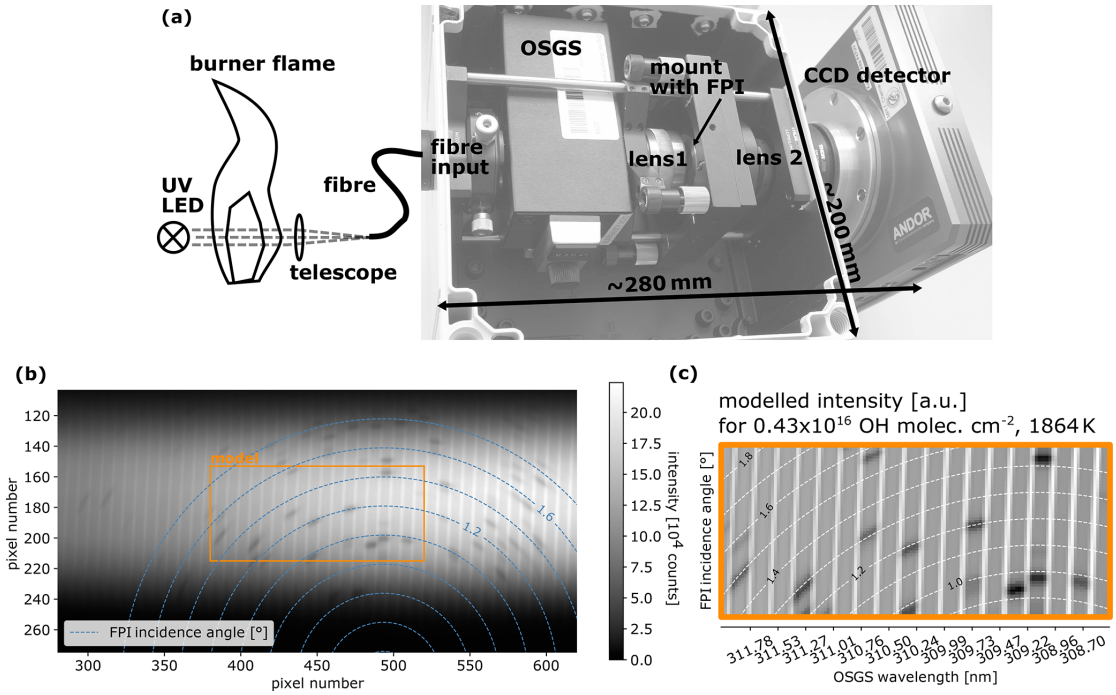

Figure 5. Prototype of an FPI spectrograph with a grating OSM recording an absorption spectrum of OH in a burner flame. Panel **(a)** outlines the instrument and experimental set-up: light from a UV LED traverses a burner flame (containing a high amount of hot OH) before being directed to the FPI spectrograph via a telescope and a fibre. The FPI imaging optics re-image the moderate-resolution spectrum of the OSGS (compare Fig. 2). Panel **(b)** shows the recorded spectrum image: the vertical bright stripes arise from slight overlapping of FPI orders, dark spots indicate the individual OH absorption lines, and the dashed blue lines indicate rings of equal FPI incidence angle α. **(c)** Modelled intensities (using high-temperature OH absorption data from Rothman et al., 2013) for a part of the measured spectrum (orange box) with an instrument model show excellent agreement.

proximately 4×10^{-5} of the moderate-resolution GS's light throughput.

Similarly to the resolving power luminosity product used by studies such as Jacquinot (1954) to generally compare FPIs to gratings, we can define a figure to quantify the applicability of spectroscopic instruments to atmospheric remote sensing studies with enhanced mobility requirements (e.g. measurements in remote areas or satellite instruments). This would then be the product of the resolving power and the square root of the light throughput (proportional to the inverse trace gas detection limits) per instrument volume. For a resolving power of 150 000, this figure is at least 3–4 orders of magnitude larger for FPI spectrographs compared with the GS.

On the one hand, the employment of mobile high-resolution FPI spectrographs would substantially increase the SNR of high-resolution measurements in the atmosphere; on the other hand, it would substantially increase the mobility of measurement instrumentation. These above-mentioned advantages basically come at the cost of spectral coverage of the spectrograph; however, for many applications, this should not be a problem.

The impact on atmospheric remote sensing measurements may be outlined with the following examples:

1. More trace gases (such as tropospheric OH) could be detectable using relatively simple passive or active absorption measurements.

2. In many cases, the detection limits of trace gases (e.g. SO_2, H_2O, HCHO, ClO, and BrO) routinely quantified by moderate-spectral-resolution DOAS measurements could be significantly lowered via the enhancement of sensitivity and selectivity due to the high spectral resolution.

3. Alternatively, the temporal or spatial resolution of such measurements could be enhanced.

4. From passive measurements using sunlight, absolute (rather than differential) column density measurements of trace gases absorbing in the UV and visible wavelength range could become possible (e.g. evaluation between Fraunhofer lines).

5. Due to the increase in the spectral resolution, the capability to separate trace gas isotopologue absorption is enhanced.

6. Line broadening could be quantified to add valuable information to the retrievals of vertical trace gas distributions.

7. Radiative transfer in haze or clouds can be studied with high-resolution measurements of O_2 rotational lines.

8. Increased spectral resolution also enhances the sensitivity of chlorophyll fluorescence quantification through in-filling of Fraunhofer lines and similar studies.

9. FPI spectrographs are expected to similarly improve trace gas measurements in the NIR, as presently performed with FTS (e.g. quantification of green house gases in the atmosphere).

All in all, the results of this study suggest that high-resolution spectroscopy with mobile FPI spectrographs has the potential to substantially advance atmospheric trace gas remote sensing, thereby opening the door to many new insights into processes in Earth's atmosphere.

Appendix A

A1 List of abbreviations

CA	Clear aperture
DOAS	Differential optical absorption spectroscopy
FPI	Fabry–Pérot interferometer
FSG	FPI spectrograph with a grating order-sorting mechanism
FSR	Free spectral range
FTS	Fourier transform spectroscopy
FWHM	Full width at half maximum
GS	Grating spectrograph
ILF	Instrument line function
NIR	Near-infrared
OSGS	Order-sorting grating spectrograph
OSM	Order-sorting mechanism
SNR	Signal-to-noise ratio
UV	Ultraviolet

A2 List of symbols

λ	Wavelength
$\delta\lambda$	Spectral resolution, spectral ILF FWHM
R	Resolving power
Γ	Optical path difference of the FPI
d	FPI mirror separation
n	Refractive index of the FPI medium
α	Incidence angle of light onto the FPI
m	Order of the FPI fringe or grating dispersion
λ_m	Wavelength at the FPI fringe with order m
$\Delta\lambda_{\mathrm{FPI}}$	FSR of the FPI
$\mathcal{F}$	Finesse of the FPI
γ	Linear thermal expansion coefficient
H	ILF
Λ	Wavelength coverage
B	Diameter of the circular entrance aperture
f	Focal length
θ	General dispersion deflection angle
$\delta\theta$	Small, linearised change in θ
r_{g}	Ruling distance of a grating
δx	Spatial separation in the focal plane through $\delta\theta$
k_{H}	Light throughput per spectral channel
I	Radiance
$J_{\mathrm{ph,H}}$	Photon flux per spectral channel
N_{ph}	Number of photons
Θ	SNR
δt	Measurement interval, exposure time
ΔS	Detection limit for a trace gas (column density)
$\overline{\sigma}$	Effective absorption cross section of a trace gas
E_{H}	Étendue per spectral channel
Ω_{H}	Beam solid angle per spectral channel
A_{H}	Surface area of beam cross section per spectral channel
μ	Factor accounting for losses at optical components
w_{S}	Slit width
h_{S}	Slit height
D_{GS}	Linear dispersion of a GS
F	F number
b	CA
κ	Uncertainty factor around unity
V	Minimum beam volume of a spectrograph

Appendix B: Relation between sensitivity and spectral resolution

Here, we wish to demonstrate that the sensitivity of an absorption measurement with a spectrograph is, in most cases, strongly dependent on the spectral resolution. The sensitivity can be approximately quantified by the peak effective absorption cross section $\overline{\sigma}$ of a gas measured by an instrument with an ILF H:

$$\overline{\sigma} = \frac{\tau}{S} = S^{-1} \log \frac{I_0 \otimes H}{I_0 \exp(-\sigma\, S) \otimes H}, \tag{B1}$$

where σ denotes the high-resolution absorption cross section, τ is the optical density, S is the column density of the gas, and the operator $\otimes$ represents the spectral convolution. The absorption of an isolated and sharp absorption line (see e.g. OH absorption cross section in Fig. 1) is diluted within the ILF of a spectrograph as long as its spectral resolution is lower than the width of the absorption line. In this case, increasing the spectral resolution results in a close to linear increase in sensitivity. This is illustrated by a simple example in Fig. B1, where we assume a 3 pm wide, Voigt-shaped absorption line and ILFs of different width modelled by sixth-order Gaussian curves.

Appendix C: The GS resolving power is mainly limited by slit imaging

The resolving power of the grating is limited by the number of illuminated grating rules N_g (i.e. $\frac{\lambda}{\delta\lambda} = N_\mathrm{g}$). This requires $\frac{f}{F_\mathrm{GS}\, r_\mathrm{g}}$ to be larger than the intended resolving power, which is almost always fulfilled by commonly used GS implementations. For an ideal choice of the grating, its effective ruling distance $r_\mathrm{eff} = r_\mathrm{g} \cos\theta_\mathrm{g}\, m^{-1}$ (see Eqs. 7 and 8) should be in the range of the measured wavelength. Gratings with that specification are available for all spectral ranges of interest for this study. Thus, one can conclude that the GS resolving power is generally limited by slit imaging. Here, we assume that $r_\mathrm{eff} = \frac{\lambda}{\kappa}$, with κ being close to unity and accounting for any uncertainties in the assumptions. With the linear dispersion $D_\mathrm{GS} = f\, r_\mathrm{eff}^{-1}$, we then find the following relation:

$$w_\mathrm{S} = \delta\lambda_\mathrm{GS}\, D_\mathrm{GS} = \frac{\delta\lambda_\mathrm{GS}}{r_\mathrm{eff}}\, f = \frac{\delta\lambda_\mathrm{GS}}{\lambda}\, \kappa\, f \;\Leftrightarrow\; \frac{\lambda}{\delta\lambda_\mathrm{GS}} = \kappa \frac{f}{w_\mathrm{S}}. \tag{C1}$$

Appendix D: Aberration-limited slit height of a compact GS

We will approximate the maximum possible slit height based on an empirical quantification of the astigmatism of GSs by Fastie (1952). The astigmatism is the deviation Δf of the focal length in the along- and across-slit directions, introduced by off-axis imaging with e.g. spherical mirrors. It is found to be proportional to the focal length and to the square of the angular distance ϕ of the slit to the normal of the focussing/collimating mirror. The entrance slit and the focal plane of the GS are separated by at least the grating's diameter b; hence, the lower limit of ϕ is given by $\frac{b}{2f} = \frac{1}{2F_\mathrm{GS}}$. With that, the empirical astigmatism quantification of Fastie (1952) can be expressed using the focal length and F number of the GS:

$$\Delta f = 0.4\, f \phi^2 = 0.1 \frac{f}{F_\mathrm{GS}^2}. \tag{D1}$$

The spread ΔL of an imaged point within the slit area along the defocussed astigmatism direction on the GS focal plane is then

$$\Delta L = \frac{\Delta f}{F_\mathrm{GS}}. \tag{D2}$$

As sharp imaging is only important in the dispersion direction for a GS, its optics are always focussed to the focal length in the across-slit direction. The astigmatism spread is then directed in the along-slit direction and is, therefore, negligible for the spectral imaging. However, due to the radial symmetry of the imaging mirrors, the across-slit component of the astigmatism increases with the distance from the slit centre (assuming the slit is centred at the imaging plane). For the ends of the slit, this component is given by the ratio of the slit height h_S to the separation of the entrance slit and slit image, which equals at least the grating's CA b. This means that at the slit ends the slit image is widened by

$$w_\mathrm{S,ast} = \Delta L \frac{h_\mathrm{S}}{b} = 0.1 \frac{h_\mathrm{S}}{F_\mathrm{GS}^2}. \tag{D3}$$

When allowing for a slit widening by a 10th of the width of the slit image, we find the slit height to be limited to

$$h_\mathrm{S} = w_\mathrm{S}\, F_\mathrm{GS}^2. \tag{D4}$$

Appendix E: The étendue of an FPI

If the FPI CA b_FPI is illuminated with a divergent light beam, only light with a wavelength between $\lambda_m^0 = \frac{2\,d\,n}{m}$ (λ_m for $\alpha = 0$) and $\lambda_m^0 - \delta\lambda_\mathrm{FPI}$ will be transmitted in the central beam part (limited by the incidence angle inducing a spectral shift of the FPI spectrum by $\delta\lambda_\mathrm{FPI}$; see Fig. 2). Each wavelength interval corresponds to an incidence angle interval limiting the solid angle of the respective transmitted beam. Using Eqs. (1) and (2) and a cosine approximation, the incidence angle α corresponding to the transmission peak wavelength λ_m is determined as follows:

$$\cos\alpha = \frac{\lambda_m\, m_\mathrm{FPI}}{2\,d\,n} = \frac{\lambda_m}{\lambda_m^0} \approx 1 - \frac{\alpha^2}{2} \Leftrightarrow \alpha \approx \sqrt{2\left(1 - \frac{\lambda_m}{\lambda_m^0}\right)}; \tag{E1}$$

thus, for $\lambda_m = \lambda_m^0 - \epsilon$,

$$\alpha(\epsilon) \approx \sqrt{2\frac{\epsilon}{\lambda_m^0}}. \tag{E2}$$

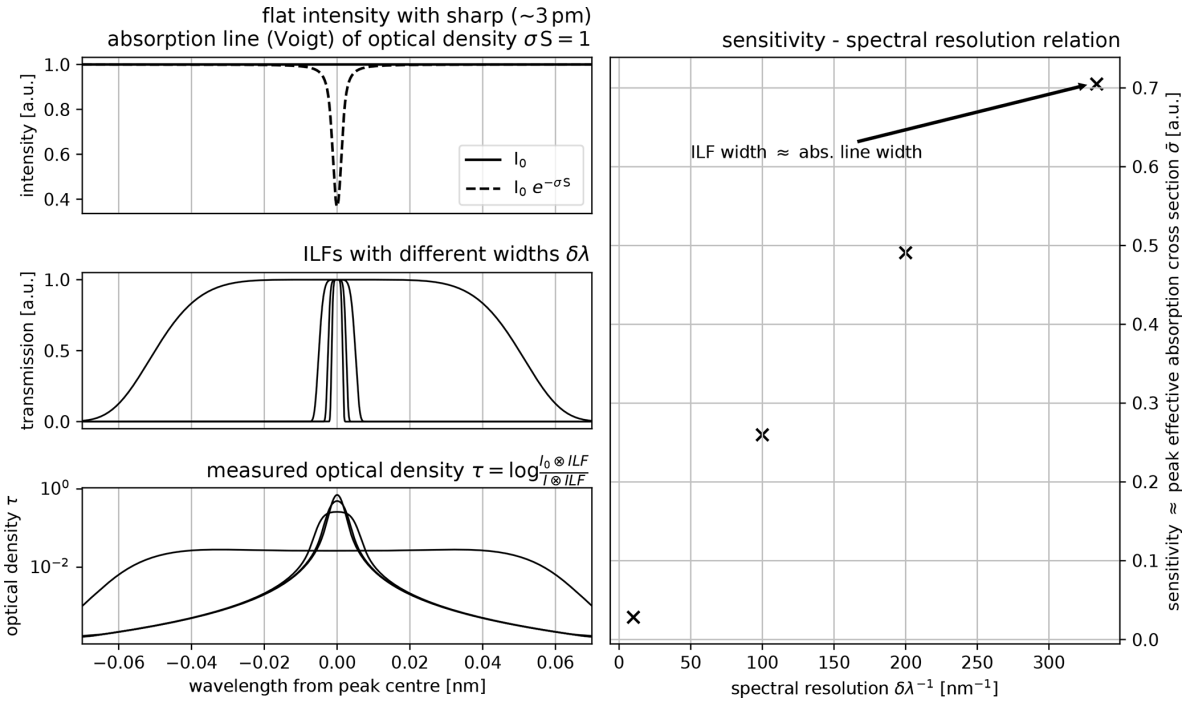

Figure B1. The absorption of a sharp line is diluted throughout the ILF of the observing spectrograph. For ILF widths $\delta\lambda$ that are much larger than the width of the absorption line, the measured absorption signal (peak optical density, i.e. peak effective absorption cross section $\overline{\sigma}$) increases approximately linearly with spectral resolution. For this visualisation, the ILF was modelled with a sixth-order Gaussian, and a Voigt profile was assumed for the absorption line.

Here, ϵ denotes the spectral displacement of λ_m with respect to λ_m^0 (see Fig. 2b). The solid angle $\Omega_{\mathrm{H,FPI}}$ of a transmitted light beam with a wavelength between $\lambda_m^0 - p\,\delta\lambda_{\mathrm{FPI}}$ and $\lambda_m^0 - (p+1)\,\delta\lambda_{\mathrm{FPI}}$ (p being a positive real number) is then approximated by

$$\Omega_{\mathrm{H,FPI}} \approx \pi(\alpha((p+1)\,\delta\lambda_{\mathrm{FPI}})^2 - \alpha(p\,\delta\lambda_{\mathrm{FPI}})^2) = 2\pi\,\frac{\delta\lambda_{\mathrm{FPI}}}{\lambda_m^0}. \quad \text{(E3)}$$

This means that the transmission solid angle of an FPI for a wavelength interval $\delta\lambda_{\mathrm{FPI}}$ is independent of the incidence angle, and the étendue $E_{\mathrm{H,FPI}}$ for a beam with a wavelength within $\delta\lambda_{\mathrm{FPI}}$ traversing the FPI CA ($A_{\mathrm{H,FPI}} = \frac{\pi}{4}\,b_{\mathrm{FPI}}^2$) is

$$E_{\mathrm{H,FPI}} \approx \frac{\pi^2}{2}\,b_{\mathrm{FPI}}^2\,\frac{\delta\lambda_{\mathrm{FPI}}}{\lambda_m^0} \approx \frac{\pi^2}{2}\,b_{\mathrm{FPI}}^2\,\frac{\delta\lambda_{\mathrm{FPI}}}{\lambda}. \quad \text{(E4)}$$

Appendix F: Étendue of an FPI spectrograph with a grating OSM

We can assume that the focal plane of an GS (i.e. its spectrum) is re-imaged with the FPI imaging optics (as that shown in Fig. 2a) with a matched F number. Furthermore, the spectral resolution of this order-sorting GS (OSGS) is matched to the FPI's FSR. The OSGS will cut out slices from the FPI ring system on the detector, where single FPI transmission orders are isolated (see Fig. 2d). The widths of these slices are given by the OSGS's ILF (i.e. its slit width). The result is a variable étendue across the FPI spectrograph's focal plane, generally decreasing with increasing distance to the centre of the ring system (i.e. increasing incidence angle α). In the following, an approximate quantification of the étendue $E_{\mathrm{H,FSG}}$ of the FPI spectrograph with a grating OSM is derived. We thereby regard the area on the detector, where the rings of equal FPI transmission are approximately parallel to the grating dispersion dimension (e.g. a bit above the centre of the FPI ring system). There, the grating dispersion and the FPI dispersion are approximately perpendicular (see Fig. 2d). Light from within a wavelength interval $\delta\lambda_{\mathrm{FPI}}$ covers the area $A_{\mathrm{H,FSG}}$ on the detector. For 1 : 1 imaging, its horizontal extent (in the grating dispersion direction) is given by the OSGS slit width w_{S}.

The vertical extent of $A_{\mathrm{H,FSG}}$ can again be approximated by the radial change in the detector location upon a shift of the transmission peak at λ_m by $\delta\lambda_{\mathrm{FPI}}$. Thus, $A_{\mathrm{H,FSG}}$ becomes a function of the imaging focal length $f_2 = f_1$ and the angle range $\Delta\alpha$ required for tuning the FPI by $\delta\lambda_{\mathrm{FPI}}$. Again, linearising Eq. (4) yields

$$\Delta\alpha \approx \frac{\delta\lambda_{\mathrm{FPI}}}{-\lambda_m\,\alpha}. \quad \text{(F1)}$$

This approximation should be fine for $\alpha > \sqrt{2\frac{\delta\lambda_{\mathrm{FPI}}}{\lambda_m^0}}$ (see Eq. E2), where the FPI angular dispersion does not diverge. The product of $\Delta\alpha$ and the imaging focal length f_2 is then the vertical extent of $A_{\mathrm{H,FSG}}$:

$$A_{\mathrm{H,FSG}} \approx w_{\mathrm{S}} \frac{f_2}{\alpha} \frac{\delta\lambda_{\mathrm{FPI}}}{\lambda_m}. \tag{F2}$$

The solid angle of a light beam reaching a detector spot is again given by the imaging optics' F number (which should be matched to the OSGS's F number):

$$\Omega_{\mathrm{H,FSG}} \approx \frac{\pi}{4F^2}. \tag{F3}$$

Finally, we obtain the étendue of the FPI spectrograph with a grating OSM:

$$\begin{aligned} E_{\mathrm{H,FSG}} &\approx A_{\mathrm{H,FSG}} \cdot \Omega_{\mathrm{H,FSG}} \\ &\approx \frac{\pi}{4F^2} w_{\mathrm{S}} \frac{f_2}{\alpha} \frac{\delta\lambda_{\mathrm{FPI}}}{\lambda_m} = \frac{\pi}{4f_2} \frac{w_{\mathrm{S}} b_{\mathrm{FPI}}^2}{\alpha} \frac{\delta\lambda_{\mathrm{FPI}}}{\lambda_m} \\ &\approx \frac{w_{\mathrm{S}}}{2\pi f_2 \alpha} E_{\mathrm{H,FPI}}. \end{aligned} \tag{F4}$$

Appendix G: On the implementation of the interferometric OSM

In principle, the FPI can be used with a bandpass filter with a transmission FWHM of the FSR of the FPI. For an FPI with resolving power of $R = 150\,000$ and a finesse of $\mathcal{F} = 100$, the bandpass FWHM should be around 0.2 nm in the UV at around 300 nm. Such filters with a transmission of about 25 %–35 % are available (see e.g. Klanner et al., 2021).

Alternatively, an additional FPI with lower resolving power can be used to increase the effective FSR and, thus, the required FWHM of the interference filter bandpass (as e.g. in Mack et al., 1963). The étendue will then still be limited by the FPI with the highest resolving power (see Eq. 25).

The resulting ring-shaped raw spectra are translated into linear spectra by co-adding the intensity of all of the pixels with the same distance to the centre of the ring system. Alternatively, a hardware-based circle-to-line converter (as e.g. proposed in Hays, 1990) can be used.

Data availability. The spectrum shown in Fig. 5b can be obtained from the authors upon request.

Author contributions. JK conceptualised and conducted the theoretical study, built the prototype, and wrote the draft of the paper. All co-authors substantially contributed to the refinement of the study and revised the paper.

Competing interests. At least one of the (co-)authors is a member of the editorial board of *Atmospheric Measurement Techniques*. The peer-review process was guided by an independent editor, and the authors also have no other competing interests to declare.

Disclaimer. Publisher's note: Copernicus Publications remains neutral with regard to jurisdictional claims in published maps and institutional affiliations.

Acknowledgements. The authors would like to thank SLS Optics Ltd for sharing their expertise in designing and manufacturing etalons.

Financial support. This research has been partially funded by the German Science Foundation (DFG; project no. PL 193/23-1).

The article processing charges for this open-access publication were covered by the Max Planck Society.

Review statement. This paper was edited by Alyn Lambert and reviewed by Ivan Prokhorov and two anonymous referees.

References

Arellano, S., Galle, B., Apaza, F., Avard, G., Barrington, C., Bobrowski, N., Bucarey, C., Burbano, V., Burton, M., Chacón, Z., Chigna, G., Clarito, C. J., Conde, V., Costa, F., De Moor, M., Delgado-Granados, H., Di Muro, A., Fernandez, D., Garzón, G., Gunawan, H., Haerani, N., Hansteen, T. H., Hidalgo, S., Inguaggiato, S., Johansson, M., Kern, C., Kihlman, M., Kowalski, P., Masias, P., Montalvo, F., Möller, J., Platt, U., Rivera, C., Saballos, A., Salerno, G., Taisne, B., Vásconez, F., Velásquez, G., Vita, F., and Yalire, M.: Synoptic analysis of a decade of daily measurements of SO_2 emission in the troposphere from volcanoes of the global ground-based Network for Observation of Volcanic and Atmospheric Change, Earth Syst. Sci. Data, 13, 1167–1188, https://doi.org/10.5194/essd-13-1167-2021, 2021.

Barton, S. A., Coxon, J. A., and Roychowdhury, U. K.: Absolute absorption cross sections at high resolution in the $A^2\Pi_i - X^2\Pi_i$ band system of ClO, Can. J. Phys., 62, 473–486, https://doi.org/10.1139/p84-066, 1984.

Burnett, C. R. and Burnett, E. B.: Spectroscopic measurements of the vertical column, abundance of hydroxyl (OH) in the earth's atmosphere, J. Geophys. Res., 86, 5185, https://doi.org/10.1029/jc086ic06p05185, 1981.

Cattolica, R. J., Yoon, S., and Knuth, E. L.: OH Concentration in an Atmospheric-Pressure Methane-Air Flame from Molecular-Beam Mass Spectrometry and Laser-Absorption Spectroscopy, Combust. Sci. Technol., 28, 225–239, https://doi.org/10.1080/00102208208952557, 1982.

Crisp, D., Pollock, H. R., Rosenberg, R., Chapsky, L., Lee, R. A. M., Oyafuso, F. A., Frankenberg, C., O'Dell, C. W., Bruegge, C. J., Doran, G. B., Eldering, A., Fisher, B. M., Fu, D., Gunson, M. R., Mandrake, L., Osterman, G. B., Schwandner, F. M., Sun, K., Taylor, T. E., Wennberg, P. O., and Wunch, D.: The on-orbit perfor-

mance of the Orbiting Carbon Observatory-2 (OCO-2) instrument and its radiometrically calibrated products, Atmos. Meas. Tech., 10, 59–81, https://doi.org/10.5194/amt-10-59-2017, 2017.

Danielache, S. O., Eskebjerg, C., Johnson, M. S., Ueno, Y., and Yoshida, N.: High-precision spectroscopy of ^{32}S, ^{33}S, and ^{34}S sulfur dioxide: Ultraviolet absorption cross sections and isotope effects, J. Geophys. Res., 113, D17314, https://doi.org/10.1029/2007jd009695, 2008.

Dorn, H.-P., Brandenburger, U., Brauers, T., Hausmann, M., and Ehhalt, D. H.: In-situ detection of tropospheric OH radicals by folded long-path laser absorption. Results from the POPCORN Field Campaign in August 1994, Geophys. Res. Lett., 23, 2537–2540, https://doi.org/10.1029/96gl02206, 1996.

Ernest, C. T., Bauer, D., and Hynes, A. J.: High-Resolution Absorption Cross Sections of Formaldehyde in the 30285–32890 cm^{-1} (304–330 nm) Spectral Region, J. Phys. Chem. C, 116, 5910–5922, https://doi.org/10.1021/jp210008g, 2012.

Fabry, C. and Buisson, H.: Wavelength measurements for the establishment of a system of spectroscopic standards, Astrophys. J., 27, 169–196, 1908.

Fastie, W. G.: Image forming properties of the Ebert monochromator, J. Opt. Soc. Am., 42, 647–651, 1952.

Frankenberg, C., Yoshimura, K., Warneke, T., Aben, I., Butz, A., Deutscher, N., Griffith, D., Hase, F., Notholt, J., Schneider, M., Schrijver, H., and Rockmann, T.: Dynamic Processes Governing Lower-Tropospheric HDO/H_2O ratios as Observed from Space and Ground, Science, 325, 1374–1377, https://doi.org/10.1126/science.1173791, 2009.

Galle, B., Johansson, M., Rivera, C., Zhang, Y., Kihlman, M., Kern, C., Lehmann, T., Platt, U., Arellano, S., and Hidalgo, S.: Network for Observation of Volcanic and Atmospheric Change (NOVAC) – A global network for volcanic gas monitoring: Network layout and instrument description, J. Geophys. Res., 115, D05304, https://doi.org/10.1029/2009JD011823, 2010.

Grossmann, K., Frankenberg, C., Magney, T. S., Hurlock, S. C., Seibt, U., and Stutz, J.: PhotoSpec: A new instrument to measure spatially distributed red and far-red Solar-Induced Chlorophyll Fluorescence, Remote Sens. Environ., 216, 311–327, https://doi.org/10.1016/j.rse.2018.07.002, 2018.

Hays, P. B.: Circle to line interferometer optical system, Appl. Optics, 29, 1482, https://doi.org/10.1364/ao.29.001482, 1990.

Hübler, G., Perner, D., Platt, U., Tönnissen, A., and Ehhalt, D. H.: Groundlevel OH radical concentration: New measurements by optical absorption, J. Geophys. Res., 89, 1309–1319, https://doi.org/10.1029/jd089id01p01309, 1984.

Iwagami, N., Inomata, S., Murata, I., and Ogawa, T.: Doppler detection of hydroxyl column abundance in the middle atmosphere, J. Atmos. Chem., 20, 1–15, https://doi.org/10.1007/bf01099915, 1995.

Jacquinot, P.: The Luminosity of Spectrometers with Prisms, Gratings, or Fabry-Perot Etalons, J. Opt. Soc. Am., 44, 761–765, https://doi.org/10.1364/josa.44.000761, 1954.

Jacquinot, P.: New developments in interference spectroscopy, Rep. Prog. Phys., 23, 267–312, https://doi.org/10.1088/0034-4885/23/1/305, 1960.

Klanner, L., Höveler, K., Khordakova, D., Perfahl, M., Rolf, C., Trickl, T., and Vogelmann, H.: A powerful lidar system capable of 1 h measurements of water vapour in the troposphere and the lower stratosphere as well as the temperature in the upper stratosphere and mesosphere, Atmos. Meas. Tech., 14, 531–555, https://doi.org/10.5194/amt-14-531-2021, 2021.

Kuhn, J., Bobrowski, N., Lübcke, P., Vogel, L., and Platt, U.: A Fabry–Perot interferometer-based camera for two-dimensional mapping of SO_2 distributions, Atmos. Meas. Tech., 7, 3705–3715, https://doi.org/10.5194/amt-7-3705-2014, 2014.

Kuhn, J., Platt, U., Bobrowski, N., and Wagner, T.: Towards imaging of atmospheric trace gases using Fabry–Pérot interferometer correlation spectroscopy in the UV and visible spectral range, Atmos. Meas. Tech., 12, 735–747, https://doi.org/10.5194/amt-12-735-2019, 2019.

Lampel, J., Wang, Y., Hilboll, A., Beirle, S., Sihler, H., Puķīte, J., Platt, U., and Wagner, T.: The tilt effect in DOAS observations, Atmos. Meas. Tech., 10, 4819–4831, https://doi.org/10.5194/amt-10-4819-2017, 2017.

Lauster, B., Dörner, S., Beirle, S., Donner, S., Gromov, S., Uhlmannsiek, K., and Wagner, T.: Estimating real driving emissions from multi-axis differential optical absorption spectroscopy (MAX-DOAS) measurements at the A60 motorway near Mainz, Germany, Atmos. Meas. Tech., 14, 769–783, https://doi.org/10.5194/amt-14-769-2021, 2021.

Mack, J. E., McNutt, D. P., Roesler, F. L., and Chabbal, R.: The PEPSIOS Purely Interferometric High-Resolution Scanning Spectrometer I The Pilot Model, Appl. Optics, 2, 873–885, https://doi.org/10.1364/ao.2.000873, 1963.

Neuroth, R., Dorn, H. P., and Platt, U.: High resolution spectral features of a series of aromatic hydrocarbons and BrO: Potential interferences in atmospheric OH-measurements, J. Atmos. Chem., 12, 287–298, https://doi.org/10.1007/bf00048077, 1991.

Notholt, J., Schütt, H., and Keens, A.: Solar absorption measurements of stratospheric OH in the UV with a Fourier-transform spectrometer, Appl. Optics, 36, 6076–6082, https://doi.org/10.1364/ao.36.006076, 1997.

Perner, D., Ehhalt, D. H., Pätz, H. W., Platt, U., Röth, E. P., and Volz, A.: OH – Radicals in the lower troposphere, Geophys. Res. Lett., 3, 466–468, https://doi.org/10.1029/gl003i008p00466, 1976.

Perot, A. and Fabry, C.: On the Application of Interference Phenomena to the Solution of Various Problems of Spectroscopy and Metrology, Astrophys. J., 9, 87, https://doi.org/10.1086/140557, 1899.

Pfeilsticker, K., Erle, F., Funk, O., Veitel, H., and Platt, U.: First geometrical pathlengths probability density function derivation of the skylight from spectroscopically highly resolving oxygen A-band observations: 1. Measurement technique, atmospheric observations and model calculations, J. Geophys. Res.-Atmos., 103, 11483–11504, https://doi.org/10.1029/98jd00725, 1998.

Plascyk, J. A. and Gabriel, F. C.: The Fraunhofer Line Discriminator MKII-An Airborne Instrument for Precise and Standardized Ecological Luminescence Measurement, IEEE T. Instrum. Meas., 24, 306–313, https://doi.org/10.1109/tim.1975.4314448, 1975.

Platt, U. and Stutz, J.: Differential optical absorption spectroscopy, Springer Verlag, Berlin, Heidelberg, ISBN: 978-3-540-75776-4, 2008.

Platt, U., Rateike, M., Junkermann, W., Rudolph, J., and Ehhalt, D. H.: New tropospheric OH measurements, J. Geophys. Res., 93, 5159–5166, https://doi.org/10.1029/jd093id05p05159, 1988.

Platt, U., Wagner, T., Kuhn, J., and Leisner, T.: The "ideal" spectrograph for atmospheric observations, Atmos. Meas. Tech., 14, 6867–6883, https://doi.org/10.5194/amt-14-6867-2021, 2021.

Poghosyan, A. and Golkar, A.: CubeSat evolution: Analyzing CubeSat capabilities for conducting science missions, Prog. Aerosp. Sci., 88, 59–83, https://doi.org/10.1016/j.paerosci.2016.11.002, 2017.

Rothman, L., Gordon, I., Babikov, Y., Barbe, A., Benner, D. C., Bernath, P., Birk, M., Bizzocchi, L., Boudon, V., Brown, L., Campargue, A., Chance, K., Cohen, E., Coudert, L., Devi, V., Drouin, B., Fayt, A., Flaud, J.-M., Gamache, R., Harrison, J., Hartmann, J.-M., Hill, C., Hodges, J., Jacquemart, D., Jolly, A., Lamouroux, J., Roy, R. L., Li, G., Long, D., Lyulin, O., Mackie, C., Massie, S., Mikhailenko, S., Müller, H., Naumenko, O., Nikitin, A., Orphal, J., Perevalov, V., Perrin, A., Polovtseva, E., Richard, C., Smith, M., Starikova, E., Sung, K., Tashkun, S., Tennyson, J., Toon, G., Tyuterev, V., and Wagner, G.: The HITRAN2012 molecular spectroscopic database, J. Quant. Spectrosc. Ra., 130, 4–50, https://doi.org/10.1016/j.jqsrt.2013.07.002, 2013.

Rufus, J., Stark, G., Smith, P. L., Pickering, J. C., and Thorne, A. P.: High-resolution photoabsorption cross section measurements of SO_2, 2: 220 to 325 nm at 295 K, J Geophys. Res., 108, 5011, https://doi.org/10.1029/2002je001931, 2003.

Stone, D., Whalley, L. K., and Heard, D. E.: Tropospheric OH and HO_2 radicals: field measurements and model comparisons, Chem. Soc. Rev., 41, 6348–6404, https://doi.org/10.1039/c2cs35140d, 2012.

Vargas-Rodríguez, E. and Rutt, H.: Design of CO, CO_2 and CH_4 gas sensors based on correlation spectroscopy using a Fabry–Perot interferometer, Sensor. Actuat. B-Chem., 137, 410–419, https://doi.org/10.1016/j.snb.2009.01.013, 2009.

Vaughan, M.: The Fabry-Perot Interferometer History, Theory, Practice and Applications, CRC Press, Boca Raton, ISBN 9780852741382, 1989.

Vogel, L., Sihler, H., Lampel, J., Wagner, T., and Platt, U.: Retrieval interval mapping: a tool to visualize the impact of the spectral retrieval range on differential optical absorption spectroscopy evaluations, Atmos. Meas. Tech., 6, 275–299, https://doi.org/10.5194/amt-6-275-2013, 2013.

The interface between magma and Earth's atmosphere

Jonas Kuhn(1,2), Nicole Bobrowski(1,3), and Ulrich Platt(1,2)

(1) Institut für Umweltphysik, Universität Heidelberg, Heidelberg, Germany
(2) Max Planck Institut für Chemie, Mainz, Germany
(3) Istituto Nazionale di Geofisica e Vulcanologica – Osservatorio Etneo, Catania, Italy

Correspondence: Jonas Kuhn (jkuhn@iup.uni-heidelberg.de)

Abstract Volatiles released from magma form bubbles that can leave the magma body to eventually mix with atmospheric air. The composition of those volatiles, as derived from measurements after their emission, is used to draw conclusions on processes in the Earth's interior or their influences on Earth's atmosphere. It is commonly assumed that the volcanic gas composition describes a state of thermodynamic equilibrium (TE) followed by passive dilution once released to the atmosphere. We show that the latter approach is frequently not justified. By modeling the combined effects of reaction kinetics, turbulent mixing, and associated cooling during the first moments after gas release we find that gas compositions can differ by many orders of magnitude from TE states. Moreover, the fast oxidation of reduced magmatic species can lead to considerable net heating of the plume. Our results have major implications for volcanic gas studies, particularly for (1) the present understanding of auto-catalytic conversion of volcanic halogen species in the atmosphere and (2) redox state determination from volcanic gas measurements. Also, (3) it calls for due care, when deriving the volcanic gas composition from melt equilibria, as done for instance in studies of Earth's early atmosphere.

Volcanic gases crucially influence Earth's atmosphere, on long time scales by gradually altering the atmospheric redox state (Kasting, 1993; Gaillard et al., 2011), as well as on short time scales when large amounts are emitted instantaneously during large eruptions (Robock, 2000). Volcanic gas measurements, besides monitoring purposes, reveal information about Earth's interior, and the chemistry within the cooled and diluted volcanic plume. In that context, the interface between the magmatic gases and the atmosphere and its influence on the gas composition requires consideration. Gas-rock and gas-fluid interactions of fumarole emissions have become a central part of volcanic gas analysis (Giggenbach, 1996; Henley and Fischer, 2021). In contrast to that, high temperature volcanic emission processes remain largely inaccessible for present-day measurement techniques and thus, poorly understood. Volcanic gases are commonly described by thermodynamic equilibrium (TE, i.e. the Gibbs free energy is always minimised – by fast reaction rates – prior to macroscopic changes of the system). While this is likely to hold for instance for hot gases within bubbles in the magma, we show that – in contrast to usual assumptions (Gerlach and Nordlie, 1975; Martin et al., 2006; Gaillard et al., 2011; Moussallam et al., 2019) – TE is not suited to describe magmatic gases after being directly emitted into atmospheric air. Chemical reactions, cooling, and mixing usually take place on comparable time scales leading to complex interaction of these processes ultimately determining the gas composition, which then can greatly deviate from TE.

OH radicals in a high temperature mixture of water and oxygen

Numerous approaches to modeling hot volcanic gases found considerable amounts of OH (up to tens of ppm for higher temperatures, e.g. Gerlach, 2004; Bobrowski et al., 2007; von Glasow, 2010; Martin et al., 2012; Roberts et al., 2014, 2019, summarised in Fig. 3 below) and drew the

attention to volcanic HO_X ($OH + HO_2$). However, these studies remain without a comprehensive assessment of its origin and impacts since relying on TE models or using a kinetic approach to only a fraction of one individual eruptive emission scenario.
The OH radical is extremely reactive and substantially influences atmospheric processes even when present in amounts as small as 0.1 ppt (Levy, 1971; Crutzen, 1974). Generally, the abundance of OH as an intermediate species is linked to high rates of chemical conversion. For instance, large amounts of OH are present in combustion flames (e.g. Cattolica et al., 1982) and the oxyhydrogen gas explosion (see Willbourn and Hinshelwood, 1946).
The following mechanism illustrates a plausible HO_X formation process in volcanic gases, its strong dependence on mixing dynamics, and its impact on the plume's composition. Simplified, the emission of hot magmatic gases into the atmosphere, can be thought of as hot water vapour rapidly mixing with O_2 (see Fig. 1). Before leaving the magma body, magmatic gases are assumed to be in TE because of the high temperatures and considerable dwelling times of gas bubbles within magma (Giggenbach, 1996; Oppenheimer et al., 2018). Thus, within a hot gas bubble, a certain amount of OH and H is formed from water decomposition (Bonhoeffer and Reichardt, 1928; Gerlach, 2004, Fig. 1c). Immediately after the emission of the hot gas from the magma, mixing with ambient air introduces O_2, which, together with the emitted OH and H, provide the initiation of chain branching mechanisms that lead to further enhanced OH levels.

$$O_2\big|_{\mathrm{atm}} + H \rightarrow OH + O \tag{R1}$$

$$O_2\big|_{\mathrm{atm}} + H \xrightarrow{M} HO_2 \tag{R2}$$

$$H_2O\big|_{\mathrm{mag}} + O \rightarrow 2\,OH \tag{R3}$$

$$R\big|_{\mathrm{mag}} + OH \rightarrow RO + H \tag{R4}$$

This mechanism (rate constants in Fig. 1b) oxidises reduced plume components (e.g. H_2 or CO, denoted by R) in fast catalytic cycles. Mixing with atmospheric air also causes rapid plume cooling, which slows down (R3) and changes branching between (R1) and (R2), ultimately leading to the formation of the more stable HO_2.
This is only a small fraction of the kinetic processes accounted for in this work (see below). However, it outlines the large extend to which the amount of OH (and other short-lived species) affects the chemical composition of volcanic gases with a strong dependence on mixing and cooling time scales. The widespread assumption that 'the ambient air will simply quench and dilute the magmatic gas' (Gerlach and Nordlie, 1975; Martin et al., 2006) is therefore likely to be an oversimplification of a decisive process in volcanic degassing. The observations of flames occurring related to volcanic gas emissions (see e.g. Jaggar, 1917, and Fig. A2) supports these considerations, though they may represent extreme examples of the processes examined in this study.

Rapid atmospheric mixing and cooling of magmatic gas

We use a C-H-O-S chemical mechanism of Zeng et al. (2021) and model the first seconds after the magmatic gas is emitted into the atmosphere with a parametrisation of the turbulent mixing process that introduces atmsopheric O_2 to the plume and dominantly drives plume cooling (Methods). The entire cooling process is covered. In this study we initialise the model based on measurements at Nyiragongo lava lake (DR Congo, Tazieff, 1984; Sawyer et al., 2008). The degassing scheme of open lava lakes represents an extreme (end-member-like) case of open vent volcanism, which accounts for a major part of volcanic gas emissions to Earth's atmosphere (Carn et al., 2017). We vary the emission temperature, and allow the gas mixture to attain TE

before emission (Fig. A3). The intensity of turbulent mixing is approximated based on viscous energy dissipation in the boundary layer (Dinger et al., 2018) and Richardson-Obukhov constant quantification by Franzese and Cassiani (2007). The examined three mixing scenarios (MSs, Fig. A1) correspond to circular sources (or bubbles) with radii from 0.075 m (MS III) to 7.5 m (MS I) that also allow a coarse assessment of heterogeneity throughout the plume. While MS I (slower mixing) represents the core part of larger plumes, MS III (fast mixing) accounts for the situation at the very edge of that same plume. Tab. 1 summarises key processes according to reaction rate analysis (Supplementary Fig. 1-16).

Figure 2a shows the modeled temporal evolution of the mixing ratios of key radicals and other plume constituents (SO_2 indicates dilution, see Fig. A4a for more gases or MSs). For an initial temperature of 1370 K, OH amounts are already in the ppm range at the time of emission. Upon mixing with air, the OH levels further increase (to about 100 ppm) before decaying rapidly. In accordance with the processes sketched above (Fig. 1) the OH peak coincides with the maximum CO conversion rate. The time scale of the respective MS determines the oxidised CO amount.

In Fig. 2b the temporal evolution of the mixing ratios of OH, HO_2, CO, and SO_3 from the kinetic model run is compared to their corresponding TE mixing ratios (MS II and III in Fig. A4b). TE concentrations quickly change due to the rising O_2 amounts and the dropping temperature in the plume. The OH equilibrium levels are generally lower but follow the kinetic model rather closely, indicating that the involved reactions are fast with respect to the mixing time scales. In contrast, while TE mixing ratios of CO and HO_2 are much lower than the kinetic values, those of SO_3 are strongly enhanced. The time scales of formation or destruction of those species exceed the mixing time scale and lead to a composition of the cooled plume that depends on its early mixing history.

The rapid and mostly exothermic oxidation processes also cause considerable net heating of the plume (more than 50 K, Fig. 2b), which further influences the chemistry and in part explains the remaining deviation of kinetic OH levels from TE. Effects of plume heating through exothermic reactions was supposed before (Jaggar, 1917; Le Guern et al., 1979) but rarely discussed within the scope of volcanic gas measurements.

Gas composition changes and emission temperature

The temperature of the volcanic gas at the time of its emission to the atmosphere is among the major unknowns of the emission process. It depends on the lava temperature, which varies with magma type and activity and remains challenging to measure (Li et al., 2021). Moreover, it is influenced by cooling through adiabatic expansion of bubbles within the magma (Daly, 1911; Oppenheimer et al., 2018). The temperature evolution in the atmosphere is determined by fast mixing, thermal radiation, interaction with volcanic ash and aerosol, and the heat released by enthalpy changes through chemical conversions.

As shown above, the kinetic OH levels are fairly well represented by TE. They also are in accordance with TE calculations of mixtures of magmatic and atmospheric gas assumed in earlier studies (example for 0.5 s plume age, MS I in Fig. 3). The considerable range of typically observed magmatic gas compositions covered by these studies only weakly influences the OH levels, i.e. they are mainly determined by temperature. For lower temperature HO_X levels are dominated by HO_2 (Fig. A4c, A4d) and start to become more sensitive to the abundance of reduced plume species. Hence, the emission temperature decisively determines the chemical regime of the gas emission process.

The case of CO (Fig. 4a) demonstrates that the plume composition is substantially altered already a tenths of a second after emission. While reduced at high temperature through oxidation by OH, the CO to CO_2 ratio increases at lower temperatures with respect to the initial TE

value. This is due to the dominance of the fast conversion of OCS to CO (Zeng et al., 2021) and demonstrates the drastic relevance of intermediate species. Consequently, any derived redox parameter (e.g. the oxygen fugacity f_{O_2}, Fig. 4b, Oppenheimer et al., 2018; Moussallam et al., 2019) can be either biased high (CO oxidation) or low (CO formation from OCS).
Figure 4c and 4d show the ratios of different emitted gases (H_2S, OCS, and H_2) or secondary plume constituents (HO_2, H_2O_2, SO_3) to SO_2 (dilution tracer) after the plume cooled to 400 K. The large deviations of the gas ratios to their TE state at emission are induced by kinetic processes and their changes along the cooling trajectory (processes listed in Tab. 1 are indicated in Fig. 4).

Implications for volcanic gas studies

Our modelling of the reaction kinetics of hot volcanic gas emissions reveals fundamental inconsistencies between state-of-the-art chemical knowledge (i.e. reaction rates) and many interpretations of volcanic degassing processes based on TE considerations. Examples include:

1. H_2S, H_2, and CO are observed in seconds-to-minutes-old volcanic plumes (Aiuppa et al., 2007, 2011; Schumann et al., 2011). However, their abundance is not compatible with TE considerations. So far, these inconsistencies are accounted for by the exclusion of specific species from TE calculations (Martin et al., 2009; Aiuppa et al., 2011), which appears inappropriate. These studies furthermore explain elevated amounts of reduced gases in volcanic plumes by their hot and direct emission to the atmosphere. In contrast, our results show that the direct intrusion of O_2 into such hot magmatic gas emissions strongly supports the destruction of reduced species. Through site-specific adaptions of the emission scenarios of our model (e.g. lowered O_2 levels in vent systems) the presence of reduced plume species (and also that of sulphate, Roberts et al., 2019) can be explained in a more comprehensive manner.

2. Volcanic gas measurements are thought to be representative for the magmatic gas redox state, which, in turn, is assumed to equal the redox state of their formerly hosting magmas (Giggenbach, 1996). Thus, the compositions of so-called 'disequilibrium' gas samples were modified to resemble TE states in 'restoration' procedures (Gerlach, 1980, 1993; Symonds et al., 1994). Intermediate species and other details of reaction kinetics remained excluded from those considerations. These data on the volcanic gas composition is used in interpretations of the evolution of the early Earth's atmosphere, which furthermore assume the emission of unaltered TE magmatic gas compositions into the atmosphere (e.g. Holland, 2002; Gaillard et al., 2011). Our findings suggest that a comprehensive treatment of the hot magma-atmosphere interface might improve the related interpretations.

3. We find a strong influence of reaction kinetics on the redox state of volcanic gas samples (e.g. f_{O_2} as measured in a 0.1 s old plume, Fig. 4b), which, besides its temperature dependence, is also strongly influenced by the degassing style (MSs are related to bubble sizes). This, provides an additional explanation for the discrepancies between observed gas redox states and that of the hosting melts, which was formerly solely attributed to thermal decoupling of gas bubbles from the surrounding magma (Oppenheimer et al., 2018; Moussallam et al., 2019).

4. Models of reactive halogen chemistry in the minutes-to-hours-old plume strongly depend on the exact amount of HO_2 in the assumed initial plume composition (Surl et al., 2021). Previous reactive halogen studies always used high temperature TE calculations to initiate the plume model, typically resulting in HO_2 levels in the ppm range. With the considerably

lower HO_2 levels (ppb range) resulting from our kinetic model in the cooled plume, reactive halogen plume models can no longer reproduce the observed BrO levels in the plume. Including halogens into the chemical mechanism of our model enables a straight-forward and entirely kinetic treatment of reactive halogen chemistry in volcanic plumes.

In order to resolve the listed shortcomings and inconsistencies, dedicated studies of magma degassing at open vents should employ refined and volcano-specific models combining mixing dynamics with reaction kinetics in addition to improved field observations (e.g. OH measurements, Kuhn et al., 2021).

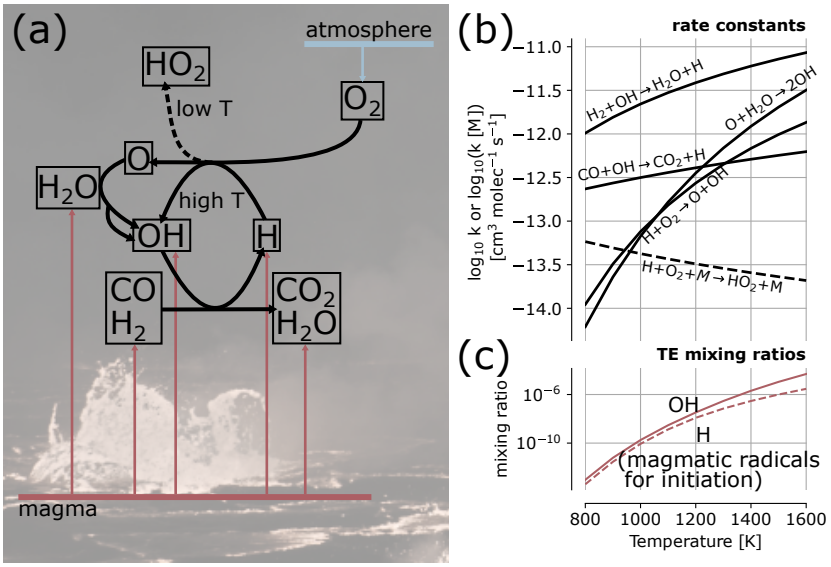

Figure 1: (a) Reaction scheme of an exemplary fast oxidation process when hot magmatic gases (in TE) mix with atmospheric O_2; (b) Respective reaction rate constants as a function of temperature (pressure dependent reactions for 670 hPa); OH and H are formed from the decay of H_2O within magmatic gas bubbles and initiate the oxidation processes. (c) shows the initial amounts of OH and H (in TE) as a function of emission temperature (670 hPa pressure).

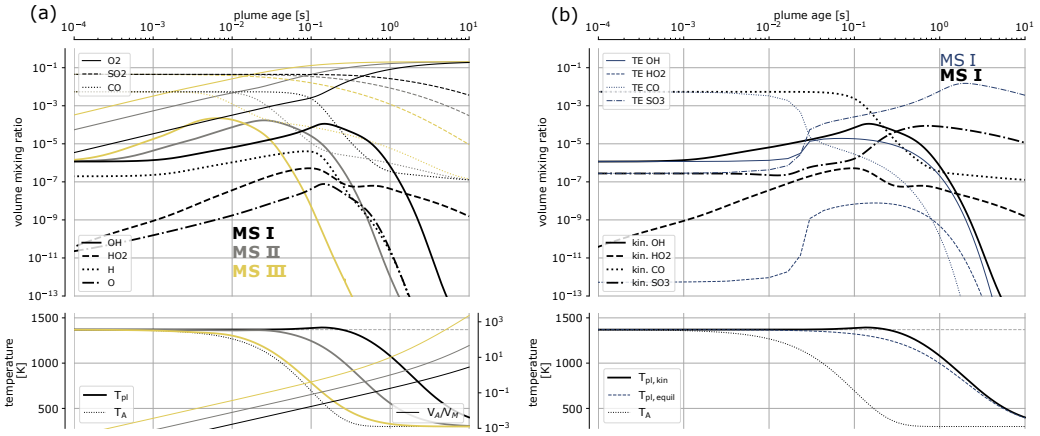

Figure 2: (a) Temporal evolution of the mixing ratios of key radicals and other plume constituents, plume temperature and mixing state (bottom panel) as given by the kinetic model for the three MSs (colours indicate MS I–MS III) and an initial temperature of 1370 K. In (b) the result of the kinetic simulation (thick lines) for OH, HO_2, CO, and SO_3 are shown together with the results of respective TE calculations (thin blue lines), where the composition determined by mixing was brought to TE at each time instance. High OH amounts drive gradual CO oxidation. HO_2, CO, and SO_3 show extreme deviation from the TE state. See supplementary Fig. A4 for a plot with lower initial temperature and for further gases and MSs.

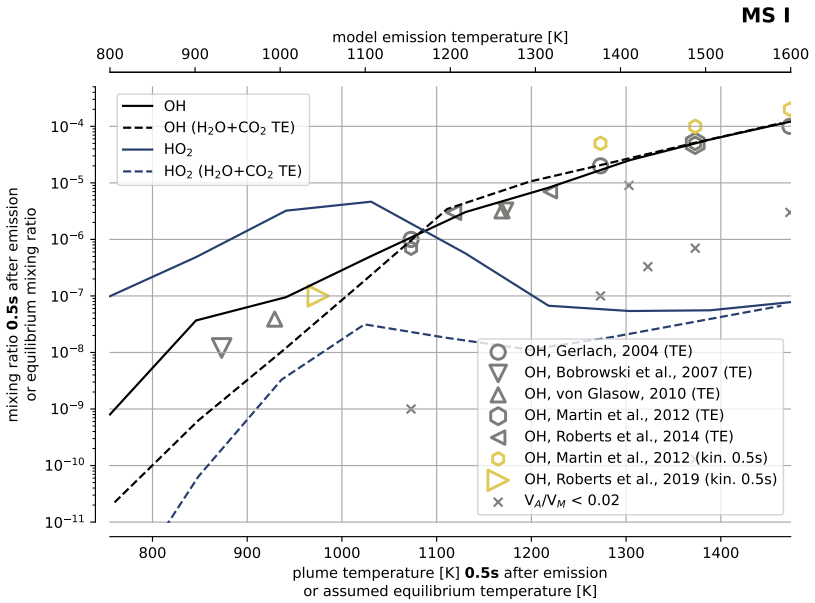

Figure 3: The modeled OH and HO_2 mixing ratio in the plume, 0.5 s after emission, plotted against its instantaneous temperature for model runs with different initial temperature for MS I. Alongside, modeled OH amounts reported in the literature are plotted. In a large temperature range (>1000 K) OH levels are consistent with other studies that assume at least about 2 % atmospheric air content, without a considerable impact of the assumed initial magmatic gas composition. HO_2 levels dominate at lower temperatures. The dashed lines show the results of model runs initialised with a TE of only H_2O and CO_2. In this case, lower levels of reduced gases reduce HO_X levels at lower temperatures.

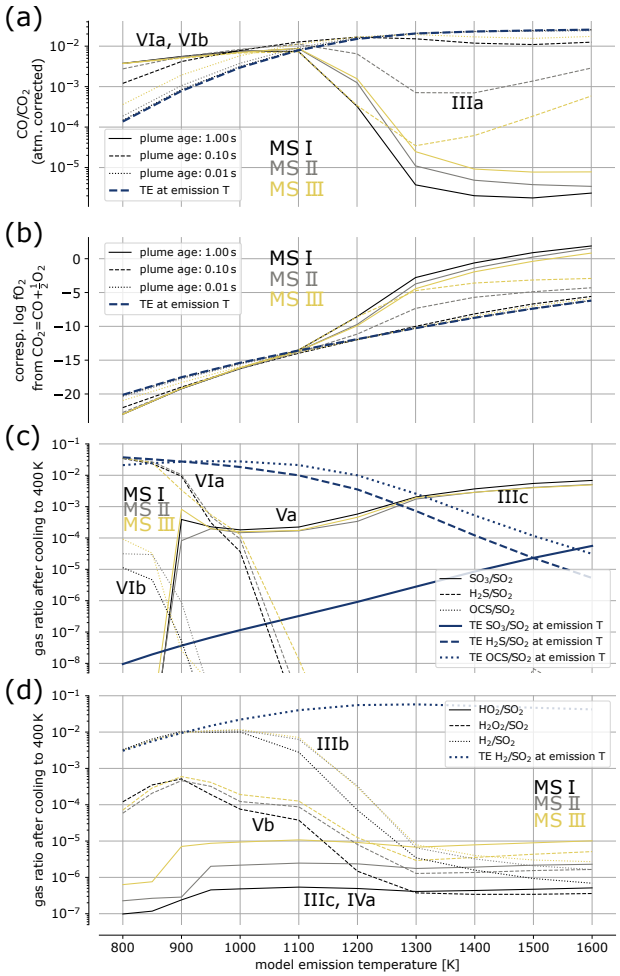

Figure 4: Panel (a) shows volcanic CO/CO_2 as a function of gas emission temperature for different MSs and at different plume age. The influence of atmospheric CO and CO_2 is excluded. At high temperatures CO oxidation by OH causes reduced CO/CO_2 with respect to TE. At lower temperatures CO/CO_2 is enhanced by CO production from OCS. (b) Logarithmic oxygen fugacity f_{O_2} calculated from the CO/CO_2 values in (a) according to Moussallam et al. (2019) for the respective gas emission temperature. An inversion of the effect of high temperature reaction kinetics is found at temperatures between 1100 and 1200 K. (c) Modeled SO_3, H_2S, and OCS amount normalised to SO_2 after cooling of the plume to 400 K, starting from different model emission temperatures and assuming different MSs. Within the plots links to the relevant kinetic processes in Tab. 1 are provided. The SO_3/SO_2 ratios represent measured sulphate/SO_2 ratios (Roberts et al., 2019), while OCS and H_2S are depleted at high temperature. (d) Same as (c) for HO_2, H_2O_2, and H_2. While H_2 is significantly oxidised at higher temperature, HO_2 and H_2O_2 survive plume cooling in amounts exceeding atmospheric background and TE levels.

Table 1: Selection of key net chemical conversions within the first moments of a volcanic plume as identified by reaction rate analysis of the kinetic model calculations (see Supplementary Fig. 1-16).

reference	reaction	comment
I. O production from in-mixed O_2 at high T		
Ia	$SO + O_2 \rightarrow SO_2 + O$	SO, H from magm. TE
Ib	$H + O_2 \rightarrow OH + O$	
II. OH production from O produced by Ia and Ib		
IIa	$H_2O + O \rightarrow 2\,OH$	
III. OH conversion of plume constituents		
IIIa	$OH + CO \rightarrow CO_2 + H$	
IIIb	$OH + H_2 \rightarrow H_2O + H$	
IIIc	$OH + SO_2 \xrightarrow{M,O_2} SO_3 + HO_2$	$OH + SO_2 \xrightarrow{M} HOSO_2$
		$HOSO_2 \xrightarrow{O_2} SO_3 + HO_2$
IV. HO_2 production from in-mixed O_2 at lower T		
IVa	$H + O_2 \xrightarrow{M} HO_2$	
IVb	$HOSO + O_2 \rightarrow HO_2 + SO_2$	(e.g. $SO_2 + H \xrightarrow{M} HOSO$)
V. HO_2 conversion		
Va	$HO_2 + SO_2 \rightarrow SO_3 + OH$	
Vb	$HO_2 + HO_2 \rightarrow H_2O_2 + O_2$	(e.g. $H_2O_2 \xrightarrow{M} 2\,OH$)
VI. Further relevant processes without direct HO_X impact		
VIa	$H_2S + CO_2 \rightarrow COS + H_2O$	
VIb	$COS + O_2 \rightarrow CO + SO_2$	

Methods

A model for the assessment of early-stage volcanic gas emissions

We introduce a model that covers large ranges of turbulent mixing scenarios by a simple but comprehensive parametrisation and combines it with a kinetic treatment of the relevant chemical mechanisms. The model allows to identify the driving chemical processes inside the plume during the entire cooling process and to study their sensitivity on parameters such as the gas emission temperature for different turbulent mixing scenarios.
We use a 1-box approach to calculate the plume's chemical composition $\vec{c}_{\mathrm{pl}}$ (concentrations in molec cm^{-3}) and temperature T_{pl} (in K) as a function of time t. A stationary emission plume with circular cross section is assumed with advection determining the transport along the plume axis and neglecting mixing in that direction. The process is then basically governed by lateral mixing with the atmosphere and chemistry, so that for a given set of initial values ($\vec{c}_{\mathrm{pl},0}$, $T_{\mathrm{pl},0}$) the progression of plume composition and temperature can be inferred numerically through integration of the two derivatives:

$$\frac{\mathrm{d}T_{\mathrm{pl}}}{\mathrm{d}t} = \left.\frac{\mathrm{d}T_{\mathrm{pl}}}{\mathrm{d}t}\right|_{\mathrm{mix}} + \left.\frac{\mathrm{d}T_{\mathrm{pl}}}{\mathrm{d}t}\right|_{\mathrm{chem}} \tag{1}$$

$$\frac{\mathrm{d}\vec{c}_{\mathrm{pl}}}{\mathrm{d}t} = \left.\frac{\mathrm{d}\vec{c}_{\mathrm{pl}}}{\mathrm{d}t}\right|_{\mathrm{mix}} + \left.\frac{\mathrm{d}\vec{c}_{\mathrm{pl}}}{\mathrm{d}t}\right|_{\mathrm{chem}} \tag{2}$$

Mixing

The plume box expands with time and at any time includes all the emitted gas molecules (von Glasow et al., 2003). Turbulence will cause an absolute dispersion of the plume, consisting of both meandering and relative dispersion with respect to its center of mass. The relative plume dispersion is driven by in-mixing of the surrounding air. In young plumes, the increase of plume size leads to an increase of (larger) turbulence elements (eddies) contributing to mixing instead of meandering, thereby causing an accelerated plume growth with time (Batchelor, 1952). With the assumption of isotropic turbulence and characteristic plume sizes within the so-called 'inertial subrange' (i.e. some mm up to hundreds of m in the atmosphere, MacCready, 1962), the mean squared displacement of a plume element from its center of mass $\sigma^2_{\mathrm{pl,rel}}$ can be approximated by (Franzese and Cassiani, 2007):

$$\sigma^2_{\mathrm{pl,rel}} = C\epsilon(t + t_{\mathrm{s}})^3 \tag{3}$$

C is the Richardson-Obukhov constant accounting for the turbulence scenario and ϵ denotes the viscous energy dissipation. The emission source's size, i.e. the non-zero plume size at $t = 0$ is accounted for by the translation t_{s} of the time origin with respect to the point source emission case (i.e. $t_{\mathrm{s}} = 0$). That is to say that the emission plume of a source with given size is approximated by a point source plume after the time t_{s} that it takes to reach the source size. In order to reach an average displacement according to the effective initial emission radius r_0, t_{s} is given by

$$t_{\mathrm{s}} = (r_0^2/C\epsilon)^{1/3} \tag{4}$$

(which is obtained by setting $\sigma_{\mathrm{pl,rel}} = r_0$ in Eq. (3)). Franzese and Cassiani (2007) found that this approximation describes finite source effects reasonably well.
The situation, for instance at a gas emitting lava lake is certainly more complex. Turbulence might not be isotropic and the turbulence scenario, as well as the viscous energy dissipation are difficult to quantify. Nevertheless and because slightly accelerated plume growth fits many observations in nature, we will use Eq. 3 to quantify the expansion of the plume box in our

model. We combine $C\epsilon$ to a parameter γ, which has the dimension of an energy dissipation ($\mathrm{m^2\,s^{-3}}$) and parameterises the strength of turbulent mixing. Together with the effective initial source radius r_0 the plume geometry (plume radius r) is described by:

$$r(t) = \sqrt{\gamma(t_\mathrm{s} + t)^3} \tag{5}$$

From geometrical considerations and assuming the atmosphere to be a static reservoir for atmospheric gases, temperature, and pressure, the mixing terms in Eqs. 1 and 2 can be derived as (see Supplementary Note 1):

$$\left.\frac{\mathrm{d}T_\mathrm{pl}}{\mathrm{d}t}\right|_\mathrm{mix} = 3(t_\mathrm{s} + t)^{-1}\beta(T_\mathrm{A} - T_\mathrm{pl}) \tag{6}$$

$$\left.\frac{\mathrm{d}\vec{c}_\mathrm{pl}}{\mathrm{d}t}\right|_\mathrm{mix} = 3(t_\mathrm{s} + t)^{-1}(\vec{c}_\mathrm{A} - \vec{c}_\mathrm{pl}) \tag{7}$$

T_A and $\vec{c}_\mathrm{A}$ represent the temperature and composition of the atmospheric reservoir. The factor β contains the ratio of specific heat per unit volume of the atmosphere to that of the plume. The mixing process is described by a single parameter that is the temporal translation of the point source case t_s, which depends on the ratio of r_0 and γ (see Eq. (4)). Thereby, within a specific model mixing scenario (MS, determined by the choice of t_s) uncertainties in the turbulent mixing process are absorbed by a slight variation of the bubble radius. Or, one MS describes the situation for the range of bubble radii linked (via t_s) to realistic turbulence scenarios (see Tab. A1 for examples).

In this mixing scheme, there remains a slight imbalance between the expansion of the in-mixed and quickly heated atmospheric air and the contraction of the slightly cooled plume gas. This effect (details in Supplementary Note 2) will lead to a slight plume expansion ($< 25\%$ in the more extreme cases used in this study) and thus, to a deviation of the real plume volume to the that determined by Eq. (5). The associated inaccuracy is minor regarding the high level of simplification of the model and has a negligible effect on the results as these only rely on intensive quantities.

The state of mixing is commonly given by the ratio M of the volume of atmospheric gas that is mixed into the plume V_A to that of the initial gas emission (magmatic gas) V_M (see e.g. Gerlach, 2004). For the assumptions made here it can be calculated as:

$$M(t) = \frac{V_A(t)}{V_M} = \frac{r(t)^2}{r_0^2} - 1 \tag{8}$$

The hot lava impacts atmospheric temperature right above its surface and close to the location of gas emission. This is accounted for by a fast exponential decay (time constant $\tau = 0.1\,\mathrm{s}$) of T_A from magmatic gas temperature to the atmospheric temperature $T_{\mathrm{A},\infty}$ far from the lava surface (see Fig. A1c and Fig. 2):

$$T_\mathrm{A} = T_{\mathrm{A},\infty} + (T_\mathrm{pl} - T_{\mathrm{A},\infty})\,\exp\left(-\frac{t}{\tau}\right) \tag{9}$$

This process is implemented as a static boundary condition to the model. Figure A1 illustrates the mixing process of the MS used in this study.

Chemistry

Chemical conversion rates as well as thermodynamic data of the gas species can be found in numerous literature reaction mechanism compilations. Reaction mechanisms in volcanic gas

emissions are - to some extent - similar to processes in combustion chemistry, which are well studied due to their importance in many branches of engineering. In this study, we use a C-H-O-S combustion mechanism of Zeng et al. (2021), which is based on former work of e.g. Glarborg et al. (2014). The mechanism includes major volcanic plume constituents (H_2O, CO_2, SO_2, CO), while it does not include e.g. halogens or reactive nitrogen species. We removed a H_2O-SO_2 van der Waals complex from the mechanism of Zeng et al. (2021) since it has negligible influence on the chemistry and due to the respective fast reaction rates and the large amounts of H_2O and SO_2 it disturbed the analysis of the conversion rates during the cooling process.
The reaction mechanism is compiled with the open-source software package Cantera (Goodwin et al., 2021). The chemical conversion rates (second term on the right hand side in Eq. 2) are calculated from all the reactions in the mechanism for the instantaneous plume state. At the same time the temperature influence through chemistry (second term on the right hand side in Eq. 1) is calculated according to

$$\left.\frac{\mathrm{d}T_{\mathrm{pl}}}{\mathrm{d}t}\right|_{\mathrm{chem}} = \frac{1}{s_{\mathrm{p,pl}}\,\rho_{\mathrm{pl}}} \sum_i h_{\mathrm{i}} \left.\frac{\mathrm{d}c_{\mathrm{pl,i}}}{\mathrm{d}t}\right|_{\mathrm{chem}} \tag{10}$$

from the molar enthalpies h (in $\mathrm{J\,molec^{-1}}$) and the conversion rates of all species i, the density ρ_{pl} (in $\mathrm{molec\,cm^{-3}}$), and specific heat capacity $s_{\mathrm{p,pl}}$ (in $\mathrm{J\,K^{-1}\,molec^{-1}}$) of the plume.
For given initial conditions and mixing parameters the model is solved by an ordinary differential equation solver. We used a backward differentiation formula method (see e.g. Curtiss and Hirschfelder, 1952) implemented in the SciPy package (Virtanen et al., 2020) in Python. Depending on the chemical mechanism used, a single run modeling the first plume seconds (covering the entire cooling process) takes on the order of a second on a personal computer from the year 2012 (1.9 GHz).
Besides kinetic studies, the Cantera software also enables the calculation of TE in gas mixtures e.g. for a given temperature and pressure. This is used to compare TE with kinetic results.

Limitations of volcanic gas emission models

The simplifications made by the model enable a comprehensive study and reasonable quantitative approximation of the volcanic gas emission process. On the other hand, they call for due care, when interpreting the results. However, the analysis of uncertainties has to encompass both, the simplifications made by the model and the major uncertainties and unknowns concerning the initial conditions. The latter are significant due to the coarsely studied and hardly approachable processes of the degassing interface of hot magma and the atmosphere.
The major simplifications made by the model are:

1. The 1-box implementation of the model assumes spatial homogeneity across the plume cross section for each MS. In reality large (concentration and temperature) gradients across the plume might severely influence the chemistry in the early plume. Evaluating different MSs enables to approximate spatial in-homogeneity to some extent.

2. The plume temperature is likely to be influenced by processes other than mixing and chemistry (as assumed in the model, see Eq. (1)), for instance thermal radiation effects or interactions with ash and aerosol particles.

3. The chemistry mechanism used in this model study only includes gas-phase C-H-O-S species. Halogens and reactive nitrogen chemistry, as well as heterogeneous chemistry is not considered.

The basic uncertainties concerning the involved processes - and thereby the initial conditions or boundary conditions - include:

1. The degassing temperature of the gas is very challenging to quantify, as it might be influenced by e.g. thermal radiation and adiabatic expansion. Direct measurements of absolute lava temperature are scarce and recently Li et al. (2021) found that they are bound to large uncertainties (exceeding 100 K) when relying on the thermal emissivity.

2. The initial composition of magmatic gases used in the model could be a further factor of uncertainty. Only a few plume species can be quantified reliably with today's sampling techniques. Furthermore, depending on the sampling technique, the measured gas composition could have been substantially altered between emission and the time of sampling (through the processes discussed in this study). Regarding the fact that bubble evolution can also be highly dynamic (Oppenheimer et al., 2018), it can even be questioned whether, prior to emission, the magmatic gas is in TE at all.

3. The rate constants of many reactions used in the chemical mechanism are subject to considerable uncertainties, particularly for high temperature (see e.g. Zeng et al., 2021; Glarborg et al., 2014; Roberts et al., 2019). And, the impact of possible heterogeneous reactions on the surface of volcanic ash and aerosol particles on high temperature chemistry is largely unknown.

The listed uncertainties in the degassing processes justify the simplifications made in our model to a large extent. Improving the model, e.g. with respect to its spatial resolution or its temperature dependencies, would not significantly reduce the overall uncertainties of the results, since they are substantially determined by unknown boundary and initial conditions. Nevertheless, since our model includes the major plume species and flexibly parametrises turbulent mixing, it it will also encompass the major chemical processes.

References

Aiuppa, A., Franco, A., von Glasow, R., Allen, A. G., D'Alessandro, W., Mather, T. A., Pyle, D. M., and Valenza, M.: The tropospheric processing of acidic gases and hydrogen sulphide in volcanic gas plumes as inferred from field and model investigations, Atmospheric Chemistry and Physics, 7, 1441–1450, https://doi.org/10.5194/acp-7-1441-2007, 2007.

Aiuppa, A., Shinohara, H., Tamburello, G., Giudice, G., Liuzzo, M., and Moretti, R.: Hydrogen in the gas plume of an open-vent volcano, Mount Etna, Italy, Journal of Geophysical Research, 116, https://doi.org/10.1029/2011jb008461, 2011.

Batchelor, G. K.: Diffusion in a field of homogeneous turbulence, Mathematical Proceedings of the Cambridge Philosophical Society, 48, 345–362, https://doi.org/10.1017/s0305004100027687, 1952.

Bobrowski, N., von Glasow, R., Aiuppa, A., Inguaggiato, S., Louban, I., Ibrahim, O. W., and Platt, U.: Reactive halogen chemistry in volcanic plumes, Journal of Geophysical Research, 112, https://doi.org/10.1029/2006jd007206, 2007.

Bonhoeffer, K. F. and Reichardt, H.: Zerfall von erhitztem Wasserdampf in Wasserstoff und freies Hydroxyl, Zeitschrift für Physikalische Chemie, 139A, 75–97, https://doi.org/10.1515/zpch-1928-13909, 1928.

Carn, S. A., Fioletov, V. E., McLinden, C. A., Li, C., and Krotkov, N. A.: A decade of global volcanic SO2 emissions measured from space, Scientific Reports, 7, 1, https://doi.org/10.1038/srep44095, 2017.

Cattolica, R. J., Yoon, S., and Knuth, E. L.: OH Concentration in an Atmospheric-Pressure Methane-Air Flame from Molecular-Beam Mass Spectrometry and Laser-Absorption Spectroscopy, Combustion Science and Technology, 28, 225–239, https://doi.org/10.1080/00102208208952557, 1982.

Crutzen, P. J.: Photochemical reactions initiated by and influencing ozone in unpolluted tropospheric air, Tellus, 26, 47–57, https://doi.org/10.3402/tellusa.v26i1-2.9736, 1974.

Curtiss, C. F. and Hirschfelder, J. O.: Integration of Stiff Equations, Proceedings of the National Academy of Sciences, 38, 235–243, https://doi.org/10.1073/pnas.38.3.235, 1952.

Daly, R. A.: The Nature of Volcanic Action, Proceedings of the American Academy of Arts and Sciences, 47, 47, https://doi.org/10.2307/20022712, 1911.

Dinger, A. S., Stebel, K., Cassiani, M., Ardeshiri, H., Bernardo, C., Kylling, A., Park, S.-Y., Pisso, I., Schmidbauer, N., Wasseng, J., and Stohl, A.: Observation of turbulent dispersion of artificially released SO2 puffs with UV cameras, Atmospheric Measurement Techniques, 11, 6169–6188, https://doi.org/10.5194/amt-11-6169-2018, 2018.

Franzese, P. and Cassiani, M.: A statistical theory of turbulent relative dispersion, Journal of Fluid Mechanics, 571, 391–417, https://doi.org/10.1017/s0022112006003375, 2007.

Gaillard, F., Scaillet, B., and Arndt, N. T.: Atmospheric oxygenation caused by a change in volcanic degassing pressure, Nature, 478, 229–232, https://doi.org/10.1038/nature10460, 2011.

Gerlach, T.: Chemical characteristics of the volcanic gases from Nyiragongo lava lake and the generation of CH4-rich fluid inclusions in alkaline rocks, Journal of Volcanology and Geothermal Research, 8, 177–189, https://doi.org/10.1016/0377-0273(80)90103-1, 1980.

Gerlach, T. M.: Thermodynamic evaluation and restoration of volcanic gas analyses: An example based on modern collection and analytical methods., Geochemical Journal, 27, 305–322, https://doi.org/10.2343/geochemj.27.305, 1993.

Gerlach, T. M.: Volcanic sources of tropospheric ozone-depleting trace gases, Geochemistry, Geophysics, Geosystems, 5, 9, https://doi.org/10.1029/2004gc000747, 2004.

Gerlach, T. M. and Nordlie, B. E.: The C-O-H-S gaseous system; Part II, Temperature, atomic composition, and molecular equilibria in volcanic gases, American Journal of Science, 275, 377–394, https://doi.org/10.2475/ajs.275.4.377, 1975.

Giggenbach, W. F.: Chemical Composition of Volcanic Gases, in: Monitoring and Mitigation of Volcano Hazards, pp. 221–256, Springer Berlin Heidelberg, https://doi.org/10.1007/978-3-642-80087-0_7, 1996.

Glarborg, P., Halaburt, B., Marshall, P., Guillory, A., Troe, J., Thellefsen, M., and Christensen, K.: Oxidation of Reduced Sulfur Species: Carbon Disulfide, The Journal of Physical Chemistry A, 118, 6798–6809, https://doi.org/10.1021/jp5058012, 2014.

Goodwin, D. G., Speth, R. L., Moffat, H. K., and Weber, B. W.: Cantera: An Object-oriented Software Toolkit for Chemical Kinetics, Thermodynamics, and Transport Processes, https://www.cantera.org, https://doi.org/10.5281/zenodo.4527812, version 2.5.1, 2021.

Henley, R. W. and Fischer, T. P.: Sulfur sequestration and redox equilibria in volcanic gases, Journal of Volcanology and Geothermal Research, 414, 107 181, https://doi.org/10.1016/j.jvolgeores.2021.107181, 2021.

Holland, H. D.: Volcanic gases, black smokers, and the great oxidation event, Geochimica et Cosmochimica Acta, 66, 3811–3826, https://doi.org/10.1016/s0016-7037(02)00950-x, 2002.

Jaggar, T. A.: Volcanologic investigations at Kilauea, American Journal of Science, s4-44, 161–220, https://doi.org/10.2475/ajs.s4-44.261.161, 1917.

Kasting, J. F.: Earth's Early Atmosphere, Science, 259, 920–926, https://doi.org/10.1126/science.11536547, 1993.

Kuhn, J., Bobrowski, N., Wagner, T., and Platt, U.: Mobile and high-spectral-resolution Fabry–Pérot interferometer spectrographs for atmospheric remote sensing, Atmospheric Measurement Techniques, 14, 7873–7892, https://doi.org/10.5194/amt-14-7873-2021, 2021.

Le Guern, F., Carbonnelle, J., and Tazieff, H.: Erta'ale lava lake: heat and gas transfer to the atmosphere, Journal of Volcanology and Geothermal Research, 6, 27–48, https://doi.org/10.1016/0377-0273(79)90045-3, 1979.

Levy, H.: Normal Atmosphere: Large Radical and Formaldehyde Concentrations Predicted, Science, 173, 141–143, https://doi.org/10.1126/science.173.3992.141, 1971.

Li, H., Andujar, J., Slodczyk, A., Meneses, D. D. S., Scaillet, B., Echegut, P., Biren, J., and Oppenheimer, C.: Spectral Emissivity of Phonolite Lava at High Temperature, IEEE Transactions On Geoscience And Remote Sensing, pp. 1–15, https://doi.org/10.1109/tgrs.2021.3104657, 2021.

MacCready, P. B.: The inertial subrange of atmospheric turbulence, Journal of Geophysical Research, 67, 1051–1059, https://doi.org/10.1029/jz067i003p01051, 1962.

Martin, R., Roberts, T., Mather, T., and Pyle, D.: The implications of H2S and H2 kinetic stability in high-T mixtures of magmatic and atmospheric gases for the production of oxidized trace species (e.g., BrO and NOx), Chemical Geology, 263, 143–150, https://doi.org/10.1016/j.chemgeo.2008.12.028, 2009.

Martin, R., Ilyinskaya, E., and Oppenheimer, C.: The enigma of reactive nitrogen in volcanic emissions, Geochimica et Cosmochimica Acta, 95, 93–105, https://doi.org/10.1016/j.gca.2012.07.027, 2012.

Martin, R. S., Mather, T. A., and Pyle, D. M.: High-temperature mixtures of magmatic and atmospheric gases, Geochemistry, Geophysics, Geosystems, 7, 4, https://doi.org/10.1029/2005gc001186, 2006.

Moussallam, Y., Oppenheimer, C., and Scaillet, B.: On the relationship between oxidation state and temperature of volcanic gas emissions, Earth and Planetary Science Letters, 520, 260–267, https://doi.org/10.1016/j.epsl.2019.05.036, 2019.

Oppenheimer, C., Scaillet, B., Woods, A., Sutton, A. J., Elias, T., and Moussallam, Y.: Influence of eruptive style on volcanic gas emission chemistry and temperature, Nature Geoscience, 11, 678–681, https://doi.org/10.1038/s41561-018-0194-5, 2018.

Roberts, T., Martin, R., and Jourdain, L.: Reactive bromine chemistry in Mount Etna's volcanic plume: the influence of total Br, high-temperature processing, aerosol loading and plume–air mixing, Atmospheric Chemistry and Physics, 14, 11 201–11 219, 2014.

Roberts, T., Dayma, G., and Oppenheimer, C.: Reaction Rates Control High-Temperature Chemistry of Volcanic Gases in Air, Frontiers in Earth Science, 7, https://doi.org/10.3389/feart.2019.00154, 2019.

Robock, A.: Volcanic eruptions and climate, Reviews of Geophysics, 38, 191–219, https://doi.org/10.1029/1998rg000054, 2000.

Sawyer, G. M., Carn, S. A., Tsanev, V. I., Oppenheimer, C., and Burton, M.: Investigation into magma degassing at Nyiragongo volcano, Democratic Republic of the Congo, Geochemistry, Geophysics, Geosystems, 9, 2, https://doi.org/10.1029/2007gc001829, 2008.

Schumann, U., Weinzierl, B., Reitebuch, O., Schlager, H., Minikin, A., Forster, C., Baumann, R., Sailer, T., Graf, K., Mannstein, H., Voigt, C., Rahm, S., Simmet, R., Scheibe, M., Lichtenstern, M., Stock, P., Rüba, H., Schäuble, D., Tafferner, A., Rautenhaus, M., Gerz, T., Ziereis, H., Krautstrunk, M., Mallaun, C., Gayet, J.-F., Lieke, K., Kandler, K., Ebert, M., Weinbruch, S., Stohl, A., Gasteiger, J., Groß, S., Freudenthaler, V., Wiegner, M., Ansmann, A., Tesche, M., Olafsson, H., and Sturm, K.: Airborne observations of the Eyjafjalla volcano ash cloud over Europe during air space closure in April and May 2010, Atmospheric Chemistry and Physics, 11, 2245–2279, https://doi.org/10.5194/acp-11-2245-2011, 2011.

Surl, L., Roberts, T., and Bekki, S.: Observation and modelling of ozone-destructive halogen chemistry in a passively degassing volcanic plume, Atmospheric Chemistry and Physics, 21, 12 413–12 441, https://doi.org/10.5194/acp-21-12413-2021, 2021.

Symonds, R. B., Rose, W. I., Bluth, G. J. S., and Gerlach, T. M.: Volcanic-gas studies; methods, results, and applications, Reviews in Mineralogy and Geochemistry, 30, 1–66, 1994.

Tazieff, H.: Mt. Niragongo: renewed activity of the lava lake, Journal of Volcanology and Geothermal Research, 20, 267–280, https://doi.org/10.1016/0377-0273(84)90043-x, 1984.

Virtanen, P., Gommers, R., Oliphant, T. E., Haberland, M., Reddy, T., Cournapeau, D., Burovski, E., Peterson, P., Weckesser, W., Bright, J., van der Walt, S. J., Brett, M., Wilson, J., Millman, K. J., Mayorov, N., Nelson, A. R. J., Jones, E., Kern, R., Larson, E., Carey, C. J., Polat, İ., Feng, Y., Moore, E. W., VanderPlas, J., Laxalde, D., Perktold, J., Cimrman, R., Henriksen, I., Quintero, E. A., Harris, C. R., Archibald, A. M., Ribeiro, A. H., Pedregosa, F., van Mulbregt, P., and SciPy 1.0 Contributors: SciPy 1.0: Fundamental Algorithms for Scientific Computing in Python, Nature Methods, 17, 261–272, https://doi.org/10.1038/s41592-019-0686-2, 2020.

von Glasow, R.: Atmospheric chemistry in volcanic plumes, Proceedings of the National Academy of Sciences, 107, 6594–6599, 2010.

von Glasow, R., Lawrence, M. G., Sander, R., and Crutzen, P. J.: Modeling the chemical effects of ship exhaust in the cloud-free marine boundary layer, Atmospheric Chemistry and Physics, 3, 233–250, https://doi.org/10.5194/acp-3-233-2003, 2003.

Willbourn, A. H. and Hinshelwood, C. N.: The mechanism of the hydrogen-oxygen reaction I. The third explosion limit, Proceedings of the Royal Society of London. Series A. Mathematical and Physical Sciences, 185, 353–369, https://doi.org/10.1098/rspa.1946.0023, 1946.

Zeng, Z., Dlugogorski, B. Z., Oluwoye, I., and Altarawneh, M.: Combustion chemistry of COS and occurrence of intersystem crossing, Fuel, 283, 119 257, https://doi.org/10.1016/j.fuel.2020.119257, 2021.

Extended Data

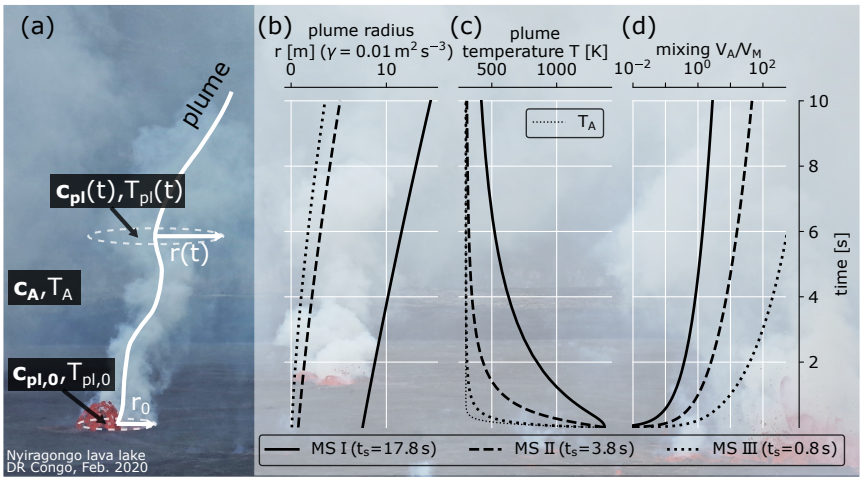

Figure A1: A parametrised increase of the radius of the assumed circular plume box drives mixing in the model. This is schematically illustrated in panel (a). Plume radius (b), temperature (c) and mixing (d) are shown for the three MSs assumed in this study.

Table A1: MS used for the model calculations with exemplary effective source radius (r_0) - turbulent mixing strength (γ) pairs, combining to the mixing parameter t_S (see Eq. 4)

	mixing scenario					
	MS I		MS II		MS III	
t_s [s]	17.8		3.8		0.8	
r_0 [m]	7.5	2.4	0.75	2.4	0.075	0.24
γ [$m^2\,s^{-3}$]	0.01	0.001	0.01	0.1	0.01	0.1

Figure A2: Flames related to high temperature gas emissions at Nyamulagira volcano in the Democratic Republic of Congo, 03.02.2020

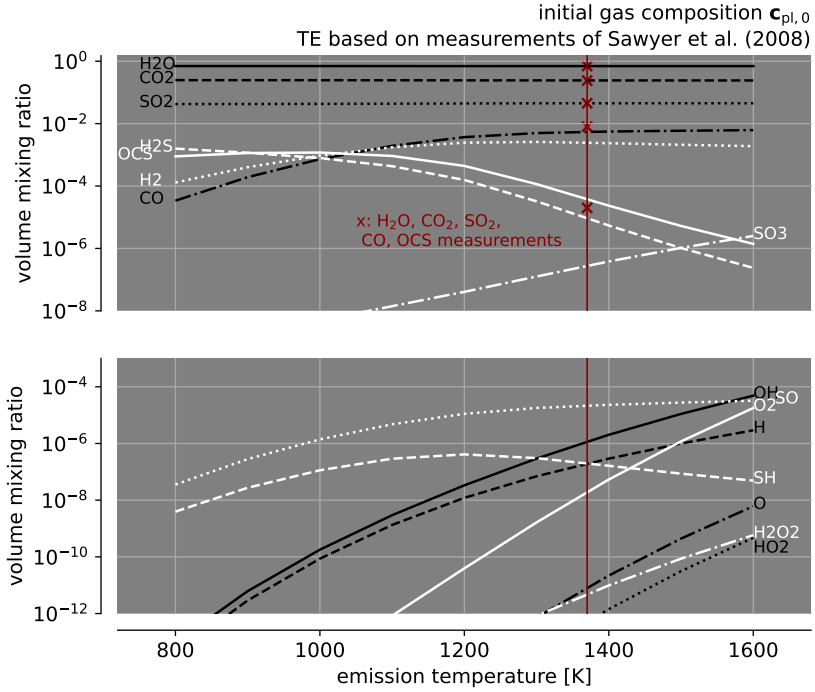

Figure A3: Initial gas composition assumed in the modeling study. They are oriented towards the measurements of Sawyer et al., 2008 who measured H_2O, CO_2, SO_2, CO, and OCS (red crosses) and determined the emission temperature to be 1370 K (red vertical line) in accordance to temperature measurements of Tazieff (1984). We used the Cantera software package to calculate TE from this reported composition for the reported temperature (with a slight deviation of CO and OCS levels) and for the given range of assumed intial temperatures used in the study.

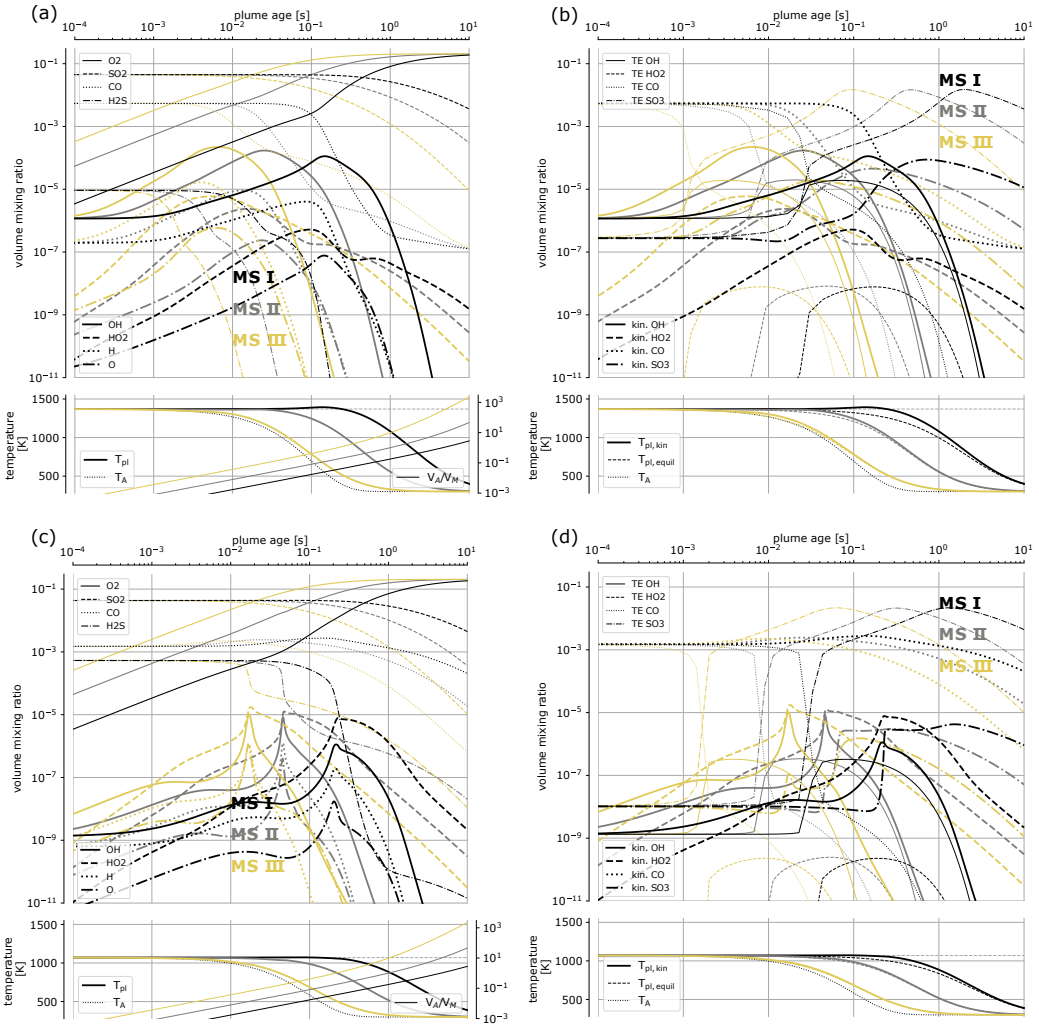

Figure A4: (a), (b): Same as Fig. 2, increased number of plotted gases and MSs. (c), (d): same as (a), (b), initial plume temperature reduced to 1070 K.

Supplementary Information

Supplementary Note 1: Dilution of magmatic gas in atmospheric air

We derive the mixing term for the temporal gradient of the concentration of a single gas species (Eq. (7), Methods) for the expanding plume box and assume independent mixing of all species. The concentration of a gas in the plume $c_{\mathrm{pl}} = N\,V^{-1}$, with N particles in the plume volume V chances according to:

$$\mathrm{d}c_{\mathrm{pl}} = \frac{\mathrm{d}c_{\mathrm{pl}}}{\mathrm{d}N}\,\mathrm{d}N + \frac{\mathrm{d}c_{\mathrm{pl}}}{\mathrm{d}V}\,\mathrm{d}V = \frac{\mathrm{d}N}{V} - \frac{N}{V^2}\,\mathrm{d}V = \frac{c_{\mathrm{A}}\,\mathrm{d}V}{V} - \frac{c_{\mathrm{pl}}\mathrm{d}V}{V} = (c_{\mathrm{A}} - c_{\mathrm{pl}})\,\frac{dV}{V} \tag{11}$$

The first (left) of the two terms in the expression describes the influx of atmospheric particles driven by the increase of volume ($\mathrm{d}N = c_{\mathrm{A}}\,\mathrm{d}V$). The right therm accounts for the dilution of the concentration of the gas in the growing plume volume. With Eq. (5) (Methods) we get for a circular plume:

$$\frac{\mathrm{d}c_{\mathrm{pl}}}{\mathrm{d}t} = (c_{\mathrm{A}} - c_{\mathrm{pl}})\,\frac{1}{V}\,\frac{\mathrm{d}V}{\mathrm{d}t} = (c_{\mathrm{A}} - c_{\mathrm{pl}})\,\frac{2}{r}\,\frac{\mathrm{d}r}{\mathrm{d}t} = (c_{\mathrm{A}} - c_{\mathrm{pl}})\,\frac{3}{r}\,\sqrt{\gamma(t_{\mathrm{s}} + t)} = \frac{3\,(c_{\mathrm{A}} - c_{\mathrm{pl}})}{(t_{\mathrm{s}} + t)} \tag{12}$$

For the temperature we find a similar expression by regarding the density of free energy in the plume $u_{\mathrm{pl}} = n_{\mathrm{pl}}\,c_{\mathrm{P,pl}}\,T_{\mathrm{pl}}$ with the plume's particle density n_{pl} and the plume's specific heat capacity at constant pressure s_{pl}. Here, the mixing influence on the plume temperature is - analogous to concentration mixing - determined on the one hand by the influx of atmospheric particles with the free energy density $u_{\mathrm{A}} = n_{\mathrm{A}}\,s_{\mathrm{A}}\,T_{\mathrm{A}}$ and the dilution of u_{pl} by the increase $\mathrm{d}V$ of the plume box volume. In analogy to Eq. (11) we find:

$$\mathrm{d}u_{\mathrm{pl}} = (u_{\mathrm{A}} - u_{\mathrm{pl}})\frac{\mathrm{d}V}{V} \tag{13}$$

For any time instance $\mathrm{d}T_{\mathrm{pl}} = \frac{\mathrm{d}u_{\mathrm{pl}}}{n_{\mathrm{pl}}\,s_{\mathrm{pl}}}$, so that the analogy to Eq. (12) leads to:

$$\frac{\mathrm{d}T_{\mathrm{pl}}}{\mathrm{d}t} = \frac{3}{(t_{\mathrm{s}} + t)}\,\frac{(u_{\mathrm{A}} - u_{\mathrm{pl}})}{n_{\mathrm{pl}}\,s_{\mathrm{pl}}} = \frac{3}{(t_{\mathrm{s}} + t)}\left(\frac{n_{\mathrm{A}}\,s_{\mathrm{A}}}{n_{\mathrm{pl}}\,s_{\mathrm{pl}}}T_{\mathrm{A}} - T_{\mathrm{pl}}\right) = \frac{3\,(\beta\,T_{\mathrm{A}} - T_{\mathrm{pl}})}{(t_{\mathrm{s}} + t)} \tag{14}$$

with $\beta = \frac{n_{\mathrm{A}}\,s_{\mathrm{A}}}{n_{\mathrm{pl}}\,s_{\mathrm{pl}}}$ being calculated for each time instance from thermodynamic data by the Cantera software package.

Supplemtary Note 2: The impact of temperature on turbulent mixing

The mixing scheme of the model assumes a plume growth based on turbulence considerations. These do not include the large temperature difference between magmatic and atmospheric gas. This results in a deviation of the plume volume in the isobaric plume model due to the imbalance of:

- the expansion of air with atmospheric temperature, introduced to the plume box and instantaneously heated to about plume temperature, and
- the deflation of the plume gas due to the cooling, introduced by intruding atmospheric air.

We want to assess the impact on the representativity of our model. At a given time instance, the volume of the plume is V_{pl} and contains plume gas with the temperature T_{pl}. After a time step

the plume volume grows by the amount of $\mathrm{d}V_{\mathrm{pl}}$, which contains atmospheric gas with temperature T_{A}. After that time step the plume temperature will differ by (see Supplementary Note 1):

$$\mathrm{d}T_{\mathrm{pl}} = \beta\,\Delta T \frac{\mathrm{d}V_{\mathrm{pl}}}{V_{\mathrm{pl}}} \tag{15}$$

The temperature difference between atmosphere and plume is denoted by $\Delta T = T_{\mathrm{A}} - T_{\mathrm{pl}}$. For an ideal gas at constant pressure, the temperature changes the volume according to:

$$\delta V = \frac{V}{T}\delta T \tag{16}$$

The volume of the in-mixed atmospheric gas is $\mathrm{d}V_{\mathrm{pl}}$, its initial temperature is T_{A}, and its temperature changes by about $-\Delta T$. Per time step the deviation in volume change through in-mixed atmospheric air δV^* is given by:

$$\delta V^* = -\frac{\Delta T}{T_{\mathrm{A}}}\mathrm{d}V_{\mathrm{pl}} \tag{17}$$

The volume of the plume is V_{pl}, its temperature is about T_{pl} and changes by $\mathrm{d}T_{\mathrm{pl}}$. Per time step the deviation in volume change through the contraction of the cooling of plume gas $\delta V^\dagger$ is given by:

$$\delta V^\dagger = \frac{V_{\mathrm{pl}}}{T_{\mathrm{pl}}}\mathrm{d}T_{\mathrm{pl}} = \frac{\beta\Delta T}{T_{\mathrm{pl}}}\mathrm{d}V_{\mathrm{pl}} \tag{18}$$

The absolute deviation of the plume's volume change in the model $\overline{\mathrm{d}V}$ is then:

$$\overline{\mathrm{d}V} = \delta V^* + \delta V^\dagger = \left(\frac{\beta}{T_{\mathrm{pl}}} - \frac{1}{T_{\mathrm{A}}}\right)\Delta T\,\mathrm{d}V_{\mathrm{pl}} = \kappa\,\mathrm{d}V_{\mathrm{pl}} \tag{19}$$

Since β quickly approaches unity for $T_{\mathrm{pl}} \to T_{\mathrm{A}}$, the factor κ is positive (ΔT is negative) throughout the cooling processes regarded. This corresponds to a slight expansion of the plume. At $T_{\mathrm{pl}} = 1500\,\mathrm{K}$ and $T_{\mathrm{A}} = 300\,\mathrm{K}$, κ is about 2. Such values can be reached for a short time in slower mixing scenarios (e.g. MS I). The atmospheric temperature gradient assumed in the model study dampens this effect and the highest deviation from the assumed plume volume is about 25% for MS I and 1600 K initial plume temperature. This effect only leads to a deviation of the actual plume volume from that assumed in the mixing scheme. In other words, the plume grows faster, but that faster growth does not contribute to mixing. Since basically relying only on intensive quantities (temperature and concentrations) the model results will not be affected.

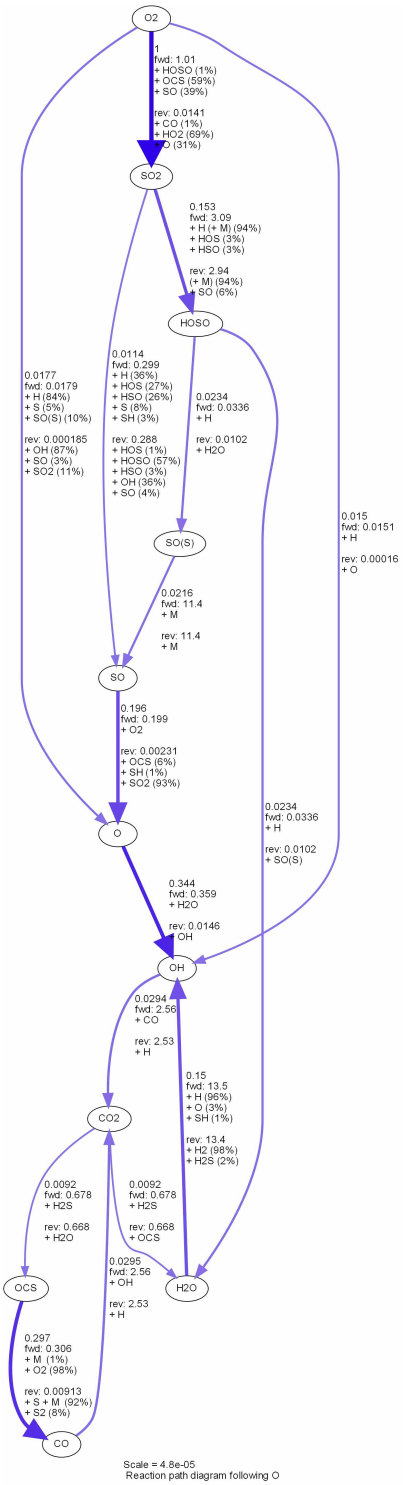

Figure S1: Reaction paths for O-species, MS II, t=0.001s, T=1370K. The arrow size indicates the respective rate. The arrow labels contain the exact rate (relative to the 'scale' value at the bottom in $\mathrm{kmol\,m^{-3}\,s^{-1}}$) and specify the relative contribution of individual reaction paths in forward ('fwd') and reverse ('rev') direction.

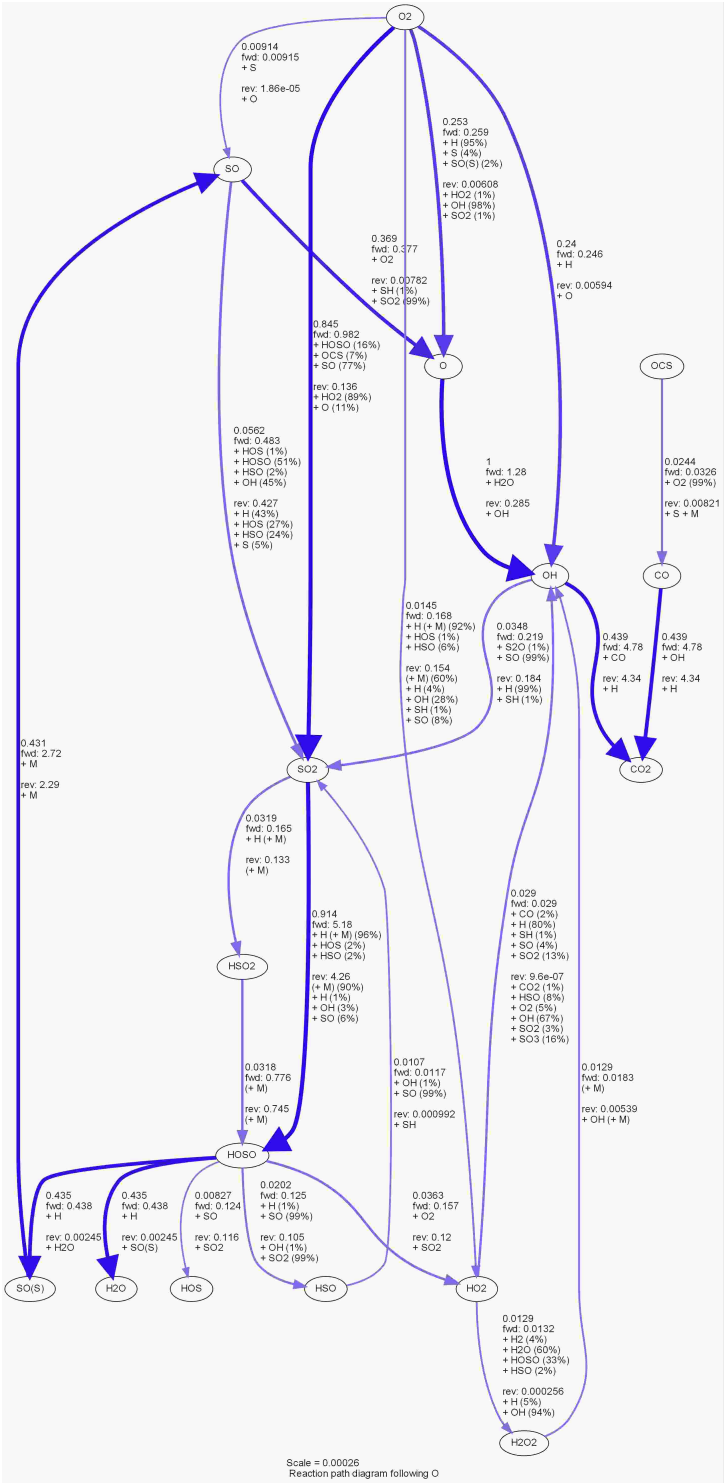

Figure S2: Reaction paths for O-species, MS II, t=0.01s, T=1370K. The arrow size indicates the respective rate. The arrow labels contain the exact rate (relative to the 'scale' value at the bottom in $\mathrm{kmol\,m^{-3}\,s^{-1}}$) and specify the relative contribution of individual reaction paths in forward ('fwd') and reverse ('rev') direction.

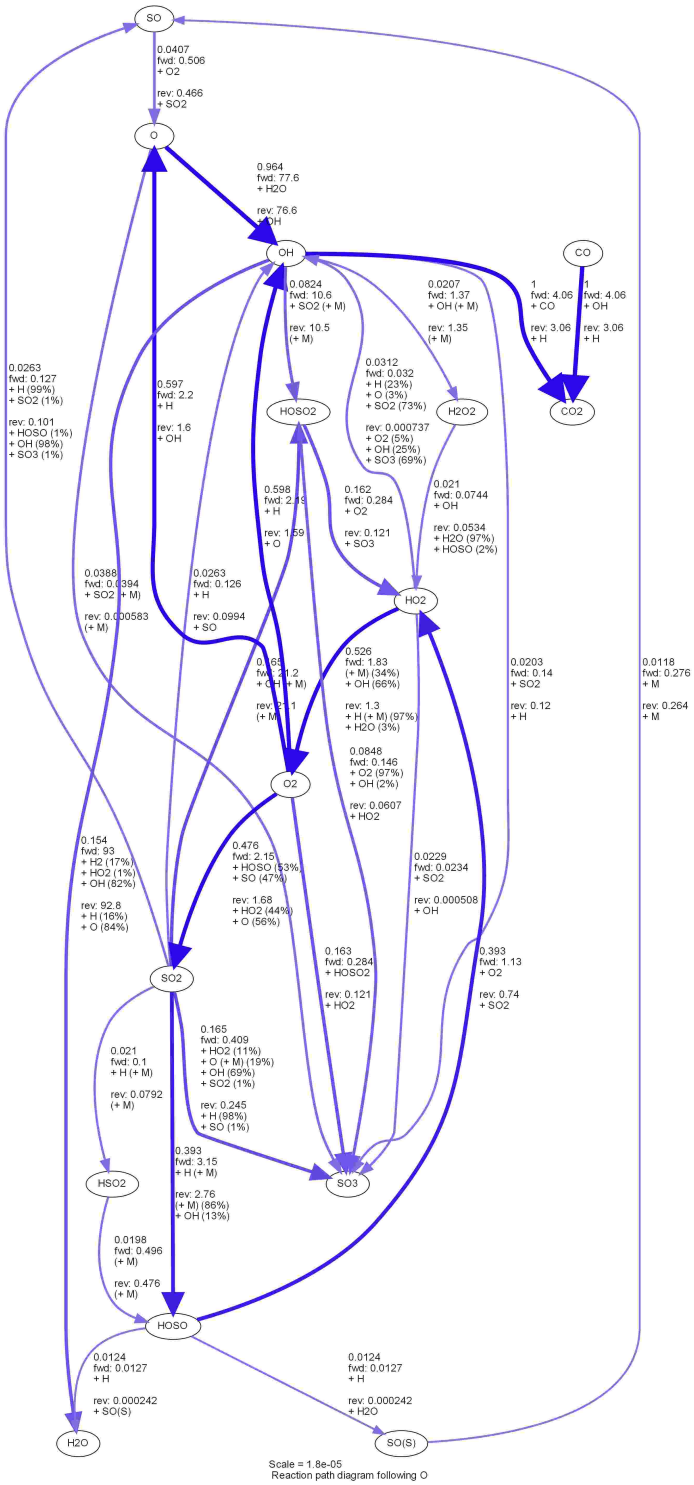

Figure S3: Reaction paths for O-species, MS II, t=0.1s, T=1379K. The arrow size indicates the respective rate. The arrow labels contain the exact rate (relative to the 'scale' value at the bottom in $\mathrm{kmol\,m^{-3}\,s^{-1}}$) and specify the relative contribution of individual reaction paths in forward ('fwd') and reverse ('rev') direction.

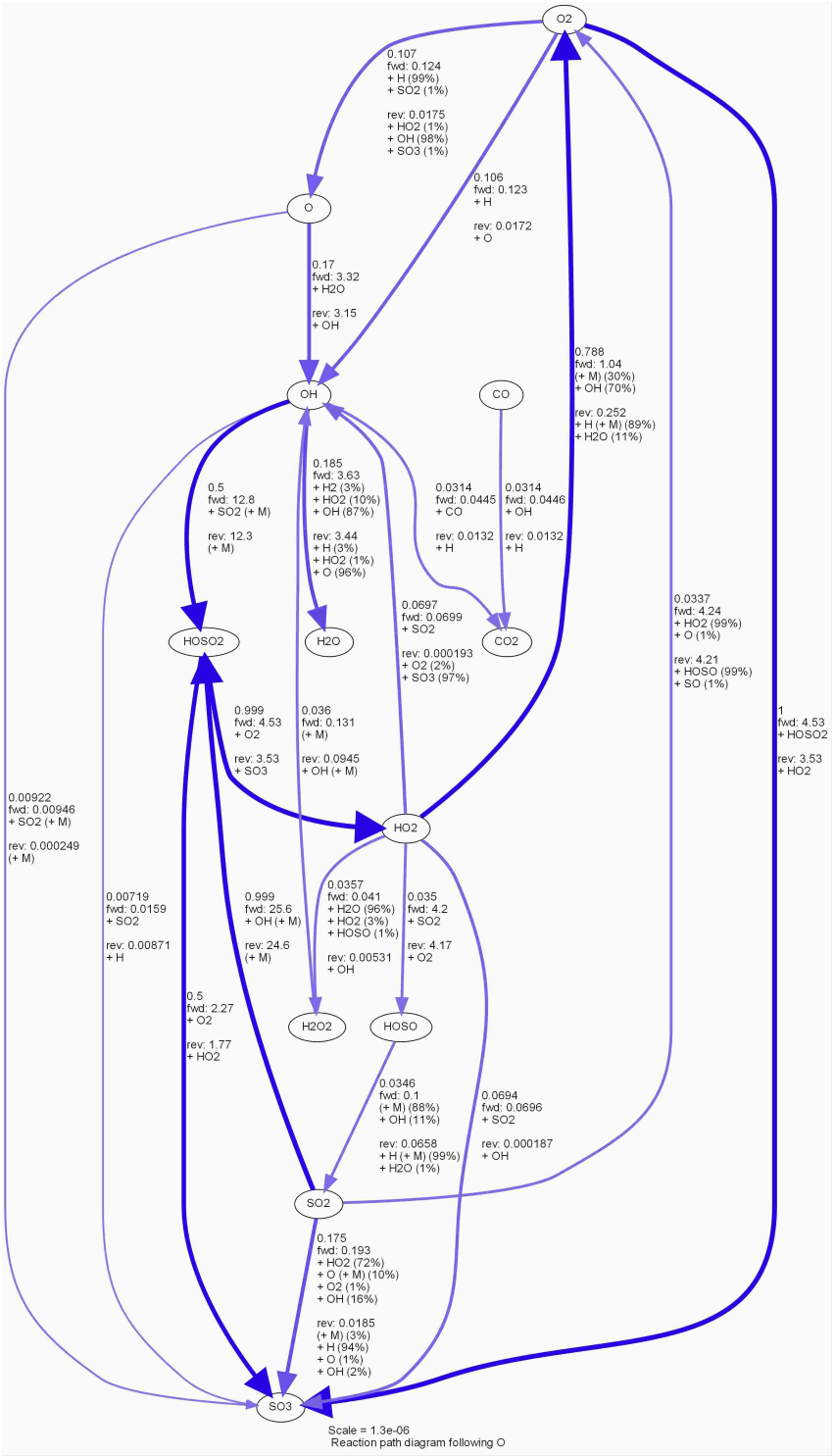

Figure S4: Reaction paths for O-species, MS II, t=0.3s, T=1168K. The arrow size indicates the respective rate. The arrow labels contain the exact rate (relative to the 'scale' value at the bottom in $\mathrm{kmol\,m^{-3}\,s^{-1}}$) and specify the relative contribution of individual reaction paths in forward ('fwd') and reverse ('rev') direction.

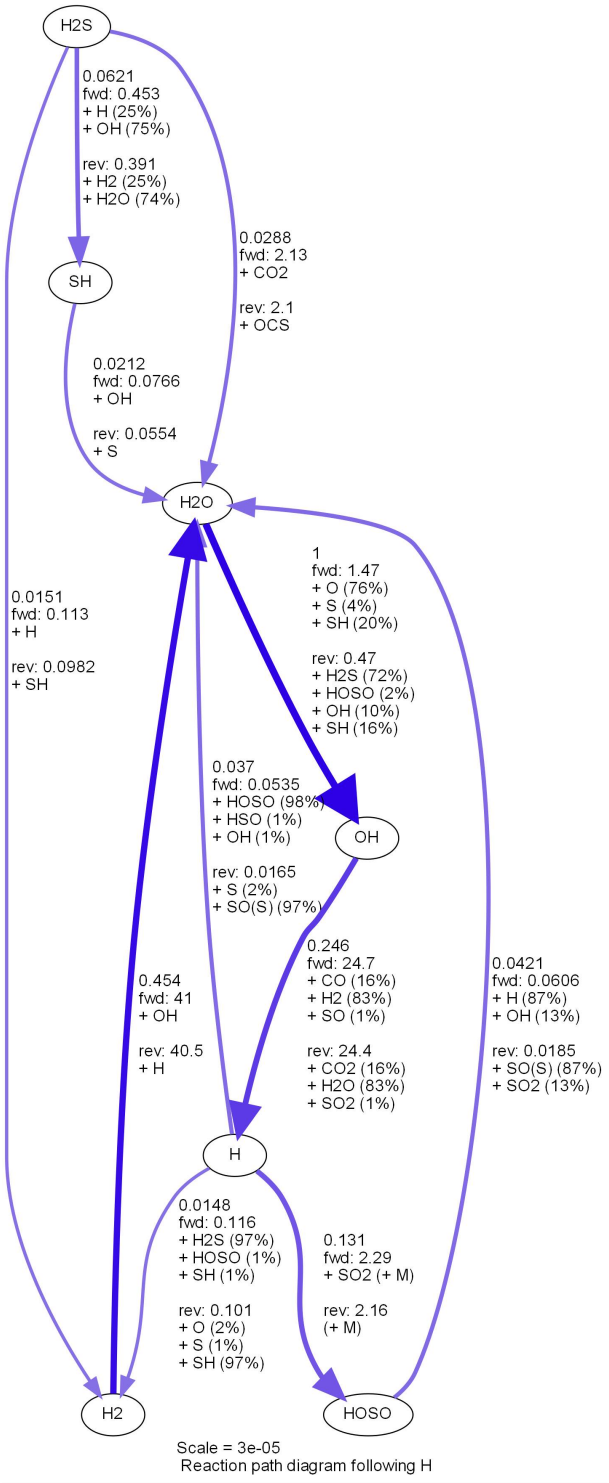

Figure S5: Reaction paths for H-species, MS II, t=0.001s, T=1370K. The arrow size indicates the respective rate. The arrow labels contain the exact rate (relative to the 'scale' value at the bottom in $\mathrm{kmol\,m^{-3}\,s^{-1}}$) and specify the relative contribution of individual reaction paths in forward ('fwd') and reverse ('rev') direction.

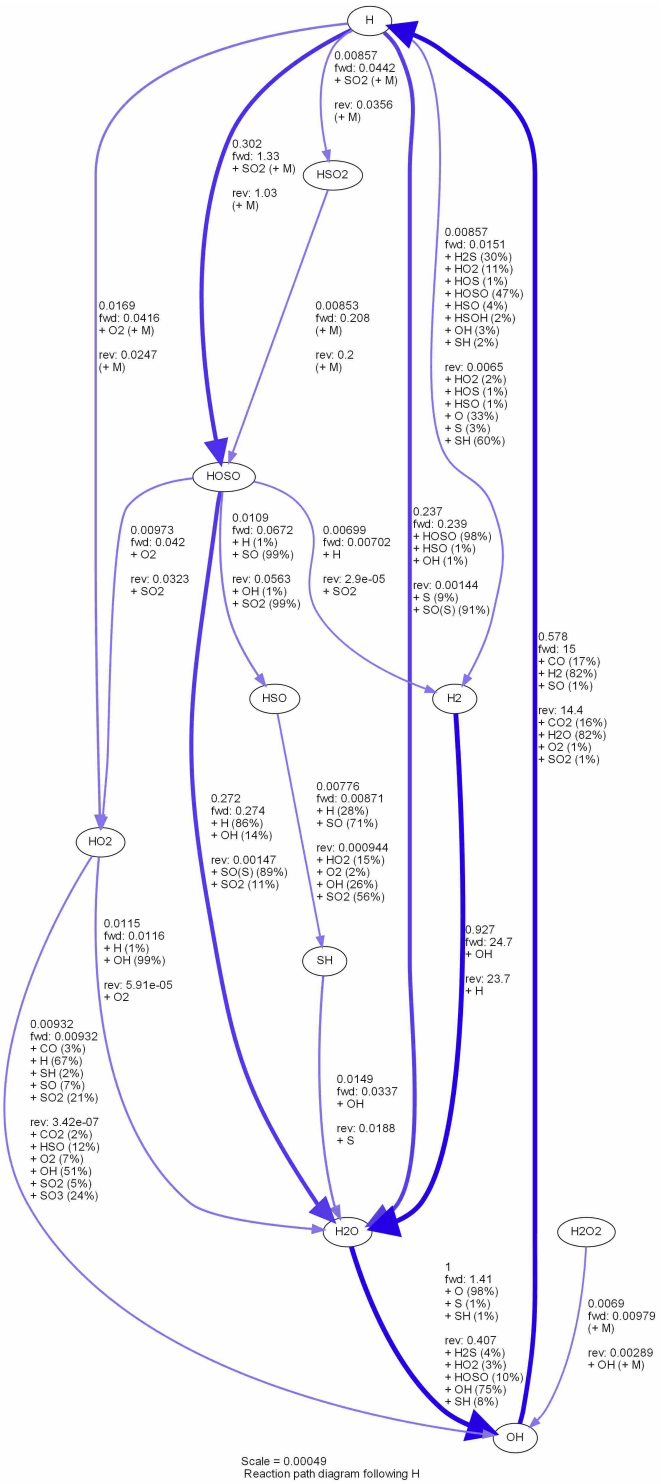

Figure S6: Reaction paths for H-species, MS II, t=0.01s, T=1370K. The arrow size indicates the respective rate. The arrow labels contain the exact rate (relative to the 'scale' value at the bottom in $\mathrm{kmol\,m^{-3}\,s^{-1}}$) and specify the relative contribution of individual reaction paths in forward ('fwd') and reverse ('rev') direction.

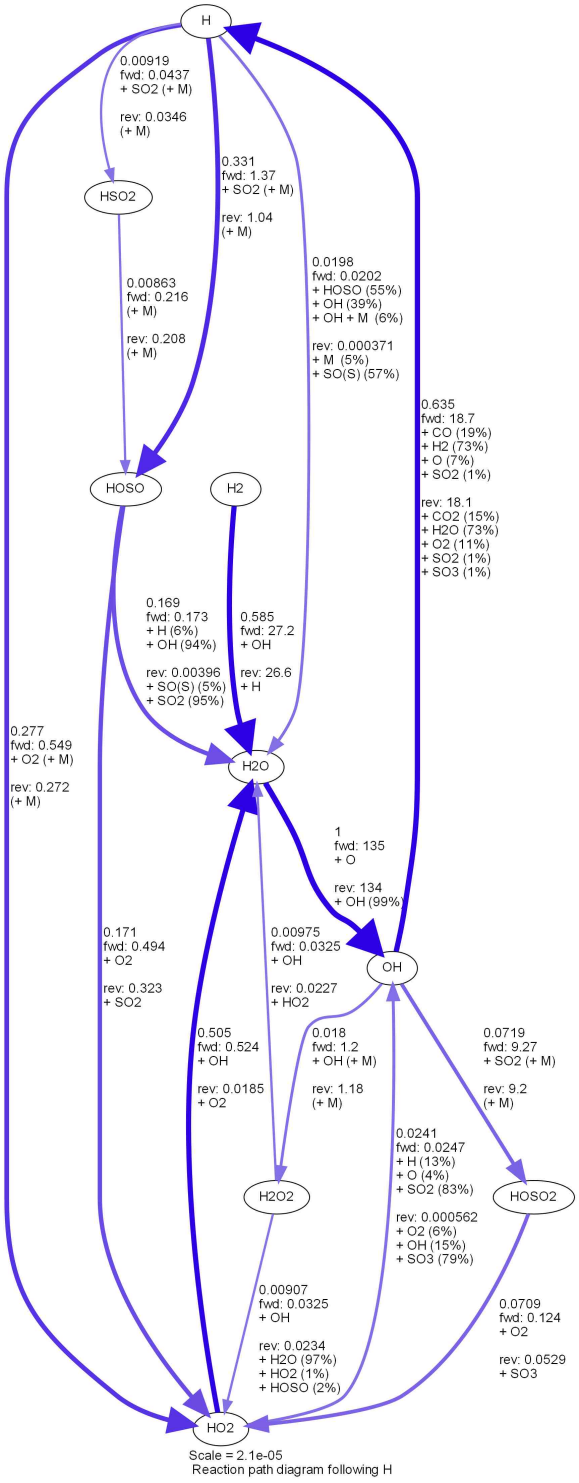

Figure S7: Reaction paths for H-species, MS II, t=0.1s, T=1379K. The arrow size indicates the respective rate. The arrow labels contain the exact rate (relative to the 'scale' value at the bottom in $\mathrm{kmol\,m^{-3}\,s^{-1}}$) and specify the relative contribution of individual reaction paths in forward ('fwd') and reverse ('rev') direction.

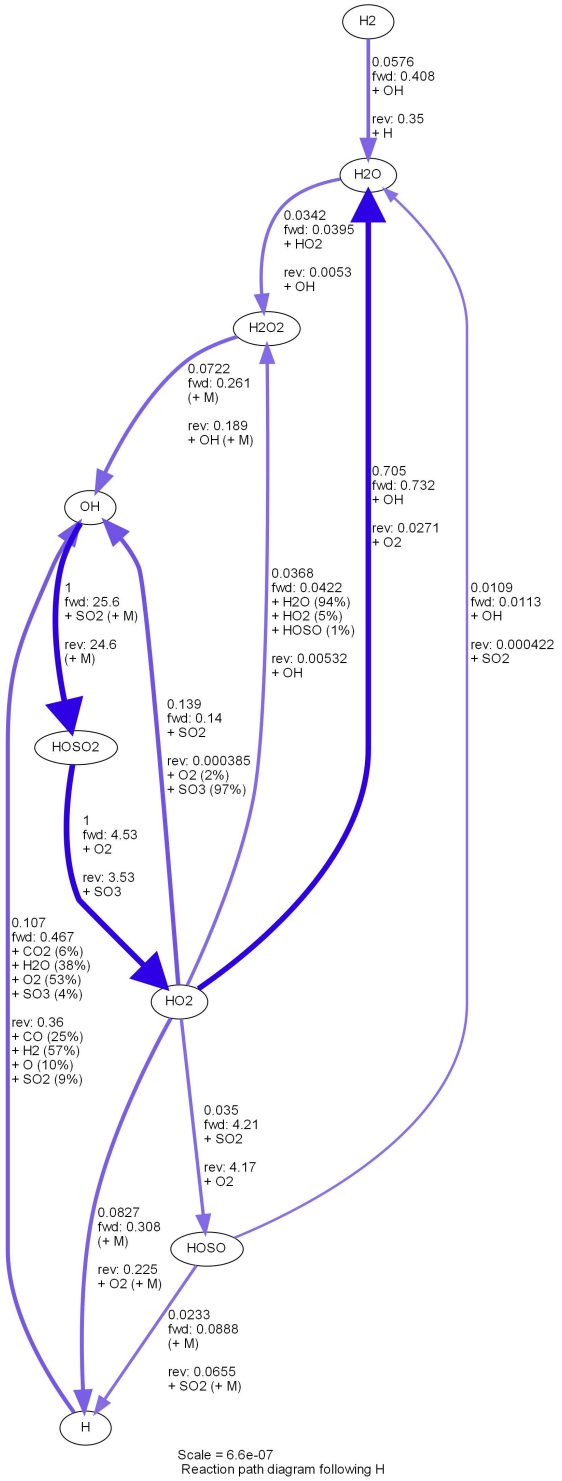

Figure S8: Reaction paths for H-species, MS II, t=0.3s, T=1168K. The arrow size indicates the respective rate. The arrow labels contain the exact rate (relative to the 'scale' value at the bottom in $\mathrm{kmol\,m^{-3}\,s^{-1}}$) and specify the relative contribution of individual reaction paths in forward ('fwd') and reverse ('rev') direction.

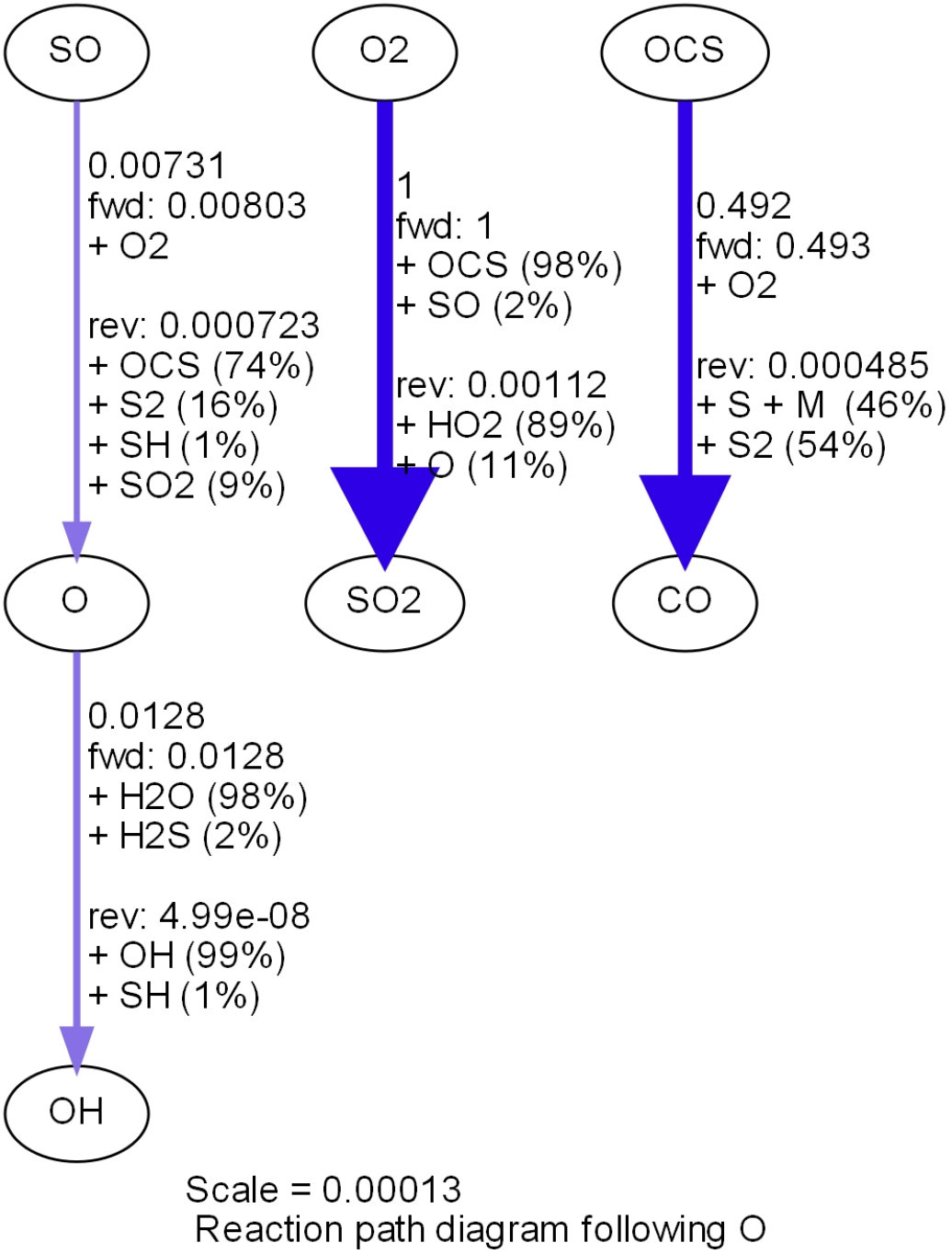

Figure S9: Reaction paths for O-species, MS II, t=0.001s, T=1070K. The arrow size indicates the respective rate. The arrow labels contain the exact rate (relative to the 'scale' value at the bottom in $\mathrm{kmol\,m^{-3}\,s^{-1}}$) and specify the relative contribution of individual reaction paths in forward ('fwd') and reverse ('rev') direction.

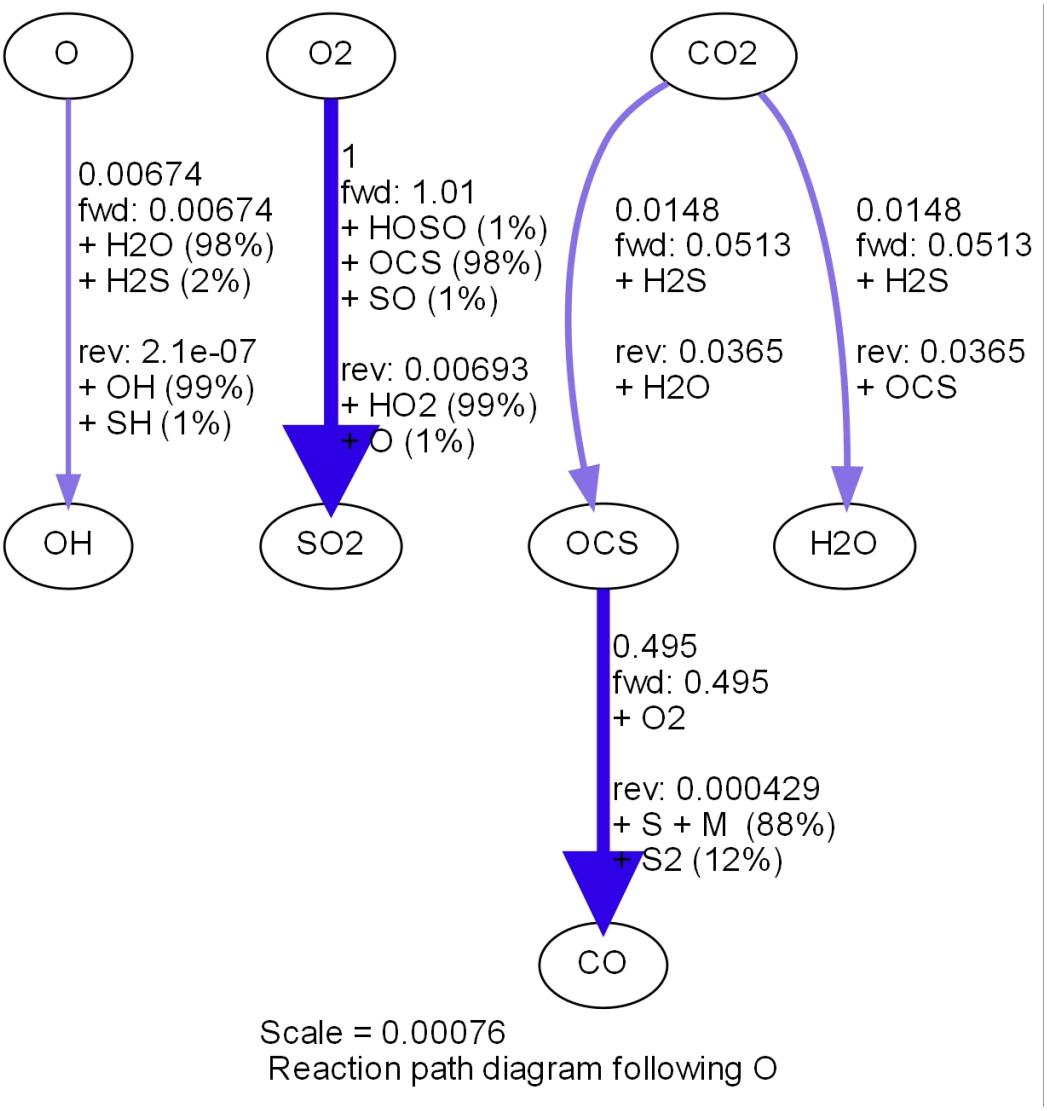

Figure S10: Reaction paths for O-species, MS II, t=0.01s, T=1071K. The arrow size indicates the respective rate. The arrow labels contain the exact rate (relative to the 'scale' value at the bottom in $\mathrm{kmol\,m^{-3}\,s^{-1}}$) and specify the relative contribution of individual reaction paths in forward ('fwd') and reverse ('rev') direction.

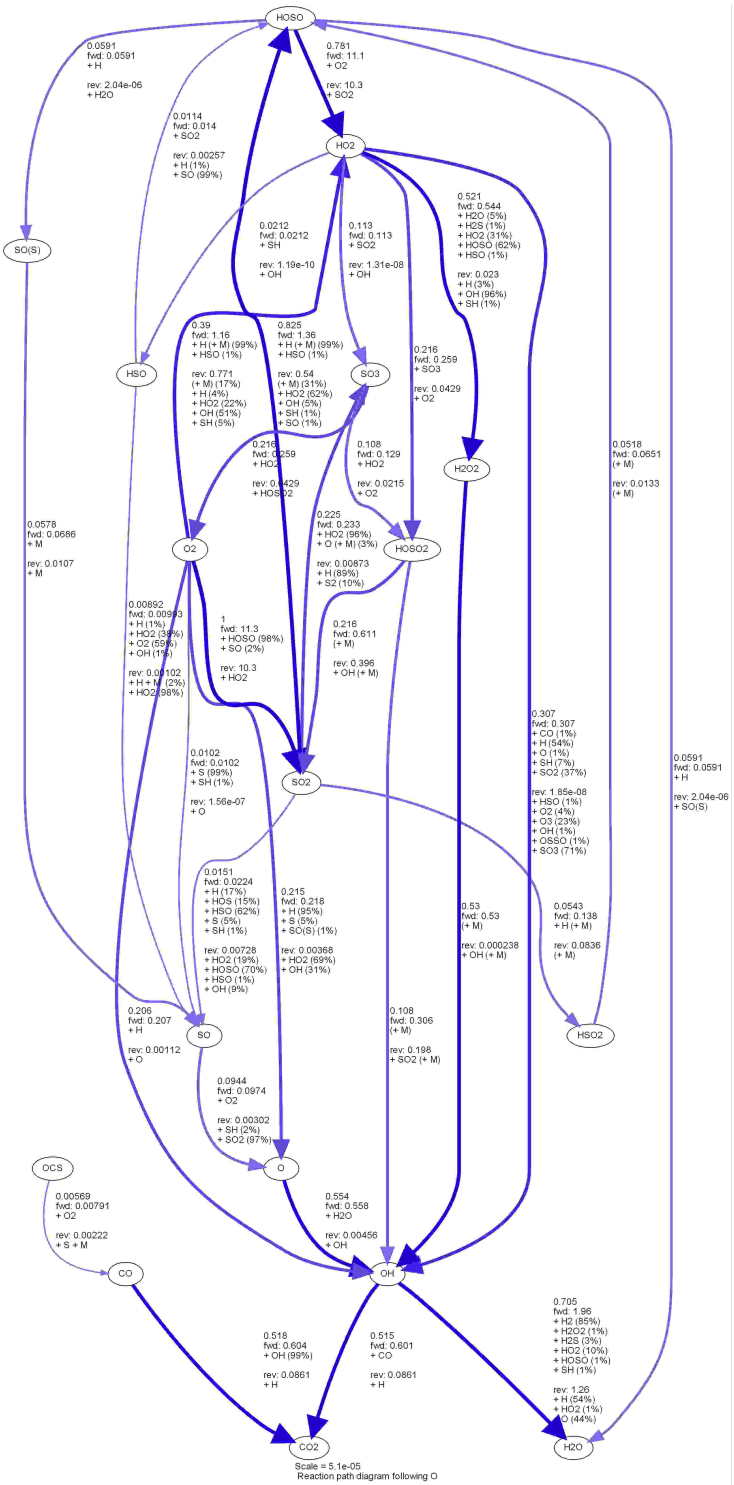

Figure S11: Reaction paths for O-species, MS II, t=0.1s, T=1063K. The arrow size indicates the respective rate. The arrow labels contain the exact rate (relative to the 'scale' value at the bottom in $\mathrm{kmol\,m^{-3}\,s^{-1}}$) and specify the relative contribution of individual reaction paths in forward ('fwd') and reverse ('rev') direction.

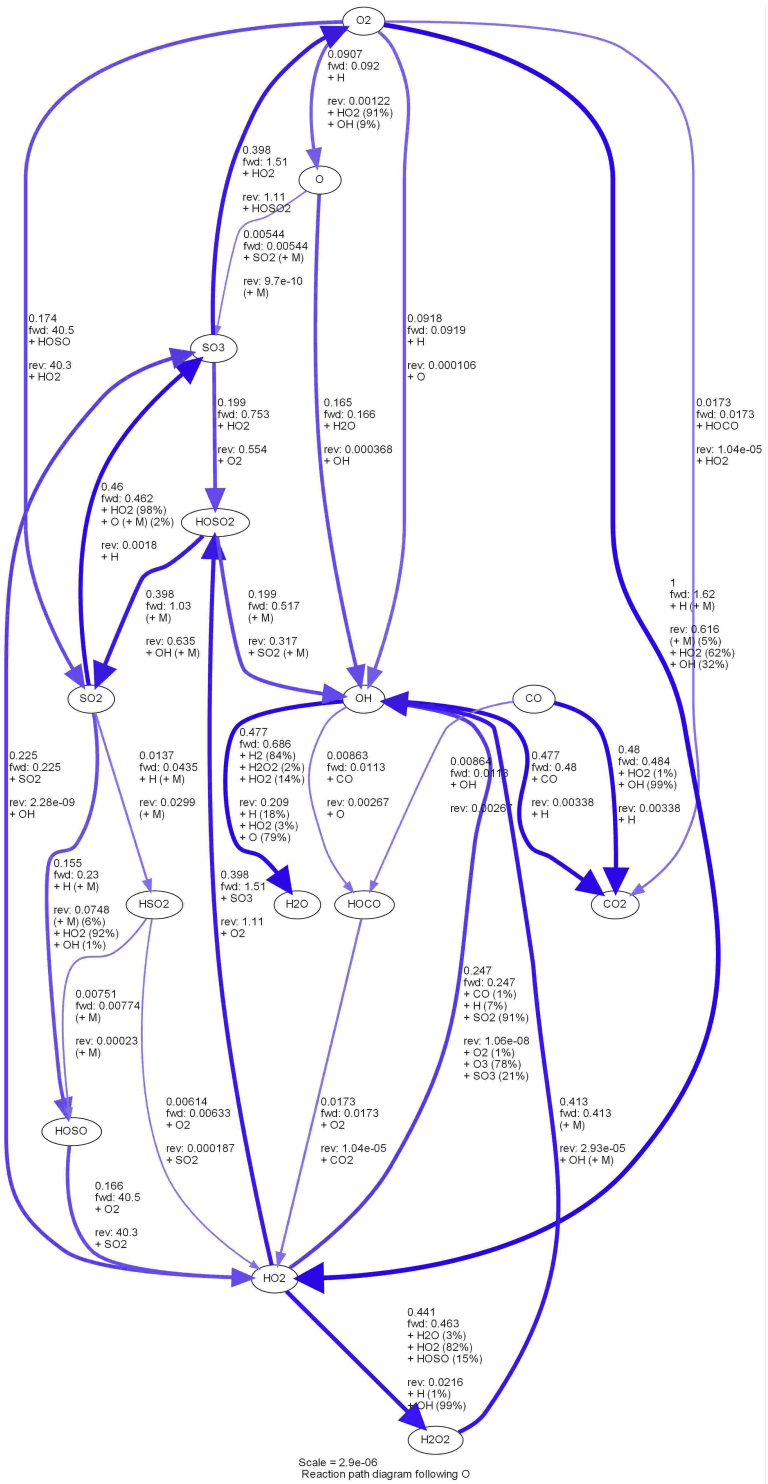

Figure S12: Reaction paths for O-species, MS II, t=0.3s, T=928K. The arrow size indicates the respective rate. The arrow labels contain the exact rate (relative to the 'scale' value at the bottom in $\mathrm{kmol\,m^{-3}\,s^{-1}}$) and specify the relative contribution of individual reaction paths in forward ('fwd') and reverse ('rev') direction.

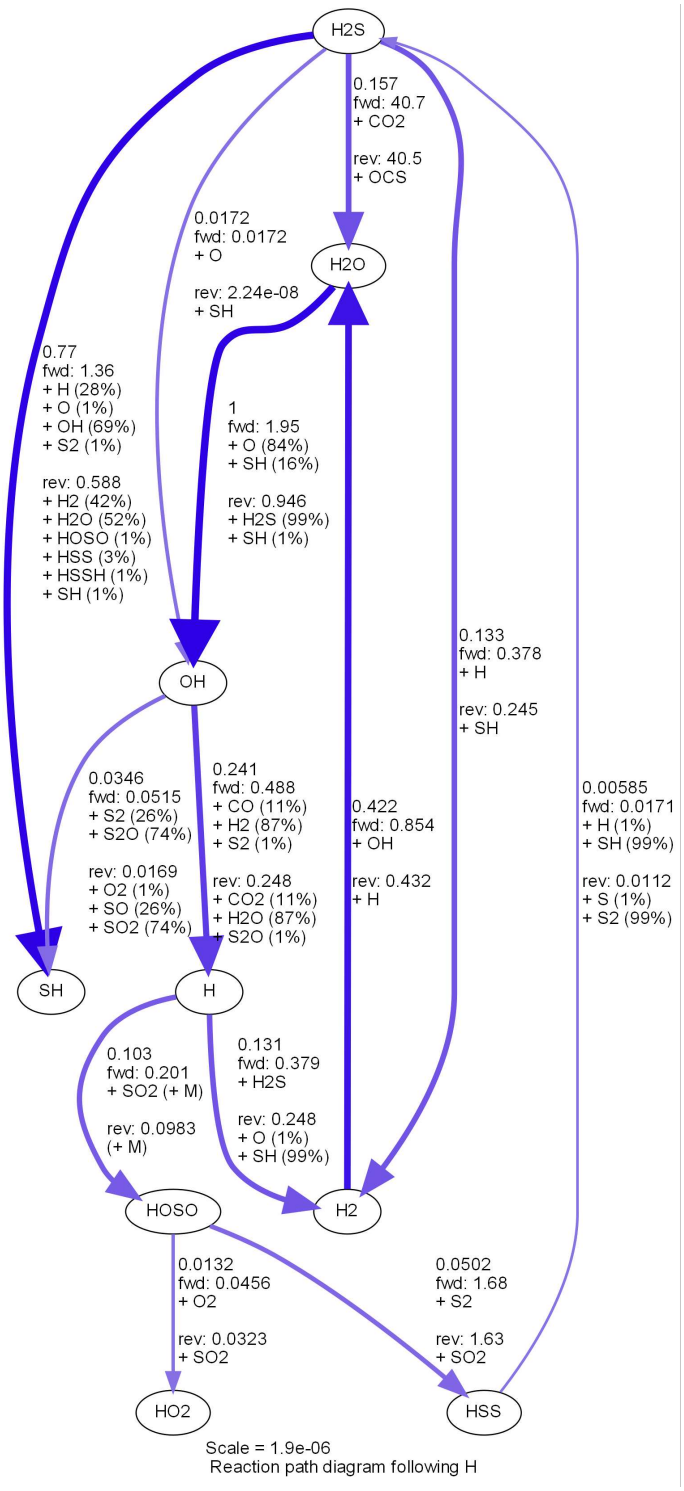

Figure S13: Reaction paths for H-species, MS II, t=0.001s, T=1070K. The arrow size indicates the respective rate. The arrow labels contain the exact rate (relative to the 'scale' value at the bottom in $\mathrm{kmol\,m^{-3}\,s^{-1}}$) and specify the relative contribution of individual reaction paths in forward ('fwd') and reverse ('rev') direction.

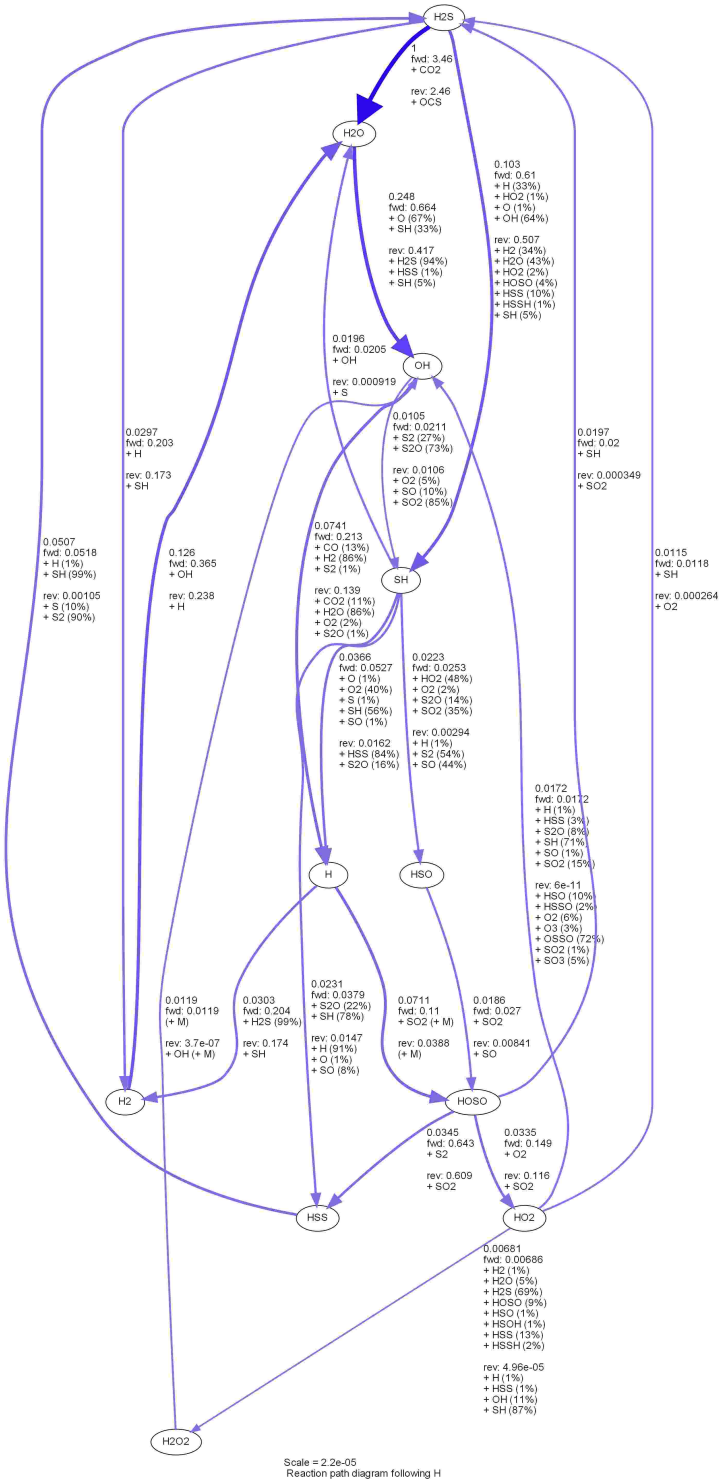

Figure S14: Reaction paths for H-species, MS II, t=0.01s, T=1071K. The arrow size indicates the respective rate. The arrow labels contain the exact rate (relative to the 'scale' value at the bottom in $\mathrm{kmol\,m^{-3}\,s^{-1}}$) and specify the relative contribution of individual reaction paths in forward ('fwd') and reverse ('rev') direction.

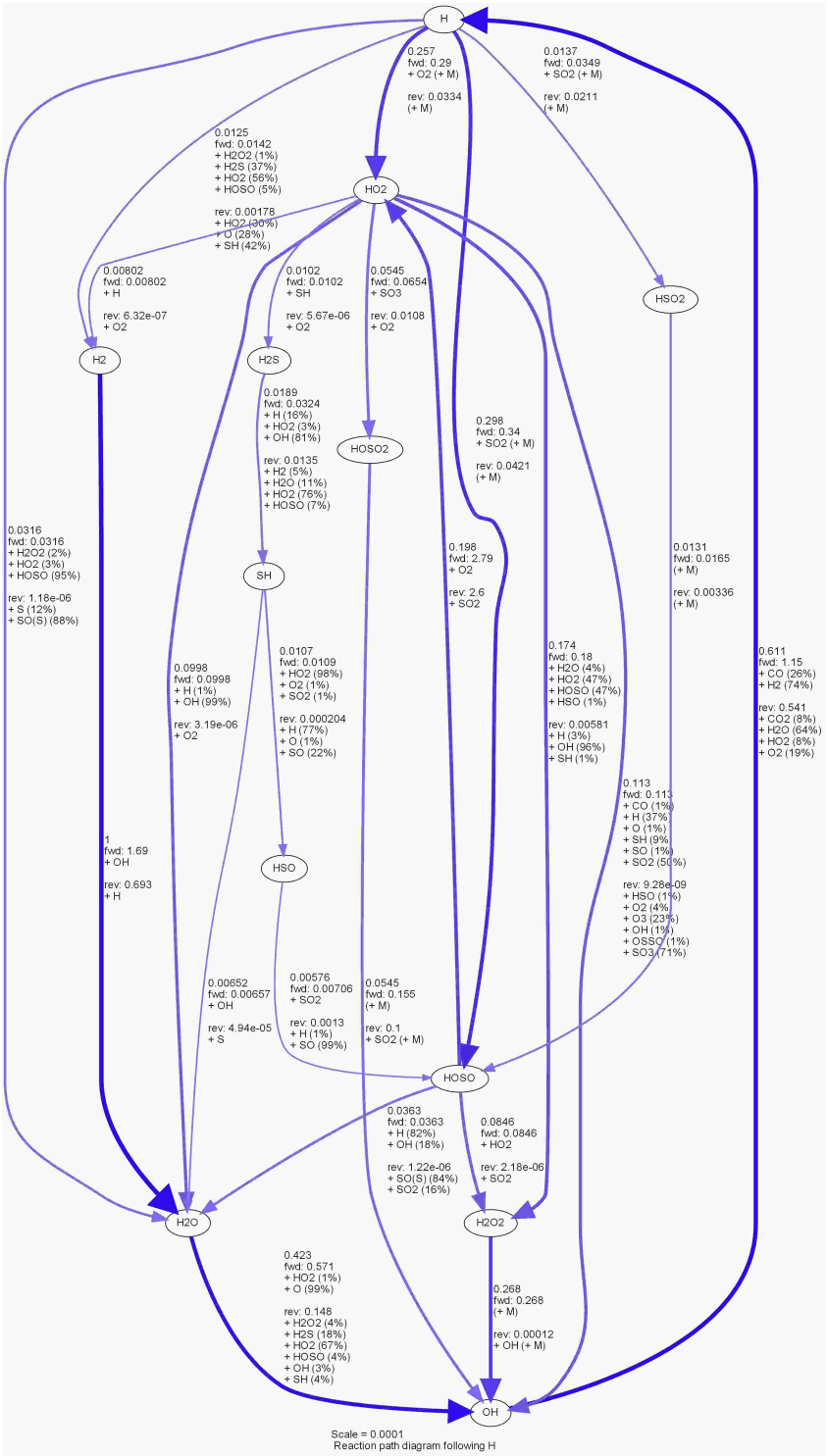

Figure S15: Reaction paths for H-species, MS II, t=0.1s, T=1063K. The arrow size indicates the respective rate. The arrow labels contain the exact rate (relative to the 'scale' value at the bottom in $\mathrm{kmol\,m^{-3}\,s^{-1}}$) and specify the relative contribution of individual reaction paths in forward ('fwd') and reverse ('rev') direction.

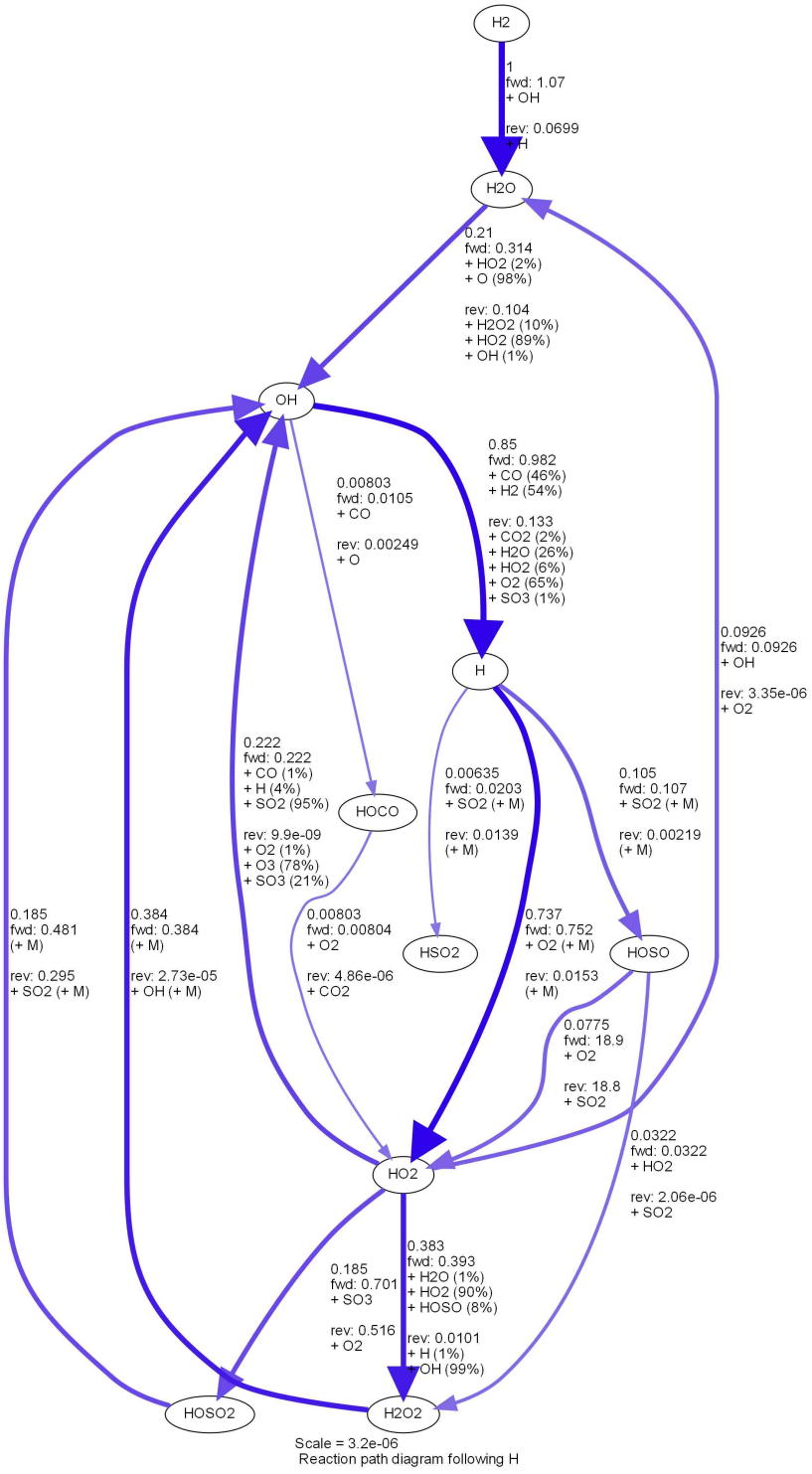

Figure S16: Reaction paths for H-species, MS II, t=0.3s, T=928K. The arrow size indicates the respective rate. The arrow labels contain the exact rate (relative to the 'scale' value at the bottom in $\mathrm{kmol\,m^{-3}\,s^{-1}}$) and specify the relative contribution of individual reaction paths in forward ('fwd') and reverse ('rev') direction.

3 Discussion

The results of this thesis have major implications for volcanic gas measurements and their interpretation. Beyond that, each study exhibits a considerable relevance for other scientific fields, particularly for atmospheric sciences.

3.1 Imaging trace gases in the atmosphere with FPI correlation spectroscopy

Kuhn et al. (2019) and Fuchs et al. (2021) document the development of IFPICS, a novel trace gas imaging technique in the UV spectral range (proposed by Kuhn et al., 2014). It largely combines the advantages of DOAS and SO_2 cameras (see Tab. 3.1), the two techniques that are mainly used for volcanic trace gas remote sensing in these days. Accurate and sensitive trace gas detection is provided through matching the spectral transmission structure of a FPI to the absorption spectra of the target trace gas. The high light throughput of the FPI and its image-conserving properties enable straight-forward parallelisation of the measurement and thus, high spatio-temporal resolution.
Within the scope of this thesis, IFPICS instruments were implemented from scratch and successful first SO_2 measurements were performed at Mt. Etna. The SO_2 detection limit determined in the field measurements (Fuchs et al., 2021) is in excellent accordance with the theoretical predictions by Kuhn et al. (2019). Moreover, it is demonstrated that simplistic instrument models enable an inherent calibration of the technique, i.e. using trace gas absorption data from the literature (similar to the DOAS technique). Subsequent studies extending the technique to BrO measurements are in progress with promising results (see Nies, 2021).

3.1.1 Significance for volcanic gas studies

Volcanic volatile fluxes

The measurement of the emission flux of volcanic gases is important for volatile budgets to constrain global chemical cycles. Furthermore, temporally resolved volatile flux analysis provides information on shallow magmatic processes and is used as a volcanic monitoring parameter. Volcanic SO_2 flux measurements are preferred due to the high contrast between plume abundance and the low atmospheric background, and the availability of mobile remote sensing devices. These fluxes are typically used to determine the emission flux of other plume constituents by scaling in-plume point measurements (e.g. Aiuppa et al., 2011; Carn et al., 2017).
For more than a decade, volcanic SO_2 fluxes are measured routinely with the DOAS technique. The volcanic emission plume is either traversed, for instance by car with an upward-looking telescope (e.g. Kern et al., 2020), or scanned spatially by a motorized tiltable tele-

Table 3.1: Summarised comparison of IFPICS (theoretical study and proof-of-concept field measurements) with conventional UV remote sensing techniques used at volcanoes

technique	gases	detection scheme	accuracy	spatio-temp. resolution (10^{17} molec cm^{-2} SO_2)
former studies				
DOAS	SO_2, BrO, OClO, ...	full spectrum $\delta\lambda \approx 1$ nm	high	ca. 1 pixel s^{-1}
SO_2 camera	SO_2	two wavelength $\delta\lambda \approx 10$ nm	low	ca. 10^6 pixel s^{-1}
this study: IFPICS (Kuhn et al., 2019; Fuchs, 2019)				
theoretical	SO_2, BrO, OClO, ...	matched FPI $\delta\lambda \approx 1$ nm	high	ca. $5 \cdot 10^4$ pixel s^{-1}
proof-of-concept	SO_2	matched FPI $\delta\lambda \approx 1$ nm	high	ca. $4 \cdot 10^4$ pixel s^{-1}

scope (e.g. Galle et al., 2010). Geometrical considerations allow a straight-forward determination of the SO_2 emission flux. These measurements, however, typically require at least several minutes for a full spatial coverage of the plume. Changing atmospheric conditions (e.g. wind direction) or variations in the volcanic SO_2 on that time scale can substantially distort the measured emission rates. The major uncertainty, however, is in most cases related to the absolute wind (or plume propagation) speed, required for the flux calculation. The SO_2 camera to a certain extent overcomes these complications by drastically increasing the spatio-temporal resolution, literally recording videos of the plume's SO_2 distribution. The flux determination becomes much more accurate by retrieving the plume's propagation speed from the resolved turbulent transport features. The drawback, however, is the coarse spectral detection scheme (based on the use of two band-pass-filters). The applicability of SO_2 cameras is thereby limited to strong SO_2 emitters with low aerosol in the plume and require frequent calibration (e.g. Lübcke et al., 2013). Moreover, their limitation to clear-sky conditions renders them useless at volcanic sites with nearly permanent cloud cover (e.g. close to the equator).
The IFPICS technique largely resolves the issues of DOAS and SO_2 cameras regarding volcanic emission flux determination by providing both fast and accurate measurements. High-temporal-resolution volcanic gas emission fluxes can be determined also at weaker emitters and in an vastly extended range of atmospheric conditions.

Gradients of reactive plume constituents

Despite being a secondary plume species, BrO can be representative for the emitted amount of volcanic bromine. Remote sensing of volcanic BrO from space and ground-based platforms provides unique, continuous, and global gas data records with a high potential for volcanic emission studies, including monitoring, global distributions, and many more. However, the underlying processes of BrO formation need to be reasonably constrained in order to separate volcanic signals from those induced by chemistry.
Reactive bromine chemistry within volcanic plumes remains a debated topic. In particular, decisive processes within the first minutes of the plume's evolution are not well understood. These include the initiation of the chemical cycles and the building up of BrO levels until a more or less stable steady-state plateau is reached (e.g. Bobrowski and Giuffrida,

2012; Roberts et al., 2014). Besides in-situ measurements of the bromine speciation (e.g. Rüdiger et al., 2018; Gutmann et al., 2018), the measurement of BrO gradients within the early plume with high spatio-temporal resolution could deliver vital boundary conditions for the yet poorly constrained models. Former approaches using line-scanning imaging DOAS schemes (e.g. Louban et al., 2009) were limited by the GS's light throughput and thus, poor temporal resolution.
The IFPICS technique has the potential to measure BrO gradients within volcanic plumes with high spatio-temporal resolution. Thereby it may significantly contribute to the further understanding of reactive halogen chemistry in volcanic plumes and the profound interpretation of volcanic BrO records.

3.1.2 Significance for other fields

In principle, the IFPICS technique can be adapted to many trace gases that absorb in the UV and visible spectral range and allows the quantification of smaller scale gradients thereof. The application of IFPICS to the detection of BrO, OClO or IO gradients may help to constrain reactive halogen chemistry within other tropospheric environments, such as polar regions or salt deserts (Platt and Hönninger, 2003). The application to NO_2 was assessed in Kuhn et al. (2019) and showed that IFPICS can be used to image NO_2 stack emissions with high resolution and to study the related chemical processes. Thereby, IFPICS could again offer a compromise between existing techniques, which are either accurate or fast (see e.g. Dekemper et al., 2016; Manago et al., 2018; Kuhn et al., 2022b).
During the adaption of the IFPICS technique to BrO it turned out useful to exploit partial spectral correlation of the BrO and formaldehyde (HCHO) absorption cross sections. In contrast to the highly reactive BrO, HCHO can easily be filled into glass cells for characterisation measurements in the laboratory (Fuchs, 2019; Nies, 2021). The study of highly resolved gradients of HCHO for instance within biomass burning emission plumes (e.g. Holzinger et al., 1999) is one among many examples where a drastic increase of spatio-temporal resolution of conventional atmospheric observations may be beneficial.

3.2 Mobile FPI spectrographs with high spectral resolution and high light throughput

Kuhn et al. (2021) investigate the use of FPI spectrographs in atmospheric remote sensing. The results show that with nowadays available technology, FPI spectrographs can outperform GSs by orders of magnitude in many respects with high relevance for atmospheric research. It is known for a long time that FPIs have much higher light throughput than GSs for high resolving powers (e.g. Jacquinot, 1954). The light throughput fundamentally limits a large range of atmospheric remote sensing observations, particularly passive measurements (i.e. with scattered or reflected sunlight as light source, see e.g. Platt et al., 2021). FPI spectrographs combine high spectral resolution with high light throughput and high mobility, which are key properties determining the feasibility of a volcanic (or atmospheric) observation with a passive remote sensing technique. In principle, they allow spectral detection schemes with the intrinsic spectral resolution of molecular absorption at atmospheric conditions, that is about the width of a single rovibronic absorption line (some picometres in the UV). Compared to e.g. DOAS measurements in the UV and visible spectral range, this leads to enhanced sensitivity and selectivity of the detection, and might render the need for a reference spectrum unnecessary. On top of that, the amount of routinely measurable

Table 3.2: Selection of high resolution atmospheric observations in the UV and visible

reference	measurement	instr.	light source	$\frac{\lambda}{\delta\lambda}$	mobility
selection of former studies					
Dorn et al. (1996)	trop. OH	GS	broad-band laser	$1.8 \cdot 10^5$	low
Burnett and Burnett (1981)	tot. columm OH	FPI	direct sun	$1.5 \cdot 10^6$	low
Pfeilsticker et al. (1998)	O_2	GS	clouds	$3.9 \cdot 10^4$	low
Notholt et al. (1997)	tot. columm OH	FTS	direct sun	$3 \cdot 10^5$	low
this study					
Kuhn et al. (2021) (theoretical study)	trop. OH	FPI	LED / sky light	$3 \cdot 10^5$	high
proof-of-concept (App. A)	volc. OH	FPI	LED	$3 \cdot 10^5$	high

species may increase and enable the study of so far inaccessible processes.
Table 3.2 shows a selection of former studies that performed high spectral resolution remote sensing measurements in the atmosphere. They share the common feature of very low mobility, i.e. the instrumentation is either bulky and heavy (e.g. GS with 1.5m focal length in Dorn et al., 1996; Pfeilsticker et al., 1998), touchy (Burnett and Burnett, 1981) or involves mechanical scanning schemes (Notholt et al., 1997). This in combination with their low light throughput (relying on bright light sources) restricted their application to few, stationary, and cost-intensive studies at particular atmospheric conditions.
In order to validate the mostly theoretical considerations of Kuhn et al. (2021), Appendix A describes measurements of a first FPI spectrograph prototype performed in Feb. 2020 within the crater of Nyiragongo volcano in the Democratic Republic of Congo. The data confirms the high spectral resolution and high stability and shows excellent agreement between measured spectra and an instrument model. The whole instrumental set-up can be carried by one person descending and ascending the, at that time, 300 m high inner crater walls of Nyiragongo. The following subsections list a selection of potentially influential applications of FPI spectrographs.

3.2.1 Significance for volcanic gas studies

Study of the magma-atmosphere interface at open lava lakes

The high spectral resolution reached by FPI spectrographs enables the detection of the strong and distinct OH absorption lines at around 310 nm (see also Fig. 1.5c). The high light throughput and mobility of the set-up allows their use at volcanic sites (as shown in Appendix A). Models of the high temperature interface between magma and the atmosphere predict very high OH levels (up to several 10 ppm, e.g. Gerlach, 2004; Martin et al., 2012). Furthermore, this thesis shows that the presence of OH within hot magmatic gases that mix with the atmosphere is tightly linked to significant chemical conversion of many plume constituents within split seconds (Kuhn et al., 2022a). A detailed understanding of these high temperature processes is vital for many volcanic gas studies can only be gained by further constraining the boundary conditions of model calculations by improved field observations. The detection and quantification of OH in hot volcanic gases would be a

Table 3.3: Transferring the findings of Kuhn et al. (2021) towards the IR: Example for CO_2 detection at 1600 nm with a precision of $400^{-1} = 2.5 \cdot 10^{-3}$, that is about 1 ppm enhancement with respect to the atmospheric background and required for volcanic plume CO_2 measurements (e.g. Butz et al., 2017). The brightness of the sky is assumed to drop according to Rayleigh scattering efficiency (λ^{-4}). It is assumed that skylight radiance enhancement by aerosol scattering roughly balances the relatively lower sunlight radiance at 1600 nm. DOAS RMS according to Lauster et al. (2021); δt: exposure time.

wavelength	instrument $\frac{\lambda}{\delta\lambda}$	δt	RMS noise of the spectrum	detected photons per spectral channel
400 nm	GS 600 (DOAS)	30 s	10^{-4}	10^{8}
1600 nm	GS 600	30 s	$2 \cdot 10^{-3}$	$4 \cdot 10^{5}$
1600 nm	FPI 150000	30 s	$2 \cdot 10^{-2}$	$4 \cdot 10^{3}$
1600 nm	FPI 150000	1200 s	$2.5 \cdot 10^{-3}$	$1.6 \cdot 10^{5}$

great step in that direction.
Besides its detection, the high resolution measurement of the OH absorption and the temperature sensitivity of the absorption cross section might provide direct information of the gas temperature at emission. This temperature is still only coarsely known, although being a central component of many studies (e.g. Oppenheimer et al., 2018b).
Besides the detection of OH, FPI spectrographs may also allow the detection of other gases within high temperature gas mixtures. For instance, models also predict high amounts of the sulfanyl radical SH (hundreds of ppb, see Kuhn et al., 2022a), which, just as OH, exhibits narrow and strong absorption lines in the UV (Lewis and White, 1939; Porter, 1950). In order to approach the high temperature degassing processes, FPI spectrographs can be operated with light emitting diodes (LEDs) and respective optical setups (see Appendix A). Moreover, when further optimised with respect to light throughput, even measurements with sunlight reflected at the lava surface could be possible.

Remote sensing of isotopologues within the volcanic plume

A more detailed spectral analysis of volcanic SO_2 in the plume is possible with higher spectral resolution. FPI spectrographs may not only increase the sensitivity and accuracy of SO_2 measurements, but also allow for the separation of the heavier $^{34}SO_2$ isotopologue of SO_2. The absorption cross sections differ mainly by a sub-nm shift (Danielache et al., 2008). $^{34}SO_2$ can make up about 1 % of the SO_2 amount (e.g. Oppenheimer et al., 2014), however it is likely to be influenced by fractionation processes during sampling with conventional techniques (Mather et al., 2008). Remote sensing excludes such fractionation processes and could deliver valuable records for the further understanding of sulphur (or other) isotopes in the context of volcanic degassing.

Remote sensing of further plume constituents at longer wavelengths

Table 3.3 shows a brief calculation that extrapolates the findings of Kuhn et al. (2021) towards IR wavelengths. It aims at inferring the feasibility of high resolution measurements of CO_2 at 1600 nm (Rothman et al., 2013) using scattered sunlight. The basis of this approximation is the conservative assumption that the brightness of the sky decreases according to the efficiency of Rayleigh scattering (i.e. proportional to λ^{-4} Strutt, 1871). In reality the sky brightness in the near IR is governed by the atmospheric aerosol levels.

Here, in this coarse assessment it is assumed that the radiance gain induced by aerosol compared to the clear-sky (Rayleigh) case at least balances the – with respect to 400 nm – reduced incoming sunlight radiance at 1600 nm (by factor of ca. 7). Starting from the noise of typical miniature GS DOAS measurements at around 400 nm (see Lauster et al., 2021) the formalism introduced in Kuhn et al. (2021) is used to infer a photon budget for the IR application of FPI spectrographs. Remote sensing of CO_2 in Earth's atmosphere is challenging due to the high atmospheric background levels of about 400 ppm. In order to quantify the amount of CO_2 within the plume of a stronger volcanic emitter an effective enhancement of about 1 ppm on top of the background needs to be resolved (see Butz et al., 2017). For an appropriate choice of CO_2 absorption lines with the right strengths (e.g. $\tau \approx 0.5$), the relative noise of the spectrum needs to be as small as $400^{-1} = 2.5 \cdot 10^{-3}$. This is achieved by a high resolution ($R = 150000$) FPI spectrograph within 20 minutes exposure time. While this is already acceptable, the exposure time is likely to be much shorter for higher atmospheric aerosol levels or cloudy skies.
Measurements of other plume species, such as HF, HCl, or CO at similar wavelengths are much easier, because they show strong absorption (typ. HF optical densities of volcanic plumes are in the range of some 10^{-2}, Rothman et al., 2013; Butz et al., 2017) and a low atmospheric background. In addition to the high value of the remote quantification of e.g. volcanic HF to HCl ratios, halogen halides can serve as plume tracers for the more challenging CO_2 quantification.
Besides providing a much higher flexibility through using skylight (instead of direct sunlight) as a light source, FPI spectrographs are far more compact, stable, and cost-efficient than FTS instruments and yield about the 10-fold spectral resolution (compare e.g. Butz et al., 2017). Continuous records of in-plume gas ratios are highly relevant for volcanic monitoring and the study of of shallow processes within the volcanic interior (e.g. Aiuppa et al., 2007b; Lübcke et al., 2014). Remote sensing may simplify the monitoring by reducing infrastructure and maintenance requirements and extend the records to include eruptive volcanic phases, which are typically not captured by in-situ plume sampling methods.

3.2.2 Significance for other fields

Quantification of tropospheric OH levels

Besides its relevance for volcanic gas studies, OH initiates the atmospheric removal of many trace gases, including air pollutants and important greenhouse gases like methane (e.g. Crutzen, 1974). Its high reactivity leads to very low atmospheric OH concentrations, which remain challenging to measure, even with the most intricate detection schemes (see Stone et al., 2012, and references therein). Nowadays, OH levels are also inferred from secondary observations (e.g. HCHO, see Wolfe et al., 2019), which, however, already presumes profound process understanding.
Kuhn et al. (2021) show that FPI spectrographs in principle enable scattered sunlight measurements of tropospheric OH. Alternatively, active setups composed of an LED and a FPI spectrograph (similar to that introduced in Appendix A) can be used similarly to former studies with large laser systems and bulky and heavy GSs (e.g. Dorn et al., 1996).

Improved remote sensing of greenhouse gases

Generally, FPI spectrographs can replace FTS instruments in the commonly used direct sunlight measurements of greenhouse gases (e.g. Butz et al., 2017; Knapp et al., 2021). The major issue of FTS is that the spectrum is recorded in a temporal sequence of mechanically

tuning the optical set-up. Each more abrupt variation of the incident radiance leads to distortions of the recorded spectrum. Thus, the measurements are mostly not limited by photon statistics, which makes a direct comparison of the instrument's performance difficult (e.g. Notholt et al., 1997). The above calculations (Tab. 3.3) indicating that remote sensing of CO_2 with skylight might be possible with FPI spectrographs that yield a 10-fold spectral resolution than commonly used FTS direct sunlight schemes (typ. resolving power of ca. 12000, e.g. Butz et al., 2017; Knapp et al., 2021) indicate a considerable light throughput advantage of FPI spectrographs over FTS (see also Kuhn et al., 2021). However, FPI spectrographs have a much lower spectral coverage as FTS instruments. Since they are much more compact and cost-efficient, several FPI spectrographs covering relevant wavelength windows can be operated in parallel without increasing cost or instrument size. Thus, the use of FPI spectrographs may considerably enhance the data quality of state-of-the-art greenhouse gas measurements and furthermore drastically extend the range of greenhouse gas measurements by the scattered sunlight applications.

Improved remote sensing of solar induced fluorescence of plants

The photosynthesis activity of plants is linked to their ability to fluoresce in the far red spectral range. This modifies the structured spectra of sunlight (in-filling of Fraunhofer lines), which is reflected from plants and thus, enables remote sensing of plant activity (e.g. Plascyk and Gabriel, 1975; Grossmann et al., 2018) and thereby the global-scale assessment of the terrestrial carbon cycle (e.g. Frankenberg et al., 2011). The sensitivity and the accuracy of such measurements decrease when the spectral resolution is much coarser than the width of the targeted Fraunhofer lines (on the order of 10 pm). The high light throughput of high spectral resolution FPI spectrographs may significantly improve the signal-to-noise ratio of such observations.

Radiative transfer in Earth's atmosphere

Due to the known atmospheric abundance and distribution of O_2, spectroscopic measurements of atmospheric O_2 column densities provide information on atmospheric light paths. High resolution spectroscopy of individual absorption lines of atmospheric O_2 for instance allows the study of light path distributions within clouds (see e.g. Pfeilsticker et al., 1998) and could generally improve the quality of radiative transfer observations in the atmosphere. The combination of atmospheric high resolution O_2 measurements with the routinely performed O_4 (O_2 collision complex) quantification by DOAS might significantly improve atmospheric aerosol and cloud retrievals (e.g. Wagner et al., 2007). Furthermore, it could help resolving the persistent inconsistency between modeled and measured O_4 in scattered sunlight measurements (e.g. Wagner et al., 2019).

General improvement of DOAS measurements

Increasing the spectral resolution can significantly improve the quality of DOAS measurements in the UV and visible spectral range. A much more specific spectral detection is provided and a higher sensitivity is expected for trace gases with more discrete absorption lines (e.g. H_2O and BrO, Rothman et al., 2013; Neuroth et al., 1991). Moreover, absolute (instead of differential) column densities could be retrieved from measurement spectra without the need for a reference measurement. This is because the Fraunhofer lines are resolved on their intrinsic spectral scale and could for instance be avoided in the spectral trace gas retrieval.

3.3 Novel modeling approaches for high temperature interfaces of volcanic gas emissions

The discussion of the influence of reaction kinetics within the scope of volcanic gas emissions has been avoided for a long time. Instead, almost exclusively TE terminology is used in the analysis of volcanic gas measurements.
TE calculations of mixtures of magmatic and atmospheric gases predict largely depleted H_2S or H_2 in volcanic plumes (see. e.g. Martin et al., 2006, 2012). The observation of larger amounts of these gases within volcanic plumes (e.g. Aiuppa et al., 2007a, 2011) is explained by the mere statement of their 'kinetic stability' (Martin et al., 2009). This is unsatisfactory, particularly because it is known, that at high temperature, reactions involving H_2 and O_2 are fast (e.g. Willbourn and Hinshelwood, 1946).
Roberts et al. (2019) introduce an approach to modeling the high temperature kinetic processes in early volcanic emissions. Despite analysing only a fraction of the cooling process within one specific eruptive emission scenario, they find substantial influence of reaction kinetics on the plume composition and draw respective conclusions concerning the relevance for volcanic gas measurements. However, these conclusions rely on a single model run without a more detailed analysis of the chemical processes involved.
This thesis presents a kinetic chemistry model for the first seconds after magmatic gas emission into the atmosphere. It covers the entire plume cooling process and parametrises the turbulent mixing process in a comprehensive and flexible manner. The model architecture is based on an adaptive plume cell that encompasses the processes on their relevant length scale at each time instance. Thus the model is fast and allows to investigate huge ranges of boundary conditions at once, which is vital for volcanic gas studies, since the boundary conditions are not well-constrained.
Kuhn et al. (2022a) presents a model study for an open lava lake degassing scenario. The significance of reaction kinetics is found for a large range of initial conditions (e.g. emission temperature, gas bubble size, turbulence scenario, magmatic gas composition). Moreover, effects on the plume after cooling are analysed and the resulting alterations of the gas composition are linked to the respective key chemical processes.
The result implicates major relevance for volcanic gas studies, despite the remaining uncertainties and the simplifications made by the model. For instance, a hypothetical uncertainty of two orders of magnitude (as induced e.g. by poorly constrained high temperature reaction rates for some of the involved processes) would not much alter the central conclusions of the study.

3.3.1 Significance for volcanic gas studies

The model study shows substantial alteration of the plume composition within split seconds after the emission of gas bubbles from their hosting magma. Non-linear reactive cycles quickly can drive the volcanic gas composition far from TE states, which are characterized by high amounts of intermediate species. The alterations are largely determined by the reaction rates and the timescale of plume cooling (determined e.g. by turbulence or gas bubble size). The initial emission temperature basically determines, which key chemical processes are dominant.

Volcanic gas measurements

The degassing interface at open vent volcanic systems needs to enter the discussion and interpretation of the respective gas measurements. Air contamination of samples of hot volcanic gas emissions could have a more intricate influence on the gas composition than previously assumed (e.g. by Gerlach, 1993). For instance, CO levels can be lowered by its oxidation but also enhanced by OCS oxidation (see Kuhn et al., 2022a). Furthermore, FTS measurements of the degassing lava surface encompass plume parts of different age and temperature and are likely to be significantly influenced by fast chemical conversions. The assumption that these measurements represent the unaltered magmatic gas composition (e.g. Sawyer et al., 2008; Oppenheimer et al., 2018b; Moussallam et al., 2019) requires revision.

Influence of volcanic gases on the early atmosphere

The redox state of the emitted gases has been frequently linked to that of their formerly hosting magma (e.g. Giggenbach, 1996). Vice versa, the volcanic gas composition in studies of the early Earth is inferred from melt redox states (e.g. Holland, 2002). TE between gas bubbles and their hosting magma is the central presupposition of those studies. This has recently been questioned by indications for the thermodynamic decoupling of gas bubbles from the magma through adiabatic cooling upon bubble growth (e.g. Oppenheimer et al., 2018b). Also the findings of this thesis suggest that the links between the redox state of magmas and that of the emitted gas might be much more intricate than previously assumed. Non-linear chemical conversions and also temperature influences through reaction kinetics can lead to large differences between emitted magmatic gas and the plume gas that reaches, and gradually influences the atmosphere.

Reactive halogen chemistry in volcanic plumes

The observation of e.g. BrO in volcanic plumes is assessed by models that simulate reactive halogen chemistry in diluted plumes at atmospheric conditions (e.g. Bobrowski et al., 2007; von Glasow, 2010; Surl et al., 2021). These models are typically initialised with a high temperature TE gas composition as calculated from a mixture of magmatic and atmospheric gas. Such mixtures contain high levels of OH. Within the kinetic mechanism of the low temperature reactive halogen model, OH is almost completely converted to HO_2, which represents a key oxidant in the auto-catalytic cycles related to HBr oxidation and BrO formation. Surl et al. (2021) found that the modeled BrO evolution strongly depends on the initial OH amount and that changes thereof by a factor of 4 can lead to results that largely differ from field observations.
In Kuhn et al. (2022a) kinetic chemistry modeling encompasses the entire plume cooling phase and thereby allows inferring the remaining oxidant amounts. OH is abundant at high tempearture, as expected from TE calculations. During plume cooling, however, only a small fraction of the OH radicals are effectively converted into HO_2 (e.g. via SO_2 oxidation). Most of the OH molecules at lower temperatures eventually form water. As a result, kinetic modeling of the plume chemistry during its entire cooling phase results in in-plume HO_2 levels that are 2-3 orders of magnitude lower than the values typically assumed in order to explain reactive halogen chemistry in volcanic plumes. Slower plume cooling rates, e.g. induced by the emission dynamics in vent systems would further reduce the plume's HO_x

levels. This calls for a major revision of the BrO formation processes in volcanic plumes. Most of the reactive halogen plume models calculate the plume evolution and spatial gradients based on a regular grid (e.g. von Glasow, 2010; Surl et al., 2021) and are initialised with a single TE calculation. The extention of the here introduced model can provide the comprehensive simulation of volcanic plume chemistry from the first moment after magmatic gas emissions to hours-old diluted plumes in the atmosphere. Spatial gradients of gases can be accounted for by formulating the transport equations between concentric radial plume boxes, basically refining the adaptive 1-box approach of this study. With this, accurate and fast approximations of volcanic plume processes can be made, integrating all relevant length scales of the process (i.e. cm at high temperature emission to km at large scale atmospheric mixing).

3.3.2 Significance for other fields

The introduced model is simple, flexible and yet includes a fundamental treatment of turbulent mixing. In principle, it can be applied to any atmospheric emission point source that involves faster chemical conversions during the emission phase (e.g. stacks, fires, etc.). On one hand, since it is fast, it can be used to invert emission measurements, on the other hand it can serve as a processor of chemical conversion for specific atmospheric emissions in larger scale models.

4 Conclusion

The analysis of volcanic degassing improves the understanding of our planet and its long-term evolution. Processes in the interior of the Earth are made tangible and ultimately provide links between degassing and volcanic activity, which serve as tools for volcanic monitoring and eruption forecasting. Moreover, processing of volcanic gases in the atmosphere closes global geochemical cycles, while decisively altering the atmospheric state on local to global, and minute to millennia scales.
In the last decades the analysis of volcanic degassing has made tremendous progress. Novel and refined measurement techniques and models have been developed and lead to more consolidated theories of volcanic degassing processes. In particular, optical remote sensing techniques for volcanic plumes have been established. Their averaged, non-invasive, real-time, long-term and global records of volcanic gas emissions significantly contributed to this success.
However nowadays continuous remote sensing observations are only possible for few gas species, basically SO_2 and BrO. Moreover, processes that are central to the field of volcanic degassing remain poorly studied and often neglected in the scientific discourse. For instance, the chemical kinetics in high-temperature magmatic gas that rapidly mixes with atmospheric air is known to be potentially significant. The limited ability to constrain such processes in nature with state-of-the-art measurement techniques as well as the absence of appropriate modeling approaches prevented detailed studies and thus, also their inclusion in the interpretation of volcanic gas measurements.
This thesis combines three novel approaches to volcanic gas analysis (summarised in Tab. 4.1). A novel trace gas imaging technique with optimised spectral trace gas detection scheme (IFPICS, Kuhn et al., 2019; Fuchs et al., 2021) enables a drastic enhancement of the spatio-temporal resolution and the accuracy of volcanic gas measurements. This significantly improves the reliability of volcanic gas emission flux measurements and the quantification of spatial gradients of reactive plume constituents.
Furthermore, this thesis introduces mobile high-resolution FPI spectrographs (Kuhn et al., 2021). Their superior light throughput is likely to enable a range of new volcanic gas observations. The detection of so far unmeasurable species (e.g. OH) is made possible and the range of volcanic gas species that can be quantified by means of simple and robust remote sensing schemes can be extended (e.g. by HF, HCl and CO_2).
Both techniques are implemented in field-tested prototypes that demonstrate their anticipated potential. And, most notably, the here introduced instrument developments are similar or less cost-intensive and complex than the instrumentation of conventional measurements.
In addition, a kinetic chemistry model for the first seconds of the volcanic plume is developed within this thesis (Kuhn et al., 2022a). For the first time, chemical conversion within the turbulent mixing process of hot magmatic gases with the atmosphere is examined in detail. The results challenge the wide-spread TE assumptions prevailing in interpretations

and discussions of volcanic gas measurements and demand the inclusion of high-temperature reaction kinetics into the scope of volcanic gas studies.
The individual studies of this thesis – and their combination – allow a much more comprehensive investigation of the important early degassing processes and their inclusion in interpretations of field observations. Furthermore, besides improving the performance of current measurement approaches, they open the door for whole new volcanic gas studies, for instance:

1. Improved remote sensing schemes can extend the range of routinely measured and continuously monitored volcanic gases (e.g. CO_2, HF, HCl). Based on that, degassing models and volcano-specific theories can be refined and broadened, ultimately leading to improved links between gas emission measurements and volcanic activity.

2. The kinetic models of the magma-atmosphere interface can be extended to simulate the further plume evolution including state-of-the-art reactive halogen schemes. Radical measurements within the hot plume part and the high-resolution measurements of spatial BrO gradients within the cooled volcanic plume would crucially constrain such models and lead to largely improved understanding of volcanic plume chemistry.

3. Kinetic volcanic gas emission models may allow to draw conclusions on the dynamics of volcanic degassing processes when they are linked to (temporally resolved) measurements of reduced plume constituents. These could be provided for instance by novel high-spectral-resolution CO remote sensing schemes.

Moreover, the concepts of the measurement techniques established within this thesis exhibit broad applicability beyond the field of volcanic gas analysis. These include the substantial improvement of environmental observations of atmospheric radiative transfer, greenhouse gases, air pollutants, atmospheric oxidants and the activity of plants. Human activities have lead to severe impacts on Earth's atmosphere (nowadays exceeding that of volcanoes) with a potentially drastic and in large parts unforeseeable future development. Improved monitoring of the atmosphere can be a vital tool to identify, better understand, and respond to these developments.
All in all, this thesis outlines a promising – and at the same time inexpensive – perspective for future studies of volcanic gases and atmospheric phenomena.

Table 4.1: Brief overview on the contributions of this thesis

state-of-the-art	contribution of this thesis	significance
Kuhn et al. (2019); Fuchs et al. (2021)		
UV remote sensing of volcanic trace gases with either, high accuracy (DOAS) or high spatial resolution filter-based SO_2 cameras	Combination of high accuracy with high spatial resolution of volcanic trace gas measurements by the novel IFPICS technique; Proof-of-concept in field measurements	More accurate determination of volatile fluxes; spatial gradients of reactive halogen species within the volcanic plume; broad applicability to other atmospheric studies
Kuhn et al. (2021)		
UV remote sensing of volcanic trace gases with moderate resolving power ($\frac{\lambda}{\delta\lambda} \approx 10^3$, DOAS)	Novel mobile FPI spectrographs with high resolving power ($\frac{\lambda}{\delta\lambda} \approx 10^5$) and high light throughput; Proof-of-concept in field measurements (Appendix A)	Study of the hot degassing interface by measurements of OH and other gases previously not measurable at volcanoes; broad applicability to other atmospheric studies
Kuhn et al. (2022a)		
High temperature magma-atmosphere interface described by TE calculations	Comprehensive and flexible model of the turbulent magmatic gas release into the atmosphere encompassing the entire cooling phase	Better accordance to field observations; Disproof of common TE assumptions; Broad implications for volcanic gas measurements and their interpretation; Detailed studies of magma-atmosphere interfaces required at open vent volcanoes

Appendix

A FPI spectrograph measurements at Nyiragongo volcano

A.1 Introduction

The FPI spectrograph prototype (as introduced in Kuhn et al., 2021) was tested during a field campaign at Nyiragongo volcano in the Democratic Republic of Congo in February 2020. The objective of this measurement was the assessment of the feasibility of quantification of the high OH amounts in hot volcanic emissions predicted by chemistry models (e.g. Gerlach, 2004) and hence, the verification of the impact of high temperature chemistry on magmatic gases after their release from the magma (Kuhn et al., 2022a). For many years, Nyiragongo hosts an active lava lake and occasional lava flows inside its crater (see Fig. A.1a and A.1b). The crater floor at that time was about 300 m below the altitude of the rim, which is at about 3470 m a.s.l. It is accessible via a steep descent with three terraces (see Fig. A.1b). Here, mobile instrumentation is vital.
A compact telescope (76 mm diameter, f=300 mm) and a y-shaped quartz fibre bundle were used to send the light of a UV LED (305 nm centre wavelength, ca. 10 nm width) across the gas emission of a lava flow (less than 0.5 m above the lava surface, site I, see Fig. A.1c). A retro reflector (see Fig. A.1d) on the opposite side sent the light back to the telescope, where it is again coupled into a fibre leading to the high-resolution FPI spectrograph (see Fig. A.1c, A.1f and Merten et al., 2011, for details). The whole instrument setup including spectrograph, telescope, light source, retro reflector, fibre, batteries and computer weighs ca. 20 kg and fits into a backpack.
After that measurement and after climbing back up, a further measurement was performed at the crater rim inside a small shelter (site II, see Fig. A.1e). There, for calibration purposes an absorption spectrum of the flame of a camping stove (with high OH levels) was recorded.
Hereafter, an instrument model for the FPI spectrograph is introduced (Sect. A.2) and then used for preliminary evaluation fo the spectra recorded in the field (Sect. A.3).

A.2 FPI spectrograph instrument model

The principle of FPI spectrographs is described in detail in Kuhn et al. (2021). Here we describe an instrument forward model for the evaluation of spectra recorded with FPI spectrographs. This model mainly refers to the grating order sorting mechanism (OSM) implementation of an FPI spectrograph (as implemented in the used prototype), it can similarly be used for interferometric OSM approach. The grating OSM implementation of an FPI spectrograph uses an order sorting grating spectrograph (OSGS) in line with the FPI imaging unit.
The spectral characteristics of the optical components in use are well-known and enable accurate modeling of the spectral instrument transfer function $T_{\text{inst}}(\lambda; i, j)$, which converts a spectral radiance into measured intensities at each detector pixel (i, j). The relative amount of light received by a pixel (with respect to its neighbouring pixels) is determined by the overlay of the OSGS's spectral transmission $H(\lambda; i, j)$ and the FPI transmission spectrum $T_{\text{FPI}}(\lambda; i, j)$. Broadband spectral contributions (e.g. through lens transmission, grating efficiency, etc.) are not considered here because they are negligible on the regarded spectral scale. The spectral instrument transfer function is then:

$$T_{\text{inst}}(\lambda; i, j) = H(\lambda; i, j) \cdot T_{\text{FPI}}(\lambda; i, j) \tag{4.1}$$

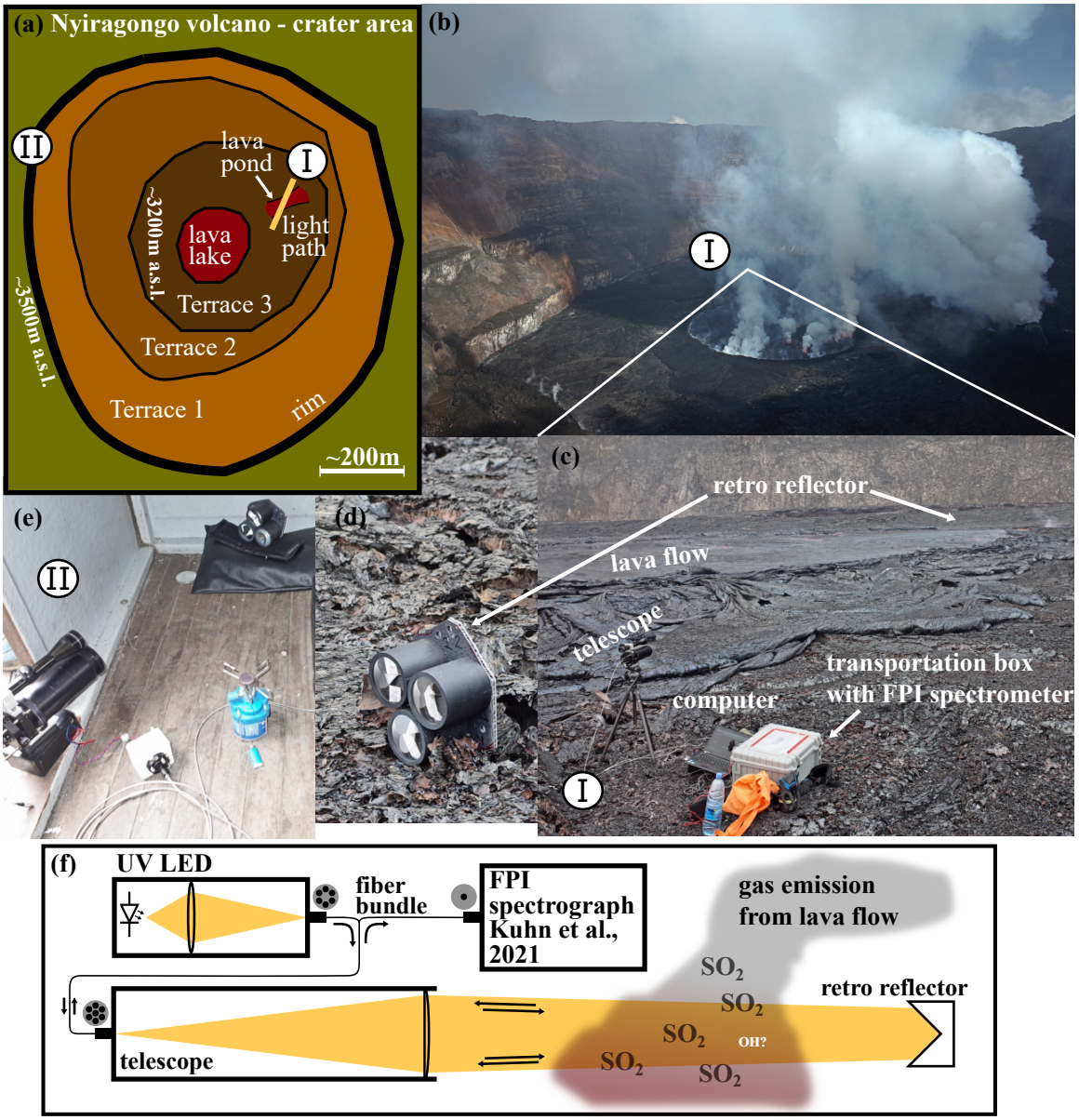

Figure A.1: (a) Schematic map of Nyiragongo crater indicating the site of the lava flow measurement (I) and that of the OH calibration measurement (II); (b) Photograph of the crater showing the lava lake and the crater walls. (c) Measurement set-up at the lava flow with retro reflectors on the other side (d); (e) shows the calibration set-up inside a shelter at the crater rim (site II) (f) Schematic set-up of the measurement, using a fibre bundle to send the light of an LED across the hot lava emission and to receive it after it is sent back into the telescope by the retro reflector.

The instrument line function of the OSGS and thus its spectral transmission can be approximated with a higher order Gaussian (e.g. Beirle et al., 2017):

$$H(\lambda; i, j) = \exp\left(\frac{(\lambda_c(i) - \lambda)^2}{2c^2}\right)^p \tag{4.2}$$

with a full width at half maximum $\delta_H = 2c\sqrt{2(\log 2)^{\frac{1}{p}}}$ and the order p. The centre wavelength λ_c of the instrument line function depends on the pixel location i on the detector in grating dispersion direction and determined via the linear dispersion of the OSGS and a reference wavelength.
The full FPI transmission spectrum is given for a single light beam (index sb) by the Airy function (e.g. Perot and Fabry, 1899):

$$T_{\mathrm{FPI,sb}}(\lambda; i, j) = \left[1 + \frac{4\mathcal{F}^2}{\pi^2}\sin^2\left(\frac{2\,n\,d\,\pi}{\lambda}\cos\left(\alpha(i,j)\right)\right)\right]^{-1} \tag{4.3}$$

For the FPI spectrograph d and $\mathcal{F}$ are fixed and n-1 is assumed to be proportional to the outside pressure since the used etalon is not sealed. The incidence angle $\alpha(i, j)$ is dependent on the location on the detector, i.e. on the individual pixel (i, j):

$$\alpha(i,j) = \sqrt{\arctan^2\left(\frac{(i - i_{\mathrm{oa}})\,d_{\mathrm{pix}}}{f_2}\right) + \arctan^2\left(\frac{(j - j_{\mathrm{oa}})\,d_{\mathrm{pix}}}{f_2}\right)} \tag{4.4}$$

with the pixel size d_{pix}, the focal length f_2 of the imaging lens (lens 2 in Fig. 2a in Kuhn et al., 2021) and the pixel $(i_{\mathrm{oa}}, j_{\mathrm{oa}})$, where the FPI surface normal (generally the optical axis) intersects the image plane (i.e. the detector surface).
Furthermore, the spatial extent of the detector pixels needs to be accounted for. It imposes a slight divergence of the beams reaching an individual pixel, which can be approximated by a cone geometry delimited by the pixel size and the focal length of the imaging lens. Integrating the FPI transmission spectra along the cone's dimensions yields the effective FPI transmission spectrum (see also Kuhn, 2015; Fuchs et al., 2021) for each pixel:

$$T_{\mathrm{FPI}}(\lambda; \alpha(i,j)) \approx 2\pi \int_{\alpha - \tan\frac{d_{\mathrm{pix}}}{2f_2}}^{\alpha + \tan\frac{d_{\mathrm{pix}}}{2f_2}} T_{\mathrm{FPI_{sb}}}(\lambda; \theta)\,\sin\theta \mathrm{d}\theta \tag{4.5}$$

Here it is assumed that the angle range delimited by a pixel is independent of the pixel's location. Accounting for finite pixel size leads to a slight blurring of the FPI transmission spectra at pixels that correspond to higher FPI incidence angles α (see Fig. 1.5d and Fig. 1b in Kuhn et al., 2021).
The instrument transfer function can now be used to convert literature spectra to detector images. This simple model is sufficient to fit trace gas spectra to measured photon flux distributions on the detector, at least for parts of the spectrum.

A.3 Preliminary Analysis and Results

The spectra are corrected for dark current contributions and variations in pixel sensitivities (flat field correction). Then, within a region of interest (ROI) on the detector, the narrow band contribution of the spectral optical density is extracted. A polynomial (here 7th order) is fitted to the intensity of each pixel column within the ROI (which are oriented roughly in

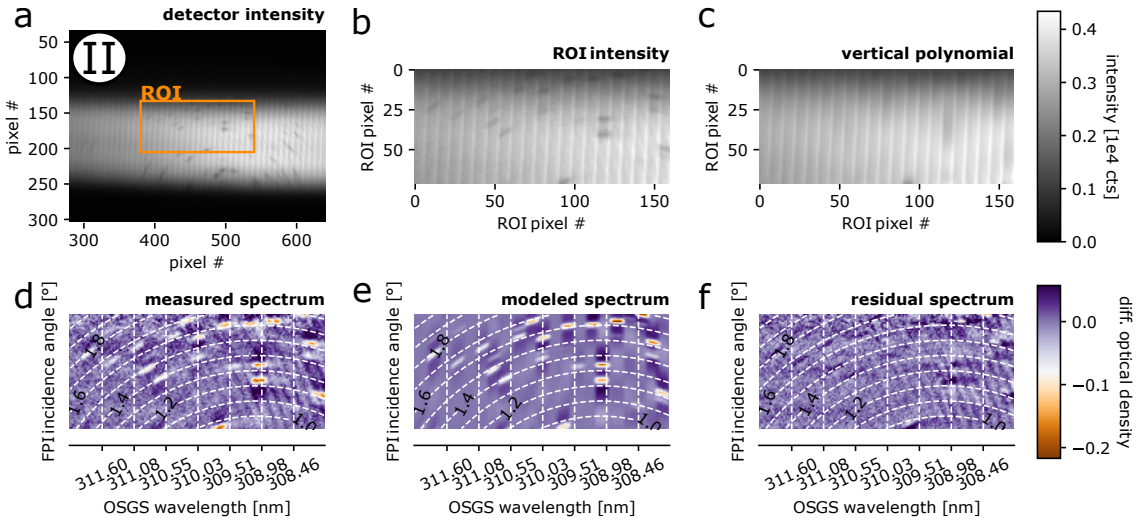

Figure A.2: (a) Intensity distribution on the detector of the FPI spectrograph for the measurement with the camping stove at the crater rim (site II, see Fig. A.1). The region of interest (ROI) for the spectral evaluation is indicated; (b) intensity distribution within the ROI, Individual OH rovibronic absorption lines are visible; (c) a vertical polynomial (here 7th order) is fitted to each column of (b), which reduces differences between measurement and model for slow intensity variations. (d) logarithm of the ratio of (b) and (c) showing the narrow-band OH optical density with a picometre resolution. (e) modeled spectrum; (f) residuum spectrum (d)-(e).

the direction of FPI dispersion). This accounts for broadband intensity differences between model and measurement. Panels a–c of Figs. A.2 and A.3 document this process for the measurements at both sites. The logarithm of the ratio between measured radiance and the respective polynomial is then used to approximate the narrow-band optical density component of the spectrum (see panel d of the respective figures). Now, the above described instrument model is used to reproduce the optical density distribution on the detector. Based on the knowledge of the optics and the spectral absorption of the gases the column amounts of the gases along the measurement light path can be retrieved.

Calibration measurement at the crater rim

An off-the-shelf camping stove is used for calibration measurements by directing the light of the LED through its flame, which contains high OH levels. The strong and sharp OH absorption lines are represented by dark dots in the intensity image (Fig. A.2b). The alignment of these dots in Fig. A.2a indicates the radial symmetry of the spectral FPI transmission. A slight overlay of the FPI orders separated by the OSGS induces bright vertical stripes within the spectrum images. Due to their mostly vertical alignment they are removed by the polynomial fit procedure (Fig. A.2c).
Figure A.2e shows the resulting model output for the measurement at site II after a fit with the OH amount and temperature as free parameters (see Tab. A.1 for a list of all model parameters). It accurately reproduces the OH absorption lines in the measured spectrum and thereby confirms the instrument model and also provides a wavelength to pixel mapping of the spectrograph. The retrieved OH column amount of about $8 \cdot 10^{15}\,\mathrm{molec\,cm^{-2}}$ corresponds to a mixing ratio of ca. 10^{-3} at 1760 K. The amount is realistic (Cattolica et al., 1982), however the temperature might be slightly over-estimated and rather represent an effective temperature across gradients within the flame.

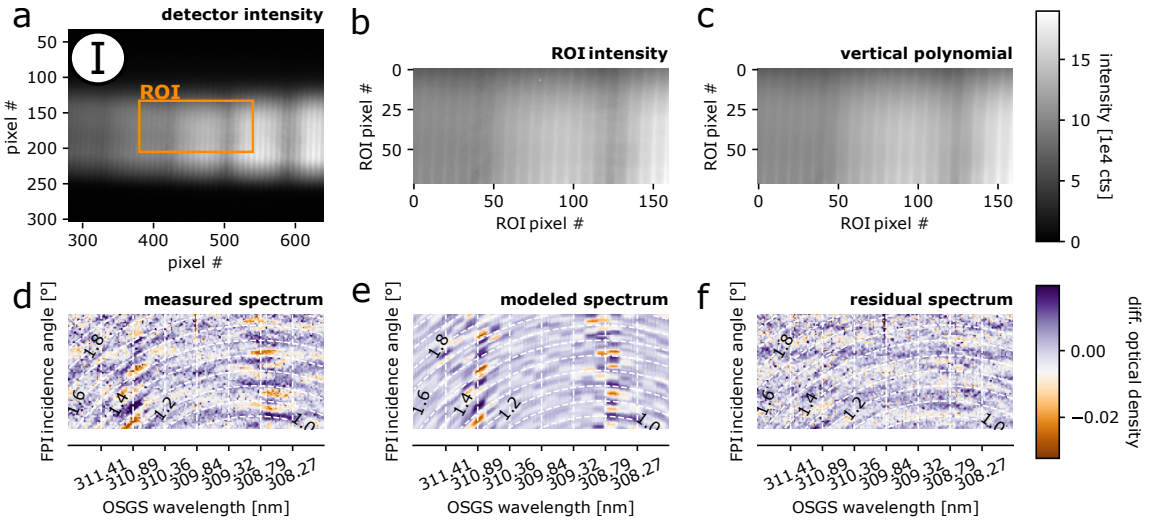

Figure A.3: Same as Fig. A.2 for the measurement at the lava flow inside the crater (site I, see Fig. A.1)

Measurement at a lava flow within Nyiragongo's crater

Hot volcanic gases remain difficult to approach even when using mobile instrumentation. Many factors, like wind, rain, visibility, volcanic activity, presence of inconvenient gases, limited time and battery, and many more impact the feasibility measurements. Ultimately, it was possible to set up a measurement light path about 0.5 m above a lava flow.

Figure A.3 shows the evaluation of a recorded spectrum at that site. The high resolution SO_2 absorption features of the measurement (Fig. A.3d) can nicely be reproduced by the model (Fig. A.3e). The retrieved SO_2 column of $5 \cdot 10^{17}$ molec cm^{-2} (Tab. A.1) corresponds to 2.5 ppm of SO_2 averaged over the light path of about 100 m. It confirms the low gas emission expected at such lava flows. Figure A.4 indicates the pixel to wavelength mapping for this measurement. It confirms that strong OH lines are covered by the spectrum ROI and allows to infer an approximate OH detection limit. The root means square noise of the residuum (Fig. A.3f) for each column is about 0.01. Based on strengths of OH absorption lines within the spectrum, the noise equivalent column amount of OH can be determined to be about 10^{14} molec cm^{-2}. This corresponds to a mixing ratio of about 10 ppb when assuming a 5 m light path within a potentially hot plume part. This is quite low compared to the OH levels expected in high temperature volcanic gases. However, at this site and since at the height of our light path the gases were already substantially cooled, the detection of OH was not possible. While this first attempt generated important knowledge on the operation of spectroscopic instruments in such extreme volcanic environments, similar studies in the future with improved instruments (e.g. interferometric OSM implementation Kuhn et al., 2021) could provide volcanic OH measurements, which are so vitally needed.

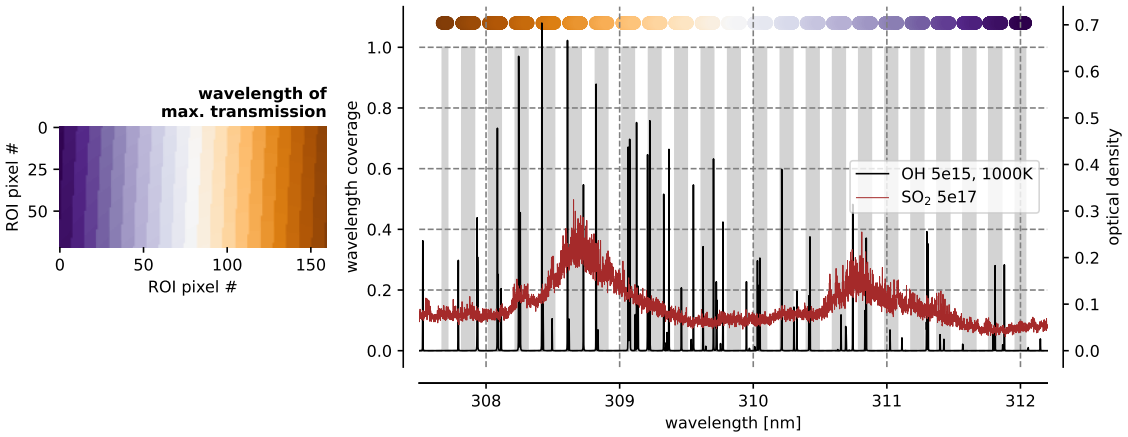

Figure A.4: The colour code in the left panel shows the major FPI transmission order contributing to the respective detector pixel within the ROI for the evaluation of the spectrum from site I, see Fig. A.3. The right panel shows the spectral coverage (due the range of FPI incidence angles, see also Fig. 1.5d) of the individual FPI transmission orders (grey surfaces). In addition, the optical densities of SO_2 and OH are shown for the approximate amounts measured at site I and II.

Table A.1: Model parameters for measurement at site I and II, see Fig. A.3e and A.2e.

parameter	unit	Site I (lava flow)	Site II (burner shelter)
FPI			
d	µm	239.854	
$\mathcal{F}$		95.2	
$n_{\text{air}}(1013\,\text{hPa})$		1.0002916	
pressure	hPa	660	645
OSGS			
λ_c	nm	308.96	309.15
δ_{H}	nm	0.2065	
p		2.42	
D_{GS}	$\text{nm}\,\text{pix}^{-1}$	0.2065	
optics			
f_2	mm	70.75	
d_{pix}	mm	0.013	
i_{oa}	pix	493.6	
j_{oa}	pix	280.3	
spectral			
S_{SO_2}	$\text{molec}\,\text{cm}^{-2}$	$5.21 \cdot 10^{17}$	-
S_{OH}	$\text{molec}\,\text{cm}^{-2}$	-	$7.94 \cdot 10^{15}$
T_{OH}	K	-	1760

B List of Abbreviations

Abbreviation	
TE	thermodynamic equilibrium
UV	ultraviolet
FOV	field of view
IR	infrared
DOAS	differential optical absorption spectroscopy
FTS	fourier transform spectroscopy
GS	grating spectrograph
FPI	Fabry-Pérot interferometer
IFPICS	imaging FPI correlation spectroscopy
OSM	order sorting mechanism
OSGS	order sorting grating spectrograph
ROI	region of interest

C List of Figures

D List of Tables

References

Aiuppa, A., Burton, M., Murè, F., and Inguaggiato, S.: Intercomparison of volcanic gas monitoring methodologies performed on Vulcano Island, Italy, Geophysical Research Letters, 31, https://doi.org/10.1029/2003gl018651, 2004.

Aiuppa, A., Franco, A., von Glasow, R., Allen, A. G., D'Alessandro, W., Mather, T. A., Pyle, D. M., and Valenza, M.: The tropospheric processing of acidic gases and hydrogen sulphide in volcanic gas plumes as inferred from field and model investigations, Atmospheric Chemistry and Physics, 7, 1441–1450, https://doi.org/10.5194/acp-7-1441-2007, 2007a.

Aiuppa, A., Moretti, R., Federico, C., Giudice, G., Gurrieri, S., Liuzzo, M., Papale, P., Shinohara, H., and Valenza, M.: Forecasting Etna eruptions by real-time observation of volcanic gas composition, Geology, 35, 1115, https://doi.org/10.1130/g24149a.1, 2007b.

Aiuppa, A., Shinohara, H., Tamburello, G., Giudice, G., Liuzzo, M., and Moretti, R.: Hydrogen in the gas plume of an open-vent volcano, Mount Etna, Italy, Journal of Geophysical Research, 116, https://doi.org/10.1029/2011jb008461, 2011.

Beirle, S., Hörmann, C., Penning de Vries, M., Dörner, S., Kern, C., and Wagner, T.: Estimating the volcanic emission rate and atmospheric lifetime of SO2 from space: a case study for Kilauea volcano, Hawaii, Atmospheric Chemistry and Physics, 14, 8309–8322, https://doi.org/10.5194/acp-14-8309-2014, 2014.

Beirle, S., Lampel, J., Lerot, C., Sihler, H., and Wagner, T.: Parameterizing the instrumental spectral response function and its changes by a super-Gaussian and its derivatives, Atmospheric Measurement Techniques, 10, 581–598, https://doi.org/10.5194/amt-10-581-2017, 2017.

Bluth, G., Shannon, J., Watson, I., Prata, A., and Realmuto, V.: Development of an ultra-violet digital camera for volcanic SO2 imaging, Journal of Volcanology and Geothermal Research, 161, 47–56, 2007.

Bluth, G. J. S., Schnetzler, C. C., Krueger, A. J., and Walter, L. S.: The contribution of explosive volcanism to global atmospheric sulphur dioxide concentrations, Nature, 366, 327–329, https://doi.org/10.1038/366327a0, 1993.

Bobrowski, N. and Giuffrida, G.: Bromine monoxide/sulphur dioxide ratios in relation to volcanological observations at Mt. Etna 2006-2009, Solid Earth, 3, 433, 2012.

Bobrowski, N. and Platt, U.: SO2/BrO ratios studied in five volcanic plumes, Journal of Volcanology and Geothermal Research, 166, 147–160, https://doi.org/10.1016/j.jvolgeores.2007.07.003, 2007.

Bobrowski, N., Hönninger, G., Galle, B., and Platt, U.: Detection of bromine monoxide in a volcanic plume, Nature, 423, 273–276, https://doi.org/10.1038/nature01625, 2003.

Bobrowski, N., von Glasow, R., Aiuppa, A., Inguaggiato, S., Louban, I., Ibrahim, O. W., and Platt, U.: Reactive halogen chemistry in volcanic plumes, Journal of Geophysical Research, 112, https://doi.org/10.1029/2006jd007206, 2007.

Bonhoeffer, K. F. and Reichardt, H.: Zerfall von erhitztem Wasserdampf in Wasserstoff und freies Hydroxyl, Zeitschrift für Physikalische Chemie, 139A, 75–97, https://doi.org/10.1515/zpch-1928-13909, 1928.

Burnett, C. R. and Burnett, E. B.: Spectroscopic measurements of the vertical column, abundance of hydroxyl (OH) in the earth's atmosphere, Journal of Geophysical Research, 86, 5185, https://doi.org/10.1029/jc086ic06p05185, 1981.

Burton, M., Allard, P., Mure, F., and Spina, A. L.: Magmatic Gas Composition Reveals the Source Depth of Slug-Driven Strombolian Explosive Activity, Science, 317, 227–230, https://doi.org/10.1126/science.1141900, 2007.

Butz, A., Dinger, A. S., Bobrowski, N., Kostinek, J., Fieber, L., Fischerkeller, C., Giuffrida, G. B., Hase, F., Klappenbach, F., Kuhn, J., Lübcke, P., Tirpitz, L., and Tu, Q.: Remote sensing of volcanic CO2, HF, HCl, SO2, and BrO in the downwind plume of Mt. Etna, Atmospheric Measurement Techniques, 10, 1–14, https://doi.org/10.5194/amt-10-1-2017, 2017.

Carn, S. A., Fioletov, V. E., McLinden, C. A., Li, C., and Krotkov, N. A.: A decade of global volcanic SO2 emissions measured from space, Scientific Reports, 7, 1, https://doi.org/10.1038/srep44095, 2017.

Cattolica, R. J., Yoon, S., and Knuth, E. L.: OH Concentration in an Atmospheric-Pressure Methane-Air Flame from Molecular-Beam Mass Spectrometry and Laser-Absorption Spectroscopy, Combustion Science and Technology, 28, 225–239, https://doi.org/10.1080/00102208208952557, 1982.

Chance, K. and Kurucz, R.: An improved high-resolution solar reference spectrum for earth's atmosphere measurements in the ultraviolet, visible, and near infrared, J. Quant. Spec. Rad. Trans., 111, 1289–1295, https://doi.org/10.1016/j.jqsrt.2010.01.036, 2010.

Crutzen, P. J.: Photochemical reactions initiated by and influencing ozone in unpolluted tropospheric air, Tellus, 26, 47–57, https://doi.org/10.3402/tellusa.v26i1-2.9736, 1974.

Danielache, S. O., Eskebjerg, C., Johnson, M. S., Ueno, Y., and Yoshida, N.: High-precision spectroscopy of 32S, 33S, and 34S sulfur dioxide: Ultraviolet absorption cross sections and isotope effects, Journal of Geophysical Research, 113, D17, https://doi.org/10.1029/2007jd009695, 2008.

Dekemper, E., Vanhamel, J., Opstal, B. V., and Fussen, D.: The AOTF-based NO2 camera, Atmospheric Measurement Techniques, 9, 6025–6034, https://doi.org/10.5194/amt-9-6025-2016, 2016.

Delmelle, P., Stix, J., Baxter, P., Garcia-Alvarez, J., and Barquero, J.: Atmospheric dispersion, environmental effects and potential health hazard associated with the low-altitude gas plume of Masaya volcano, Nicaragua, Bulletin of Volcanology, 64, 423–434, https://doi.org/10.1007/s00445-002-0221-6, 2002.

Dorn, H.-P., Brandenburger, U., Brauers, T., Hausmann, M., and Ehhalt, D. H.: In-situ detection of tropospheric OH radicals by folded long-path laser absorption. Results from the POPCORN Field Campaign in August 1994, Geophysical Research Letters, 23, 2537–2540, https://doi.org/10.1029/96gl02206, 1996.

Edner, H., Ragnarson, P., Svanberg, S., Wallinder, E., Ferrara, R., Cioni, R., Raco, B., and Taddeucci, G.: Total fluxes of sulfur dioxide from the Italian volcanoes Etna, Stromboli, and Vulcano measured by differential absorption lidar and passive differential optical absorption spectroscopy, Journal of Geophysical Research, 99, 18 827, https://doi.org/10.1029/94jd01515, 1994.

Fabry, C. and Buisson, H.: Wavelength measurements for the establishment of a system of spectroscopic standards, The Astrophysical Journal, 27, 169–196, 1908.

Fleischmann, O. C., Hartmann, M., Burrows, J. P., and Orphal, J.: New ultraviolet absorption cross-sections of BrO at atmospheric temperatures measured by time-windowing Fourier transform spectroscopy, Journal of Photochemistry and Photobiology A: Chemistry, 168, 117 – 132, https://doi.org/http://dx.doi.org/10.1016/j.jphotochem.2004.03.026, 2004.

Frankenberg, C., Fisher, J. B., Worden, J., Badgley, G., Saatchi, S. S., Lee, J.-E., Toon, G. C., Butz, A., Jung, M., Kuze, A., and Yokota, T.: New global observations of the terrestrial carbon cycle from GOSAT: Patterns of plant fluorescence with gross primary productivity, Geophysical Research Letters, 38, 17, https://doi.org/10.1029/2011gl048738, 2011.

Fuchs, C.: Imaging of volcanic trace gases by Fabry-Perot interferometer correlation spectroscopy, https://doi.org/10.11588/HEIDOK.00029495, Master's thesis, University of Heidelberg, 2019.

Fuchs, C., Kuhn, J., Bobrowski, N., and Platt, U.: Quantitative imaging of volcanic SO2 plumes using Fabry–Pérot interferometer correlation spectroscopy, Atmospheric Measurement Techniques, 14, 295–307, https://doi.org/10.5194/amt-14-295-2021, 2021.

Gaillard, F., Scaillet, B., and Arndt, N. T.: Atmospheric oxygenation caused by a change in volcanic degassing pressure, Nature, 478, 229–232, https://doi.org/10.1038/nature10460, 2011.

Galle, B., Johansson, M., Rivera, C., Zhang, Y., Kihlman, M., Kern, C., Lehmann, T., Platt, U., Arellano, S., and Hidalgo, S.: Network for Observation of Volcanic and Atmospheric Change (NOVAC) - A global network for volcanic gas monitoring: Network layout and instrument description, J. Geophys. Res., 115, D05 304, https://doi.org/10.1029/2009JD011823, 2010.

General, S., Pöhler, D., Sihler, H., Bobrowski, N., Frieß, U., Zielcke, J., Horbanski, M., Shepson, P. B., Stirm, B. H., Simpson, W. R., Weber, K., Fischer, C., and Platt, U.: The Heidelberg Airborne Imaging DOAS Instrument (HAIDI) – a novel imaging DOAS device for 2-D and 3-D imaging of trace gases and aerosols, Atmospheric Measurement Techniques, 7, 3459–3485, https://doi.org/10.5194/amt-7-3459-2014, 2014.

General, S., Bobrowski, N., Pöhler, D., Weber, K., Fischer, C., and Platt, U.: Airborne I-DOAS measurements at Mt. Etna: BrO and OClO evolution in the plume, Journal of Volcanology and Geothermal Research, 300, 175–186, https://doi.org/10.1016/j.jvolgeores.2014.05.012, 2015.

Gerlach, T.: Chemical characteristics of the volcanic gases from Nyiragongo lava lake and the generation of CH4-rich fluid inclusions in alkaline rocks, Journal of Volcanology and Geothermal Research, 8, 177–189, https://doi.org/10.1016/0377-0273(80)90103-1, 1980.

Gerlach, T. M.: Thermodynamic evaluation and restoration of volcanic gas analyses: An example based on modern collection and analytical methods., Geochemical Journal, 27, 305–322, https://doi.org/10.2343/geochemj.27.305, 1993.

Gerlach, T. M.: Volcanic sources of tropospheric ozone-depleting trace gases, Geochemistry, Geophysics, Geosystems, 5, 9, https://doi.org/10.1029/2004gc000747, 2004.

Gerlach, T. M. and Nordlie, B. E.: The C-O-H-S gaseous system; Part II, Temperature, atomic composition, and molecular equilibria in volcanic gases, American Journal of Science, 275, 377–394, https://doi.org/10.2475/ajs.275.4.377, 1975.

Giggenbach, W., Tedesco, D., Sulistiyo, Y., Caprai, A., Cioni, R., Favara, R., Fischer, T., Hirabayashi, J.-I., Korzhinsky, M., Martini, M., Menyailov, I., and Shinohara, H.: Evaluation of results from the fourth and fifth IAVCEI field workshops on volcanic gases, Vulcano island, Italy and Java, Indonesia, Journal of Volcanology and Geothermal Research, 108, 157–172, https://doi.org/10.1016/s0377-0273(00)00283-3, 2001.

Giggenbach, W. F.: A simple method for the collection and analysis of volcanic gas samples, Bulletin Volcanologique, 39, 132–145, https://doi.org/10.1007/bf02596953, 1975.

Giggenbach, W. F.: Chemical Composition of Volcanic Gases, in: Monitoring and Mitigation of Volcano Hazards, pp. 221–256, Springer Berlin Heidelberg, https://doi.org/10.1007/978-3-642-80087-0_7, 1996.

Grainger, J. F. and Ring, J.: Anomalous Fraunhofer line profiles, Nature, 193, 762, https://doi.org/10.1038/193762a0, 1962.

Grossmann, K., Frankenberg, C., Magney, T. S., Hurlock, S. C., Seibt, U., and Stutz, J.: PhotoSpec: A new instrument to measure spatially distributed red and far-red Solar-Induced Chlorophyll Fluorescence, Remote Sensing of Environment, 216, 311–327, https://doi.org/10.1016/j.rse.2018.07.002, 2018.

Gutmann, A., Bobrowski, N., Roberts, T. J., Rüdiger, J., and Hoffmann, T.: Advances in Bromine Speciation in Volcanic Plumes, Frontiers in Earth Science, 6, https://doi.org/10.3389/feart.2018.00213, 2018.

Halevy, I., Johnston, D. T., and Schrag, D. P.: Explaining the Structure of the Archean Mass-Independent Sulfur Isotope Record, Science, 329, 204–207, https://doi.org/10.1126/science.1190298, 2010.

Holland, H. D.: Volcanic gases, black smokers, and the great oxidation event, Geochimica et Cosmochimica Acta, 66, 3811–3826, https://doi.org/10.1016/s0016-7037(02)00950-x, 2002.

Holzinger, R., Warneke, C., Hansel, A., Jordan, A., Lindinger, W., Scharffe, D. H., Schade, G., and Crutzen, P. J.: Biomass burning as a source of formaldehyde, acetaldehyde, methanol, acetone, acetonitrile, and hydrogen cyanide, Geophysical Research Letters, 26, 1161–1164, https://doi.org/10.1029/1999gl900156, 1999.

Hörmann, C., Sihler, H., Bobrowski, N., Beirle, S., Penning de Vries, M., Platt, U., and Wagner, T.: Systematic investigation of bromine monoxide in volcanic plumes from space by using the GOME-2 instrument, Atmospheric Chemistry and Physics, 13, 4749–4781, https://doi.org/10.5194/acp-13-4749-2013, 2013.

Jacquinot, P.: The Luminosity of Spectrometers with Prisms, Gratings, or Fabry-Perot Etalons, Journal of the Optical Society of America, 44, 761, https://doi.org/10.1364/josa.44.000761, 1954.

Jacquinot, P.: New developments in interference spectroscopy, Reports on Progress in Physics, 23, 267–312, https://doi.org/10.1088/0034-4885/23/1/305, 1960.

Jaggar, T. A.: Volcanologic investigations at Kilauea, American Journal of Science, s4-44, 161–220, https://doi.org/10.2475/ajs.s4-44.261.161, 1917.

Kasting, J. F.: Earth's Early Atmosphere, Science, 259, 920–926, https://doi.org/10.1126/science.11536547, 1993.

Kern, C. and Lyons, J. J.: Spatial Distribution of Halogen Oxides in the Plume of Mount Pagan Volcano, Mariana Islands, Geophysical Research Letters, 45, 9588–9596, https://doi.org/10.1029/2018gl079245, 2018.

Kern, C., Kick, F., Lübcke, P., Vogel, L., Wöhrbach, M., and Platt, U.: Theoretical description of functionality, applications, and limitations of SO_2 cameras for the remote sensing of volcanic plumes, Atmospheric Measurement Techniques, 3, 733–749, https://doi.org/10.5194/amt-3-733-2010, 2010.

Kern, C., Masias, P., Apaza, F., Reath, K. A., and Platt, U.: Remote measurement of high preeruptive water vapor emissions at Sabancaya volcano by passive differential optical absorption spectroscopy, Journal of Geophysical Research: Solid Earth, 122, 3540–3564, https://doi.org/10.1002/2017jb014020, 2017.

Kern, C., Lerner, A. H., Elias, T., Nadeau, P. A., Holland, L., Kelly, P. J., Werner, C. A., Clor, L. E., and Cappos, M.: Quantifying gas emissions associated with the 2018 rift eruption of Kīlauea Volcano using ground-based DOAS measurements, Bulletin of Volcanology, 82, 7, https://doi.org/10.1007/s00445-020-01390-8, 2020.

Knapp, M., Kleinschek, R., Hase, F., Agustí-Panareda, A., Inness, A., Barré, J., Landgraf, J., Borsdorff, T., Kinne, S., and Butz, A.: Shipborne measurements of XCO2, XCH4, and XCO above the Pacific Ocean and comparison to CAMS atmospheric analyses and S5P/TROPOMI, Earth System Science Data, 13, 199–211, https://doi.org/10.5194/essd-13-199-2021, 2021.

Kuhn, J.: Trace gas imaging in the atmosphere with a Fabry–Pérot interferometer - a case study for sulfur dioxide, https://doi.org/10.11588/HEIDOK.00029948, Master's thesis, University of Heidelberg, 2015.

Kuhn, J., Bobrowski, N., Lübcke, P., Vogel, L., and Platt, U.: A Fabry Perot interferometer-based camera for two-dimensional mapping of SO_2 distributions, Atmospheric Measurement Techniques, 7, 3705–3715, https://doi.org/10.5194/amt-7-3705-2014, 2014.

Kuhn, J., Platt, U., Bobrowski, N., and Wagner, T.: Towards imaging of atmospheric trace gases using Fabry–Pérot interferometer correlation spectroscopy in the UV and visible spectral range, Atmospheric Measurement Techniques, 12, 735–747, https://doi.org/10.5194/amt-12-735-2019, 2019.

Kuhn, J., Bobrowski, N., Wagner, T., and Platt, U.: Mobile and high-spectral-resolution Fabry–Pérot interferometer spectrographs for atmospheric remote sensing, Atmospheric Measurement Techniques, 14, 7873–7892, https://doi.org/10.5194/amt-14-7873-2021, 2021.

Kuhn, J., Bobrowski, N., and Platt, U.: The interface between magma and Earth's atmosphere, unpublished manuscript, 2022a.

Kuhn, L., Kuhn, J., Wagner, T., and Platt, U.: The NO2 camera based on gas correlation spectroscopy, Atmospheric Measurement Techniques, 15, 1395–1414, https://doi.org/10.5194/amt-15-1395-2022, 2022b.

Lauster, B., Dörner, S., Beirle, S., Donner, S., Gromov, S., Uhlmannsiek, K., and Wagner, T.: Estimating real driving emissions from multi-axis differential optical absorption spectroscopy (MAX-DOAS) measurements at the A60 motorway near Mainz, Germany, Atmospheric Measurement Techniques, 14, 769–783, https://doi.org/10.5194/amt-14-769-2021, 2021.

Le Guern, F., Carbonnelle, J., and Tazieff, H.: Erta'ale lava lake: heat and gas transfer to the atmosphere, Journal of Volcanology and Geothermal Research, 6, 27–48, https://doi.org/10.1016/0377-0273(79)90045-3, 1979.

Lewis, M. N. and White, J. U.: The Band Spectrum of HS, Physical Review, 55, 894–898, https://doi.org/10.1103/physrev.55.894, 1939.

Louban, I., Bobrowski, N., Rouwet, D., Inguaggiato, S., and Platt, U.: Imaging DOAS for volcanological applications, Bulletin of Volcanology, 71, 753–765, https://doi.org/10.1007/s00445-008-0262-6, 2009.

Lübcke, P., Bobrowski, N., Illing, S., Kern, C., Nieves, J. M. A., Vogel, L., Zielcke, J., Granados, H. D., and Platt, U.: On the absolute calibration of SO2 cameras, Atmospheric Measurement Techniques, 6, 677–696, https://doi.org/10.5194/amt-6-677-2013, 2013.

Lübcke, P., Bobrowski, N., Arellano, S., Galle, B., Garzón, G., Vogel, L., and Platt, U.: BrO/SO2 molar ratios from scanning DOAS measurements in the NOVAC network, Solid Earth, 5, 409–424, https://doi.org/10.5194/se-5-409-2014, 2014.

Malinconico, L. L.: Fluctuations in SO2 emission during recent eruptions of Etna, Nature, 278, 43–45, https://doi.org/10.1038/278043a0, 1979.

Manago, N., Takara, Y., Ando, F., Noro, N., Suzuki, M., Irie, H., and Kuze, H.: Visualizing spatial distribution of atmospheric nitrogen dioxide by means of hyperspectral imaging, Applied Optics, 57, 5970, https://doi.org/10.1364/ao.57.005970, 2018.

Martin, R., Roberts, T., Mather, T., and Pyle, D.: The implications of H2S and H2 kinetic stability in high-T mixtures of magmatic and atmospheric gases for the production of oxidized trace species (e.g., BrO and NOx), Chemical Geology, 263, 143–150, https://doi.org/10.1016/j.chemgeo.2008.12.028, 2009.

Martin, R., Ilyinskaya, E., and Oppenheimer, C.: The enigma of reactive nitrogen in volcanic emissions, Geochimica et Cosmochimica Acta, 95, 93–105, https://doi.org/10.1016/j.gca.2012.07.027, 2012.

Martin, R. S., Mather, T. A., and Pyle, D. M.: High-temperature mixtures of magmatic and atmospheric gases, Geochemistry, Geophysics, Geosystems, 7, 4, https://doi.org/10.1029/2005gc001186, 2006.

Mather, T., Pyle, D., and Heaton, T.: Investigation of the use of filter packs to measure the sulphur isotopic composition of volcanic sulphur dioxide and the sulphur and oxygen isotopic composition of volcanic sulphate aerosol, Atmospheric Environment, 42, 4611–4618, https://doi.org/10.1016/j.atmosenv.2008.01.052, 2008.

McGonigle, A. J. S., Aiuppa, A., Ripepe, M., Kantzas, E. P., and Tamburello, G.: Spectroscopic capture of 1 Hz volcanic SO2 fluxes and integration with volcano geophysical data, Geophysical Research Letters, 36, 21, https://doi.org/10.1029/2009gl040494, 2009.

Menyailov, I. A.: Prediction of eruptions using changes in composition of volcanic gases, Bulletin Volcanologique, 39, 112–125, https://doi.org/10.1007/bf02596951, 1975.

Merten, A., Tschritter, J., and Platt, U.: Design of differential optical absorption spectroscopy long-path telescopes based on fiber optics, Applied Optics, 50, 738–754, https://doi.org/10.1364/AO.50.000738, 2011.

Moffat, A. J. and Millan, M. M.: The applications of optical correlation techniques to the remote sensing of SO2 plumes using sky light, Atmospheric Environment, 5, 677–690, https://doi.org/10.1016/0004-6981(71)90125-9, 1971.

Mori, T. and Burton, M.: The SO2 camera: A simple, fast and cheap method for ground-based imaging of SO2 in volcanic plumes, Geophysical Research Letters, 33, 24, 2006.

Moussallam, Y., Bani, P., Curtis, A., Barnie, T., Moussallam, M., Peters, N., Schipper, C. I., Aiuppa, A., Giudice, G., Amigo, Á., Velasquez, G., and Cardona, C.: Sustaining persistent lava lakes: Observations from high-resolution gas measurements at Villarrica volcano, Chile, Earth and Planetary Science Letters, 454, 237–247, https://doi.org/10.1016/j.epsl.2016.09.012, 2016.

Moussallam, Y., Oppenheimer, C., and Scaillet, B.: On the relationship between oxidation state and temperature of volcanic gas emissions, Earth and Planetary Science Letters, 520, 260–267, https://doi.org/10.1016/j.epsl.2019.05.036, 2019.

Neuroth, R., Dorn, H. P., and Platt, U.: High resolution spectral features of a series of aromatic hydrocarbons and BrO: Potential interferences in atmospheric OH-measurements, Journal of Atmospheric Chemistry, 12, 287–298, https://doi.org/10.1007/bf00048077, 1991.

Nies, A.: Imaging of bromine oxide and formaldehyde using Fabry-Perot interferometer correlation spectroscopy, Master's thesis, University of Heidelberg, 2021.

Notholt, J., Schütt, H., and Keens, A.: Solar absorption measurements of stratospheric OH in the UV with a Fourier-transform spectrometer, Applied Optics, 36, 6076, https://doi.org/10.1364/ao.36.006076, 1997.

Oppenheimer, C., Fischer, T., and Scaillet, B.: Volcanic Degassing: Process and Impact, in: Treatise on Geochemistry, pp. 111–179, Elsevier, https://doi.org/10.1016/b978-0-08-095975-7.00304-1, 2014.

Oppenheimer, C., Orchard, A., Stoffel, M., Newfield, T. P., Guillet, S., Corona, C., Sigl, M., Cosmo, N. D., and Büntgen, U.: The Eldgjá eruption: timing, long-range impacts and influence on the Christianisation of Iceland, Climatic Change, 147, 369–381, https://doi.org/10.1007/s10584-018-2171-9, 2018a.

Oppenheimer, C., Scaillet, B., Woods, A., Sutton, A. J., Elias, T., and Moussallam, Y.: Influence of eruptive style on volcanic gas emission chemistry and temperature, Nature Geoscience, 11, 678–681, https://doi.org/10.1038/s41561-018-0194-5, 2018b.

Perot, A. and Fabry, C.: On the Application of Interference Phenomena to the Solution of Various Problems of Spectroscopy and Metrology, The Astrophysical Journal, 9, 87, https://doi.org/10.1086/140557, 1899.

Pfeilsticker, K., Erle, F., Funk, O., Veitel, H., and Platt, U.: First geometrical pathlengths probability density function derivation of the skylight from spectroscopically highly resolving oxygen A-band observations: 1. Measurement technique, atmospheric observations and model calculations, Journal of Geophysical Research: Atmospheres, 103, 11 483–11 504, https://doi.org/10.1029/98jd00725, 1998.

Plascyk, J. A. and Gabriel, F. C.: The Fraunhofer Line Discriminator MKII-An Airborne Instrument for Precise and Standardized Ecological Luminescence Measurement, IEEE Transactions on Instrumentation and Measurement, 24, 306–313, https://doi.org/10.1109/tim.1975.4314448, 1975.

Platt, U. and Hönninger, G.: The role of halogen species in the troposphere, Chemosphere, 52, 325–338, https://doi.org/10.1016/S0045-6535(03)00216-9, 2003.

Platt, U. and Stutz, J.: Differential optical absorption spectroscopy, Springer, Berlin Heidelberg, ISBN: 978-3-540-21193-8, 2008.

Platt, U., Lübcke, P., Kuhn, J., Bobrowski, N., Prata, F., Burton, M., and Kern, C.: Quantitative imaging of volcanic plumes - Results, needs, and future trends, Journal of Volcanology and Geothermal Research, 300, 7–21, 2015.

Platt, U., Wagner, T., Kuhn, J., and Leisner, T.: The "ideal" spectrograph for atmospheric observations, Atmospheric Measurement Techniques, 14, 6867–6883, https://doi.org/10.5194/amt-14-6867-2021, 2021.

Porter, G.: The absorption spectroscopy of substances of short life, Discussions of the Faraday Society, 9, 60–69, 1950.

Roberts, T., Martin, R., and Jourdain, L.: Reactive bromine chemistry in Mount Etna's volcanic plume: the influence of total Br, high-temperature processing, aerosol loading and plume–air mixing, Atmospheric Chemistry and Physics, 14, 11 201–11 219, 2014.

Roberts, T., Dayma, G., and Oppenheimer, C.: Reaction Rates Control High-Temperature Chemistry of Volcanic Gases in Air, Frontiers in Earth Science, 7, https://doi.org/10.3389/feart.2019.00154, 2019.

Robock, A.: Volcanic eruptions and climate, Reviews of Geophysics, 38, 191–219, https://doi.org/10.1029/1998rg000054, 2000.

Rothman, L., Gordon, I., Babikov, Y., Barbe, A., Benner, D. C., Bernath, P., Birk, M., Bizzocchi, L., Boudon, V., Brown, L., Campargue, A., Chance, K., Cohen, E., Coudert, L., Devi, V., Drouin, B., Fayt, A., Flaud, J.-M., Gamache, R., Harrison, J., Hartmann, J.-M., Hill, C., Hodges, J.,

Jacquemart, D., Jolly, A., Lamouroux, J., Roy, R. L., Li, G., Long, D., Lyulin, O., Mackie, C., Massie, S., Mikhailenko, S., Müller, H., Naumenko, O., Nikitin, A., Orphal, J., Perevalov, V., Perrin, A., Polovtseva, E., Richard, C., Smith, M., Starikova, E., Sung, K., Tashkun, S., Tennyson, J., Toon, G., Tyuterev, V., and Wagner, G.: The HITRAN2012 molecular spectroscopic database, Journal of Quantitative Spectroscopy and Radiative Transfer, 130, 4 – 50, https://doi.org/10.1016/j.jqsrt.2013.07.002, HITRAN2012 special issue, 2013.

Rüdiger, J., Tirpitz, J.-L., de Moor, J. M., Bobrowski, N., Gutmann, A., Liuzzo, M., Ibarra, M., and Hoffmann, T.: Implementation of electrochemical, optical and denuder-based sensors and sampling techniques on UAV for volcanic gas measurements: examples from Masaya, Turrialba and Stromboli volcanoes, Atmospheric Measurement Techniques, 11, 2441–2457, https://doi.org/10.5194/amt-11-2441-2018, 2018.

Rufus, J., Stark, G., Smith, P. L., Pickering, J. C., and Thorne, A. P.: High-resolution photoabsorption cross section measurements of SO2, 2: 220 to 325 nm at 295 K, Journal of Geophysical Research: Planets, 108, E2, https://doi.org/10.1029/2002je001931, 2003.

Sawyer, G. M., Carn, S. A., Tsanev, V. I., Oppenheimer, C., and Burton, M.: Investigation into magma degassing at Nyiragongo volcano, Democratic Republic of the Congo, Geochemistry, Geophysics, Geosystems, 9, 2, https://doi.org/10.1029/2007gc001829, 2008.

Shinohara, H.: A new technique to estimate volcanic gas composition: plume measurements with a portable multi-sensor system, Journal of Volcanology and Geothermal Research, 143, 319–333, https://doi.org/10.1016/j.jvolgeores.2004.12.004, 2005.

Stone, D., Whalley, L. K., and Heard, D. E.: Tropospheric OH and HO2 radicals: field measurements and model comparisons, Chemical Society Reviews, 41, 6348, https://doi.org/10.1039/c2cs35140d, 2012.

Strutt, J.: XV. On the light from the sky, its polarization and colour, The London, Edinburgh, and Dublin Philosophical Magazine and Journal of Science, 41, 107–120, https://doi.org/10.1080/14786447108640452, 1871.

Surl, L., Roberts, T., and Bekki, S.: Observation and modelling of ozone-destructive halogen chemistry in a passively degassing volcanic plume, Atmospheric Chemistry and Physics, 21, 12 413–12 441, https://doi.org/10.5194/acp-21-12413-2021, 2021.

Symonds, R. B., Rose, W. I., Bluth, G. J. S., and Gerlach, T. M.: Volcanic-gas studies; methods, results, and applications, Reviews in Mineralogy and Geochemistry, 30, 1–66, 1994.

Tirpitz, J.-L., Pöhler, D., Bobrowski, N., Christenson, B., Rdiger, J., Schmitt, S., and Platt, U.: Non-dispersive UV Absorption Spectroscopy: A Promising New Approach for in-situ Detection of Sulfur Dioxide, Frontiers in Earth Science, 7, https://doi.org/10.3389/feart.2019.00026, 2019.

Vaughan, M.: The Fabry-Perot Interferometer History, Theory, Practice and Applications, CRC Press, Boca Raton, ISBN: 978-08-527-4138-2, 1989.

von Glasow, R.: Atmospheric chemistry in volcanic plumes, Proceedings of the National Academy of Sciences, 107, 6594–6599, 2010.

Wagner, T., Burrows, J. P., Deutschmann, T., Dix, B., von Friedeburg, C., Frieß, U., Hendrick, F., Heue, K.-P., Irie, H., Iwabuchi, H., Kanaya, Y., Keller, J., McLinden, C. A., Oetjen, H., Palazzi, E., Petritoli, A., Platt, U., Postylyakov, O., Pukite, J., Richter, A., van Roozendael, M., Rozanov, A., Rozanov, V., Sinreich, R., Sanghavi, S., and Wittrock, F.: Comparison of box-air-mass-factors and radiances for Multiple-Axis Differential Optical Absorption Spectroscopy (MAX-DOAS) geometries calculated from different UV/visible radiative transfer models, Atmospheric Chememistry and Physics, 7, 1809–1833, https://doi.org/10.5194/acp-7-1809-2007, 2007.

Wagner, T., Beirle, S., Benavent, N., Bösch, T., Chan, K. L., Donner, S., Dörner, S., Fayt, C., Frieß, U., García-Nieto, D., Gielen, C., González-Bartolome, D., Gomez, L., Hendrick, F., Henzing, B., Jin, J. L., Lampel, J., Ma, J., Mies, K., Navarro, M., Peters, E., Pinardi, G., Puentedura, O., Puķīte, J., Remmers, J., Richter, A., Saiz-Lopez, A., Shaiganfar, R., Sihler, H., Roozendael, M. V., Wang, Y., and Yela, M.: Is a scaling factor required to obtain closure between measured and modelled atmospheric O4 absorptions? An assessment of uncertainties of measurements and radiative transfer simulations for 2 selected days during the MAD-CAT campaign, Atmospheric Measurement Techniques, 12, 2745–2817, https://doi.org/10.5194/amt-12-2745-2019, 2019.

Warnach, S., Bobrowski, N., Hidalgo, S., Arellano, S., Sihler, H., Dinger, F., Lübcke, P., Battaglia, J., Steele, A., Galle, B., Platt, U., and Wagner, T.: Variation of the BrO/SO2 Molar Ratio in the Plume of Tungurahua Volcano Between 2007 and 2017 and its Relationship to Volcanic Activity, Frontiers in Earth Science, 7, https://doi.org/10.3389/feart.2019.00132, 2019.

Wennberg, P.: Atmospheric chemistry: Bromine explosion, Nature, 397, 299–301, https://doi.org/10.1038/16805, 1999.

Willbourn, A. H. and Hinshelwood, C. N.: The mechanism of the hydrogen-oxygen reaction I. The third explosion limit, Proceedings of the Royal Society of London. Series A. Mathematical and Physical Sciences, 185, 353–369, https://doi.org/10.1098/rspa.1946.0023, 1946.

Wittmer, J., Bobrowski, N., Liotta, M., Giuffrida, G., Calabrese, S., and Platt, U.: Active alkaline traps to determine acidic-gas ratios in volcanic plumes: Sampling techniques and analytical methods, Geochemistry, Geophysics, Geosystems, 15, 2797–2820, https://doi.org/10.1002/2013gc005133, 2014.

Wolfe, G. M., Nicely, J. M., Clair, J. M. S., Hanisco, T. F., Liao, J., Oman, L. D., Brune, W. B., Miller, D., Thames, A., Abad, G. G., Ryerson, T. B., Thompson, C. R., Peischl, J., McKain, K., Sweeney, C., Wennberg, P. O., Kim, M., Crounse, J. D., Hall, S. R., Ullmann, K., Diskin, G., Bui, P., Chang, C., and Dean-Day, J.: Mapping hydroxyl variability throughout the global remote troposphere via synthesis of airborne and satellite formaldehyde observations, Proceedings of the National Academy of Sciences, 116, 11 171–11 180, https://doi.org/10.1073/pnas.1821661116, 2019.

Danksagungen, Expression of thanks

Ich badanke mich herzlich bei Ulrich Platt für die Möglichkeit diese Doktorarbeit durchzuführen, für das hohe Maß an Freiheit und Vertrauen, die wertvollen Ratschläge und viele erleuchtende Ideen. Es waren meist sehr unterhaltsame Diskussionen, die mir in Erinnerung bleiben werden und mein Wissenschaftsverständnis über die Jahre prägten.

Nicole, insgesamt haben wir wohl fast ein halbes Jahr zusammen auf Feldkampagnen verbracht. Tagelange Anreisen, Zelten, kalte und windige Vulkanspitzen, aber auch ab und zu wärmende Lava. Im Nachhinein ist die Fülle an Erinnerungen an einzigartige und unglaubliche Erlebnisse kaum fassbar (vorallem in Worten). Ohne Deine Erfahrung, Begeisterung und Anbindung an die Vulkangas-Community wäre diese Arbeit kaum möglich gewesen. Vielen Dank für alles!

Danke Chris für die gute Zeit, ob am IUP, am Ätna oder beim meditativen Brombeerjäten im Garten. Du hast die Fabry-Pérot-Kameras zu Deinem Projekt gemacht und es bedeutend weitergeführt. Nach dem ich selbst Jahre daran gearbeitet habe bedeutet das viel für mich und es war das Größte die Begeisterung daran mit Dir teilen zu können.

Ich danke Thomas Wagner für viele wertvolle Diskussionsbeiträge und Ratschläge und für gelegentliches unkompliziertes finanzielles Aushelfen. Es war außerdem bereichernd für meine Doktorarbeit weiterhin ein Mitglied Deiner Arbeitsgruppe in Mainz bleiben zu können.

Ganz herzlich danke ich auch Simon, Sanam, Nicole, Marcel, Chris und Lukas T. für hilfreiche Kommentare und Korrekturen zu dieser Arbeit.

Thomas Leisner danke ich herzlich für die Übernahme des Zweitgutachtens.

Ich danke André Butz für das Vertrauen und die Unterstützung nach seinem Einzug ins IUP (Laborplatz, etc.) sowie für die Genehmigung speziellerer Dienstreisen.

Ich danke allen heutigen und früheren Kollginnen und Kollegen am IUP für das angenehme Umfeld. Die Gemeinschaft bei vielen Kaffee- und Mittagspausen, Konferenzbesuchen oder Messkampagnen bleiben in schöner Erinnerung und boten neben fachlichen Diskussionen oft auch Antrieb, Halt und natürlich viel Spaß. Besonders möchte ich mich diesbezüglich bei Lukas Tirpitz, Christopher Fuchs, Simon Warnach und Ralph Kleinschek bedanken. Außerdem bei: Peter Lübcke, Leif Vogel, Stefan Schmitt, Holger Sihler, Leon Kuhn, Florian Dinger, Udo Frieß, Martin Horbanski, Denis Pöhler, Johannes Lampel, Moritz Schöne, Juan Sebastian Moreno Ordonez, Alexander Nies, Maja Rüth, Joshua Marks, Jaro Heimann, Katja Bigge, Marvin Knapp, Tobias Schmitt, Lukas Pilz, Benedikt Hemmer, Sanam Vardag.
Weiterhin danke ich der Satelliten-Gruppe am MPI in Mainz für die schöne Zeit dort, viele hilfreiche Diskussionen und das kurzfristige Ausleihen von Messgeräten.

In the scope of this thesis I was lucky to be part of many small groups of people that met at volcanoes to conduct field campaigns or organise summer schools. I want to express my thanks for their invaluable contribution to enabling the field measurements of this thesis, for sharing experience in the field, and for their reliability and pleasant company, in particular:
Giovanni Giuffrida, Sergio Calabrese, Marco Liuzzo, Guillaume Boudoire, Kyriaki Daskalopoulou, Giovanella Pecoraino, Luciana Randazzo, Artur Ionescu, Silvana Hidalgo, Jorge Córdova, Zoraida Chacon Ortiz, Gustavo Garcon Valencia, Maria Clara Lamberti, Mariano Agusto, Sebastian Garcia, Emmanuel Dekemper, Dario Tedesco, Katcho Karume, Pierre-Yves Burgi, Patrick Marcel, Thorsten Hoffmann.

I gratefully thank Vinod Kumar for organising and including me to this amazing, extreme and rewarding measurement campaign in the Rann of Kachchh. I also like to mention Hareendra Baraiya and thank him for being such a warm and creative host in the desert. Furthermore, I thank

Abhishek Mishra, Gaurav Sharma for their great hospitality at IISER Mohali.

Ich danke meinen Freundinnen und Freunden. In der schönen Zeit, der Ablenkung, der Geborgenheit und der Unterstützung die ich durch Euch erfahren habe liegt ein bedeutender Beitrag zu dieser Arbeit. Danke Marcel, Laura, Miguel, David, Felix, Lisa, Jannis, Selma ihr habt euch besonders oft meine Sorgen zur Doktorarbeit angehört oder wart meiner zeitweise vielleicht auch beängstigend überschwänglichen Begeisterung ausgesetzt. Danke Anja.

Ich danke meiner Familie, besonders meinen Eltern Susanne und Martin und meinen Geschwistern Simone, Peter und Verena. Eure Unterstützung war immer das Selbstverständlichste und zusammen mit der Erfahrung von Heimat und Geborgenheit ein unschätzbares Privileg. Danke, dass ihr da seid.